

# Freeze Casting of Ceramics: Pore Design from Solidification Principles

Thesis by  
Noriaki Arai

In Partial Fulfillment of the Requirements for the  
Degree of  
Doctor of Philosophy

The logo for the California Institute of Technology (Caltech), featuring the word "Caltech" in a bold, orange, sans-serif font.

CALIFORNIA INSTITUTE OF TECHNOLOGY  
Pasadena, California

2021  
Defended October 26, 2020

© 2021

Noriaki Arai

ORCID: 0000-0002-3040-2997

All rights reserved

*To Shiori and Luna.*

## ACKNOWLEDGEMENTS

First and foremost, I am sincerely grateful to my advisor, Professor Katherine Faber, for your patience and support during my graduate study. For five years, your continuous guidance have shaped me as a researcher, and your encouragement cultivated my entrepreneurial mindset to ask important research questions and to pursue originality. Joining the Faber group was one of the best decisions I have made at Caltech.

To Professor Brent Fultz, Professor Julia Kornfield, and Professor William Johnson: thank you for serving as committee members in both my candidacy examination and defense, and providing invaluable support and advice on my research. Professor Kornfield, it was exciting to work with you on different projects. Your advice always let me look at researches from different perspectives and drove me to explore new ideas.

I would like to thank all the people I have worked with. Professor Peter Voorhees, thank you for the insightful discussions. Your broad and deep knowledge on solidification led us to a new research and a collaboration with Dr. Tiberiu Stan, Sophie Macfarland, Dr. Nancy Senabulya, and Professor Ashwin Shahani. Thank you all for your guidance, patience and all the fruitful discussions. I also would like to thank Professor Paolo Colombo for your support and advice regarding preceramic polymers. I also enjoyed the visit to the University of Padova.

At Caltech, I had the privilege to work with Orland Bateman, on a multiple projects for almost three years. I enjoyed and learned from you a lot. I also enjoyed the time I spent together with your families outside researches. I would like to thank Dr. Mamadou Diallo for your guidance and weekly tutorial sessions.

To the Faber group, Matthew Johnson, Maninpat Naviroj, Neal Brodник, Claire Kuo, Xiaomei Zeng, Benjamin Herren, Rafa Cabezas Rodríguez, Celia Chari, Vince Wu, Laura Quinn, Natalie Nicolas, Carl Keck, Christopher Long, thank you for all your comments and feedback during the group meeting and for reviewing my papers.

I also would like to thank the administrative staff, Angie Riley, Christy Jenstad, Celene Gates and Jennifer Blankenship for making sure that I can focus on my research, travel for the conferences safely, and stay safe during this pandemic.

I would like to acknowledge Kenji Higashi, Dr. Hitoshi Ohmori, and Dr. Koji

Ishibashi, who encouraged me to pursue this career. I would not be able to come this far without your understanding and support.

This five-year journey would not have been possible without unconditional support from my entire family in Japan: my father, my mother, Michiko, Hatsuko, Tomoe, Tsutomu, Yuko, Soma, and Masaki. My studies abroad have not been possible without your support.

Lastly, but most importantly, thank you so much, Shiori and Luna, for your love, support and dedication. The achievements at Caltech belong to all of us. I am looking forward to what awaits us in the future.

- Nori

## ABSTRACT

Freeze casting is a porous material processing method which allows the creation of directionally aligned pores by the solidification process. Pores are generated by sublimation of solidified crystals which reject suspending particles or dissolved solutes during freezing. Although freeze-cast ceramics have been identified for applications such as filtration and bioceramics, the lack of understanding of the process often results in a discrepancy between the desired pore structure and the fabricated structures.

Since solidification is the foundation upon which freeze casting is built, this work seeks to understand the solidification process, especially the growth and time evolution of dendrites. To understand the dendritic growth process, two solidification parameters, freezing front velocity and temperature gradient, are independently controlled to investigate the effects of each parameter. Dendritic pore size changes with solidification parameters and shows good agreement with dendrite growth theory. The theory of constitutional supercooling serves as a guide to control pore morphology between dendritic pores and cellular pores. Furthermore, dendrite growth under the effects of the gravitational force is investigated by changing the solidification direction with respect to the gravity direction. Convection changes the degree of constitutional supercooling, and results in different pore sizes as well as pore morphology.

Time evolution of dendrites through isothermal coarsening is investigated. During the coarsening of dendrites, they are transformed to cylinder-like crystals, which yield honeycomb-like structures. Moreover, dendrite size changes linearly with the cube root of coarsening time. Both findings are well-established phenomena in alloy solidification. Further comparison with alloy systems are achieved with tomography-based analysis where similar microstructural evolution with alloy system is demonstrated.

Based upon the understanding of underlying solidification principles in freeze casting, three applications are explored. First, the freeze-cast structure is designed to improve shape-memory properties. Processing variables are controlled such that shape-memory porous zirconia can enable martensitic phase transformations and shape deformation without fracture. Other applications utilize unique pore space. Dendritic pores are investigated for size-based filtration to preferentially capture

small particles. Flow-through experiments and in-situ observation by confocal microscopy confirm that pores created by secondary dendrites capture small particles. Finally, honeycomb-like structures are filled with functional microgels to create a ceramic/polymer composite as an application for membrane chromatography. The fabricated composite demonstrates advantages such as mechanical stability during the fluid flow.

## PUBLISHED CONTENT AND CONTRIBUTIONS

- [1] Noriaki Arai and Katherine T. Faber. “Freeze-cast Honeycomb Structures via Gravity-Enhanced Convection”. *In Preparation*, 2020  
N. Arai performed experimental design, sample fabrication, characterization, and data analysis.
- [2] Noriaki Arai and Katherine T. Faber. “Gradient-controlled freeze casting of preceramic polymers”. *In Preparation*, 2020  
N. Arai performed experimental design, sample fabrication, characterization, and data analysis.
- [3] Noriaki Arai, Tiberiu Stan, Sophie Macfarland, Peter W. Voorhees, Nancy Senabulya, Ashwin J. Shahani, and Katherine T. Faber. “Coarsening of dendrites in freeze-cast ceramic systems”. *In Preparation*, 2020  
N. Arai designed experiments, fabricated samples, performed SEM imaging and pore size measurement by mercury intrusion porosimetry, and analyzed the data.
- [4] Orland Bateman, Noriaki Arai, Julia A. Kornfield, Mamadou S. Diallo, and Katherine T. Faber. “Freeze-cast SiOC/mixed matrix PVDF membrane composite for chromatography for monoclonal antibody polishing”. *In Preparation*, 2020  
N. Arai and O. Bateman contributed equally to this work. N. Arai fabricated and analyzed freeze-cast ceramics. N. Arai also performed SEM imaging and water flux measurement.
- [5] Noriaki Arai and Katherine T. Faber. “Hierarchical porous ceramics via two-stage freeze casting of preceramic polymers”. In: *Scripta Materialia* 162 (Mar. 2019), pp. 72–76. ISSN: 13596462. DOI: 10.1002/adem.201900398. URL: <https://doi.org/10.1016/j.scriptamat.2018.10.037>.  
N. Arai performed experimental design, sample fabrication, characterization, mechanical and permeability test, and data analysis.
- [6] Xiaomei Zeng, Noriaki Arai, and Katherine T. Faber. “Robust Cellular Shape-Memory Ceramics via Gradient-Controlled Freeze Casting”. In: *Advanced Engineering Materials* 21.12 (Dec. 2019), p. 1900398. ISSN: 1438-1656. DOI: 10.1002/adem.201900398. URL: <https://onlinelibrary.wiley.com/doi/abs/10.1002/adem.201900398>.  
X. Zeng and N. Arai both contributed to this work equally.



## TABLE OF CONTENTS

Acknowledgements . . . . .	iv
Abstract . . . . .	vi
Published Content and Contributions . . . . .	viii
Table of Contents . . . . .	viii
List of Illustrations . . . . .	xi
List of Tables . . . . .	xxi
Chapter I: Introduction . . . . .	1
1.1 Motivation . . . . .	1
1.2 Objectives . . . . .	1
1.3 Thesis organization . . . . .	2
Chapter II: Background . . . . .	3
2.1 Review of the porous ceramic processing method . . . . .	3
2.2 Freeze casting . . . . .	5
2.3 Solidification . . . . .	14
2.4 Polymer-derived ceramics (PDC) . . . . .	19
Chapter III: Gradient-Controlled Freeze Casting . . . . .	31
3.1 Introduction . . . . .	31
3.2 Experimental methods . . . . .	33
3.3 Results . . . . .	35
3.4 Discussions . . . . .	39
3.5 Conclusion . . . . .	44
Chapter IV: Freeze-cast Honeycomb Structures via Gravity-Enhanced Con- vection . . . . .	46
4.1 Introduction . . . . .	46
4.2 Experimental methods . . . . .	47
4.3 Results . . . . .	48
4.4 Discussions . . . . .	51
4.5 Conclusion . . . . .	54
Chapter V: Coarsening of Dendrites in Freeze-Cast Systems . . . . .	57
5.1 Introduction . . . . .	57
5.2 Experimental methods . . . . .	58
5.3 Analysis of XCT images . . . . .	61
5.4 Results and discussion . . . . .	65
5.5 Conclusions . . . . .	80
Chapter VI: Application of Freeze-Cast Structure: Microstructural Engineer- ing of Material Space for Functional Properties . . . . .	85
6.1 Introduction . . . . .	85
6.2 Experimental methods . . . . .	88
6.3 Results and discussion . . . . .	90

6.4 Conclusions . . . . .	102
Chapter VII: Applications of Freeze-Cast Ceramics: Pore Space Design for Filtration . . . . .	105
7.1 Size-based filtration by dendritic pores . . . . .	105
7.2 Ceramic/polymer composites for membrane chromatography . . . . .	119
Chapter VIII: Summary and Future Work . . . . .	129
8.1 Summary and conclusions . . . . .	129
8.2 Suggestions for Future work . . . . .	131
Appendix A: Hierarchical Pore Structure . . . . .	136
A.1 Introduction . . . . .	136
A.2 Experimental methods . . . . .	137
A.3 Results and discussion . . . . .	139
Appendix B: Freezing conditions . . . . .	149
Appendix C: Comparison of the conventional freezing and the gradient con- trolled freezing . . . . .	150
Appendix D: Influence of preceramic polymer concentration . . . . .	152

## LIST OF ILLUSTRATIONS

<i>Number</i>	<i>Page</i>
2.1 A schematic showing three different types of porous material processing methods [1]. This figure is reproduced with permission. . . .	3
2.2 Micrographs showing porous materials fabricated by the replica method (LiCoO <sub>2</sub> cathode by wood templating) [3], the sacrificial template method (macroporous SiC fabricated by silica template) [6] and (c) direct foaming (porous SiOC) [7]. Figures are reproduced with permission. . . . .	5
2.3 A diagram showing the freeze casting process [19]. . . . .	6
2.4 Pictures during the directional solidification of (a) suspension and (b) solution [18]. . . . .	8
2.5 SEM images showing freeze-cast SiOC with dendritic pores from (a, b) solution and (c, d) suspension [19]. . . . .	10
2.6 SEM images showing three different freeze-cast structures: (a) isotropic structure from cyclooctane, (b) dendritic structure from cyclohexane, and (c) lamellar structure from dimethyl carbonate [19]. The solutions were frozen with a freezing front velocity of 15 $\mu\text{m/s}$ . . . . .	10
2.7 Pore size distribution of dendritic pores showing the effect of pre-ceramic polymer concentration [18]. . . . .	11
2.8 Longitudinal SEM image of (a) a 20 wt.% polymer concentration and XCT image of (b) a 5 wt.% polymer concentration in cyclohexane [18].	11
2.9 A sample freeze-cast (a) and (b) without a polydimethylsiloxane (PDMS) wedge frozen with (b) multiple nucleation site and a single vertical temperature gradient. It shows short-range lamellar pores in (c) the SEM image. A sample freeze-cast (d) with a PDMS wedge frozen (e) with a confined nucleation site and a dual temperature gradient: vertical temperature gradient and horizontal temperature gradient. It shows long-range lamellar pores in (f) the SEM image. From ref. [36]. Reprinted with permission from AAAS. . . . .	13

2.10	A schematic of the constitutional gradient during solidification and the liquidus temperature gradient ahead of the freezing front. The applied temperature gradient, $G = \left(\frac{dT_q(z)}{dz}\right)_{z=0}$ , is lower than the liquidus temperature gradient, $G_c = \left(\frac{dT_L(z)}{dz}\right)_{z=0}$ , resulting in the constitutional supercooling (cross-hatched region) [24] Credit:W. Kurz and D. J. Fisher, Fundamentals of solidification, Third edition, Trans Tech Publication, 1992. . . . .	15
2.11	Illustrations showing (a) small perturbation grow and (b) small perturbation disappear [24]. Credit:W. Kurz and D. J. Fisher, Fundamentals of solidification, Third edition, Trans Tech Publication, 1992. . . . .	17
2.12	A schematic showing the stability of the interface as a function of wavelength for Al-2wt.%Cu [24]. Credit:W. Kurz and D. J. Fisher, Fundamentals of solidification, Third edition, Trans Tech Publication, 1992. . . . .	18
2.13	Images showing (a) non-faceted crystals (dendrites) and (b) faceted crystals [47]. This figure is reproduced with permission. . . . .	18
2.14	Free energy curve as a function of adatom coverage with different values of the Jackson $\alpha$ factor [48]. This figure is reproduced with permission. . . . .	20
2.15	Optical micrographs showing freezing microstructures of preceramic polymer solutions with (a) cyclooctane, (b) cyclohexane, (c) tert-Butanol, and (d) dimethyl carbonate [18]. . . . .	20
2.16	Si-based preceramic polymer with different backbones [54]. This figure is reproduced with permission. . . . .	21
2.17	A model for the nanodomains in SiOC [68]. This colored image was taken from [54]. This figure is reproduced with permission. . . . .	23
3.1	Stability-microstructure map showing the independent control of freezing front velocity and temperature gradient allows one to change crystal morphology (a). Modified from ref. [9]. (b) Illustration of cells and dendrites. . . . .	32
3.2	A photograph showing gradient-controlled freeze-casting setup. . . . .	34

3.3	SEM images showing a control sample at (a) low and (b) high magnifications and a gradient-controlled sample at (c) low and (d) high magnifications in transverse direction. Yellow arrows in low magnification and high magnification images indicate primary pores and tertiary pores, respectively. (e) Pore size distribution of control sample and gradient-controlled sample. . . . .	36
3.4	SEM images of the sample frozen with $V = 17 \mu\text{m/s}$ and $G = 2.2 \text{ K/mm}$ in (a) transverse and (b) longitudinal direction, the sample frozen with $V = 1.8 \mu\text{m/s}$ and $G = 2.4 \text{ K/mm}$ in (c) transverse and (d) longitudinal direction, and the sample frozen with $V = 1.5 \mu\text{m/s}$ and $G = 5.0 \text{ K/mm}$ in (e) transverse and (f) longitudinal direction. (g) A stability-microstructure map showing examined conditions by colored marker. (h) Pore size distributions of corresponding samples. . . . .	38
3.5	SEM images showing dendritic structure from (a) 20 wt.% solution and (b) 10 wt.% solution in transverse direction. (c) Corresponding pore size distribution from MIP. . . . .	39
3.6	SEM images showing a SiOC from cyclohexane crystals (20 wt.% polymer solution) in (a) transverse and (b) longitudinal directions, from cyclohexane crystals (10 wt.% polymer solution) in (c) transverse and (d) longitudinal directions, and from dioxane crystals in (e) transverse and (f) longitudinal directions. . . . .	40
3.7	Plots of (a) Primary pore size as a function of $V$ with different $G$ and (b) secondary pore size as a function of cooling rate. . . . .	41
4.1	Freeze-casting setup of (a) conventional freezing and (b) convection-enhanced freezing. (c) Freezing front position as a function of time with images of (d) the freezing front in conventional freezing, and in convection-enhanced freezing at (e) $t = 45 \text{ min}$ and (f) $t = 47 \text{ min}$ (Red dashed line indicates the freezing front), and (g) the associated freezing front velocity and temperature gradient as a function of freezing front position. . . . .	48

4.2	SEM images of conventional freeze-cast samples showing transverse images at (a) FFP is $\sim 1.6$ mm and (b) FFP is $\sim 5$ mm from nucleation face, and (c) longitudinal image. SEM images of convection-enhanced freeze-cast sample showing transverse images (d) FFP is $\sim 1.6$ mm and (e) FFP is $\sim 5$ mm from nucleation face, and (f) longitudinal image. Yellow arrows indicate freezing direction, $v$ , and gravity direction, $g$ . Red lines in (c) and (f) indicate the nucleation face	49
4.3	Pore size distribution data from (a) nucleation section and (b) middle section from samples from conventional freezing and convection-enhanced freezing. . . . .	50
4.4	Illustrations showing temperature and concentration variation in (a) conventional freezing and (b) convection-enhanced freezing. (c) An illustration showing convective flows in liquid phase in convection-enhanced freezing. (d) Stability-microstructure map. (e) Pore size distribution of conventional freeze-cast sample frozen under $0.7 \mu\text{m/s}$ and $4.9 \text{ K/mm}$ . (f) Porosity difference between top section and three sections (middle-top, middle-bottom, and bottom). Three samples were investigated for each freezing direction. . . . .	51
5.1	Schematic of the gradient-controlled freeze casting setup . . . . .	59
5.2	Cross-section of XCT data from (a) a control sample, (b) a sample coarsened at $2^\circ\text{C}$ for one hour, and (c) a sample coarsened at $4^\circ\text{C}$ for three hours. Scale bar: $200 \mu\text{m}$ . . . . .	61
5.3	A map of interfacial shapes of patches for the Interfacial Shape Distribution (ISD). This is a modified figure from ref. [20]. . . . .	62
5.4	SEM images showing (a, b) control sample, and sample coarsened at (c, d) $2^\circ\text{C}$ for one hour, (e, f) $2^\circ\text{C}$ for three hours, (g, h) $4^\circ\text{C}$ for one hour, and (i, j) $4^\circ\text{C}$ for three hours. Inset images in (a) and (b) show primary pore and secondary pores, respectively, as indicated by red arrows, (scale bar: (a) $60 \mu\text{m}$ and (b) $40 \mu\text{m}$ ). Transverse images and longitudinal images show cross-sections perpendicular and parallel to the freezing direction, respectively. . . . .	64
5.5	SEM images showing longitudinal direction of (a) the control sample and (b) the sample coarsened at $4^\circ\text{C}$ for one hour. Flat surface and circular surface are indicated by red arrows in (a) and (b), respectively.	66

5.6	SEM images of the samples coarsened at 4 °C for three hours (a: Transverse image, b: Longitudinal image) and five hours (c: Transverse image, d: Longitudinal image). . . . .	66
5.7	Pore size distribution data of samples coarsened for 30 minutes and one hour at (a) 2 °C and (b) 4 °C (including three hours). . . . .	67
5.8	Primary pore fraction as a function of coarsening time. . . . .	68
5.9	Plots of (a) Primary pore size and (b) secondary pore size as a function of the cube root of coarsening time at different coarsening temperatures. . . . .	68
5.10	Illustration showing four different coarsening models for secondary arm coarsening: (1) radial remelting, (2) axial remelting, (3) arm detachment, and (4) arm coalescence. Based on ref. [27]. . . . .	70
5.11	Pore size distribution from samples coarsened at 2 °C for three hours and 4 °C for one hour (a). SEM images showing a sample coarsened at (b, c) 2 °C for three hours, and (d, e) 4 °C for one hour. (Red arrows indicate some of the thin solid tubes). . . . .	73
5.12	3D XCT reconstructions and subsections for the (a, d) control sample, (b, e) the sample coarsened at 2 °C for one hour, and (c, f) sample coarsened at 4 °C for three hours. The sides of the solid-pore interfaces that face the dendritic pores are colored according to the normalized mean curvature ( $H/S_S$ ), as indicated by the color bar in (c). White arrows in (e) show secondary pores with positive curvature caps, while the red arrow indicates a ligature with negative curvature. . . . .	74
5.13	Interface Shape Distributions (ISDs) for the (a) control sample, (b) sample coarsened at 2 °C for one hour, and (c) sample coarsened at 4 °C for three hours. (d) Map of the interface shapes possible in an ISD where P is pore and S is solid. This is a modified figure from ref. [20]. Sections of the 2 °C coarsened sample cylindrical patches colored in red (e) and porous caps colored in pink (f). . . . .	77
5.14	Interface Normal Distributions (INDs) for the (a) control sample, (b) sample coarsened at 2 °C for one hour, and (c) sample coarsened at 4 °C for three hours. The green arrow in (a) corresponds to the green patches in (d). The purple arrow in (b) corresponds to purple patches in (e). The blue arrow in (b) corresponds to the blue patches in (f). . . . .	79
6.1	A schematic showing shape-memory effect and superelastic effect [2]. This figure is reproduced with permission. . . . .	86

6.2	Stability-microstructure map based on constitutional supercooling of a solid–liquid interface controlled by freezing front velocity and temperature gradient (modified based on Rettenmayr and Exner [13]). Schematic illustration of b) dendrites and c) cells. . . . .	87
6.3	The proposed shape-memory effect in a unidirectional cellular structure during uniaxial compression and heat treatment. The red highlights represent transformed grains within the cellular walls. . . . .	88
6.4	Plots showing (a) freezing front velocity and (b) temperature gradient as a function of frozen height. . . . .	89
6.5	Stability-microstructure map based on measured freezing front velocity and temperature gradient of cyclohexane, with the corresponding longitudinal microstructures of freeze-cast zirconia-based ceramics. . . . .	91
6.6	Microstructure of freeze-cast cellular zirconia-based ceramics viewed from (a) the transverse (the inset image shows an off-axis view of pores) and (b) the longitudinal directions. Oligocrystalline cellular walls from (c) the transverse and (d) longitudinal directions. (e) Pore size distribution within the measurement range of 100 nm–80 $\mu\text{m}$ from mercury intrusion porosimetry, with inserted sample image after machining. . . . .	92
6.7	Stress–strain behavior of the cellular structure ( $v = 1.43 \mu\text{m s}^{-1}$ ), transitional structure ( $v = 3.87 \mu\text{m s}^{-1}$ ), and dendritic structure ( $v = 11.57 \mu\text{m s}^{-1}$ ) under a compressive stress of 25 MPa (a). (b) The evolution of phase content on compression and after heat treatment, with inserted XRD patterns of cellular structure corresponding to each condition. (c) Stress–strain curves of the transitional structure tested consecutively at stresses from 10 to 40 MPa. (d) The change in the monoclinic content of all samples after compression as a function of applied stress, with inserted XRD patterns of the transitional structure in between each compression test. . . . .	93
6.8	XRD spectrum of a sample (a) after machining, and (b) after annealing without experiencing mechanical compression. . . . .	94
6.9	The stress-strain curve of the sample used for the shape recovery measurement. . . . .	95
6.10	Stress-strain curves showing (a) five loading-unloading cycles. (b) Monoclinic composition after each five cycles and after each anneal. . . . .	98



6.11	Slope of stress-strain curves as a function of applied stress (a). Each data represents the slope of the 5th loading cycles from each set of five loading-unloading cycles. (b) Magnified plateau region. . . . .	98
6.12	Stress-strain curves showing five loading-unloading steps at 10 MPa, 20 MPa, and 24 MPa. . . . .	100
6.13	Slopes of stress-strain curves as a function of applied stress(a). XRD peak before and after compression (b). . . . .	101
6.14	Slope of stress-strain curves as a function of the applied stress. The material was compressed to 24 MPa for 5 times, and above. . . . .	101
7.1	A graph showing patient survival rate and patients with effective antibiotic therapy [1]. . . . .	106
7.2	Illustration of (a) elasto-inertial based particle focusing and separation [7] (Reproduced under Creative Commons) and (b) larger cells enter into vortices due to the larger net-force acting on larger cells [8] (Reproduced with permission.) . . . . .	107
7.3	An illustration showing fluid flow in the dendritic pores. Large blood cells flow through the primary pores while small pathogens enter a recirculating flow in secondary pores. . . . .	108
7.4	Cooling profiles for top and bottom thermoelectric plates to create a dual structure. The red-shaded region creates dendritic pores and the green-shaded region creates cellular pores. . . . .	109
7.5	A picture of the flow-through experimental setup. . . . .	111
7.6	A picture of the confocal microscope setup. . . . .	112
7.7	An SEM image and pore size distribution of a membrane used in the flow-through study. . . . .	112
7.8	Pictures of freeze-cast SiOC pyrolyzed under (a) Ar and (b) Ar with water vapor. . . . .	114
7.9	Pictures showing SiOC pyrolyzed under Ar and H <sub>2</sub> O atmosphere with pores filled with (a) air, (b) DI water, and (c) canola oil (n: refractive index). . . . .	115
7.10	Overlay of bright field and fluorescence micrographs from laser scanning confocal microscope. The series of micrographs shows a 2 μm particle (indicated by the red arrow) flowing along the main channel and being captured at the side cavity after 45 seconds. . . . .	116

7.11	SEM images showing transverse direction of dendritic structure after flow-through experiment at (a) low magnification and (b) high magnification. SEM images showing transverse direction of honeycomb-like structure after flow-through experiment at (c) low magnification and (d) high magnification. Some of the 2 $\mu\text{m}$ and a group of the 0.3 $\mu\text{m}$ particles are indicated by yellow and red circles, respectively. . . . .	117
7.12	SEM images showing (a) longitudinal direction and transverse direction of (b) cellular pore region, and (c) dendritic pore region. (d) Pore size distribution of a dual structure. . . . .	118
7.13	A schematic of (a) permeability setup. A figure taken from [20]. (b) A picture of an acrylic fixture. (c) An illustration of side view of the acrylic fixture holding a composite. . . . .	122
7.14	SEM images showing a composite without gel layer ((a) transverse and (b) longitudinal direction) and a composite with gel layer ((c) transverse and (d) longitudinal direction) . . . . .	123
7.15	An SEM image showing a PVDF membrane, PEI gel layer, and SiOC wall. Yellow dashed lines indicate boundaries between a gel layer and SiOC wall. . . . .	124
7.16	An SEM image showing a thickness of around 1.5 mm composite. . . . .	125
7.17	A plot of (a) water flux and pressure drop as a function of time. (b) Water flux at different pressure drops as a function of time (from the study by Kotte et al. [13]). This figure is reproduced with permission. SEM images of (c) inlet and (d) outlet side after permeability measurement with sample pictures as insets. . . . .	126
8.1	SEM images of freeze-cast structures using cyclooctane as a solvent in longitudinal direction. As the higher temperature gradient is applied, the directionality of pores improved. Left image is taken from a study by Naviroj et al. [1] . . . . .	131
8.2	SEM images showing freeze-cast lamellar structures with (a) 5 minutes and (b) 6 hours of stirring after adding the cross-linking agent. . . . .	132
8.3	Compressive strength and permeability constants of different structures. Data for "Lamellar 15 $\mu\text{m/s}$ " and "Dendritic 15 $\mu\text{m/s}$ " are taken from the work by Naviroj [2]. . . . .	133
8.4	A stability-microstructure map with an arrow indicating an increase of diffusion coefficient results in change in stability criterion. . . . .	134

A.1	Freezing solution by (a) conventional unidirectional freezing and (b) conventional conditions coupled with mold heating. . . . .	137
A.2	SEM images of a plane perpendicular to the freezing direction from (a) single-stage freeze casting with 20 vol% polymer concentration, (b) two-stage freeze casting with 5 vol% polymer concentration at the second stage, (c) two-stage freeze casting with 10 vol% polymer concentration at the second stage. (d) Schematic illustration showing bridge formation during the second stage. . . . .	139
A.3	Compressive strength by single-stage freeze casting and two-stage freeze casting (a). (b) Load displacement curve of single-stage freeze-cast sample. (c) Load displacement curve of two-stage freeze-cast sample. The insets show samples after compression. Note the difference in y-axis scales in (b) and (c). . . . .	140
A.4	Example of a domain boundary in (a) single-stage freeze-cast sample (20 vol.%), and (b) two-stage freeze-cast sample (5 vol.% at the second stage). . . . .	142
A.5	Load-displacement curve of the two-stage freeze-cast sample which exhibited noticeable low strength. The inset shows sample after compression. . . . .	142
A.6	Permeability constants of samples by single-stage freeze casting and two-stage freeze casting. . . . .	143
A.7	Compressive strength and permeability constants compared to the Naviroj study on lamellar and dendritic pore structures [11]. . . . .	144
A.8	SEM images of two-stage freeze-cast SiOC using DMC as the solvent in the first stage and cyclohexane at the second stage. (a) Transverse image (a plane perpendicular to freezing direction) and (b) longitudinal image (a plane parallel to freezing direction). . . . .	145
A.9	SEM images of the hierarchical pore structure in two-stage freeze-cast SiOC using cyclohexane as the solvent in the first stage and cyclooctane at the second stage at (a) low magnification and (b) high magnification. A grain-selection template [25] was used at the first stage. . . . .	146
C.1	Freezing profile of Conventional freezing ( $V = 15 \mu\text{m/s}$ ) and gradient-controlled freezing ( $V = 15 \mu\text{m/s}$ , $G = 2.6 \text{ K/mm}$ ) . . . . .	150
C.2	Pore size distribution from three different sections. . . . .	151

D.1 SEM images showing (a, b) a control sample, and (c,d) a sample coarsened at 3 °C for 1 hour. (e) Pore size distribution from 30 wt.% preceramic polymer solution. . . . .	152
---	-----

## LIST OF TABLES

<i>Number</i>	<i>Page</i>
5.1 The slope of linear fit from Figure 5.9 . . . . .	70
5.2 Metrics from the three XCT datasets. $S_S^{-1}$ is the inverse specific interface area, calculated as the total pore volume divided by the total solid-pore interface area. . . . .	76
6.1 Sample height and diameter before compression, after compression, and after heat treatment; associated residual and recovered displacements used to establish recovered strain. . . . .	96
7.1 Particles captured in the flow-through experiments. . . . .	113
A.1 Average porosity of single-stage freeze-cast samples and two-stage freeze-cast samples. . . . .	138
A.2 Bridge density of two-stage freeze-cast samples. . . . .	140
B.1 List of freezing front velocities and temperature gradients used in Chapter 3 for 20 wt.% polymer-cyclohexane solution. . . . .	149
C.1 List of the peak pore diameters for primary and secondary pores from Figure C.2 . . . . .	151

*Chapter 1*

## INTRODUCTION

**1.1 Motivation**

Porous ceramics can be found in many industrial applications such as filtration, catalyst supports, bioceramics, insulators, etc., and demands for engineered porosity have been driving porous ceramic processing research. Each application requires its own specification of pores, including pore concentration, size, morphology, and connectivity. Hence, it is essential to not only know the desired pore characteristics and properties, but also to have a deep understanding of the processing methods to manipulate pores. The present work was established based upon such needs. Directional freeze casting creates directionally aligned pores by using solidifying crystals, which push particles or segregated preceramic polymer aside, and act as sacrificial templates. Subsequent sublimation removes the frozen crystals, leaving pores in their place. Compared to other porous ceramic processing methods, this method indirectly controls the resulting pores through solidification. The long history of theoretical and experimental alloy solidification research provides a foundation to apply to freeze casting method to achieve control of pore characteristics. The majority of freeze casting studies involve suspensions, in which particles and dissolved additives (binders and dispersants) present complexities in thermal fields and solute fields in the liquid phase during solidification. Alternatively, solutions, which consist of only a solvent and solute, allows the application of alloy solidification principles to better understand the relationship between processing variables and the resultant freeze-cast structure. Hence, this is the focus of the present work.

**1.2 Objectives**

There are two objectives in the present work. The first objective is to understand the freeze casting process from the standpoint of fundamental solidification principles. Solidification parameters such as freezing front velocity and temperature gradient are independently manipulated so as to investigate their influence on pore structure. Moreover, the effects of the ubiquitous external force, the gravitational force, on dendrite growth was investigated. Because solidification microstructures are not only determined by the crystal growth process, but also the solidified crystals' evolution with time, the coarsening process is also explored. The morphological

changes and the relationship between coarsening time and pore size are investigated. Tomography-based curvature analysis is used to reveal the mechanism of coarsening. Taking what has been learned in solidification studies, the second objective is to create porous ceramics for engineering applications. Honeycomb shape-memory ceramics are created to mitigate intergranular cracking, unavoidable in bulk shape-memory ceramics. While this is an example of engineering porous microstructures to improve the functional properties of the material space, other examples are to utilize the pore space. Two examples are demonstrated. Size-based filtration is examined with the ultimate goal to isolate pathogens from the bloodstream. It is shown that small particles can be preferentially captured by dendritic pores. A ceramic/polymer composite for membrane chromatography is also examined, and enhanced mechanical stability is demonstrated.

### **1.3 Thesis organization**

Following this chapter, Chapter 2 provides background on porous ceramic processing methods, with much attention to the freeze casting process. It further includes a discussion of solidification principles and polymer-derived ceramics. In Chapter 3, fine tuning of the freeze casting process is explored through gradient-controlled directional solidification and the resultant pore structures are discussed. Chapter 4 discusses the effects of the gravitational force in gradient-controlled freeze casting. For the first time, an in-depth study of coarsening during freeze-casting is performed. These are reported in Chapter 5. The thesis then turns to freeze-casting examples which may show promise in engineering applications. Chapter 6 explores the creation of porous shape-memory ceramics and demonstrates the shape-memory effect. Chapter 7 explores two other applications: size-based filtration and ceramic/polymer composites for membrane chromatography, highlighting the diversity of pore structure and functionality. Finally, Chapter 8 summarizes the works and proposes future research directions. One additional example which provides hierarchical pore structure by two-stage freeze casting is discussed in Appendix A.

## Chapter 2

### BACKGROUND

#### 2.1 Review of the porous ceramic processing method

Ceramics has been of interest for various applications due to hardness, chemical inertness, high temperature resistance, and low electrical and thermal conductivity. Combining these properties with engineered porosity, porous ceramics can be used in various applications such as insulators, bio-medical implants, and filtration. Since each application requires different pore characteristics and networks, there is growing research on porous ceramic processing techniques. The processing of porous ceramics can be divided into three types as shown in Figure 2.1 [1] [2].

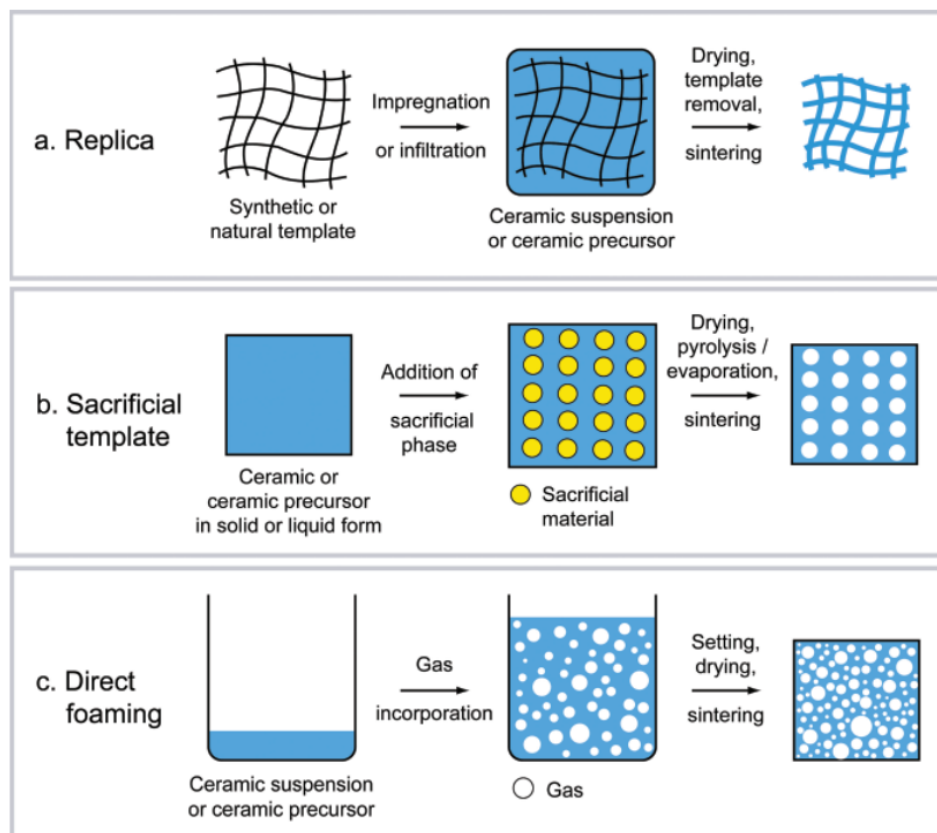


Figure 2.1: A schematic showing three different types of porous material processing methods [1]. This figure is reproduced with permission.



### **Replica method**

This method replicates the porous structure of cellular materials by infiltrating a ceramic suspension or precursor solution. The process is followed by drying and removing template materials by firing, leaving the porous structure resembling the template, but made of the desired materials. Cellular materials, which serve as templates in this method, can be synthetic templates such as polymeric sponge or natural templates such as coral, diatoms, and wood. Synthetic templates have been used to create filters in industry due to its simplicity. The natural template is an alternative option when templating porous structure or pore size is challenging to synthesize with existing techniques. Typically, natural materials possess hierarchical structures which can be used in applications such as battery electrodes (Figure 2.2 a) [3] and photocatalysts [4]. The disadvantage of this method is that struts of the structure are often prone to flaws such as cracks and pores during the burning step of the replica materials, leading to degraded mechanical properties.

### **Sacrificial template method**

In this method, the sacrificial phase is dispersed in a ceramic matrix or ceramic precursor, and removed by heat treatment or sublimation. The sacrificial template include synthetic organics, natural organics, and liquid. Figure 2.2 b shows a macroporous SiC fabricated by using a silica template. Unlike the replica method, the removal of the sacrificial phase does not introduce flaws in struts, so the processed materials by the sacrificial template method possess superior mechanical properties. Although this method offers better tailorability in porosity, pore size distribution, and pore morphologies, the main disadvantage of this process is the time-consuming step needed to remove the sacrificial phase either by heat treatment or sublimation.

### **Direct foaming**

This method directly introduces air into suspension or liquid, consolidates the material with pores by a setting agent, and sinters to produce porous solids. The porosity will be controlled by the amount of air incorporated. A critical step in this method is the stabilization of pores in the liquid by surfactant to avoid undesirable coalescence of the incorporated pores. The porous SiOC fabricated from this method is shown in Figure 2.2 c. Although this method is simple, inexpensive, and environmentally benign, due to the nature of introducing pores, pore morphologies are typically spherical. Furthermore, although pore size as small as  $\sim 40 \mu\text{m}$  is possible through

an efficient surfactant and a rapid set-in process [5], the methods mentioned above can produce smaller pore sizes.

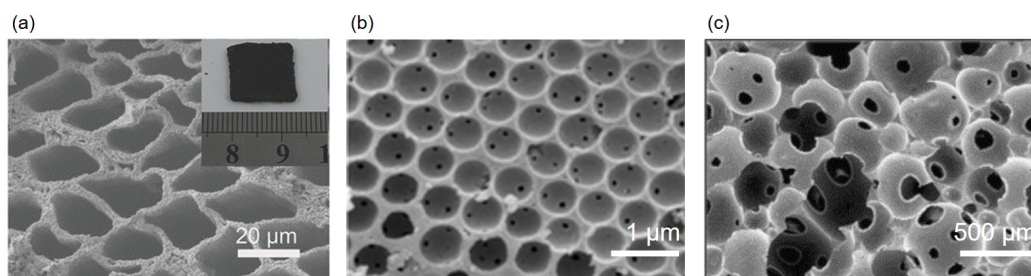


Figure 2.2: Micrographs showing porous materials fabricated by the replica method ( $\text{LiCoO}_2$  cathode by wood templating) [3], the sacrificial template method (macroporous SiC fabricated by silica template) [6] and (c) direct foaming (porous SiOC) [7]. Figures are reproduced with permission.

## 2.2 Freeze casting

Freeze casting is one of the sacrificial template methods, and uses solidified crystals as the sacrificial phase to template pores. Freeze casting was originally used to produce a preform of refractory powders for subsequent infiltration of metals to create near-net-shape turbosupercharger blades at NASA [8]. Nearly 50 years later, freeze casting started to gain attention from materials scientists [9, 10, 11]. Due to broad ranges of applications of this process, a number of review articles are available [12, 13, 14] and an open data repository was launched recently [15].

While the majority of studies focuses on freeze-casting of ceramic powders (referred to here as suspension-based freeze casting), this study primarily focuses on freeze-casting of preceramic polymers (referred to as solution-based freeze casting). The pioneering work of solution-based freeze casting was done by Yoon in 2007 [16], who investigated polycarbosilane/camphene solution and produced porous SiC with dendritic pores. Naviroj studied solution-based freeze casting in detail by exploring different solvents, polymer concentrations and solidification parameters, and demonstrated tailorability in pore size and pore morphology using solidification theory [17, 18]. Freeze casting of preceramic polymers not only expands the phase space for porous ceramics, but also makes use of fundamental solidification principles to provide a powerful tool to control pore characteristics. This section introduces the freeze-casting process, highlights differences between suspension and solution routes, and reviews processing variables.

### 2.2.1 Process overview

Figure 2.3 shows the freeze casting process. First, a suspension or solution is prepared. A suspension contains a dispersion medium, typically water, the ceramic powders, and additives such as binders and dispersants. A solution is prepared by dissolving preceramic polymer in a solvent; a cross-linking agent is added before solidification to ensure the mechanical integrity during the pyrolysis. The suspension or solution is then directionally frozen such that the growing crystals reject or segregate suspending particles or dissolved polymers. The subsequent sublimation step removes sacrificial solvent crystals, leaving pores in the materials. Sintering or pyrolysis yields porous solids. Hence, templating the pores is accomplished by the solidified crystals. Although solidification induces the phase separation in both routes, the mechanisms of the phase separation processes are different as discussed below.

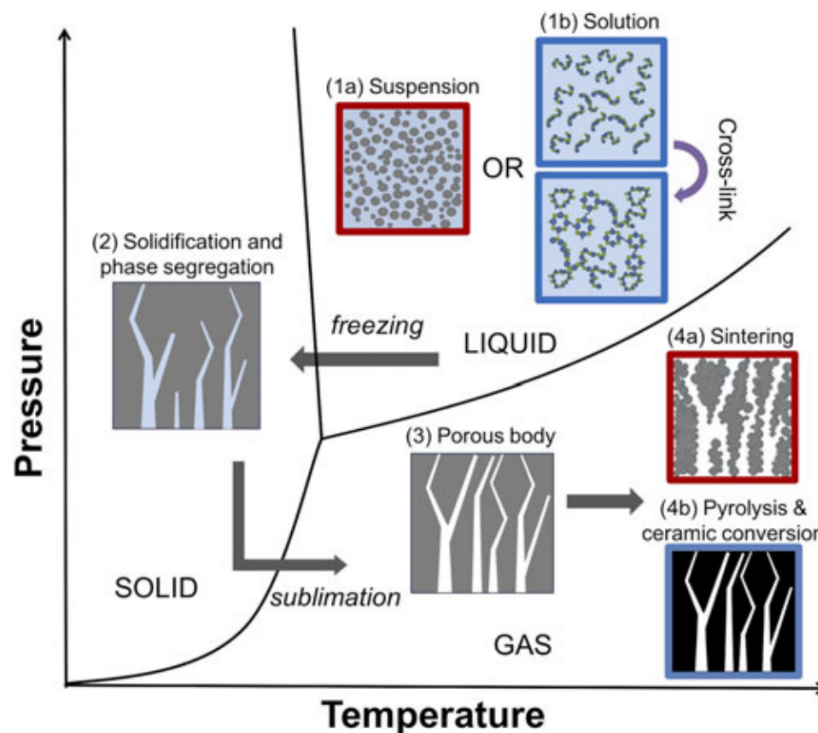


Figure 2.3: A diagram showing the freeze casting process [19].

#### Rejection of particles in suspension

In suspension-based freeze casting, when a liquid phase freezes, the freezing front rejects the particles in suspension and they are pushed into the interdendritic regions.

A particle pushed ahead by the freezing front was modeled by Korber and Rau, considering two counteracting forces, a viscous drag force and Van der Waals forces [20]. A viscous drag force is an attractive force acting on the particles toward the freezing front. The viscous drag force in a case of flat freezing front can be expressed by the following expression [21]:

$$F_{\eta} = 6\pi\eta vr^2/d$$

where  $\eta$ ,  $v$ ,  $r$ , and  $d$  are the viscosity of suspension, freezing front velocity, the particle radius, and the distance between the particle and the freezing front, respectively. Van der Waals forces come from the interfacial energy difference. The thermodynamic criterion for the rejection of the particles can be expressed by the following expression:

$$\Delta\sigma_0 = \sigma_{sp} - (\sigma_{sl} + \sigma_{lp}) > 0$$

where  $\sigma_{sp}$ ,  $\sigma_{sl}$ , and  $\sigma_{lp}$  are the surface free energy of solid-particle, solid-liquid, and liquid-particle, respectively. Using  $\Delta\sigma_0$ , the repulsive force can be expressed by the following equation:

$$F_R = 2\pi r \Delta\sigma_0 \left(\frac{a_0}{d}\right)^n$$

where  $a_0$  is the average molecular distance in the liquid film between the particle and freezing front, and  $n$  is the exponent. This exponent is the correction to the repulsive force, and can vary, for example, with particle size [20, 21, 22]. Equating the attractive force and repulsive force, the critical freezing front velocity,  $v_c$ , is:

$$v_c = \frac{\Delta\sigma_0 a_0}{3\eta r} .$$

Above  $v_c$ , the particles will be engulfed, whereas particles will be repelled below  $v_c$ . In suspension-based freeze casting, it is desirable for the majority of particles to be repelled by ensuring that the critical freezing front velocity is not exceeded so the pores are templated by the growing crystals. However, this equation also serves as a guide to deliberately engulf large particles while the small particles are rejected by adjusting freezing front velocity to improve mechanical properties. Ghosh et al. demonstrated a strengthening strategy for freeze-cast materials by engulfing platelet particles and repelling equiaxed particles [23].

### Segregation of solutes in solution

In solution-based freeze casting, a phase separation between solutes and solvent crystals is a result of segregation due to the equilibrium solubility difference between the liquid and solid phases. The relation between concentration in liquid and solid ( $C_L$  and  $C_S$ , respectively) is expressed using the equilibrium distribution coefficient,  $k_0$ , also known as the chemical segregation coefficient or the partition coefficient:

$$k_0 \equiv \frac{C_S}{C_L} .$$

During solidification, if the freezing front velocity is slow enough to assume that the local thermodynamic equilibrium holds at the solid-liquid interface, the equilibrium distribution coefficient can be used to assess the redistribution of solute between solids and liquid. Similarly to suspension-based freeze casting, the solute should be segregated by the solid phase so the pores are templated by the crystals. Ideally, the equilibrium distribution coefficient should be as small as possible so as to segregate the majority of the solute. However, when the freezing front velocity is sufficiently high such that the atoms have no time to rearrange themselves at the solid-liquid interface, the solute will be frozen with the same composition as they arrive from the melt, an effect known as solute trapping [24]. In such a case, the distribution coefficient approaches unity, meaning that there is no segregation.

### Advantages of solution-based freeze casting

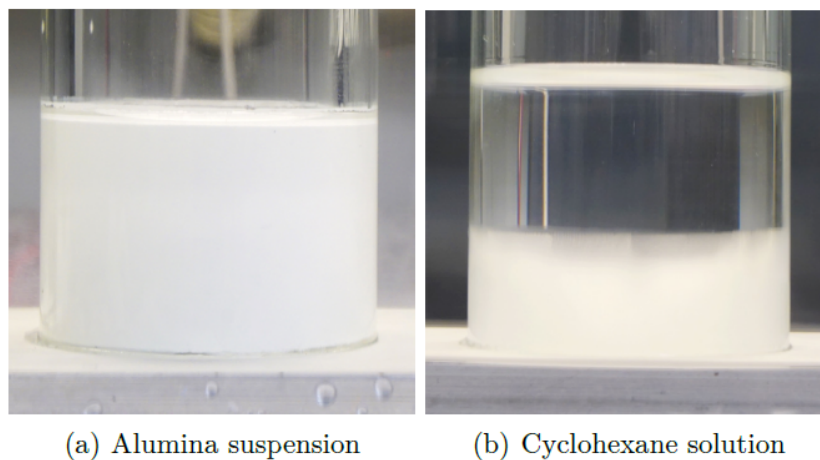


Figure 2.4: Pictures during the directional solidification of (a) suspension and (b) solution [18].

Naviroj et al. investigated both suspension- and solution-based freeze casting with different solvents and reported the differences between the two routes [19]. In suspension-based freeze casting, one has a variety of materials choices, ranging from metals [25, 26, 27], ceramics [12], and even polymers [28] as long as a stable suspension can be prepared. Thus, the majority of the reports in the literature focus on suspension-based freeze casting. In contrast, solution-based freeze casting requires a solute which is soluble in solvent. Although the material choice is limited compared to the suspension route, it offers a few advantages. In suspensions (Figure 2.4a), due to opacity, one has to use a method such as X-ray radiography to observe the freezing front [29]. On the other hand, since the solution is transparent (Figure 2.4b), the measurement and the control of freezing front velocity is possible using a camera so that the resulting pore size is easily tailorable. Second, suspensions contain additives such as binders and dispersants, in addition to particles, which make the system more complex. It was observed by Naviroj et al. that particle suspensions disrupt the solidification microstructure in suspension-based samples [19]. The freeze-cast microstructures by solution and suspension routes differ as shown in Figure 2.5. While solution-based freeze-cast samples clearly show dendritic morphology, the suspension-based freeze-cast samples lack fine dendritic features and anisotropy. The in-situ microtomography study of a metal alloy system also revealed that the presence of particles modifies the dendrites to hyperbranched morphologies through multiple splitting, branching, and curving of the secondary arms of the dendrites [30], which likely resulted from the local variation of solute content caused by the particles during the crystal growth. In solution-based freeze casting, however, such a complexity does not exist. As a result, the unique templated pore morphology results in ceramics microstructures appropriate for filtration for medical devices [31]. Finally, processing time and cost are longer and expensive in suspension route. Preparing suspensions require a time-consuming ball-milling process whereas a solution can be prepared within 30 minutes. Moreover, pyrolysis temperatures ( $\sim 1300$  °C or lower) are lower than sintering temperatures ( $\sim 1700$  °C or higher), saving cost and energy.

### **2.2.2 Processing variables**

Since this study primarily focuses on solution-based freeze casting, processing variables of solution-based freeze casting are mainly highlighted.

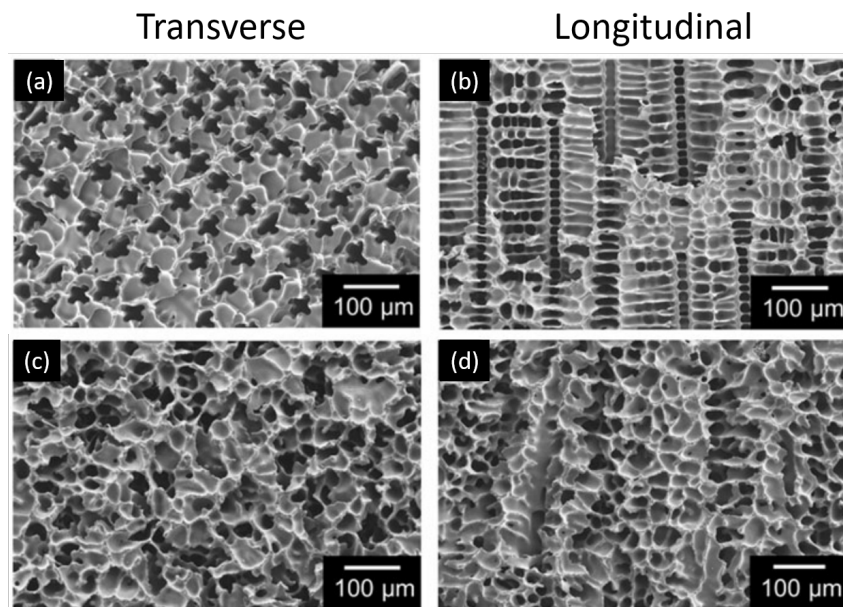


Figure 2.5: SEM images showing freeze-cast SiOC with dendritic pores from (a, b) solution and (c, d) suspension [19].

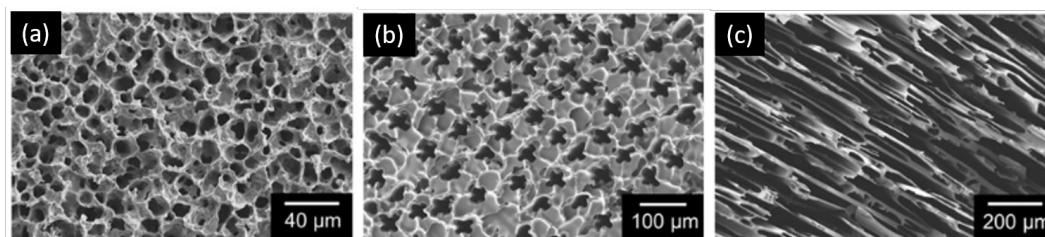


Figure 2.6: SEM images showing three different freeze-cast structures: (a) isotropic structure from cyclooctane, (b) dendritic structure from cyclohexane, and (c) lamellar structure from dimethyl carbonate [19]. The solutions were frozen with a freezing front velocity of  $15 \mu\text{m/s}$ .

### Solvent

The choice of the solvent is an essential part of freeze casting, and a few important points are as follows. First, the solvent must be chosen such that the preceramic polymer can be dissolved. Second, the cross-linking process in a solvent should be slow enough to allow solidification without gelation, but fast enough so the preceramic polymer has mechanical integrity after sublimation to survive the pyrolysis step. Third, the solvent must be compatible with the freeze casting process. The solvent needs to have a sufficiently high freezing point so that the solution can be completely frozen. In addition, the solvent also needs to be sublimable at pressures

of the freeze dryer to remove the solvent crystals. Finally, a solvent must be chosen to achieve desired pore structure since the microstructure is dependent upon solvent crystallography and solidification parameters. Figure 2.6 shows three pore structures freeze-cast from different solvents.

### Solids loading

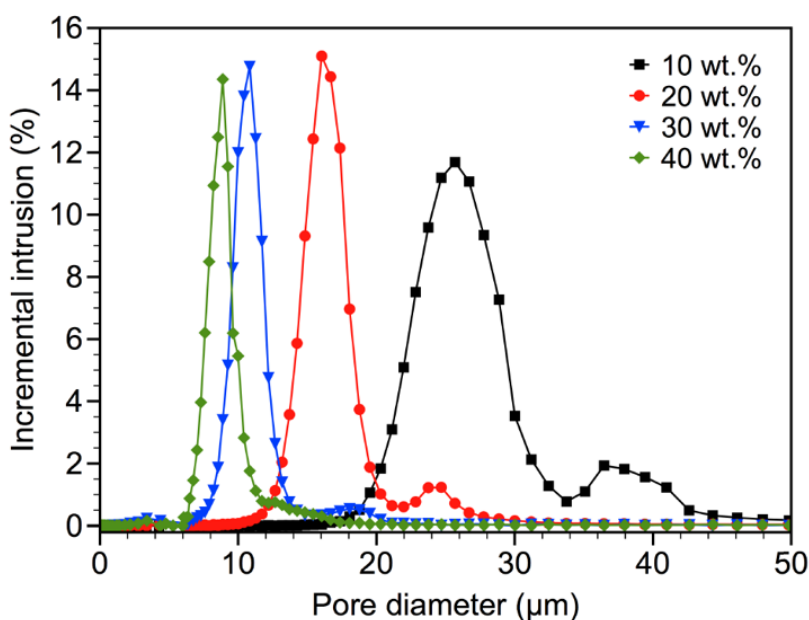


Figure 2.7: Pore size distribution of dendritic pores showing the effect of preceramic polymer concentration [18].

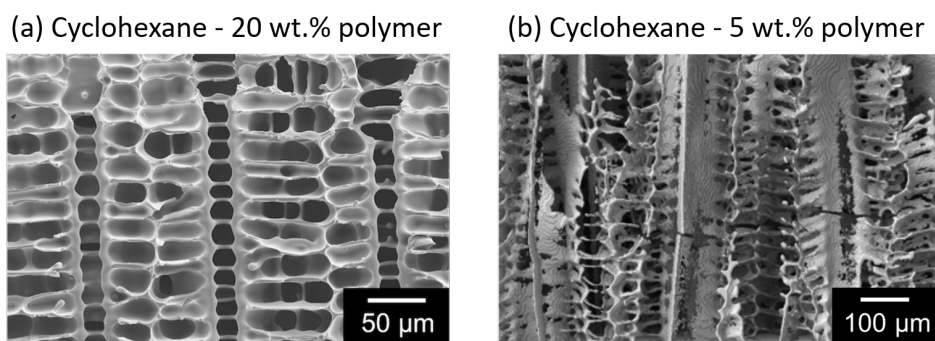


Figure 2.8: Longitudinal SEM image of (a) a 20 wt.% polymer concentration and XCT image of (b) a 5 wt.% polymer concentration in cyclohexane [18].

Solids loading is an important parameter as it determines pore characteristics such as porosity, pore size, and pore network. As the solid loading increases, the volume



of growing crystals, the sacrificial phase, decreases, resulting in lower porosity. Solids loading also modifies the pore size as shown in Figure 2.7 because the solids loading controls the space for the growing crystals. A hybrid system which contains preceramic polymer and ceramic particles were studied by Naviroj et al. [19] and Schumacher et al. [32]. These composites are useful to control not only mechanical integrity but also surface characteristics. Solids loading is also important for control of the pore network. Figure 2.8 shows freeze-cast structures from cyclohexane with different polymer concentrations: 20 wt.% and 5 wt.%. Both have dendritic structures, but possess different pore networks. Because there are enough preceramic polymers segregating into interdendritic regions in 20 wt.% solution, each dendritic pore is isolated and not connected to neighboring pores. In contrast, when the concentration is decreased, the ceramic wall became much thinner and the dendritic pores are highly interconnected.

### **Freezing conditions**

Freezing conditions are also critical as they determine the pore morphology, pore size, and pore directionality. Two important solidification variables are usually controlled: the freezing front velocity and temperature gradient.

Freezing front velocity determines the microstructural length scale of growing crystals. The rapidly growing crystals tend to exhibit sharp tips and fine features while slowly growing crystals show blunt tips and coarse features. Fine features of fast-growing crystals increase the relative surface area, which enables crystals to efficiently transport heat or solute (the so-called point effect of diffusion), so the small crystals are favored in fast freezing front velocities. Consequently, faster freezing front velocity leads to small pore size and slower freezing front velocity leads to large pore size. In freeze casting, the typical pore size of freeze-cast structures ranges from around 300 nm to 500  $\mu\text{m}$  (macropores) [33]. Smaller pores can be achieved by quenching a solution. If the solution is quenched, the solvent transitions to the glassy state. Subsequently, the temperature is slowly increased to initiate the crystallization of the solvent and phase separation. This process creates nanocrystals, and after the solvent extraction, the material is left with large free surface areas exceeding  $300 \text{ m}^2\text{g}^{-1}$  and small pore radii as low as 1.9 nm [34]. This surface area is significantly larger than those of typical freeze-cast solids which are less than  $1 \text{ m}^2\text{g}^{-1}$  [18, 35].

In contrast, the temperature gradient has an impact on the directionality of the

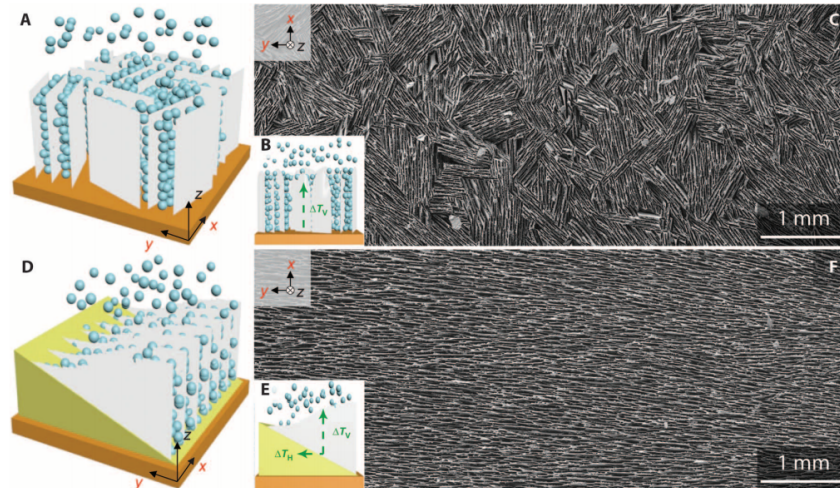


Figure 2.9: A sample freeze-cast (a) and (b) without a polydimethylsiloxane (PDMS) wedge frozen with (b) multiple nucleation site and a single vertical temperature gradient. It shows short-range lamellar pores in (c) the SEM image. A sample freeze-cast (d) with a PDMS wedge frozen (e) with a confined nucleation site and a dual temperature gradient: vertical temperature gradient and horizontal temperature gradient. It shows long-range lamellar pores in (f) the SEM image. From ref. [36]. Reprinted with permission from AAAS.

pores. Although the majority of the solidification in freeze casting were conducted from bottom to the top by the vertical temperature gradient, there are a number of studies controlling the directionality of temperature gradient or combining several temperature gradients. In suspension-based freeze casting, Bai et al. used a mold with the copper cold finger rod placed in the center so that the ceramic slurry was frozen radially to mimic the structure of the bones [37]. In another study by Bai et al., a polydimethylsiloxane wedge was used to limit the nucleation site and control the growth direction by creating a dual temperature gradient to attain long-range order alignment of lamellar pores [36] (Figure 2.9). The temperature gradient not only affects the pore directionality but also their morphologies.

Freezing front velocity and temperature gradient are variables during the crystal growth, however, the solidification microstructure can be controlled through nucleation process or post-crystal growth process. To control the nucleation process, Munch et al. modified the surface pattern of the cold finger to control the orientation of lamellar pores [38]. Naviroj et al. controlled the nucleation process by applying grain selector templates to align the dendritic pores with improved permeability [39]. Post-crystal growth processes such as coarsening were also studied. Pawelec et al. investigated low-temperature ice annealing in a collagen suspension,

and observed coarsened microstructures after twenty hours of annealing. Liu et al. examined coarsening of camphene crystals in freeze casting of bioactive glass to obtain a controllable pore diameter, ranging from 15  $\mu\text{m}$  to 160  $\mu\text{m}$ . However, both were restricted to pore size measurement and a qualitative image analysis. Chapter 5 reports a quantitative study of morphological evolution of dendritic pores by coarsening using a tomography-based analysis.

### **Rheology of solution**

Rheological property of solution is another parameter to control freeze casting, and the polymer solution viscosity can be controlled in a simple way. Xue et al. changed the rheological properties of the solution by increasing the cross-linking agent for polycarbosilane, and demonstrated improved mechanical robustness by tuning cross-linking agent concentration. It is also possible to change the rheological properties by changing the molecular weight of preceramic polymer by thermal curing, which will be discussed in Chapter 8. Typically, a cross-linking agent is introduced prior to the solidification. As a result, viscosity changes over time and the solution eventually gels, which limits the solidification time. However, recent work by Obmann et al. demonstrated that photopolymerization is possible at temperatures below  $-10\text{ }^{\circ}\text{C}$  after the solidification [40]. This work not only offers different processing avenues for solution-based freeze casting, but also provides more flexibility in solidification time. Because the cross-linking step can be carried out after the solidification, longer solidification is feasible. Longer solidification time in suspension-based freeze casting poses an issue due to the sedimentation of the suspended particles. In suspension-based freeze casting, controlling rheological properties requires additives such as glycerol [41], polyethylene glycol [42], or gelatin [43].

## **2.3 Solidification**

As the crystal templates the pores in freeze casting, an understanding of the solidification is fundamental. In this section, these solidification principles are reviewed.

### **2.3.1 Constitutional supercooling and interface instability**

The recognized concept for understanding interfacial instability leading to cellular growth is constitutional supercooling, which was originally conceived by Rutter and Chalmers [44] to describe the breakdown of the stable planar solid-liquid interface into cellular morphologies in directional solidification. It was reported that cellular

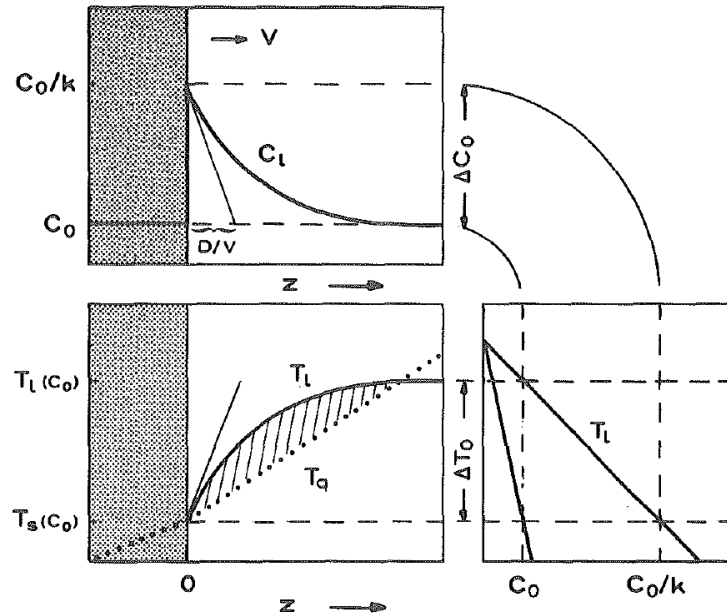


Figure 2.10: A schematic of the constitutional gradient during solidification and the liquidus temperature gradient ahead of the freezing front. The applied temperature gradient,  $G = \left(\frac{dT_q(z)}{dz}\right)_{z=0}$ , is lower than the liquidus temperature gradient,  $G_c = \left(\frac{dT_L(z)}{dz}\right)_{z=0}$ , resulting in the constitutional supercooling (cross-hatched region) [24] Credit: W. Kurz and D. J. Fisher, Fundamentals of solidification, Third edition, Trans Tech Publication, 1992.

crystal growth resulted from the instability of the interface, which was caused by the concentration gradient in the liquid ahead of the freezing front (Figure 2.10). As the solid-liquid interface advances, the solute is segregated from the interface and the segregation of solutes creates a concentration gradient. This concentration gradient in the liquid phase can be converted to the liquidus temperature gradient, using the phase diagram. If the temperature gradient in the melt,  $G = \left(\frac{dT_q(z)}{dz}\right)_{z=0}$ , is lower than the liquidus temperature gradient,  $G_c = \left(\frac{dT_L(z)}{dz}\right)_{z=0}$ , at the solid-liquid interface, there exists a zone of constitutional supercooling as shown in the hatched region (Figure 2.10). Later, this was mathematically formulated by Tiller, Rutter, and Jackson using the steady-state diffusion equation [18]. The condition for stable planar front can be expressed by the following equation,

$$G = \frac{mC_0v}{D} \left( \frac{k_0 - 1}{k_0} \right)$$

where  $G$  is the temperature gradient,  $m$  is the slope of the liquidus,  $C_0$  is initial concentration of solute in liquid,  $v$  is freezing front velocity,  $D$  is diffusivity of

solute in liquid, and  $k_0$  is the equilibrium distribution coefficient ( $k_0 \equiv C_S/C_L$ ). Chapters 3 and 6 explain the strategies based upon this concept that tailor the pore morphologies.

Although the theory of the constitutional supercooling could successfully show the conditions for the breakdown of the planar freezing front, the drawbacks of this analysis include the following: (i) it does not take the surface tension of the interface into account, (ii) it cannot predict the size scale of the morphologies after the breakdown. To overcome these drawbacks, Mullins and Sekerka considered a case where the interface is slightly disturbed and analyzed the development of this perturbation [45]. In this analysis, a sinusoidal perturbation,  $\delta$ , is introduced into the planar front. These perturbations can be insoluble particles, temperature fluctuations, or grain boundaries in the melts. The equation known as Mullins-Sekerka instability criterion is expressed as:

$$\frac{\dot{\delta}}{\delta} = \frac{V\omega\{-2T_M\Gamma\omega^2[\omega^*-(V/D)(1-k_0)]-(g'+g)[\omega^*-(V/D)(1-k_0)]+2mG_c[\omega^*-(V/D)]\}}{(g'-g)[\omega^*-(V/D)(1-k_0)]+2\omega mG_c}$$

and

$$g' + g = \frac{2}{\kappa_S + \kappa_L}(\kappa_S G' + \kappa_L G)$$

$$g' - g = \frac{2}{\kappa_S + \kappa_L}(\kappa_S G' - \kappa_L G)$$

$$\omega^* = \frac{V}{2D} + \left[\left(\frac{V}{2D}\right)^2 + \omega^2\right]^{\frac{1}{2}}$$

where  $\delta$  is the amplitude of the perturbation,  $\omega$  is a frequency of a sinusoidal perturbation,  $V$  is the freezing front velocity,  $T_M$  is the melting temperature,  $\Gamma$  is a capillary constant which involves the solid-liquid interfacial free energy and the latent heat,  $D$  is the diffusion coefficient of the solute in the liquid,  $k_0$  is the equilibrium distribution coefficient,  $G_c$  is the solute concentration gradient at the interface, and  $\kappa_S$  and  $\kappa_L$  are thermal conductivities of the solid and liquid, respectively. This analysis shows that if  $\dot{\delta}/\delta$  is positive, the perturbation will grow (Figure 2.11a). If negative, it will disappear (Figure 2.11b).

The Mullins-Sekerka instability criterion can be used to estimate the size-scale of the growing interfaces for any particular systems. In Figure 2.12,  $\dot{\delta}/\delta$  for Al-2wt.%Cu alloy under the specified solidification condition ( $V = 0.1\text{mm/s}$ ,  $G = 10\text{K/mm}$ ) is plotted as a function of wavelength,  $\lambda = 2\pi/\omega$  [24]. The wavelength range within

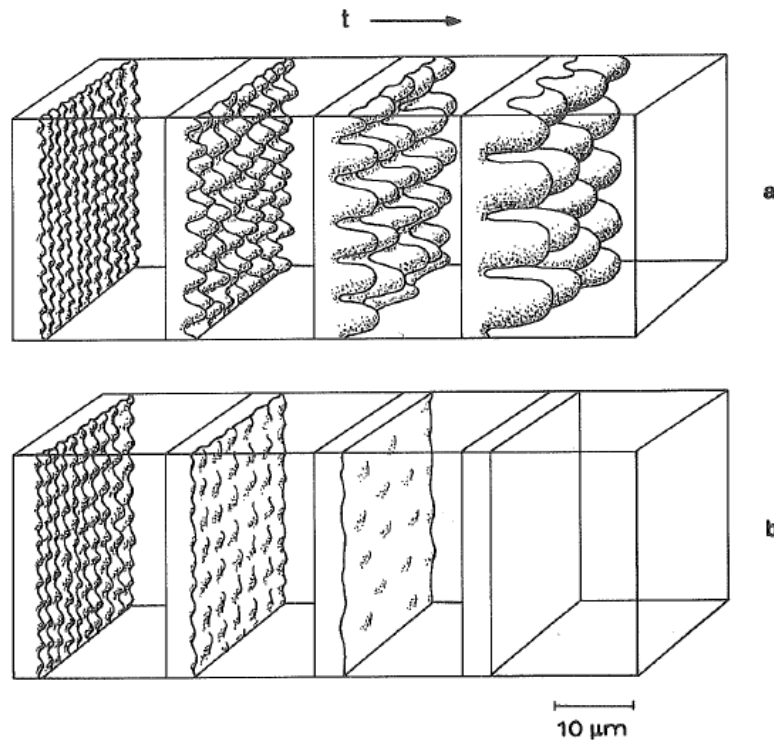


Figure 2.11: Illustrations showing (a) small perturbation grow and (b) small perturbation disappear [24].

Credit: W. Kurz and D. J. Fisher, *Fundamentals of solidification*, Third edition, Trans Tech Publication, 1992.

$\dot{\delta}/\delta$  being positive gives a rough estimate for the perturbed morphology. Kurtz and Fisher used this wavelength to further estimate the dendrite tip radius [46].

### 2.3.2 Crystal morphology

Each material exhibits its characteristic solidified morphology. Figures 2.13 a and b show two different crystal morphologies: non-faceted crystals and faceted crystals. This difference in crystal morphologies can be explained by the atomic attachment kinetics. The non-faceted crystals, also called as dendrites, are often observed in metals. The atomic attachment kinetics are independent of crystallographic planes so they are solidified with an atomically rough solid-liquid interface, where the atom can easily attach to the solid phase. In contrast, faceted crystals, a morphology seen in intermetallic compounds or minerals, have a preferential atomic attachment, depending on crystallographic planes. Hence, the interfaces tend to be flat with faceted morphologies. The analysis of the equilibrium configuration at the solid-liquid interface was performed with a two-layer interface model proposed by Jackson

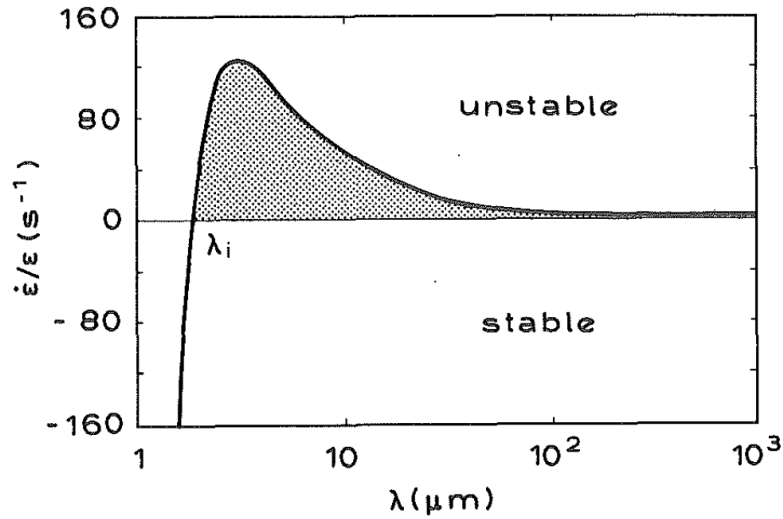


Figure 2.12: A schematic showing the stability of the interface as a function of wavelength for Al-2wt.%Cu [24].

Credit: W. Kurz and D. J. Fisher, Fundamentals of solidification, Third edition, Trans Tech Publication, 1992.

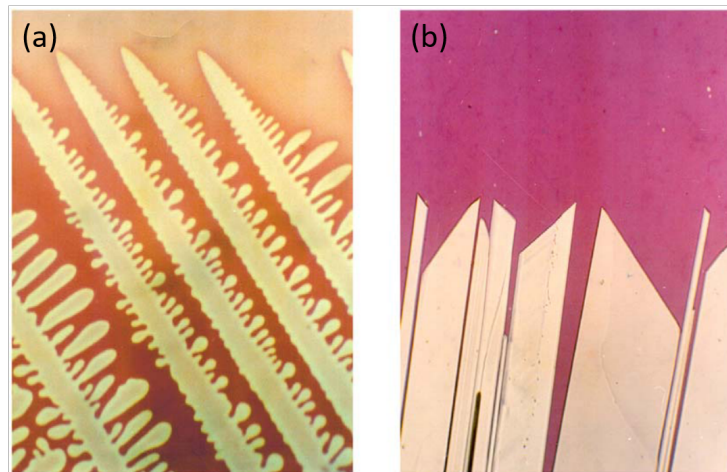


Figure 2.13: Images showing (a) non-faceted crystals (dendrites) and (b) faceted crystals [47]. This figure is reproduced with permission.

[47]. Although this analysis considers only the first nearest neighbors at the solid-liquid interfaces, it serves as a useful guide to predict the crystal morphologies. In this model, a parameter now known as the Jackson  $\alpha$  factor, was proposed:

$$\alpha = \frac{\eta}{Z} \frac{L}{k_B T_m}$$

where  $\eta$  is the number of nearest neighbors adjacent to an atom in the plane of the interface,  $Z$  is the total number of nearest neighbors in the crystal,  $L$  is the latent heat of fusion,  $k_b$  is the Boltzmann constant, and  $T_m$  is the material's melting point. The Jackson  $\alpha$  factor assesses the change in free energy of the adatoms to join the solid phase. Consequently, the location where the maximum or minimum of the free energy curve occurs changes (Figure 2.14). Above the critical value of  $\alpha = 2$ , the free energy curve finds its minimum at either near  $\xi = 0$  or  $\xi = 1$ . The physical meaning of this is that the interface is occupied by few adatoms or fully occupied with few vacancies, indicating that the interface is atomistically flat. In case of  $\alpha < 2$ , the minimum of the free energy curve is at  $\xi = 0.5$ . There are almost equal number of adatoms and vacancies, indicating the interface is atomistically rough. The Jackson  $\alpha$  factor is thereby a guide to judge whether a crystal exhibits rough or flat interfaces at specific crystallographic orientations of the material. In most cases, the crystallographic term of the Jackson  $\alpha$  factor,  $\eta/Z$ , is challenging to know for all the crystallographic planes, but the thermodynamic term,  $L/k_B T_m$  is relatively easy to estimate. Since the crystallographic term is always less than one, but greater than 1/4, the thermodynamic term is used to estimate if the  $\alpha$  factor is less than 2. Figure 2.15 shows the freezing microstructures of different solvents along with the value of the thermodynamic term [18]. As the thermodynamic term is increased, the anisotropy of the frozen crystals increases. The frozen crystals turn from round-shaped seaweed-like to dendritic, then to prismatic, and finally to lamellar.

## 2.4 Polymer-derived ceramics (PDC)

A preceramic polymer is a precursor which can be converted into ceramics by pyrolysis. The resulting ceramics are known as polymer-derived ceramics (PDCs). PDCs have brought a technological breakthrough in ceramic processing by achieving the development of ceramic fibers and ceramic coatings with impressive high-temperature properties such as resistance to crystallization and creep. A brief introduction of PDCs as well as their structures and properties are highlighted in this section.

### 2.4.1 Overview of polymer-derived ceramics

The first notable achievement for PDCs was done by Yajima et al. who developed silicon carbide fibers with high tensile strength [49], which eventually resulted in Nicalon fibers manufactured by Nippon Carbon. While traditional ceramic process-



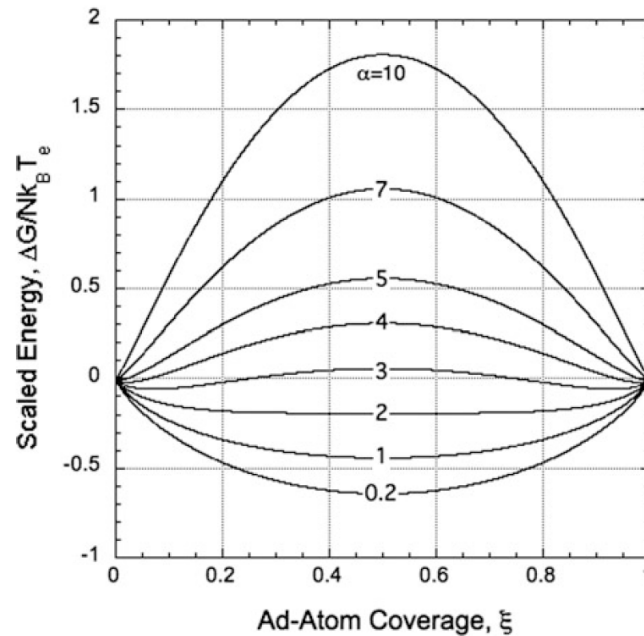


Figure 2.14: Free energy curve as a function of adatom coverage with different values of the Jackson  $\alpha$  factor [48]. This figure is reproduced with permission.

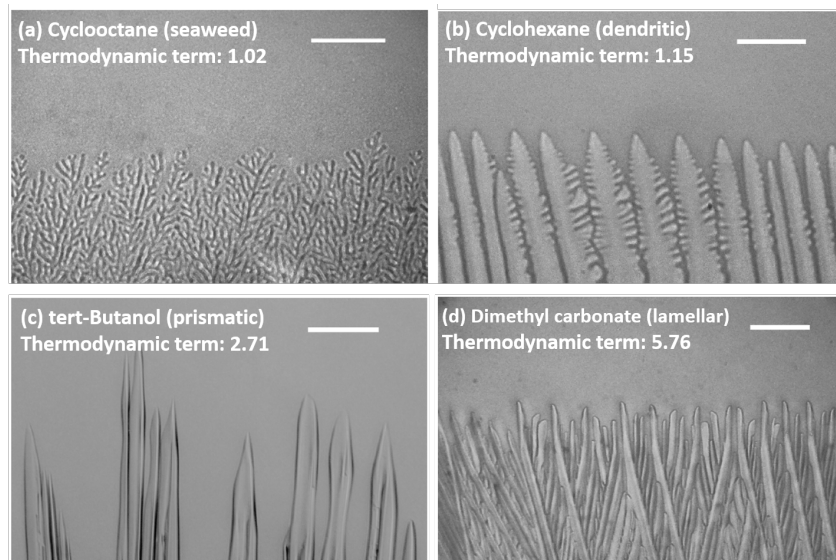


Figure 2.15: Optical micrographs showing freezing microstructures of preceramic polymer solutions with (a) cyclooctane, (b) cyclohexane, (c) tert-Butanol, and (d) dimethyl carbonate [18].

ing typically requires sintering at temperatures higher than  $\sim 1700$  °C with sintering additives, pyrolysis can be conducted at  $\sim 1300$  °C or lower. In addition, preceramic polymers can be processed by polymer-forming techniques such as injection

molding [50], fiber drawing [51], extrusion [52], or stereolithography [53]. Shaping of preceramic polymers before pyrolysis can eliminate machining, mitigating or avoiding tool wear or material brittle fracture. Due to the significant shrinkage, by-product gas release, and formation of porosity during the pyrolysis, dimensions of PDC components are limited to a few hundred micrometers or smaller (fibers, coating, etc.), otherwise they are prone to cracking. Although porosity has been viewed as a source of flaws in ceramics, producing a porous structure with wall thickness within the length scale via freeze casting opens up new opportunities for applications of PDCs.

### Preceramic polymer type

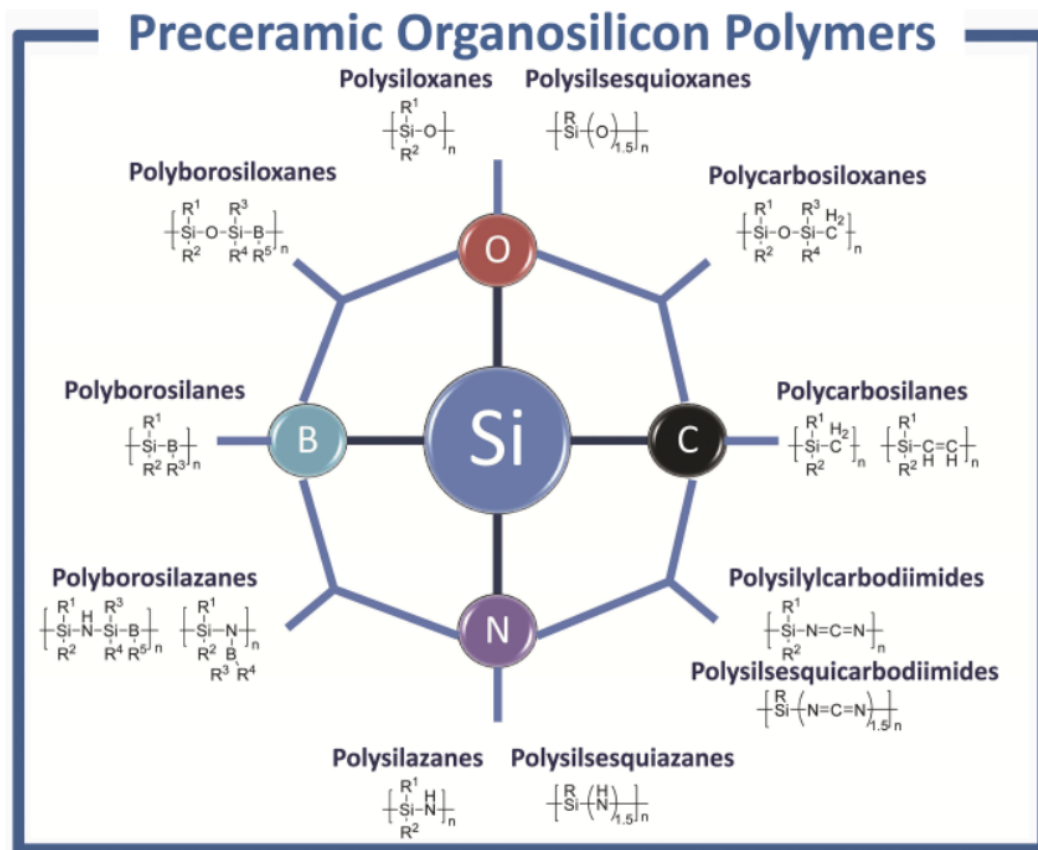


Figure 2.16: Si-based preceramic polymer with different backbones [54]. This figure is reproduced with permission.

A variety of preceramic polymers is available, which result in binary compounds such as  $\text{Si}_3\text{N}_4$ ,  $\text{SiC}$ , and  $\text{BN}$ , ternary compounds such as  $\text{SiCN}$  and  $\text{SiOC}$ , and even quaternary compounds such as  $\text{SiBCN}$  and  $\text{SiAlCO}$ . Si-based preceramic polymers

have been studied extensively as promising precursor ceramic applications beyond fibers, such as ceramic heating elements and ceramic brake disk [55]. As shown by Figure 2.16 [54], the different compositions of the backbone resulted in various classes of ceramics. The functional groups (denoted as "R" in Figure 2.16) control the carbon content in the resulting ceramics [56], which affect properties such as thermal and mechanical properties (resistance to crystallization and creep). Moreover, the addition of metal elements such as Al [57] and Ti [58] is possible. It was demonstrated that introducing Al improves high temperature stability and the solid remains crack-free at 1400 °C and up to 1700 °C [59]. In addition to Si-based preceramic polymers, other preceramic polymer systems have been studied such as B-based [60] and Al-based polymers [61]. Although the ceramic yield from preceramic polymers is still limited compared to powder routes, there is continued work to expand the material space. Recent achievements include the development of polymer-derived refractory ceramics by United States Naval Research Laboratory (NRL). This is particularly attractive as metal carbide powders are, for example, produced by carbothermal reduction at 2000 °C, followed by high pressure sintering at 2000 °C under over 1 GPa [62], which impose challenges in cost and scalability. To address this challenge, NRL developed 1,2,4,5 tetrakis(phenylethynyl)benzene (TPEB), which acts as a carbon source for carbothermal reduction [62], and demonstrated a novel polymer-derived boron carbide ( $B_4C$ ) monolith. This process can be used to fabricate components as large as  $15 \times 15 \text{ cm}^2$  panels which are over 1 cm thick. With preceramic polymers, the refractory ceramics can be processed at much lower temperatures and shorter time than powder processing. NRL further demonstrated the technology with other refractory ceramics such as titanium carbide [63], tungsten carbide [64], and tantalum carbide [65].

### **Processing of preceramic polymer**

PDCs are manufactured or fabricated from preceramic polymers by the following three steps [66]:

- Preceramic polymer synthesis from monomer or oligomer precursor with desirable rheological properties for shaping.
- Shaping of preceramic polymer by plastic forming methods such as injection molding, extrusion, fiber drawing, etc., and thermal curing at 150°C - 250°C to set structural integrity for pyrolysis.

- Pyrolysis in an inert atmosphere (Ar or N<sub>2</sub>) at temperature ~1300 °C or lower.

A preceramic polymer can be either a liquid or a solid at ambient temperatures, and must have functional groups so that it can form thermoset and retain its shape during the pyrolysis. The cross-linking can be undertaken by thermal cross-linking typically below 200°C. In case of polysiloxane, this would be the condensation of the silanol group (Si-OH). A catalyst can be also added to facilitate the cross-linking process. The degree of cross-linking needs to be carefully controlled for desired rheological properties such that plastic forming techniques can be employed. During pyrolysis, the by-product gas will be released [56]. For the pyrolysis of polysiloxane, from 100°C to 420°C, thermal cross-linking gas such as water and alcohol as well as oligomers will be released. From about 420°C to 850°C, the decomposition process will start by releasing hydrocarbons such as methane, and result in amorphous ceramics, but can be crystallized by heating at high temperatures [67].

#### 2.4.2 Structures and properties of silicon oxycarbide (SiOC)

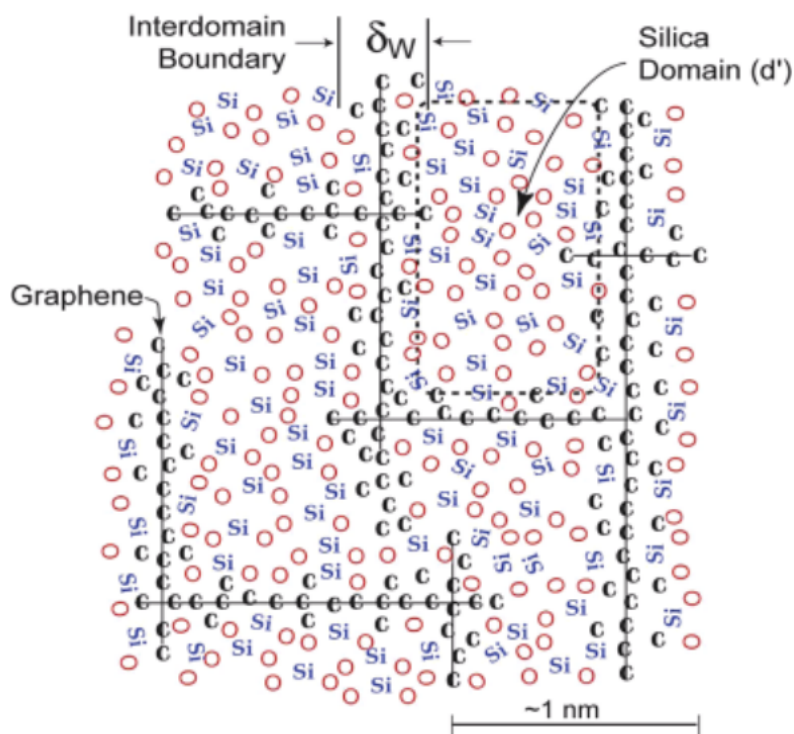


Figure 2.17: A model for the nanodomains in SiOC [68]. This colored image was taken from [54]. This figure is reproduced with permission.

Saha et al. proposed a model of the SiOC as shown in Figure 2.17, showing silica

nanodomains encased with mixed SiOC bonds and a  $sp^2$  carbon. Pyrolysis leaves a significant amount of carbon from organics which is insoluble in silica. Hence, it was postulated that the carbon is rejected as the silica nanodomains coarsen during the pyrolysis. As a result, it forms continuous SiOC mixed bonds and a  $sp^2$  carbon network, which inhibits further growth of silica domains and creation of silica nanodomains. The presence of these nanodomains were confirmed by using solid-state NMR, micro-Raman, SAXS, XRD, and HRTEM [69].

This microstructure results in unique electronic, magnetic, optical, thermal, and mechanical properties. A few properties are highlighted here. First, Si-based ceramics are known to have resistance to crystallization up to 1400°C. The nucleation of silica crystallites require embryos of a critical size. However, due to the presence of SiOC mixed bonds and the  $sp^2$  carbon network acting as diffusion obstruction, crystallization is prohibited. Varga et al. also explains this high temperature stability from a thermodynamic standpoint and attributes the energetics of domain walls, which is constituted from  $sp^2$  carbon and mixed SiOC bonds, as the source of stabilizing amorphous phase [70]. PDCs are also known to possess remarkable creep resistance due to their high viscosity, two order of magnitude higher than vitreous silica at 1400°C [71]; viscosity increases with increasing carbon content [72]. This creep resistance can also be attributed to the presence of excess carbon. Because the  $sp^2$  carbon creates scaffolding, which enables load transfer from the silica phase to  $sp^2$  carbon network, it would be difficult to deform viscously [73]. Lastly, PDCs also have chemical stability. Soraru et al. studied the chemical durability of SiOC with varied carbon content in alkaline and HF. SiOC exhibits greater chemical durability than silica glass due to the Si-C bonds and the presence of the carbon network, which impedes the local transport of the reactant [74].

## References

- [1] Andre R. Studart et al. "Processing routes to macroporous ceramics: a review". In: *Journal of the American Ceramic Society* 89.6 (2006), pp. 1771–1789.
- [2] T. Ohji and M. Fukushima. "Macro-porous ceramics: processing and properties". In: *International Materials Reviews* 57.2 (2012), pp. 115–131.
- [3] Lei-Lei Lu et al. "Wood-Inspired High-Performance Ultrathick Bulk Battery Electrodes". In: *Advanced Materials* 30.20 (2018), p. 1706745.

- [4] Shenmin Zhu et al. “Sonochemical fabrication of morpho-genetic TiO<sub>2</sub> with hierarchical structures for photocatalyst”. In: *Journal of Nanoparticle Research* 12.7 (2010), pp. 2445–2456.
- [5] Masayoshi Fuji et al. “Effects of surfactants on the microstructure and some intrinsic properties of porous building ceramics fabricated by gelcasting”. In: *Ceramics International* 32.7 (2006), pp. 797–802.
- [6] Hao Wang et al. “Fabrication and characterization of ordered macroporous PMS-derived SiC from a sacrificial template method”. In: *Journal of Materials Chemistry* 14.9 (2004), pp. 1383–1386.
- [7] Paolo Colombo and Enrico Bernardo. “Macro-and micro-cellular porous ceramics from preceramic polymers”. In: *Composites Science and Technology* 63.16 (2003), pp. 2353–2359.
- [8] W.A. Maxwell, R.S. Gurnick, and A.C. Francisco. “Preliminary Investigation of the ‘freeze-casting’ Method for Forming Refractory Powders”. In: (1954).
- [9] Sundararajan V. Madihally and Howard W.T. Matthew. “Porous chitosan scaffolds for tissue engineering”. In: *Biomaterials* 20.12 (1999), pp. 1133–1142.
- [10] Takayuki Fukasawa et al. “Synthesis of porous ceramics with complex pore structure by freeze-dry processing”. In: *Journal of the American Ceramic Society* 84.1 (2001), pp. 230–232.
- [11] Kiyoshi Araki and John W. Halloran. “New freeze-casting technique for ceramics with sublimable vehicles”. In: *Journal of the American Ceramic Society* 87.10 (2004), pp. 1859–1863.
- [12] Sylvain Deville. “Freeze-casting of porous ceramics: a review of current achievements and issues”. In: *Advanced Engineering Materials* 10.3 (2008), pp. 155–169.
- [13] W.L. Li, K. Lu, and J.Y. Walz. “Freeze casting of porous materials: review of critical factors in microstructure evolution”. In: *International materials reviews* 57.1 (2012), pp. 37–60.
- [14] Isaac Nelson and Steven E. Naleway. “Intrinsic and extrinsic control of freeze casting”. In: *Journal of Materials Research and Technology* 8.2 (2019), pp. 2372–2385.
- [15] Kristen L. Scotti and David C. Dunand. “Freeze casting—A review of processing, microstructure and properties via the open data repository, FreezeCasting.net”. In: *Progress in Materials Science* 94 (2018), pp. 243–305.
- [16] Byung-Ho Yoon et al. “Highly aligned porous silicon carbide ceramics by freezing polycarbosilane/camphene solution”. In: *Journal of the American Ceramic Society* 90.6 (2007), pp. 1753–1759.

- [17] Maninpat Naviroj et al. “Directionally aligned macroporous SiOC via freeze casting of preceramic polymers”. In: *Journal of the European Ceramic Society* 35.8 (2015), pp. 2225–2232.
- [18] Maninpat Naviroj. “Silicon-based porous ceramics via freeze casting of preceramic polymers”. PhD thesis. Northwestern University, 2017.
- [19] Maninpat Naviroj, Peter W. Voorhees, and Katherine T. Faber. “Suspension- and solution-based freeze casting for porous ceramics”. In: *Journal of Materials Research* 32.17 (2017), pp. 3372–3382.
- [20] Ch. Körber et al. “Interaction of particles and a moving ice-liquid interface”. In: *Journal of Crystal Growth* 72.3 (1985), pp. 649–662.
- [21] Donald Robert Uhlmann, B. Chalmers, and K.A. Jackson. “Interaction between particles and a solid-liquid interface”. In: *Journal of Applied Physics* 35.10 (1964), pp. 2986–2993.
- [22] Haifei Zhang et al. “Aligned two- and three-dimensional structures by directional freezing of polymers and nanoparticles”. In: *Nature materials* 4.10 (2005), pp. 787–793.
- [23] Dipankar Ghosh et al. “Platelets-induced stiffening and strengthening of ice-templated highly porous alumina scaffolds”. In: *Scripta Materialia* 125 (2016), pp. 29–33.
- [24] W. Kurtz and D.J. Fisher. *Fundamentals of solidification*, *Trans Tech*. 1998.
- [25] Aurelia I. Ramos and David C. Dunand. “Preparation and characterization of directionally freeze-cast copper foams”. In: *Metals* 2.3 (2012), pp. 265–273.
- [26] Yasumasa Chino and David C. Dunand. “Directionally freeze-cast titanium foam with aligned, elongated pores”. In: *Acta Materialia* 56.1 (2008), pp. 105–113.
- [27] Huai-Ling Gao et al. “Macroscopic free-standing hierarchical 3D architectures assembled from silver nanowires by ice templating”. In: *Angewandte Chemie* 126.18 (2014), pp. 4649–4654.
- [28] Drew Clearfield and Mei Wei. “Investigation of structural collapse in unidirectionally freeze cast collagen scaffolds”. In: *Journal of Materials Science: Materials in Medicine* 27.1 (2016), p. 15.
- [29] Sylvain Deville et al. “In situ X-ray radiography and tomography observations of the solidification of aqueous alumina particle suspensions—part i: initial instants”. In: *Journal of the American Ceramic Society* 92.11 (2009), pp. 2489–2496.
- [30] R. Daudin et al. “Particle-induced morphological modification of Al alloy equiaxed dendrites revealed by sub-second in situ microtomography”. In: *Acta Materialia* 125 (2017), pp. 303–310.

- [31] Katherine T. Faber et al. *Freeze-cast ceramic membrane for size based filtration*. US Patent App. 16/549,954. 2020.
- [32] Daniel Schumacher, Michaela Wilhelm, and Kurosch Rezwan. “Modified solution based freeze casting process of polysiloxanes to adjust pore morphology and surface functions of SiOC monoliths”. In: *Materials & Design* 160 (2018), pp. 1295–1304.
- [33] Sylvain Deville. *Freezing colloids: observations, principles, control, and use: applications in materials science, life science, earth science, food science, and engineering*. Springer, 2017.
- [34] Sadaki Samitsu et al. “Flash freezing route to mesoporous polymer nanofibre networks”. In: *Nature Communications* 4.1 (2013), pp. 1–7.
- [35] Taijung Kuo et al. “Hierarchical porous SiOC via freeze casting and self-assembly of block copolymers”. In: *Scripta Materialia* 191 (), pp. 204–209.
- [36] Hao Bai et al. “Bioinspired large-scale aligned porous materials assembled with dual temperature gradients”. In: *Science advances* 1.11 (2015), e1500849.
- [37] Hao Bai et al. “Biomimetic gradient scaffold from ice-templating for self-seeding of cells with capillary effect”. In: *Acta biomaterialia* 20 (2015), pp. 113–119.
- [38] Etienne Munch et al. “Architectural control of freeze-cast ceramics through additives and templating”. In: *Journal of the American Ceramic Society* 92.7 (2009), pp. 1534–1539.
- [39] Maninpat Naviroj et al. “Nucleation-controlled freeze casting of preceramic polymers for uniaxial pores in Si-based ceramics”. In: *Scripta Materialia* 130 (2017), pp. 32–36.
- [40] Richard Obmann et al. “Porous polysilazane-derived ceramic structures generated through photopolymerization-assisted solidification templating”. In: *Journal of the European Ceramic Society* 39.4 (2019), pp. 838–845.
- [41] Stephen W. Sofie and Fatih Dogan. “Freeze casting of aqueous alumina slurries with glycerol”. In: *Journal of the American Ceramic Society* 84.7 (2001), pp. 1459–1464.
- [42] Michael M. Porter et al. “Bioinspired scaffolds with varying pore architectures and mechanical properties”. In: *Advanced Functional Materials* 24.14 (2014), pp. 1978–1987.
- [43] Yuan Zhang, Kaihui Zuo, and Yu-Ping Zeng. “Effects of gelatin addition on the microstructure of freeze-cast porous hydroxyapatite ceramics”. In: *Ceramics International* 35.6 (2009), pp. 2151–2154.



- [44] JW. Rutter and B. Chalmers. “A prismatic substructure formed during solidification of metals”. In: *Canadian Journal of Physics* 31.1 (1953), pp. 15–39.
- [45] William W. Mullins and R.F. Sekerka. “Stability of a planar interface during solidification of a dilute binary alloy”. In: *Journal of applied physics* 35.2 (1964), pp. 444–451.
- [46] W. Kurz and D.J. Fisher. “Dendrite growth at the limit of stability: tip radius and spacing”. In: *Acta Metallurgica* 29.1 (1981), pp. 11–20.
- [47] Kenneth A. Jackson. “Constitutional supercooling surface roughening”. In: *Journal of Crystal Growth* 264.4 (2004), pp. 519–529.
- [48] Martin Eden Glicksman. *Principles of solidification: an introduction to modern casting and crystal growth concepts*. Springer Science & Business Media, 2010.
- [49] Seishi Yajima, Josaburo Hayashi, and Mamoru Omori. “Continuous silicon carbide fiber of high tensile strength”. In: *Chemistry Letters* 4.9 (1975), pp. 931–934.
- [50] T. Zhang, J.R.G. Evans, and J. Woodthorpe. “Injection moulding of silicon carbide using an organic vehicle based on a preceramic polymer”. In: *Journal of the European Ceramic Society* 15.8 (1995), pp. 729–734.
- [51] Anthony R. Bunsell and Anne Piant. “A review of the development of three generations of small diameter silicon carbide fibres”. In: *Journal of Materials Science* 41.3 (2006), pp. 823–839.
- [52] Young-Wook Kim et al. “Processing of porous silicon carbide ceramics from carbon-filled polysiloxane by extrusion and carbothermal reduction”. In: *Journal of the American Ceramic Society* 91.4 (2008), pp. 1361–1364.
- [53] Zak C. Eckel et al. “Additive manufacturing of polymer-derived ceramics”. In: *Science* 351.6268 (2016), pp. 58–62.
- [54] Paolo Colombo et al. “Polymer-derived ceramics: 40 years of research and innovation in advanced ceramics”. In: *Journal of the American Ceramic Society* 93.7 (2010), pp. 1805–1837.
- [55] Ralf Riedel et al. “Silicon-based polymer-derived ceramics: synthesis properties and applications—a review dedicated to Prof. Dr. Fritz Aldinger on the occasion of his 65th birthday”. In: *Journal of the Ceramic Society of Japan* 114.1330 (2006), pp. 425–444.
- [56] M. Scheffler et al. “Pyrolytic decomposition of preceramic organo polysiloxanes”. In: *Ceramic Transactions(USA)* 115 (2000), pp. 239–250.
- [57] Gian Domenico Sorarù et al. “Si-Al-O-N Fibers from Polymeric Precursor: Synthesis, Structural, and Mechanical Characterization”. In: *Journal of the American Ceramic Society* 76.10 (1993), pp. 2595–2600.

- [58] Takemi Yamamura et al. “Development of a new continuous Si-Ti-CO fibre using an organometallic polymer precursor”. In: *Journal of Materials science* 23.7 (1988), pp. 2589–2594.
- [59] Rahul Harshe, Corneliu Balan, and Ralf Riedel. “Amorphous Si (Al) OC ceramic from polysiloxanes: bulk ceramic processing, crystallization behavior and applications”. In: *Journal of the European Ceramic Society* 24.12 (2004), pp. 3471–3482.
- [60] Samuel Bernard et al. “Evolution of structural features and mechanical properties during the conversion of poly [(methylamino) borazine] fibers into boron nitride fibers”. In: *Journal of Solid State Chemistry* 177.6 (2004), pp. 1803–1810.
- [61] Michael M. Seibold and Christian Rüssel. “Thermal conversion of preceramic polyiminoalane precursors to aluminum nitride: characterization of pyrolysis products”. In: *Journal of the American Ceramic Society* 72.8 (1989), pp. 1503–1505.
- [62] Boris Dyatkin and Matthew Laskoski. “Commercially scalable, single-step polymer-derived reaction bonding synthesis of refractory ceramics”. In: *The American Ceramic Society Bulletin* 99.7 (2020), pp. 30–35.
- [63] Teddy M. Keller et al. “In situ formation of nanoparticle titanium carbide/nitride shaped ceramics from meltable precursor composition”. In: *The Journal of Physical Chemistry C* 118.51 (2014), pp. 30153–30161.
- [64] Manoj K. Kolel-Veetil et al. “Formation and stability of metastable tungsten carbide nanoparticles”. In: *Journal of Materials Engineering and Performance* 24.5 (2015), pp. 2060–2066.
- [65] Manoj Kolel-Veetil et al. “Superconducting TaC nanoparticle-containing ceramic nanocomposites thermally transformed from mixed Ta and aromatic molecule precursors”. In: *Journal of Materials Research* 32.17 (2017), pp. 3353–3361.
- [66] Peter Greil. “Polymer derived engineering ceramics”. In: *Advanced engineering materials* 2.6 (2000), pp. 339–348.
- [67] Atanu Saha and Rishi Raj. “Crystallization maps for SiCO amorphous ceramics”. In: *Journal of the American Ceramic Society* 90.2 (2007), pp. 578–583.
- [68] Atanu Saha, Rishi Raj, and Don L. Williamson. “A model for the nanodomains in polymer-derived SiCO”. In: *Journal of the American Ceramic Society* 89.7 (2006), pp. 2188–2195.
- [69] Gabriela Mera et al. “Polymer-derived SiCN and SiOC ceramics—structure and energetics at the nanoscale”. In: *Journal of Materials Chemistry A* 1.12 (2013), pp. 3826–3836.

- [70] Tamas Varga et al. “Thermodynamically stable SixOyCz polymer-like amorphous ceramics”. In: *Journal of the American Ceramic Society* 90.10 (2007), pp. 3213–3219.
- [71] Tanguy Rouxel, Georges Massouras, and Gian-Domenico Sorarù. “High temperature behavior of a gel-derived SiOC glass: Elasticity and viscosity”. In: *Journal of sol-gel science and technology* 14.1 (1999), pp. 87–94.
- [72] Tanguy Rouxel, Gian-Domenico Soraru, and Jean Vicens. “Creep viscosity and stress relaxation of gel-derived silicon oxycarbide glasses”. In: *Journal of the American Ceramic Society* 84.5 (2001), pp. 1052–1058.
- [73] Alberto Scarmi, Gian Domenico Sorarù, and Rishi Raj. “The role of carbon in unexpected visco (an) elastic behavior of amorphous silicon oxycarbide above 1273 K”. In: *Journal of non-crystalline solids* 351.27-29 (2005), pp. 2238–2243.
- [74] Gian Domenico Sorarù et al. “Chemical durability of silicon oxycarbide glasses”. In: *Journal of the American Ceramic Society* 85.6 (2002), pp. 1529–1536.

## GRADIENT-CONTROLLED FREEZE CASTING

**3.1 Introduction**

Because the solidifying crystals template pores, fundamental solidification principles can guide control of pore space in freeze casting. Although the fundamental understanding of the solidification in freeze casting is still incomplete [1], some studies have highlighted the importance of solidification theory as a useful guide for tailoring pore size and morphologies. Miller et al. reported a study of freeze casting which predicts freezing front velocity from cooling conditions of suspension. The work shows agreement between solidification theory predictions and dendrite or lamellar spacing [2]. Naviroj et al. explored different pore morphologies freeze-cast with various solvents, and correlated the resulting structures to the Jackson  $\alpha$ -factor, a parameter representing crystal's anisotropy. In-situ imaging by confocal microscopy of particles being rejected at the freezing front by Dedovets et al. illustrated the importance of controlling the temperature gradient and growth rate to influence crystal morphology [3]. These demonstrations motivate the further exploration of fundamental solidification principles to manipulate freeze-cast structures.

This study focuses on another aspect of solidification, constitutional supercooling. The notion of constitutional supercooling was originally conceived by Rutter and Chalmers [4], and reported that cellular crystal growth resulted from the instability of interface, which was caused by the concentration gradient in the liquid ahead of the freezing front. Later, this was mathematically formulated by Tiller, Rutter and Jackson using the steady-state diffusion equation [5]. The condition for a stable planar front can be expressed by the following equation,

$$\frac{G}{V} = \frac{k_0 - 1}{k_0} \frac{mC_0}{D} \quad (3.1)$$

where  $G$  is the temperature gradient,  $V$  is the freezing front velocity,  $k_0$  ( $= C_S/C_L$ ) is the equilibrium distribution coefficient,  $m$  is the slope of liquidus,  $C_0$  is the initial concentration of solute in liquid, and  $D$  is the diffusion coefficient of the solute in the liquid. Eqn. 3.1 defines the critical ratio,  $G/V$ , to ensure that no constitutional supercooling occurs [15][6]. As shown in a stability-microstructure map (Figure

3.1(a)), Eqn. 3.1 represents the boundary between cellular crystals and a stable planar front. Dendrites form when  $G/V$  is far away from this condition while cells form in the narrow region close to planar front in the stability-microstructure map (illustrations of cells and dendrites are shown in Fig. 1(b)). Hence, controlling the degree of constitutional supercooling by  $G$  and  $V$  allows crystal morphology to be adjusted, and therefore, serve as a useful guide to achieve the desired porous microstructure. One example which uses this constitutional supercooling theory to modify crystal morphology is additive manufacturing of metals [7, 8] as equiaxed dendritic grains are favored over columnar grains to avoid hot cracking.

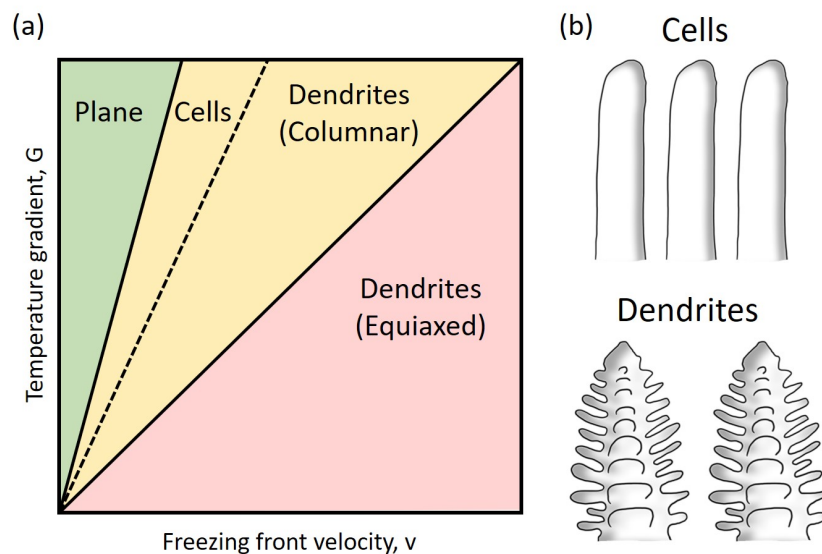


Figure 3.1: Stability-microstructure map showing the independent control of freezing front velocity and temperature gradient allows one to change crystal morphology (a). Modified from ref. [9]. (b) Illustration of cells and dendrites.

Although numerous freeze-casting investigations have demonstrated freezing-front velocity ( $V$ ) control, there is a paucity of studies which focus on the effect of temperature gradient ( $G$ ) in freeze-cast structures. Zheng et al. showed independent control of  $V$  and  $G$  to create axially homogeneous pore structure [19][10]. The first study to achieve cellular pores based on the stability-microstructure map was done by Zeng et al. [11], which reported the morphological transition of columnar dendrites to cells as  $V$  is decreased at constant  $G$  and demonstrated improved shape-memory properties. However, in suspension-based freeze casting, it is challenging to analyze the morphological change of dendritic structures in detail as the suspending particles destabilize and break down the dendrite tips, leading to less anisotropy in the porous

structure [12]. As a result, the pore size distribution exhibits a unimodal distribution instead of bimodal distribution, characteristic of dendritic structures.

In this study, freeze-cast structures are created through control of  $G$  and  $V$  based on the underlying theory of constitutional supercooling, with the goal of manipulating pore size and pore morphology. We use preceramic polymer solutions as the freeze-casting medium since distinct dendritic structures with bimodal pore size distributions can be achieved via this route. Hence, for the first time, a more quantitative analysis of the effects of  $G$  and  $V$  are possible. Dendritic structural evolution as a result of a change in  $V$  at fixed  $G$  and a change in  $G$  at fixed  $V$  is investigated using image analysis and pore size measurement by mercury intrusion porosimetry, establishing an effective tool for pore morphology control.

## **3.2 Experimental methods**

### **3.2.1 Preceramic polymer solution**

A polymer solution was prepared by dissolving polymethylsiloxane preceramic polymer (Silres®MK Powder, Wacker Chemie, Munich, Germany), in cyclohexane (Sigma-Aldrich, St. Louis, MO, USA) with the polymer concentration of 10 wt.% (6.5 vol.%) and 20 wt.% (13 vol.%). Such concentrations result in porosities of 89 % and 78 %, respectively. A solution with dioxane (Sigma-Aldrich, St. Louis, MO, USA) is also prepared with the same volume concentration as 20 wt.% cyclohexane solution. A cross-linking agent (Geniosil®GF 91, Wacker Chemie, Munich, Germany) was added at a concentration of around 1 wt.% to all polymer solutions and stirred for 5 min. Before freezing, the solutions were degassed for 10 min to avoid air bubbles during freezing.

### **3.2.2 Freeze casting**

The solution was poured into the glass mold ( $h = 12.5$  mm or 20 mm,  $\varnothing = 24$  mm) and the mold was placed on a thermoelectric plate which is continuously cooled by a circulating refrigerated silicone oil. A second thermoelectric plate was placed on top of the mold to control the temperature of the top side (Figure 3.2). Due to shrinkage during solidification, the copper plate was designed to be inserted 5 mm into the glass mold, creating a reservoir for the solution to avoid detachment of the solution from the top cold finger. The temperature of both thermoelectric plates was controlled by a PID controller. Two solidification parameters,  $V$  and  $G$  were measured from images taken by camera with the intervalometer. Images were taken at different intervals ranging from 30 seconds to 10 minutes, depending on  $V$ .

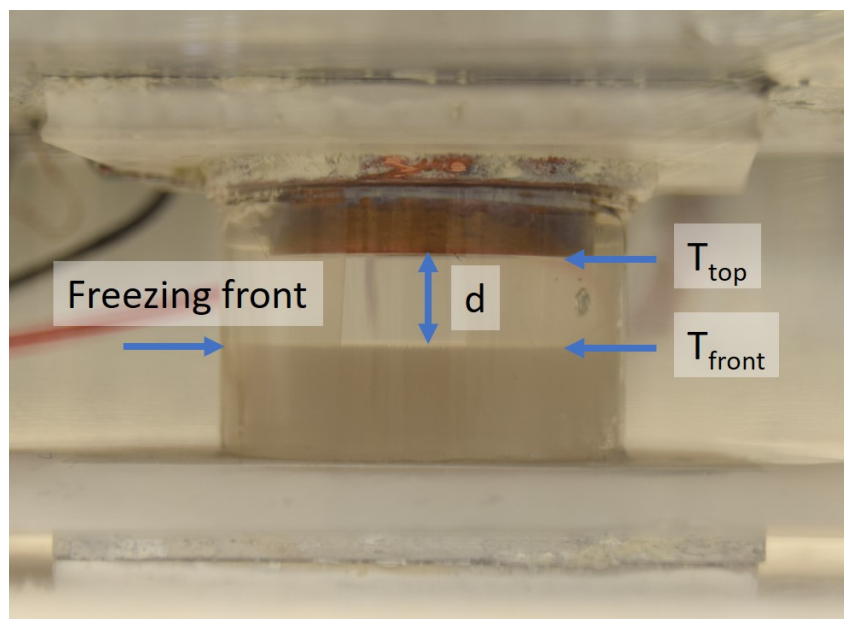


Figure 3.2: A photograph showing gradient-controlled freeze-casting setup.

Images were analyzed using ImageJ (National Institutes of Health) to determine  $V$ .  $G$  was also determined from images by the following equation:

$$G = \frac{T_{top} - T_{front}}{d} \quad (3.2)$$

where  $T_{top}$ ,  $T_{front}$ , and  $d$  are the temperature of the top thermoelectric plate, the temperature of freezing front, and the distance between the copper plate and freezing front, respectively. The temperature of the freezing front is assumed to be the liquidus temperature of the solution, the value of which is taken from the study by Naviroj [13]. A mold with a different height was chosen to alter  $G$ . The molds with 12.5 mm and 20 mm heights result roughly in temperature gradients of 5.0 K/mm and 2.5 K/mm for cyclohexane solution, respectively. Appendix B summarizes all of the examined freezing front velocities and temperature gradients. For reference, a sample with no prescribed temperature gradient was made. In this control sample, the top thermoelectric was removed and the top surface was kept open to the ambient atmosphere, as is performed in conventional suspension- or solution-based freeze casting. See Appendix C for a detailed comparison between conventional freezing and gradient-controlled freezing.

After freezing, samples were placed into a freeze drier (VirTis AdVantage 2.0, SP Scientific, Warminster, PA, USA), where the solvents were completely sublimated.

After sublimation, the green bodies were pyrolyzed at 1100 °C in argon for 4 hours with a ramp rate of 2 °C/min to convert polymethylsiloxane into silicon oxycarbide (SiOC). Sample porosity was determined using the Archimedes method.

### 3.2.3 Characterization

The porous microstructure was imaged using scanning electron microscopy (SEM; Zeiss 1550VP, Carl Zeiss AG, Oberkochen, Germany) in two different directions: the transverse direction (a cross-section perpendicular to freezing direction) and the longitudinal direction (a cross-section parallel to freezing direction). The pore size distribution was measured by mercury intrusion porosimetry (MIP; Auto Pore IV, Micromeritics, Norcross, GA, USA). For MIP, the samples were core-drilled to a diameter of ~13 mm to remove edges. Specimens for imaging and pore size measurements were sectioned from locations where V and G remain reasonably constant.

## 3.3 Results

### 3.3.1 Temperature gradient effect

Figure 3.3 shows SEM images and pore size distributions of the sample freeze-cast from 20 wt.% polymer solution with cyclohexane. Figure 3.3a is the SEM image showing the transverse direction, a cross-section perpendicular to the freezing direction, of the control sample frozen under  $V = 15 \mu\text{m/s}$ . It shows the characteristic feature of the dendritic pores having the primary pores, secondary pores, and even tertiary pores, also reported by Naviroj et al. [12]. Figure 3.3b shows a magnified image of dendritic pores, where the black contrast outlines the primary pore and four secondary branches. In some instances, tertiary pores also branch out from the secondary pores (tertiary pores are indicated by yellow arrows in Figure 3.3b). Figure 3.3c shows the analogous images of the sample frozen with  $V = 15 \mu\text{m/s}$  and  $G = 2.6 \text{ K/mm}$  (gradient-controlled sample). In contrast to Figure 3.3a, the growth of the secondary and tertiary pores is limited, leading to smaller dendritic pore spacing and higher primary pore concentrations (a tertiary pore is indicated by yellow arrows in Figure 3.3d). Figure 3.3e displays the pore size distribution data from MIP; both samples show bimodal peaks showing large primary pores and small secondary pores compared to the control. The primary pore size for both samples is approximately 20.3  $\mu\text{m}$ . In contrast, the peak secondary pore size differs by only 1  $\mu\text{m}$  (13.7  $\mu\text{m}$  from the control sample and 12.7  $\mu\text{m}$  from the gradient-controlled sample). More compelling, the volume associated with primary pores



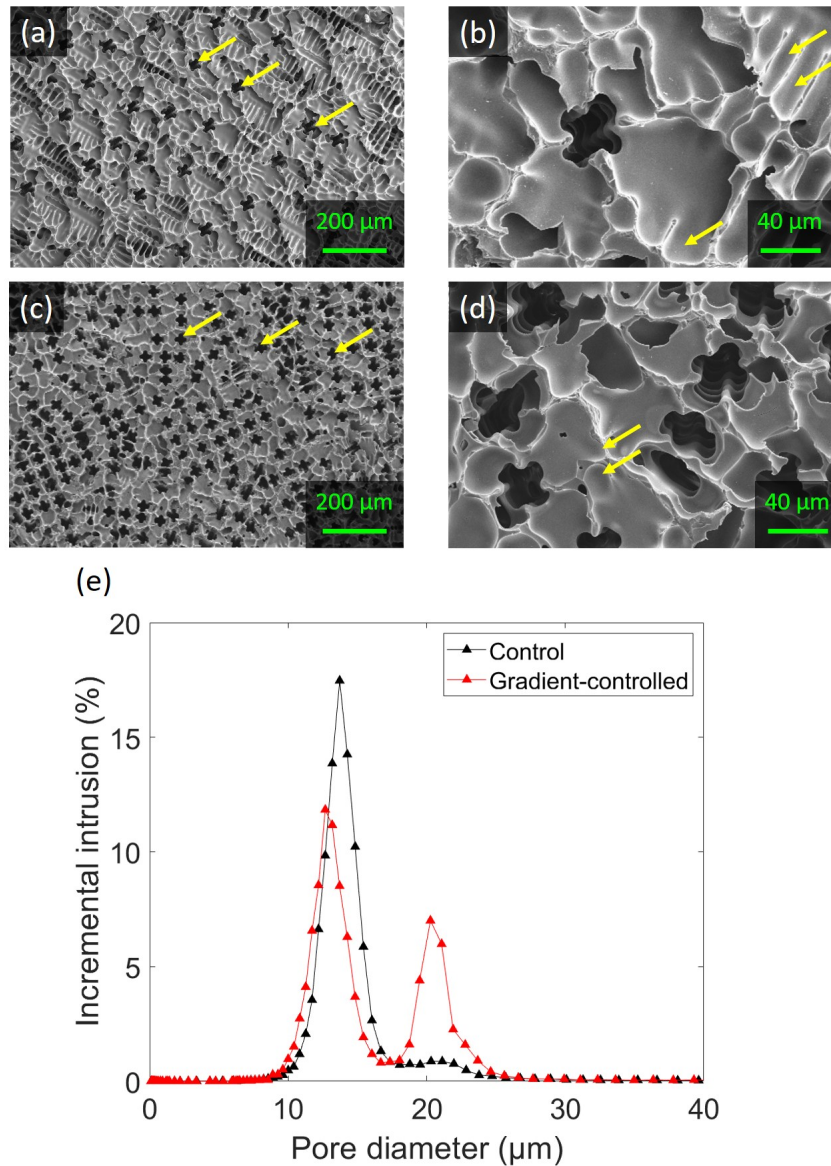


Figure 3.3: SEM images showing a control sample at (a) low and (b) high magnifications and a gradient-controlled sample at (c) low and (d) high magnifications in transverse direction. Yellow arrows in low magnification and high magnification images indicate primary pores and tertiary pores, respectively. (e) Pore size distribution of control sample and gradient-controlled sample.

and secondary pores has changed significantly as shown by the change in peak height. Summing the incremental intrusion of each type of pores gives 6 vol.% for primary pores in the control sample whereas 28 vol.% for primary pores in the gradient-controlled sample, in agreement with SEM images, an increase of more than four-fold by applying G.

### 3.3.2 Change in freezing front velocity and temperature gradient

Figures 3.4 a-e show SEM images of samples freeze-cast from 20 wt.% polymer solution in transverse direction and longitudinal direction. Figures 3.4a-d show SEM images comparing freeze-cast structures frozen under different velocities (17  $\mu\text{m/s}$  sample and 1.8  $\mu\text{m/s}$ ) at nearly the same temperature gradient. This corresponds to moving from the orange to blue marker horizontally in the stability microstructure map in Figure 3.4g. When  $V$  is decreased about an order of magnitude, pores are still dendritic, but both primary and secondary pore sizes increase. This is further confirmed by pore size distributions in Figure 3.4g. The calculated primary pore volume fractions increased from 24 to 30 vol.% by decreasing  $V$ . Figures 3.4e and f show SEM images of freeze-cast structures frozen under  $V$  of 1.5  $\mu\text{m/s}$  and  $G$  of 5.0 K/mm. The comparison between Figures 3.4c and e reveal the effect of  $G$  at constant  $V$ , which corresponds to moving from the blue to green marker vertically in Figure 3.4g. The transverse images show the primary pore spacing,  $\lambda_d$  (indicated by the yellow arrows), decreased as  $G$  is increased. Pore size distributions show that both structures have similar primary pore sizes although secondary pores size of higher  $G$  is smaller. In addition, as shown in pore size distribution, primary pore volume fraction increased by increasing  $G$ . The calculated primary pore volume is increased from 30 to 48 vol.% when  $G$  is increased at similar  $V$ .

### 3.3.3 Change in polymer concentration

The preceramic polymer concentration change from 20 wt. % to 10 wt.% at similar  $V$  and  $G$  is also investigated. SEM images and pore size distributions are shown in Figure 3.5. SEM images show that 10 wt.% preceramic polymer solution yielded dendritic structures with larger pore size, further confirmed by pore size distribution data. Both primary and secondary pore sizes are larger from 10 wt.% polymer solutions even though both samples are frozen under similar  $V$  and  $G$ . Moreover, the primary pore volume fraction increased from 30 to 51 vol.% by decreasing polymer concentration from 20 wt.% to 10 wt.%, indicating that more than half of the pore volume is attributed to primary pores from the 10 wt.% polymer solution.

### 3.3.4 Morphological change from dendrites to cells

The stability-microstructure map suggests that cellular growth is possible with low  $V$  and high  $G$ . In order to achieve cellular pores,  $V$  was significantly reduced to 0.6  $\mu\text{m/s}$  while  $G$  was fixed at 5 K/mm. Slower velocities for this 20 wt.% polymer solution would result in the gelation of the solution before freezing was complete. As shown

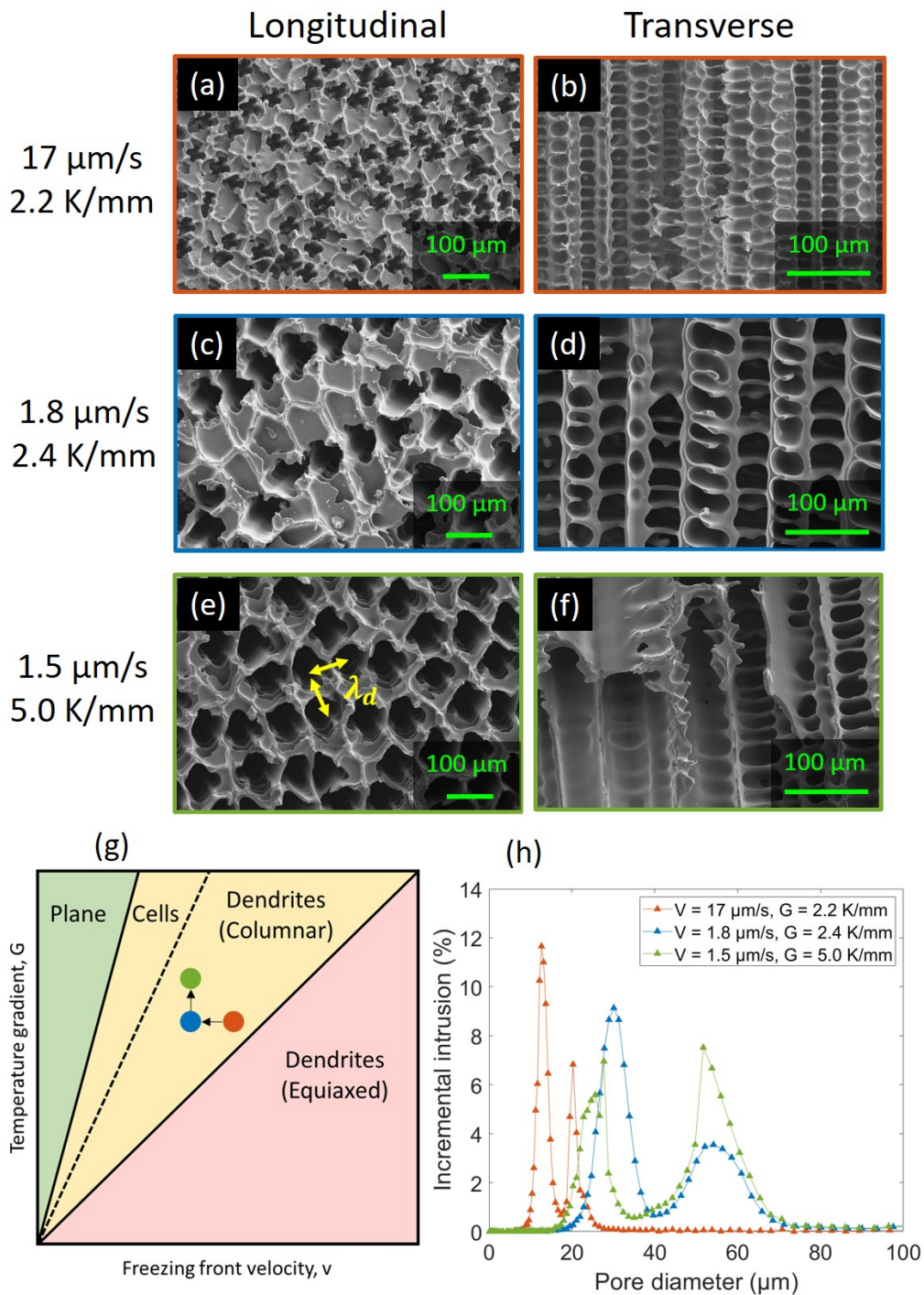


Figure 3.4: SEM images of the sample frozen with  $V = 17 \mu\text{m/s}$  and  $G = 2.2 \text{ K/mm}$  in (a) transverse and (b) longitudinal direction, the sample frozen with  $V = 1.8 \mu\text{m/s}$  and  $G = 2.4 \text{ K/mm}$  in (c) transverse and (d) longitudinal direction, and the sample frozen with  $V = 1.5 \mu\text{m/s}$  and  $G = 5.0 \text{ K/mm}$  in (e) transverse and (f) longitudinal direction. (g) A stability-microstructure map showing examined conditions by colored marker. (h) Pore size distributions of corresponding samples.

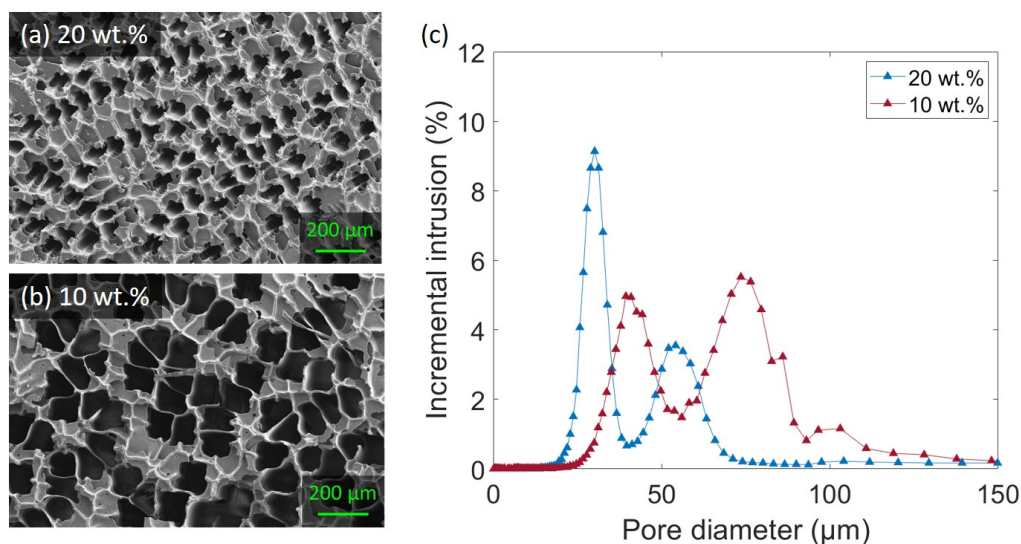


Figure 3.5: SEM images showing dendritic structure from (a) 20 wt.% solution and (b) 10 wt.% solution in transverse direction. (c) Corresponding pore size distribution from MIP.

in the Figures 3.6a and b, although the transverse image would indicate cellular or honeycomb-like morphologies, the longitudinal image shows the presence of secondary pores and the cellular morphologies limited to only a portion of the solid. When the polymer concentration is reduced to 10 wt.% and frozen under similar  $V$  and  $G$ , SEM images reveal a larger portion of cellular morphologies (Figures 3.6c and d). In contrast, dioxane, also investigated as a solvent in this study and known to yield dendritic structures [12], has a significantly longer gelation time of the solution (4 to 5 days) and higher boiling point. Hence, the solution can be frozen with slower velocities and higher temperature gradient. Figures 3.6e and f show the images of the sample freeze cast with dioxane where  $V = \sim 0.2 \mu\text{m/s}$  and  $G = 12 \text{ K/mm}$ . The transverse and longitudinal images show the complete cellular morphologies.

### 3.4 Discussions

#### 3.4.1 Pore size control

Because this setup allows independent control of  $V$  and  $G$ , the effects of the two parameters on pore structure can be analyzed separately. Figure 3.7a shows the peak values<sup>1</sup> of primary pores in pore size distribution as a function of  $V$  for two values of  $G$  in 20 wt.% polymer solution. The primary pore size decreases with increasing

<sup>1</sup>Some pore size distributions contain outliers which are probably due to the fracture of samples during the intrusion of mercury. These pore size distribution data were fitted using the software, Fityk [14], and the peaks of fitted curves were plotted in Figures 3.7a and b.

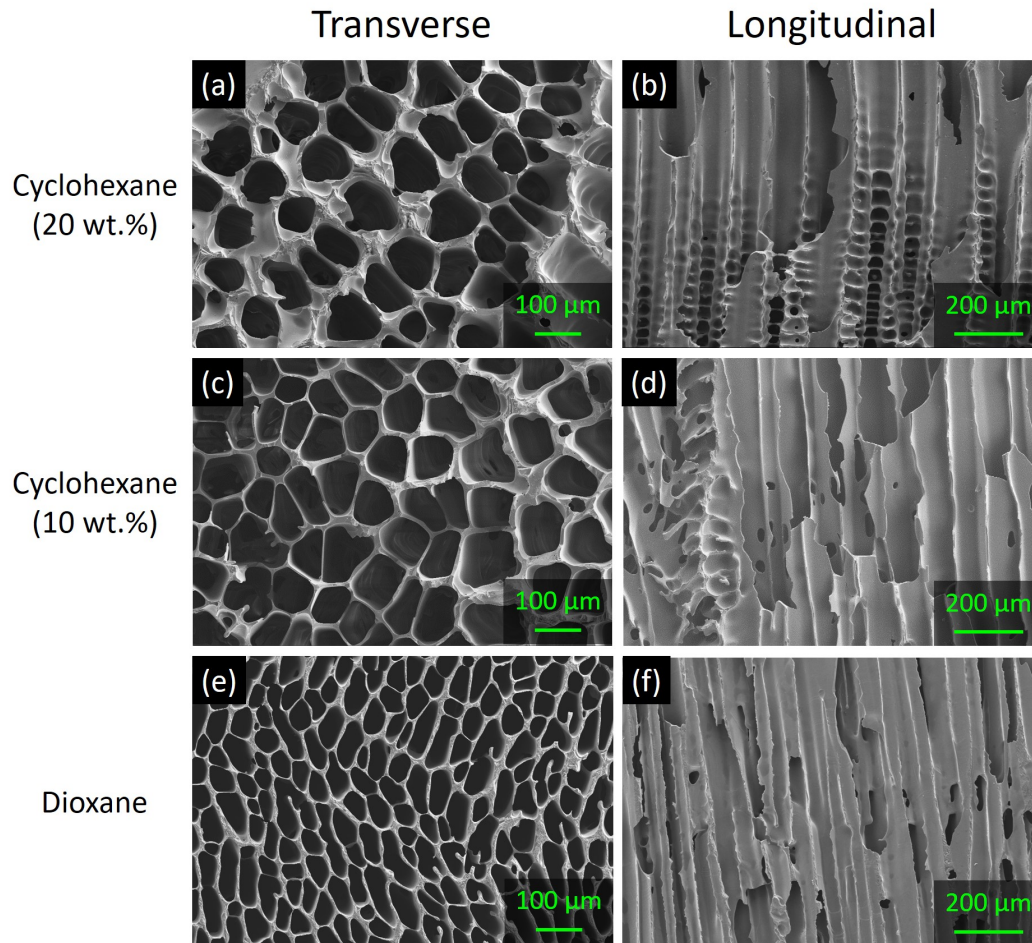


Figure 3.6: SEM images showing a SiOC from cyclohexane crystals (20 wt.% polymer solution) in (a) transverse and (b) longitudinal directions, from cyclohexane crystals (10 wt.% polymer solution) in (c) transverse and (d) longitudinal directions, and from dioxane crystals in (e) transverse and (f) longitudinal directions.

V. This is expected since freezing front velocity affects the dendrite size, and is consistent with other studies on dendritic pores [2, 13]. It also shows that primary pore sizes from two values of  $G$ , 2.5 K/mm and 5 K/mm, follow the same trend, indicating that the primary pore sizes do not strongly depend on  $G$ . Alternatively, secondary pore sizes can be described using a model for secondary arm spacing. While secondary arm spacing measures center-to-center spacing of neighboring secondary arms, which includes the secondary arm diameter and the interdendritic phase, the secondary pore size reported here is a measure solely of secondary arm diameter. Since the polymer concentration remains the same, it was assumed that the secondary arm diameter and the interdendritic phase increase their sizes at the same rate. Hence, secondary arm spacing model can be applied to analyze secondary

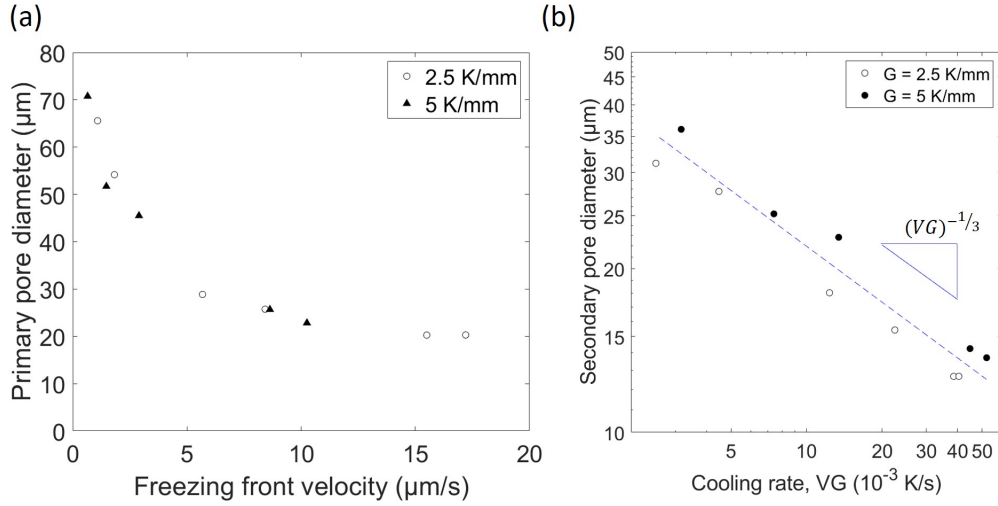


Figure 3.7: Plots of (a) Primary pore size as a function of  $V$  with different  $G$  and (b) secondary pore size as a function of cooling rate.

pore size. The secondary arm spacing is known to depend on both  $V$  and  $G$  based on the model by Feurer and Wunderlin [15]:

$$\lambda_2 = 5.5 \left[ \frac{D\Gamma \ln \frac{C_L^m}{C_0}}{m(1 - k_0)(C_0 - C_L^m)} \right]^{1/3} t_f^{1/3} \quad (3.3)$$

$$t_f = \frac{\Delta T'}{GV} \quad (3.4)$$

where  $C_L^m$  is often equal to the eutectic composition,  $t_f$  is the local solidification time, and  $\Delta T'$  is the difference between the temperature at the tip of the dendrites and the melting point of the last interdendritic liquid. The local solidification time is the time the liquid phase and solid phase coexist at a fixed point, and is determined by dividing  $\Delta T'$  by cooling rate,  $VG$ . Hence, the secondary arm spacing depends on the cube root of  $1/VG$ . Figure 3.7b shows the peak value of secondary pore size in the pore size distribution as a function of cooling rate,  $VG$ . The exponent from curve fitting is  $-0.34$ , in excellent agreement with the model.

One other dimension in dendrites, which has been studied in solidification of alloy extensively but rarely studied in freeze casting, is a dendrite spacing,  $\lambda_1$ . Kurz and Fisher reported a model for the dendrite spacing in alloys [16]:

$$\lambda_1 = 4.3(T_L - T_e - \Delta T^*)^{1/2} \left[ \frac{D\Gamma}{(T_L - T_S)k_0} \right]^{1/4} V^{-1/4} G^{-1/2} \quad (3.5)$$

where  $T_L$  is liquidus temperature,  $T_S$  is solidus temperature,  $T_e$  is eutectic temperature,  $\Delta T^*$  is tip undercooling,  $D$  is diffusion coefficient of solute,  $\Gamma$  is the Gibbs Thomson parameter, and  $k_0$  is the equilibrium distribution coefficient. This model predicts that  $\lambda_1$  decreases when  $G$  is increased at constant  $V$ , assuming all the other parameters remain constant. This is consistent with observations made in Figures 3.3a and c, and Figures 3.4c and e, which show that primary pore spacing tends to decrease with increasing  $G$ . Since pore size distribution shows that primary pore size does not change significantly by increasing  $G$ , the results imply that the lengths of secondary or even tertiary pores decrease, another dimension controlled through  $G$ .

Finally, when the preceramic polymer concentration is decreased from 20 wt.% to 10 wt.% (Figure 3.5), the primary and secondary pore sizes increased. This is also expected because the preceramic polymer concentration determines the space for the growing crystals as reported by Naviroj [13]. As a result, lower concentration yields larger pore sizes since more space is available for crystals to grow. Moreover, secondary arm spacing also directly depends on  $C_0$  in Eqn. 3.3; decrease in  $C_0$  would increase the secondary arm spacing, as shown in Eqn. 3.5. Hence, an increase in both primary and secondary pore sizes is expected with decreasing the preceramic polymer concentration.

### 3.4.2 Cellular growth

In addition to manipulation of pore size, independent control of  $V$  and  $G$  allows one to explore the stability-microstructure map in detail, especially with an aim to achieve cellular growth. As a parameter to represent transition from dendritic to cellular pores, primary pore volume fraction from pore size distribution is calculated and reported here. As solidification conditions are changed such that the conditions approach the cellular growth regime, the pore size distribution evolves from bimodal to unimodal and the primary pore fraction reaches 100%. In the case of decreasing  $V$  at constant  $G$ , one would move horizontally in the stability-microstructure map (Figure 3.4g). As expected, the primary pore volume fraction increased (from 24 vol.% to 30 vol.% for 20% polymer solutions) as the cellular growth regime is approached. With the increase in  $G$  at constant  $V$ , one would move up vertically in the stability-microstructure map. Again, by advancing toward the cellular growth

regime, an increase in primary pore fraction is expected, and was demonstrated experimentally (from 30 vol.% to 48 vol.%) in the same 20% polymer solution. As shown in Figures 3.4c and e, the pore structure starts to exhibit honeycomb-like structures when  $G$  is increased.

The conditions for stable planar growth front expressed by Eqn.3.1 provide guidance on how to achieve cellular growth in addition to controlling  $V$  and  $G$ . For example, the concentration of the solute,  $C_0$ , can be reduced, resulting in a decrease of the slope of the boundary in the stability-microstructure map. As a result, the critical conditions for  $V$  and  $G$  to establish a stable planar front become less stringent, and the structures tend to have cellular-like morphologies even if  $V$  and  $G$  are similar. This explains why reducing preceramic polymer concentration increases primary pore fraction from 30 to 51 vol.% even though  $V$  and  $G$  are similar (Figure 3.5c).

Due to the short gelling time of the cyclohexane solution and the boiling point of cyclohexane (80.7 °C), the slowest  $V$  and the highest  $G$  examined in this study was not sufficient to achieve long-range cellular growth (Figure 3.6b). To overcome this challenge, the preceramic polymer concentration was reduced to 10 wt.% and a solution was frozen with similar  $V$  and  $G$ . Although the pore structure still exhibits secondary pores, Figure 3.6d displays a larger portion of cellular pores. This demonstrates that the constitutional supercooling theory can be applied successfully to freeze casting and can be used to change dendritic pores to cellular pores through optimization of solidification parameters along with solution parameters such as solute concentration.

### 3.4.3 Anisotropy of cellular pores

Since the dioxane solution has a much longer gelling time, slower velocities were able to be examined. As a result, long-range honeycomb-like structures were yielded from the dioxane solution (Figure 3.6d). Also noteworthy is that the pores from cyclohexane crystals show more circular shapes, while the pores from dioxane crystals are elongated. This difference can be attributed to the anisotropic nature of the crystal growth. Naviroj et al. showed freeze-cast structures from cyclohexane and dioxane exhibit dendritic structures, but dioxane-derived dendritic structures exhibited a linear and two-dimensional configuration due to its higher Jackson  $\alpha$  factor (1.16 for cyclohexane and 5.21 for dioxane) [12]. While the planar freezing front follows the direction of the temperature gradient, primary dendrites and the dendritic arms grow along preferred crystallographic directions. Cells grow under



the condition close to the limit of the constitutional supercooling of the planar interface, and are intermediate morphology of the plane and dendrites [15]. Thus, the cells are still expected to exhibit some crystallographic features, and the anisotropic honeycomb pore morphology from dioxane solution is expected.

### 3.5 Conclusion

Directional solidification with controlled freezing front velocity and temperature gradient was conducted in solution-based freeze casting, and the relationship between solidification parameters and pore structures was investigated. Solidification theory explains dendritic pore size dependence on solidification parameters well, and constitutional supercooling theory can be successfully used to control pore morphologies.

While the freezing front velocity is the major solidification parameter to control primary pore size, temperature gradient does not significantly change the primary pore size in the temperature gradient range between 2.5 K/mm and 5 K/mm. Alternatively, secondary pores are determined by the cooling rate, the product of temperature gradient and freezing front velocity, and the experimental data in this study agree well with the theoretical models. The benefit of controlling temperature gradient and freezing front velocity is not only to control pore size but also pore morphology by changing the degree of constitutional supercooling. The cellular or honeycomb-like structures are observed in systems with cyclohexane by manipulation of freezing front velocity, temperature gradient, and polymer concentration, although there are still noticeable regions of dendritic pores. In contrast, the honeycomb structures are observed in systems with dioxane as the solvent, which gelled sufficiently slowly and has high a boiling point so as to permit slow freezing front velocities and high temperature gradients. Finally, similarly to dendritic pores, cellular pores also exhibit crystallographic features of solvent crystals. These concepts can be extended to other solvents or dispersion media in other freeze-casting systems for fine-tuning pore networks.

### References

- [1] Sylvain Deville. “The lure of ice-templating: Recent trends and opportunities for porous materials”. In: *Scripta Materialia* 147 (2018), pp. 119–124.
- [2] Sarah M Miller, Xianghui Xiao, and Katherine T. Faber. “Freeze-cast alumina pore networks: Effects of freezing conditions and dispersion medium”. In: *Journal of the European Ceramic Society* 35.13 (2015), pp. 3595–3605.

- [3] Dmytro Dedovets and Sylvain Deville. “Multiphase imaging of freezing particle suspensions by confocal microscopy”. In: *Journal of the European Ceramic Society* 38.7 (2018), pp. 2687–2693.
- [4] JW. Rutter and B. Chalmers. “A prismatic substructure formed during solidification of metals”. In: *Canadian Journal of Physics* 31.1 (1953), pp. 15–39.
- [5] Kenneth A. Jackson. “Constitutional supercooling surface roughening”. In: *Journal of Crystal Growth* 264.4 (2004), pp. 519–529.
- [6] W.A. Tiller et al. “The redistribution of solute atoms during the solidification of metals”. In: *Acta metallurgica* 1.4 (1953), pp. 428–437.
- [7] Fuyao Yan, Wei Xiong, and Eric J. Faierson. “Grain structure control of additively manufactured metallic materials”. In: *Materials* 10.11 (2017), p. 1260.
- [8] John H. Martin et al. “3D printing of high-strength aluminium alloys”. In: *Nature* 549.7672 (2017), pp. 365–369.
- [9] Martin Eden Glicksman. *Principles of solidification: an introduction to modern casting and crystal growth concepts*. Springer Science & Business Media, 2010.
- [10] Tao Zheng et al. “Implementing continuous freeze-casting by separated control of thermal gradient and solidification rate”. In: *International Journal of Heat and Mass Transfer* 133 (2019), pp. 986–993.
- [11] Xiaomei Zeng, Noriaki Arai, and Katherine T. Faber. “Robust Cellular Shape-Memory Ceramics via Gradient-Controlled Freeze Casting”. In: *Advanced Engineering Materials* 21.12 (2019), p. 1900398.
- [12] Maninpat Naviroj, Peter W. Voorhees, and Katherine T. Faber. “Suspension- and solution-based freeze casting for porous ceramics”. In: *Journal of Materials Research* 32.17 (2017), pp. 3372–3382.
- [13] Maninpat Naviroj. “Silicon-based porous ceramics via freeze casting of pre-ceramic polymers”. PhD thesis. Northwestern University, 2017.
- [14] Marcin Wojdyr. “Fityk: a general-purpose peak fitting program”. In: *Journal of Applied Crystallography* 43.5-1 (2010), pp. 1126–1128.
- [15] W. Kurtz and D.J. Fisher. *Fundamentals of solidification, Trans Tech*. 1998.
- [16] W. Kurz and D.J. Fisher. “Dendrite growth at the limit of stability: tip radius and spacing”. In: *Acta Metallurgica* 29.1 (1981), pp. 11–20.

*Chapter 4*FREEZE-CAST HONEYCOMB STRUCTURES VIA  
GRAVITY-ENHANCED CONVECTION**4.1 Introduction**

Gravity is known to have a significant influence on materials processing. In float glass processing, a glass ribbon is produced by flowing molten glass on a molten tin bath [1]. With the help of gravity and surface tension, a flat glass with high surface quality can be fabricated. While this is an example where the presence of gravity is advantageous in material processing, some processing is negatively influenced by the gravitational force. In colloidal suspensions, sedimentation of particles by gravitational forces must be mitigated with suspension agents [2]. In another example, directional solidification for producing semiconductor crystals or nickel-based single crystals, gravity influences the convective flow in the melt. Since convection in the melt creates defects known as freckles in casting [3], solidification under microgravity [4] or with magnetic damping [5] has been explored to alleviate convection.

Motivated by studies in directional solidification of metal alloys with convective flow [6, 7, 8], this chapter focuses on the effect of the convective flow induced by gravity during freeze casting. In alloy systems, depending on the density of the composition in alloys, convective flow may be present during the directional solidification [9, 10]. For instance, in what has been labeled downward freezing (in the same direction as the gravitational force) if the solute is denser than the solvent, the segregated solute creates a denser fluid region ahead of the freezing front, and enhanced convective flow. In general, however, convection is limited to regions near the mold-alloy interface in upward freezing. Although the effect of gravity is actively studied in alloy solidification, a limited number of studies have examined gravity effects in freeze casting. Scotti et al. investigated the effect of the freezing direction with respect to the gravity. Microstructures were found to contain tilted lamellar walls, ice lens formation and radial micro-segregation, caused by the convective flow [11]. Another study demonstrated that different gravitational forces (micro-, lunar and Martian gravity) affect the lamellar spacings [12]. Both however, were based on freeze-casting suspensions. Since suspensions are made up

of particles and additives such as binders and dispersants, they are more complex systems compared to solutions, which contain only solutes and solvents. In this study, solidification was performed with solutions in both the conventional set-up, where the gravitational force is opposite in direction than the freezing direction, and a convection-enhanced set-up, where the gravitational force is in concert with the freezing direction. The effect of the enhanced convection induced by the gravitational force on the solidification and resulting porous structures are examined. In particular, the freezing front velocity and temperature gradient are compared between two freezing conditions, and the resulting pore morphologies and pore sizes are investigated.

## 4.2 Experimental methods

A preceramic polymer, polymethylsiloxane (Silres®MK Powder, Wacker Chemie, CH<sub>3</sub>-SiO<sub>1.5</sub>, Munich, Germany), was dissolved in cyclohexane (Sigma-Aldrich, St. Louis, MO, USA) at a concentration of 20 wt.%. A cross-linking agent (Geniosil®GF 91, Wacker Chemie, Munich, Germany) was added at a concentration of 1 wt.% with respect to the solution and stirred for 5 min. The polymer solution was degassed for 10 min to avoid air bubble formation during freezing. Directional freezing was conducted using a gradient-controlled freeze-casting setup [13]. The polymer solution was poured into a cylindrical mold placed on a thermoelectric plate. A second thermoelectric plate was placed on top of the mold, enabling the control of freezing front velocity and temperature gradient. The sample was frozen in two different directions: one against the direction of gravity, referred to as conventional freezing and one along the direction of gravity, referred as to convection-enhanced freezing (Figures 4.1ab). The cooling profiles for two thermoelectric plates were programmed such that solidification took place with a freezing front velocity of 1.8 μm/s and a temperature gradient of 2.5 K/mm in conventional freezing. For the convection-enhanced freezing, the cooling profiles were switched between the upper and lower thermoelectric plates so the freezing proceeded from top to the bottom. Images of freezing front were captured once each minute by a camera with an intervalometer. Image analysis was performed using ImageJ (National Institutes of Health) to determine the freezing front velocity. The temperature gradient was defined by:

$$G = \frac{T_{hot} - T_{front}}{d}$$

where  $T_{hot}$ ,  $T_{front}$ , and  $d$  are the temperature of the thermoelectric plate toward which the crystals are growing, the temperature at the freezing front, and the distance

between points where  $T_{hot}$  and  $T_{front}$ , respectively. The freezing front was assumed to be at the liquidus temperature reported by Naviroj [14]. The frozen samples were placed in a freeze drier to completely remove solvent crystals, and then pyrolyzed under argon at 1100 °C for 4 hours, resulting in porous silicon oxycarbide (SiOC). Porosity was measured using the Archimedes' method. Porous structures were imaged using scanning electron microscopy (SEM; ZEISS 1550VP, Carl Zeiss AG, Oberkochen, Germany), and pore sizes were determined by mercury intrusion porosimetry (MIP; AutoPoreIV, Micromeritics, Norcross, GA, USA).

### 4.3 Results

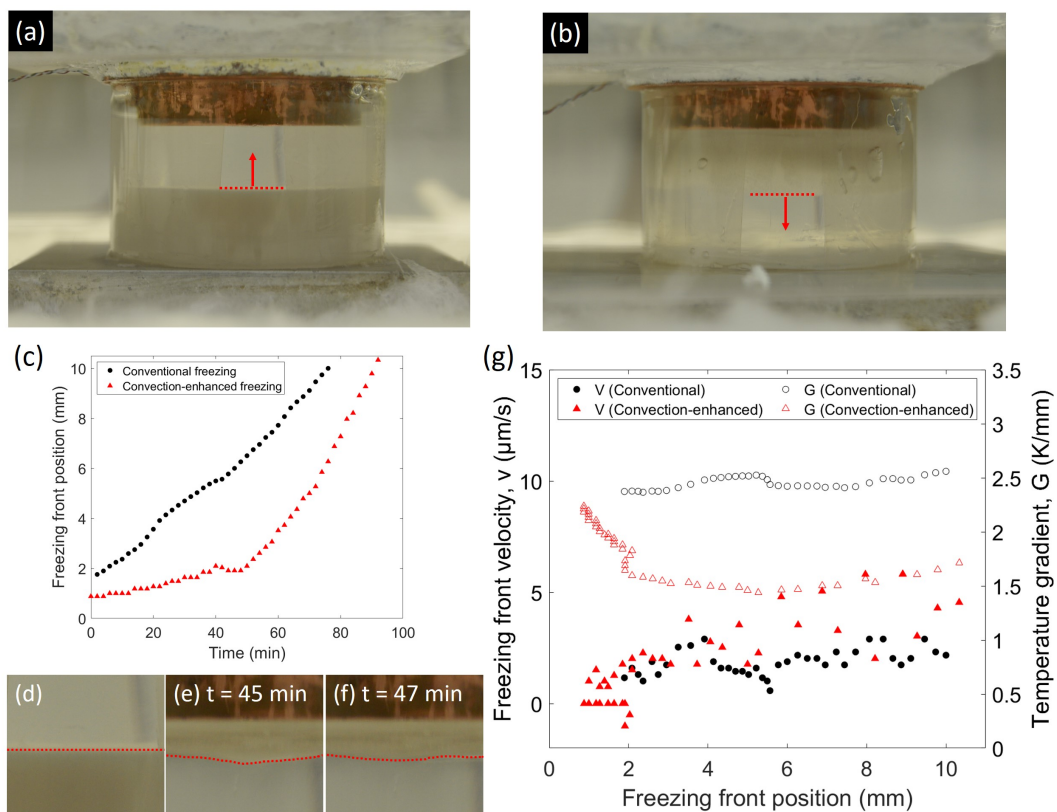


Figure 4.1: Freeze-casting setup of (a) conventional freezing and (b) convection-enhanced freezing. (c) Freezing front position as a function of time with images of (d) the freezing front in conventional freezing, and in convection-enhanced freezing at (e)  $t = 45$  min and (f)  $t = 47$  min (Red dashed line indicates the freezing front), and (g) the associated freezing front velocity and temperature gradient as a function of freezing front position.

Figure 4.1c shows the freezing front position (FFP) from the nucleation face as a function of time. Conventional freezing shows a nearly linear increase with time indicative of constant freezing front velocity, and the freezing front is planar (Figure

4.1d). In contrast, in convection-enhanced freezing, the FFP gradually increases for approximately 50 min, followed by the sudden increase in slope, representing a distinct increase in freezing front velocity, and the planar freezing front is deformed (Figure 4.1e). Between 45 min and 47 min, the freezing front even retracts, indicative of re-melting of the frozen solid. This behavior is shown in Figure 4.1e f. Figure 4.1g illustrates freezing front velocity and temperature gradient as a function of FFP from the nucleation face. Both remained nearly constant in conventional freezing, while in convection-enhanced freezing, shows a large variation. Specifically, the freezing front velocity during its first four millimeters slows to the point of arresting and then becomes negative, where the freezing front re-melts, with the average freezing front velocity being  $\sim 0.7 \mu\text{m/s}$ . After four millimeters, the freezing front velocity suddenly increases, and exceeds the average freezing front velocity of conventional freezing.

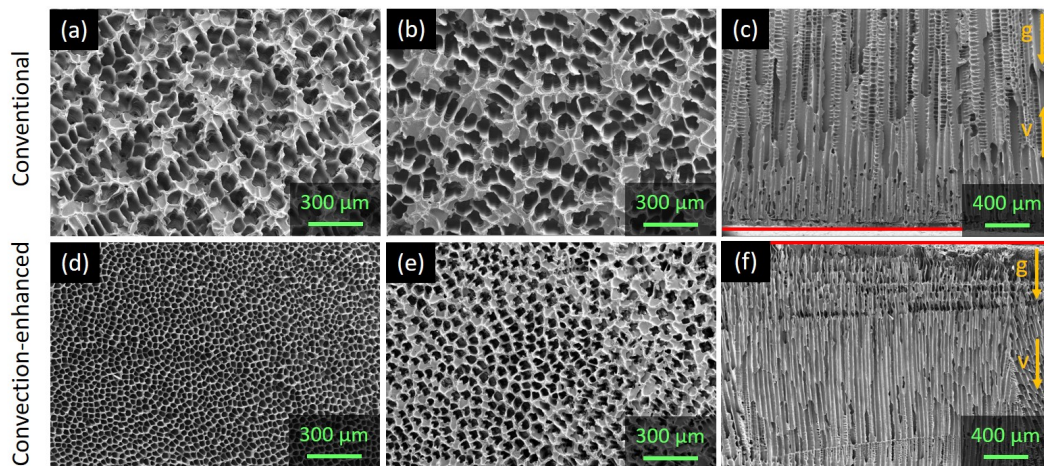


Figure 4.2: SEM images of conventional freeze-cast samples showing transverse images at (a) FFP is  $\sim 1.6$  mm and (b) FFP is  $\sim 5$  mm from nucleation face, and (c) longitudinal image. SEM images of convection-enhanced freeze-cast sample showing transverse images (d) FFP is  $\sim 1.6$  mm and (e) FFP is  $\sim 5$  mm from nucleation face, and (f) longitudinal image. Yellow arrows indicate freezing direction,  $v$ , and gravity direction,  $g$ . Red lines in (c) and (f) indicate the nucleation face

Figure 4.2 displays SEM images in transverse directions, a cross-section perpendicular to the freezing direction, and longitudinal directions, a cross-section parallel to the freezing direction. The transverse images were taken from two different regions: a cross-section with FFP of  $\sim 1.6$  mm and  $\sim 5$  mm from the nucleation point. The longitudinal images of the conventional freeze-cast sample and the convection-enhanced freeze-cast sample are shown in Figures 4.2c and Figure 4.2f,

respectively, with the nucleation face indicated by red lines. In the conventional freeze-cast samples (Figure 4.2a-c), the pore morphologies are mainly dendritic structures, which consist of primary pores templated by primary dendrites and secondary pores templated by dendritic secondary arms, and the pore size is relatively consistent between the two regions (Figure 4.2a and 4.2b). In the longitudinal image, the first several hundred micrometers consist of a cellular region but the remaining pores are dendritic. In stark contrast, the convection-enhanced freeze-cast sample shows cellular pores, which result in honeycomb-like structures, in the slow freezing region (FFP =  $\sim 1.6$  mm, Figure 4.2d) while the fast freezing region (FFP =  $\sim 5$  mm) exhibits dendritic structures (Figure 4.2e). The longitudinal image shows that the majority of pores (over more than 2 millimeters) are cellular pores. The comparison of images between Figures 4.2a-c and Figures 4.2d-f exhibits that the pore size in the convection-enhanced freezing is smaller than in the conventional freezing.

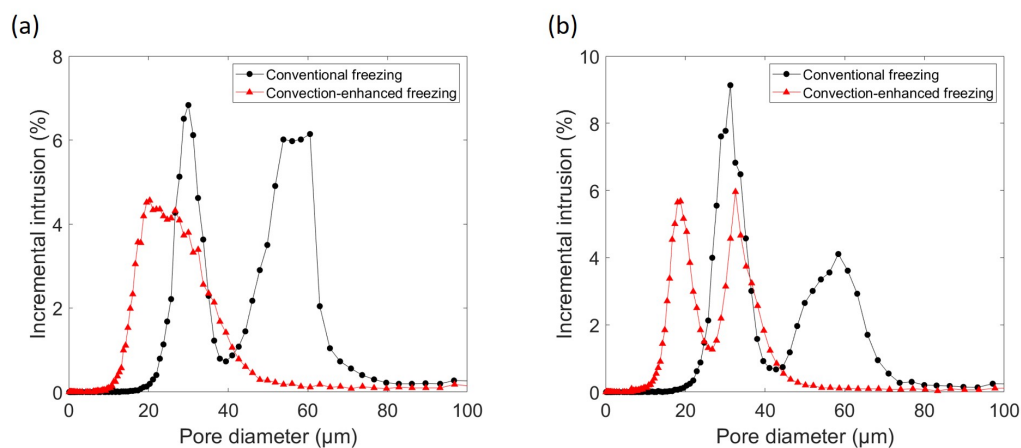


Figure 4.3: Pore size distribution data from (a) nucleation section and (b) middle section from samples from conventional freezing and convection-enhanced freezing.

Two specimens for MIP were sectioned from each sample and imaged: one near the nucleation region (FFP is around from 0.8mm to 3.3mm in Figure 4.1g – referred as nucleation section), and another from the mid-section (FFP is around from 4.5mm to 7mm in Figure 4.1g – referred as middle section). Figure 4.3a compares the pore size distributions of the specimens sectioned from nucleation section from two freezing conditions. A bimodal distribution can be observed in the conventional freeze-cast sample. Larger and smaller pores correspond to primary pores and secondary pores, respectively. In contrast, the convection-enhanced freeze-cast sample demonstrates a unimodal distribution, consistent with the SEM images (Figures 4.2d and 4.2f) showing a honeycomb-like structure. Figure 4.3b shows pore size distributions of

specimens sectioned from middle section. In this region, both samples display bimodal distributions as seen in SEM images (Figures 4.2b and e). Furthermore, the pore sizes are larger for conventional freeze-cast samples, again consistent with the SEM observations.

#### 4.4 Discussions

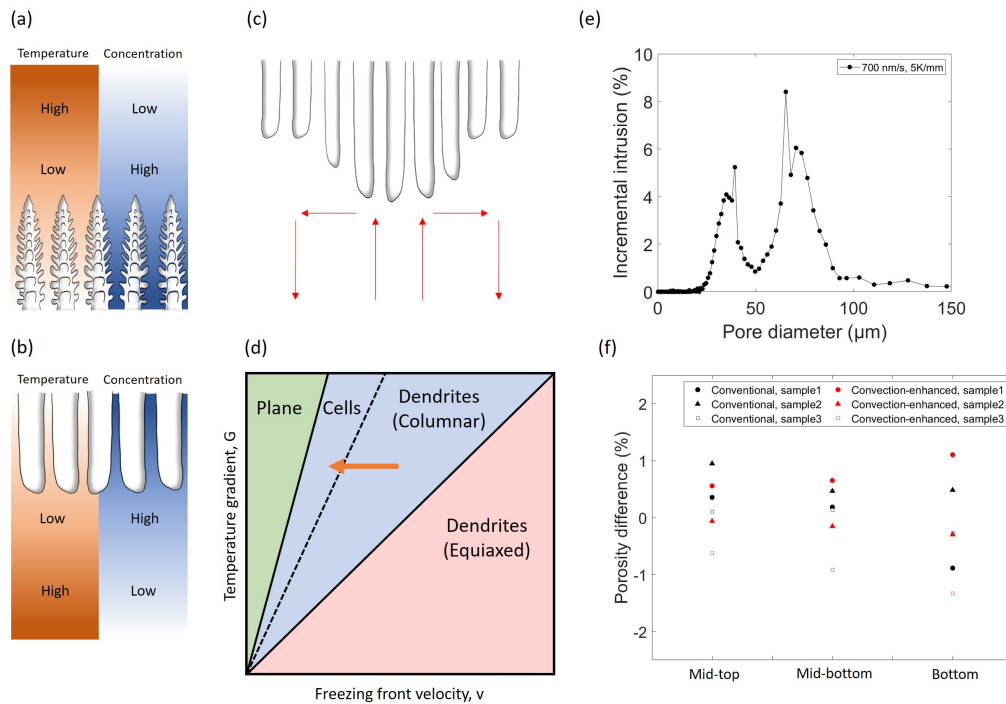


Figure 4.4: Illustrations showing temperature and concentration variation in (a) conventional freezing and (b) convection-enhanced freezing. (c) An illustration showing convective flows in liquid phase in convection-enhanced freezing. (d) Stability-microstructure map. (e) Pore size distribution of conventional freeze-cast sample frozen under  $0.7 \mu\text{m/s}$  and  $4.9 \text{ K/mm}$ . (f) Porosity difference between top section and three sections (middle-top, middle-bottom, and bottom). Three samples were investigated for each freezing direction.

As shown in Figures 4.1d and 4.1e, the conventional freezing yielded a planar freezing front while convection-enhanced freezing reveals a protruded freezing front. The difference can be attributed to the convective flow caused by the density variation in the liquid phase. This is a result of the concentration gradients of preceramic polymer and temperature gradient in the liquid phase. Figures 4.4a and 4.4b are schematic of temperature and concentration variation in the liquid region. In conventional freezing, the preceramic polymer is segregated just ahead of the freezing front, resulting in a higher concentration of preceramic polymer at the



freezing front, decaying into the liquid region. Since the segregated preceramic polymer ( $\sim 1.26 \text{ g/cm}^3$ ) is denser than cyclohexane ( $\sim 0.78 \text{ g/cm}^3$ ), the underlying liquid is heavier than that above. In addition, the region near the freezing front is colder than the overlying liquid. Since the density of the underlying liquid is higher, the conventional freezing is a convectively stable configuration (Figure 4.4a). In the case of convection-enhanced freezing, the density gradient is reversed, therefore, leading to the convective flow ahead of the freezing front (Figure 4.4b). Under such conditions, upwelling and downwelling currents are created, shown schematically in Figure 4.4c. The preceramic polymer is depleted above the upwelling current which gives rise to a crest, whereas the preceramic polymer is rich above downwelling current, which produces a trough, similar to the case reported by Drevet et al. [9]. As a result, the freezing front is deformed, consistent with the observation in Figure 4.1e. Remelting of the freezing front (the crest) was also observed (Figure 4.2f). A possible explanation is that the continuous convective flow transporting heat from the bottom to the top could remelt the frozen region.

While conventional freezing yielded nearly constant freezing front velocities and temperature gradients, that was not the case for convection-enhanced freezing. This discrepancy in freezing front velocity between conventional freezing and convection-enhanced freezing can be explained by constitutional supercooling of the solution. Due to convective flow, the solute is transported away from the solid-liquid interface and heat is transported toward the solid liquid interface in convection-enhanced freezing, decreasing the degree of constitutional supercooling and lowering the driving force for crystal growth. As a result, the freezing front velocity initially remains slow (Figure 4.1g). However, as shown in the same figure, as the temperature gradient continues to decrease, degree of the constitutional supercooling increases. This leads to a larger driving force for dendritic growth, and the freezing front velocity increases.

It is important to note that convective instabilities change both pore size and morphology. In conventional freeze-cast sample, the freezing front velocity and temperature gradient remain nearly constant, such that the pore structures and pore sizes remain similar between nucleation section and middle section (Figures 4.3a and b). Since pore structures in nucleation section and middle section are dendritic (Figures 4.2a,b), the pore size distributions are bimodal. It is worth noting that the primary pore volume fraction in nucleation section, represented by a larger incremental intrusion for primary pores, is larger than the one in middle section. This is

likely due to the presence of cellular pores found at the nucleation site and several hundred micrometers onward, as shown in longitudinal image (Figure 4.2c). These pores are templated by cellular growth which is expected in the initial stages of the dendrite growth. As the freezing front advances as a flat interface, the interface is destabilized by the Mullins-Sekerka instability [15], leading to the transition from a flat interface to cells and eventually to dendrites. This transition is also observed in another freeze-casting study by Deville et al. [16]. In contrast, convection-enhanced freezing leads to the long-range cellular regions as shown in Figure 4.2f. The theory of constitutional supercooling is a useful tool to explain cellular growth in convection-enhanced freezing. Figure 4.4d shows a stability-microstructure map, which shows that cellular morphologies are formed only in a narrow region of slow freezing front velocities and high temperature gradients. Two possible factors are considered to explain the cellular morphology. The first is slower velocities (0.6~0.7  $\mu\text{m/s}$  at 1.9 K/mm) as shown in Figure 4.1g. With the slower freezing front velocity, one would advance to the left in the stability-microstructure map in which cellular growth are expected (indicated by a orange arrow in Figure 4.4d). This is demonstrated by Zeng et al. who observed cellular pores by decreasing the freezing front velocity at constant temperature gradient [13]. However, this could not be the sole factor for the formation of the cells because the sample frozen under 0.7  $\mu\text{m/s}$  and 4.9 K/mm with conventional freezing still exhibit dendritic pores with a bimodal pore size distribution (Figure 4.4e). A second consideration is the effect of convective flow on constitutional supercooling. Convective flow in convection-enhanced freezing drives the solute transport away from the freezing front, and this effect on constitutional supercooling can be described using a stability criterion for a stable planar freezing front [17]:

$$\frac{G}{v} = \frac{mC_0}{D_L} \frac{1 - k_0}{k_0}$$

where  $G$ ,  $v$ ,  $m$ ,  $C_0$ , and  $k_0$  are temperature gradient, freezing front velocity, liquidus slope, concentration of the solution, and equilibrium distribution coefficient, respectively. This equation defines the critical ratio,  $G/v$ , which ensures no constitutional supercooling, and defines the boundary between stable planar front and cellular growth in Figure 4.4d. Based on this equation, a higher diffusion coefficient provides a less stringent criterion to achieve a planar front. While it is only diffusion which transports solutes away from the freezing front in conventional freezing, convection further enhances the transport of solute in convection-enhanced freezing. As a result, the critical ratio for convection-enhanced freezing becomes less stringent, which makes cellular growth easier to attain, and cells crystallize instead

of dendrites. Furthermore, convective flow leads to temperature homogenization in the liquid phase, which might make the actual temperature gradient larger than the measured temperature gradient in Figure 4.1g at the solid-liquid interface. This would also contribute to a reduction in the degree of constitutional supercooling [4] and cells are more likely to grow.

To assess the length scale of the preceramic polymer transport by convection, the porosity of the conventional freeze-cast samples and convection-enhanced freeze-cast samples were measured. Four specimens each with a thickness of  $\sim 1.9$  mm (corresponding to  $\sim 2.5$  mm in the liquid phase) were sectioned from each pyrolyzed sample (top, middle-top, middle-bottom, and bottom). In order to show porosity variations along the direction of gravity, porosity of top section was subtracted from porosity of three sections (middle-top, middle-bottom, and bottom) and these differences are shown in Figure 4.4f. The differences are approximately  $\pm 1$  %, and no consistent trend can be observed in either freezing direction. It is likely that the variation in porosity is due to the measurement error in the Archimedes' method. This implies that the distance over which the preceramic polymer is transported by convection during convection-enhanced freezing is less than 2.5 mm in the solution. Even though transport of the solute appears to be limited to the near vicinity of the freezing front rather than throughout the entire liquid phase, constitutional supercooling is known to take place just ahead of the solid-liquid interface. Hence, even this local solute transport reduces the degree of the constitutional supercooling, resulting in morphological and size changes of dendritic pores.

#### **4.5 Conclusion**

The effect of freezing direction with respect to the direction of the gravitational force was investigated in solution-based freeze casting. Two freezing directions were examined: conventional freezing, against the gravitational force, and convection-enhanced freezing, in concert with it. While conventional freezing allows a convectively stable configuration in the liquid phase, convection-enhanced freezing leads to convective instability. Convection in the liquid phase gives rise to transport of the preceramic polymer as well as heat in the vicinity of the solid-liquid interface. Due to the reduced degree of constitutional supercooling in convection-enhanced freezing, a long-range honeycomb-like pore structure results and the pore size decreases. Hence, the understanding of convective flow in the liquid phase during freeze casting allows further control of pore morphology and pore size.

## References

- [1] Lionel Alexander Bethune Pilkington. “Review lecture: the float glass process”. In: *Proceedings of the Royal Society of London. A. Mathematical and Physical Sciences* 314.1516 (1969), pp. 1–25.
- [2] Jennifer A. Lewis. “Colloidal processing of ceramics”. In: *Journal of the American Ceramic Society* 83.10 (2000), pp. 2341–2359.
- [3] S.M. Copley et al. “The origin of freckles in unidirectionally solidified castings”. In: *Metallurgical transactions* 1.8 (1970), pp. 2193–2204.
- [4] R. Jansen and P.R. Sahn. “Solidification under microgravity”. In: *Materials Science and Engineering* 65.1 (1984), pp. 199–212.
- [5] P.J. Prescott and F.P. Incropera. “Magnetically damped convection during solidification of a binary metal alloy”. In: *Journal of Heat Transfer* (1993).
- [6] Jose Eduardo Spinelli, Ivaldo Leao Ferreira, and Amauri Garcia. “Influence of melt convection on the columnar to equiaxed transition and microstructure of downward unsteady-state directionally solidified Sn–Pb alloys”. In: *Journal of Alloys and Compounds* 384.1-2 (2004), pp. 217–226.
- [7] José E. Spinelli et al. “Influence of melt convection on dendritic spacings of downward unsteady-state directionally solidified Al–Cu alloys”. In: *Materials Science and Engineering: A* 383.2 (2004), pp. 271–282.
- [8] Natalia Shevchenko et al. “Chimney formation in solidifying Ga-25wt pct In alloys under the influence of thermosolutal melt convection”. In: *Metallurgical and Materials Transactions A* 44.8 (2013), pp. 3797–3808.
- [9] B. Drevet et al. “Solidification of aluminium–lithium alloys near the cell/dendrite transition–influence of solutal convection”. In: *Journal of crystal growth* 218.2-4 (2000), pp. 419–433.
- [10] José Eduardo Spinelli, Otávio Fernandes Lima Rocha, and Amauri Garcia. “The influence of melt convection on dendritic spacing of downward unsteady-state directionally solidified Sn–Pb alloys”. In: *Materials Research* 9.1 (2006), pp. 51–57.
- [11] Kristen L. Scotti et al. “The effect of solidification direction with respect to gravity on ice-templated TiO<sub>2</sub> microstructures”. In: *Journal of the European Ceramic Society* 39.10 (2019), pp. 3180–3193.
- [12] Kristen L. Scotti et al. “Directional solidification of aqueous TiO<sub>2</sub> suspensions under reduced gravity”. In: *Acta Materialia* 124 (2017), pp. 608–619.
- [13] Xiaomei Zeng, Noriaki Arai, and Katherine T. Faber. “Robust Cellular Shape-Memory Ceramics via Gradient-Controlled Freeze Casting”. In: *Advanced Engineering Materials* 21.12 (2019), p. 1900398.
- [14] Maninpat Naviroj. “Silicon-based porous ceramics via freeze casting of pre-ceramic polymers”. PhD thesis. Northwestern University, 2017.

- [15] William W. Mullins and R.F. Sekerka. “Stability of a planar interface during solidification of a dilute binary alloy”. In: *Journal of applied physics* 35.2 (1964), pp. 444–451.
- [16] Sylvain Deville, Eduardo Saiz, and Antoni P. Tomsia. “Ice-templated porous alumina structures”. In: *Acta materialia* 55.6 (2007), pp. 1965–1974.
- [17] W.A. Tiller et al. “The redistribution of solute atoms during the solidification of metals”. In: *Acta metallurgica* 1.4 (1953), pp. 428–437.

## COARSENING OF DENDRITES IN FREEZE-CAST SYSTEMS

The work was done in collaboration with Tiberiu Stan, Sophie Macfarland, Peter W. Voorhees, Nancy Senabulya, Ashwin J. Shahani, and Katherine T. Faber. N. Arai designed the systems for study, fabricated and characterized freeze-cast ceramics using SEM and mercury intrusion porosimetry, and wrote the majority of the manuscript. N. Senabulya and A. Shahani performed X-ray computed tomography (XCT). T. Stan and S. Macfarland analyzed XCT datasets. K. Faber and P. Voorhees supervised this work.

### 5.1 Introduction

In this chapter, our focus extends to the morphological evolution of the frozen crystals over time. Coarsening, also known as Ostwald ripening, is a phenomenon which occurs in two-phase systems such as alloys and metal oxides [1], and this is driven by the reduction of interfacial energy to minimize the free energy of the system. The total interfacial area is decreased through mass transport, which is driven by the concentration gradient resulting from a large interfacial mean curvature to a small interfacial mean curvature due to the Gibbs-Thomson effect:

$$C_L = C_\infty + l_c H \quad (5.1)$$

where

$$H = \frac{1}{2}(\kappa_1 + \kappa_2)$$

and  $C_L$  is the composition of liquid at the solid-liquid interface,  $C_\infty$  is the composition of the liquid at flat solid-liquid interface,  $l_c$  is the capillary length, and  $H$  is the mean curvature of interfaces.  $H$  is determined by the two principle curvatures,  $\kappa_1$  and  $\kappa_2$ . Coarsening of alloys has been extensively studied in systems ranging from simple spherical geometries [2] to complex interconnected structures such as dendrites [3, 4]. Coarsening studies span from theory [5] to modeling [6, 7] to in-situ and ex-situ experimental studies [8, 9, 10, 11]. Two important results on coarsening of dendrites are highlighted here. First, Bower et al. found that secondary dendritic arm spacing,  $\lambda_2$ , increases with coarsening time as:

$$\lambda_2 \sim t_f^{1/3} \quad (5.2)$$

where  $t_f$  is local solidification time [12]. Second, Kammer et al. reported that the dendritic structures turned into cylinders or cylindrical-like shapes after coarsening Pb-Sn alloys and Al-Cu alloys for four days and three weeks, respectively [4]. These two observations motivate this work to apply coarsening to freeze casting in order to control the morphology and size of dendritic pores.

Studies of coarsening in freeze-cast systems are limited. Pawelec et al. investigated low-temperature ice annealing in a collagen suspension, and observed coarsened microstructures after twenty hours of annealing [13]. Liu et al. examined coarsening of camphene crystals in freeze casting of bioactive glass to obtain a controllable pore diameter, ranging from 15  $\mu\text{m}$  to 160  $\mu\text{m}$  [14]. Both were restricted to pore size measurements and qualitative image analysis. Hence, there remains a gap between these observations and what is understood at a fundamental level in alloy systems. Furthermore, these studies were conducted using suspension-based freeze casting, where suspended colloids or powders and dissolved additives such as dispersants and binders make a comparison to alloy systems challenging and complex.

This study focuses on solution-based freeze casting and investigates the evolution of dendrites during isothermal coarsening and its effects on dendritic pore morphology and size. By varying time and temperature, coarsening phenomena were explored using scanning electron microscopy and mercury intrusion porosimetry. To gain further insight into the coarsening processes in freeze-cast systems in three dimensions, X-ray computed tomography enabled us to quantitatively analyze morphologies and directionality by Interfacial Shape Distributions (ISD) and Interfacial Normal Distributions (IND). By coupling images, pore size distributions with tomography-derived ISDs and dendritic pore directionality through their INDs, our studies provide new understanding into coarsening in freeze-cast systems, allow comparisons with coarsening behavior of alloy system, and offer an additional means for pore network tailorability.

## 5.2 Experimental methods

### 5.2.1 Processing

A polysiloxane ( $\text{CH}_3\text{-SiO}_{1.5}$ , Silres®MK Powder, Wacker Chemie) preceramic polymer was dissolved in cyclohexane ( $\text{C}_6\text{H}_{12}$ , Sigma-Aldrich), with compositions of preceramic polymer of 20 wt.% and 30 wt.%. After a homogeneous solution was

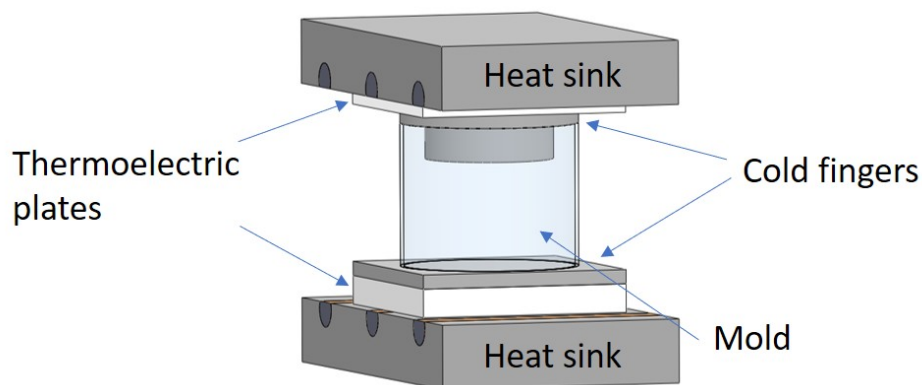


Figure 5.1: Schematic of the gradient-controlled freeze casting setup

obtained by stirring, a cross-linking agent (Geniosil®GF 91, Wacker Chemie) was added in concentrations of 1 wt.% and 0.75 wt.% in 20 and 30 wt.% solutions, respectively, and stirred for an additional 5 minutes. Subsequently, the polymer solution was degassed for 10 minutes to prevent air bubbles during freezing. Freezing was done using gradient-controlled freeze-casting setup as described in Chapter 3 (Figure 5.1). All samples were frozen at freezing front velocities of 15  $\mu\text{m/s}$  for 20 and 30 wt.% solutions, and temperature gradients of  $\sim 2.6$  K/mm to maintain homogeneous pore structures.

To induce coarsening after freezing was completed, the top and bottom thermoelectrics were set to temperatures close to the liquidus temperature of the solution ( $2^\circ\text{C}$  or  $4^\circ\text{C}$  for 20 wt.% solution and  $3^\circ\text{C}$  for 30 wt.% solution) and held for up to 5 hrs. To determine time for frozen samples to reach the prescribed temperature, a type K thermocouple was used to measure temperature of the samples during coarsening<sup>1</sup>. After coarsening, the samples were cooled to  $-30^\circ\text{C}$  to re-freeze. Once frozen, the samples were placed in a freeze drier where the solvent crystals were completely sublimated. After freeze drying, the polysiloxane green bodies were pyrolyzed in argon at  $1100^\circ\text{C}$  for four hours with a  $2^\circ\text{C}/\text{min}$  ramp rate to convert the preceramic polymer into silicon oxycarbide (SiOC). This resulted in a porosity of  $\sim 77\%$  for the 20 wt.% solution and  $64\%$  for 30 wt.% solution. The resulting sample dimensions were approximately 9.5mm in height and 18mm in diameter.

<sup>1</sup>Generally, type K thermocouples have an accuracy of  $\pm 1.1^\circ\text{C}$  or larger [15].



### 5.2.2 Characterization

Pore structures were observed using scanning electron microscopy (SEM). Longitudinal and transverse cross-sections were prepared using a diamond saw and imaged. Pore size distributions were measured using mercury intrusion porosimetry (MIP). All samples for MIP were machined with a core drill ( $\varnothing = 15.9$  mm) to remove the edges, and a  $\sim 1.8$  mm disk was sectioned from the center of the sample.

X-ray computed tomography (XCT) was performed on selected samples to quantitatively measure the morphological evolution of dendrites via Absorption Contrast Tomography (ACT) on a laboratory X-ray microscope (XCT; Zeiss Xradia Versa 520, Carl Zeiss AG, Oberkochen, Germany) at the Michigan Center for Materials Characterization. Three samples ( $h = \sim 5$  mm,  $\varnothing = \sim 1.2$  mm) were chosen for this analysis: a control sample without coarsening, one coarsened at  $2^\circ\text{C}$  for one hour, and another coarsened at  $4^\circ\text{C}$  for three hours. During the ACT measurement, each sample was positioned 5.1 mm in front of a polychromatic X-ray source tuned to 40 kV, 3 W, and  $75\ \mu\text{A}$ . The X-ray beam interacted with a sample volume of  $1025\ \mu\text{m} \times 1132\ \mu\text{m} \times 1090\ \mu\text{m}$ . A series of 1601 X-ray projection images was collected at  $0.2^\circ$  intervals while the sample rotated through  $360^\circ$  at exposure times of 1.1 s per projection. A scintillator downstream from the sample converted the X-ray projection images into visible light images and a 4X objective lens magnified the visible light image before coupling it to the  $2\text{k} \times 2\text{k}$  CCD detector placed 23.5 mm away from the sample. With the CCD operating at a pixel binning of 2, a scan pixel size of  $1.2\ \mu\text{m}/\text{voxel}$  was achieved. The collected projection images were reconstructed using a filtered back projection algorithm in the Scout and Scan software provided by Zeiss Xradia Inc. to create a virtual 3D volume of the sample. Worth noting is that phase retrieval [16] was not necessary because there was sufficient contrast between the SiOC matrix and the pore network in the traditional absorption-based images. The SiOC matrix is a light gray and the pore network is a dark gray (Figure 5.2).

The control sample (without coarsening) was segmented using Otsu's method [17] in MATLAB. Although Otsu's method is computationally straightforward and the preferred segmentation approach, it was not successful on the  $2^\circ\text{C}$  and  $4^\circ\text{C}$  coarsened datasets due to the presence of debris and bright spot artifacts at random sections throughout the reconstructions. The coarsened datasets were instead segmented using a convolutional neural network (CNN) machine learning approach as described by Stan et al. [18, 19]. First, 35 representative slices were selected from

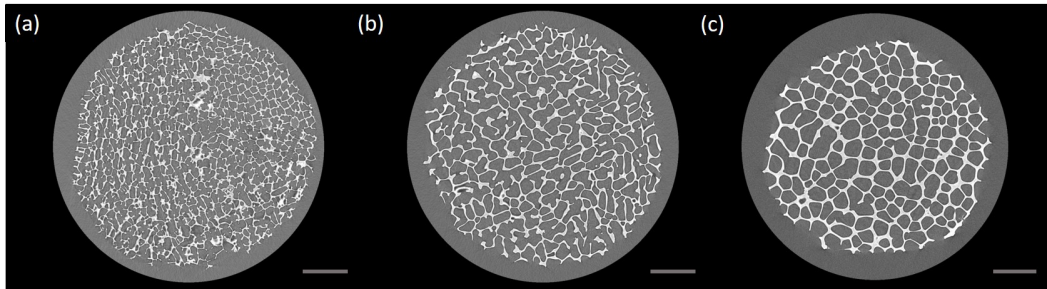


Figure 5.2: Cross-section of XCT data from (a) a control sample, (b) a sample coarsened at 2 °C for one hour, and (c) a sample coarsened at 4 °C for three hours. Scale bar: 200  $\mu\text{m}$ .

each reconstruction to include sections of debris and bright spots and split into three categories: 20 images for training, 10 images for validation, and 5 images for testing. Each image was then segmented using a combination of thresholding and manual cleaning using the GIMP software. These ground truth segmentations (along with the original images) were used to train CNNs with the SegNet architecture using the PyTorch framework. Each CNN was trained for 100 epochs on the Quest supercomputer at Northwestern University. The CNNs each achieved 99.4% segmentation accuracy when applied to test images from the 2 °C and 4 °C coarsened datasets.

MATLAB was used for all post-segmentation analysis. It was found empirically that 120  $\mu\text{m}$ -thick sections (100 z-slice images) of each XCT dataset were large enough to capture the defining morphological features, yet small enough to be computationally manageable. All three segmented datasets were meshed and smoothed using the “smoothpatch” function. The control and 2 °C datasets were smoothed for 5 iterations, while the coarser 4 °C dataset was smoothed for 15 iterations. Principle curvatures ( $\kappa_1$  and  $\kappa_2$ ) and normal vectors were calculated at each of the triangular patches. Their respective frequencies within the microstructures are plotted as interface shape distributions (ISD) and interface normal distributions (IND).

### 5.3 Analysis of XCT images

#### 5.3.1 Interfacial Shape Distribution (ISD)

The quantitative analysis of morphological evolution of dendrites (or resulting pores) was carried out by measuring the curvature of the interfacial patches. First, two invariants of the curvature tensor,  $\kappa_{ij}$ , were measured. With this measurement, the mean curvature,  $H$  is established:

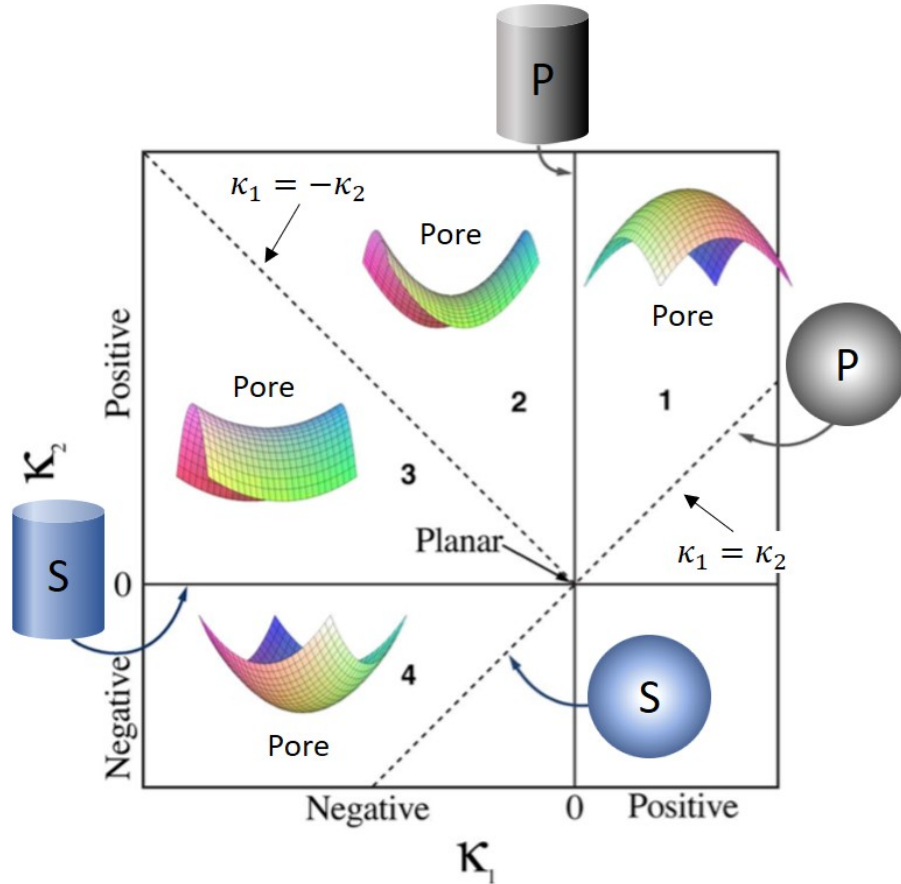


Figure 5.3: A map of interfacial shapes of patches for the Interfacial Shape Distribution (ISD). This is a modified figure from ref. [20].

$$H = \text{tr}\{\kappa_{ij}\} = \frac{1}{2}(\kappa_1 + \kappa_2) \quad (5.3)$$

where the two principle curvatures,  $\kappa_1$  and  $\kappa_2$ , the minimum and maximum principle curvatures, respectively, can be determined to construct the interfacial shape distribution (ISD). The ISD is presented as a contour plot to map the probability of finding a patch with a given pair of principal curvatures (Figure 5.3). Since  $\kappa_2$  is the maximum principle curvature of the patches, the entire distribution must reside to the left of the  $\kappa_1 = \kappa_2$  line. The plot can be divided into four regions. For dendritic porous materials:

- Region 1 represents positive  $\kappa_1$  and  $\kappa_2$  and the interface patches are concave toward the solid (SiOC walls).

- Regions 2 and 3 represent  $\kappa_1 < 0$  and  $\kappa_2 > 0$ , and interface patches are saddle shaped. Region 2 embodies interface patches which are strongly curved toward the pores whereas region 3 signifies interface patches which are strongly curved toward the solid.
- Region 4 represents negative  $\kappa_1$  and  $\kappa_2$  and interface patches are convex toward the solid.

All the principle curvatures were normalized with respect to the specific interface area,  $S_s$ , which is the total surface area of the interface divided by the volume of the dendrites, or equivalently the volume of pores. This normalization is necessary for mapping probability distributions such that microstructures with different coarsening conditions can be compared and inspected for self-similarity. One hundred slices of images, which represent 120  $\mu\text{m}$  of the sample in freezing direction with a diameter of roughly 1.2 mm, were used for analysis. Since the samples were frozen under constant freezing front velocity and temperature gradient and other 100 slices from different section show similar ISD, 100 slices are assumed to be sufficient to represent the whole structures.

### 5.3.2 Interfacial Normal Distribution (IND)

The Interfacial Normal Distribution (IND) is a contour plot which shows the probability distribution of the orientation of normals to interfacial patches, and is useful in determining the directionality of dendrites, or in this study, directionality of pores. First, the orientation of the interfacial normals to patches are determined and stored in a unit reference sphere, in which their origins sit in the center of the sphere and their ends sit in the surface of the sphere. Then, they are projected on a 2D plane, which is tangent to the sphere and, in this case, perpendicular to the direction of the freezing. The projection used in this study is an equal-area projection. Two simple cases can be considered as examples. If the porous structure has perfectly spherical shapes, the orientation of the normals is isotropic, which results in a uniform probability distribution in the IND. In contrast, in the case of cylindrical pores perfectly aligned along [001] direction, the probability distribution in the IND concentrates at the outer rim of the projection. For off-axis aligned pores, an arc-like band appears across the IND.

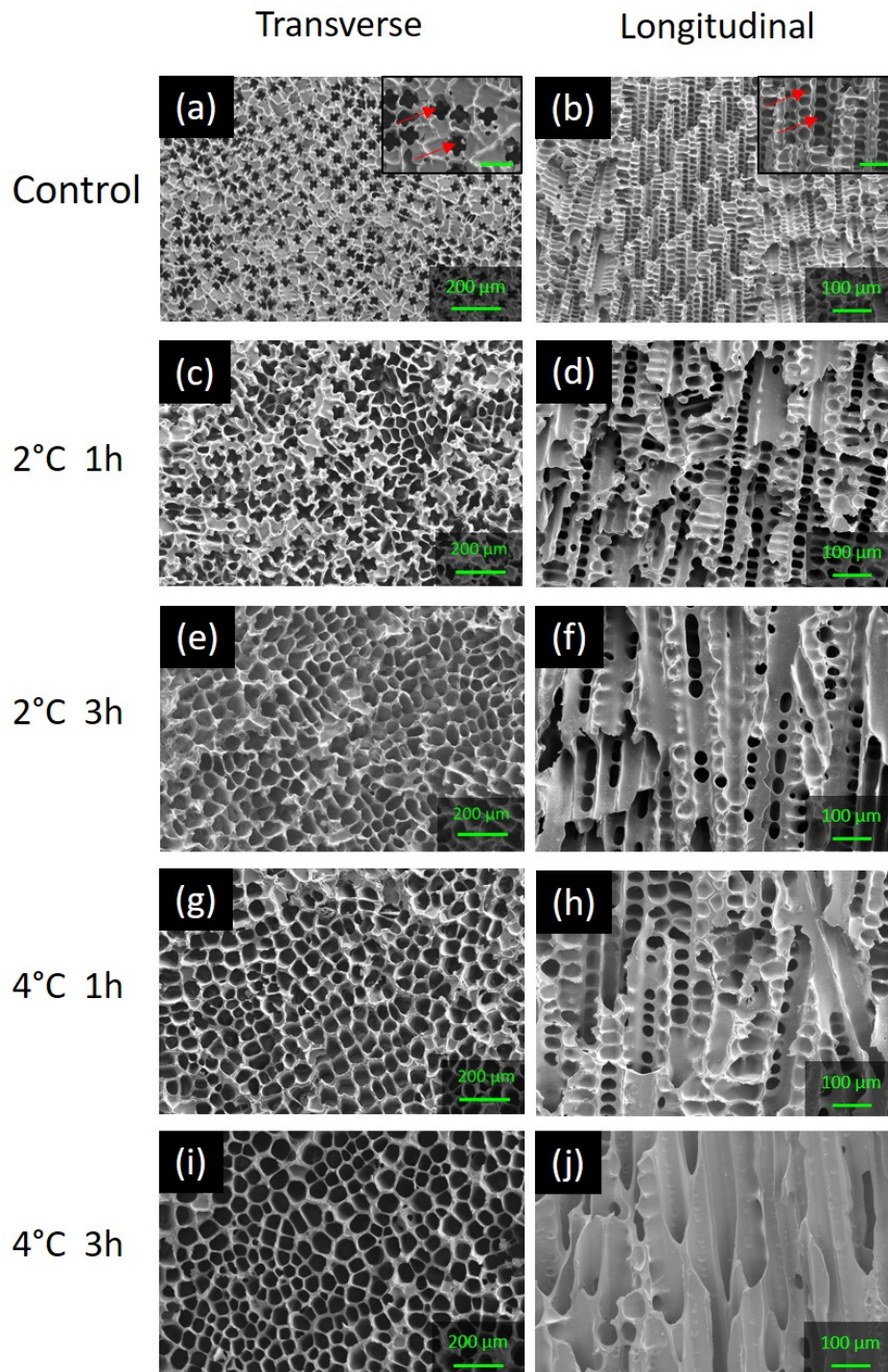


Figure 5.4: SEM images showing (a, b) control sample, and sample coarsened at (c, d) 2 °C for one hour, (e, f) 2 °C for three hours, (g, h) 4 °C for one hour, and (i, j) 4 °C for three hours. Inset images in (a) and (b) show primary pore and secondary pores, respectively, as indicated by red arrows, (scale bar: (a) 60  $\mu\text{m}$  and (b) 40  $\mu\text{m}$ ). Transverse images and longitudinal images show cross-sections perpendicular and parallel to the freezing direction, respectively.

## 5.4 Results and discussion

### 5.4.1 Pore structure

Figure 5.4 shows a series of SEM images of dendritic pores as a function of coarsening treatment beginning with the control sample as-cast and pyrolyzed (Figures 5.4a and b). Since cyclohexane dendrites template the pores, the pores (appearing black in SEM images) are the negatives of dendrites [21, 22]. The transverse image (perpendicular to the solidification direction) in Figure 5.4a shows primary pores templated by primary dendrites (red arrows), and secondary pores templated by secondary dendrite arms. Tertiary pores are occasionally observed in regions where primary interpore spacings are large. The four-fold symmetry of dendritic pores is consistent with the cubic structure of cyclohexane crystals [23]. The longitudinal image (approximately parallel to the solidification direction) (Figure 5.4b) shows the cutaway view of dendritic pores, where the red arrows in inset image indicate secondary pores. When the dendrites are coarsened at 2 °C for one hour, there is an increase in both primary and secondary pore sizes as shown in Figures 5.4c and d. After three hours of coarsening at 2 °C, the transverse image shows larger domains of honeycomb-like structures (Figure 5.4e) although the secondary pores are still present as noted in the longitudinal image (Figure 5.4f). When the coarsening temperature is increased to 4 °C, morphological evolution proceeds at a higher rate (Figures 5.4g-j). Coarsening for one hour yields larger domains of the honeycomb structure in the transverse direction (Figure 5.4g) while secondary pores are still noted in the longitudinal image (Figure 5.4h). After three hours of coarsening at 4 °C, the majority of secondary pores disappear in the longitudinal image (Figure 5.4j), producing a largely honeycomb-like structure. The morphological evolution of dendritic pores observed in this solution-based freeze casting agrees well with what has been reported in coarsening of dendrites in alloys [10, 4], where dendrites evolve into cylindrical morphologies. In addition to the overall morphological change from dendritic pores to cellular pores, these SEM images further reveal the morphological change of primary pores and secondary pores. The transverse image of the control sample shows four-fold symmetric primary pores (Figure 5.4a). When the structures are coarsened, primary pores evolve to circular-like shapes. See also secondary pores in the longitudinal images in Figure 5.5 comparing the control sample and the sample coarsened at 4 °C for one hour as an example. While the sides of secondary pores exhibit curvature, the top and bottom faces of secondary pores are nearly flat. After coarsening, these flat surfaces disappear, and the secondary pores became circular in cross-section. Longer coarsening time (five hours) at 4

$^{\circ}\text{C}$  was also investigated, but there were only minor morphological changes (Figure 5.6). These minor changes can be attributed to the decreasing diffusion coefficient of preceramic polymer as the gelation of the solution started around 5-6 hours. The influence of diffusion coefficient can also be demonstrated by changing the polymer concentration in the solution, as described in Appendix D.

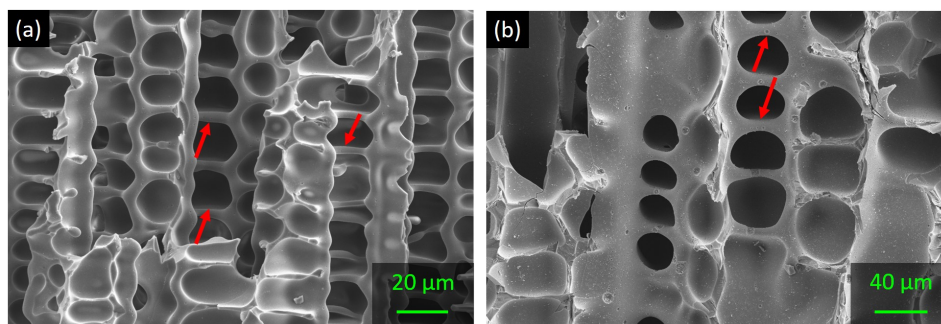


Figure 5.5: SEM images showing longitudinal direction of (a) the control sample and (b) the sample coarsened at 4  $^{\circ}\text{C}$  for one hour. Flat surface and circular surface are indicated by red arrows in (a) and (b), respectively.

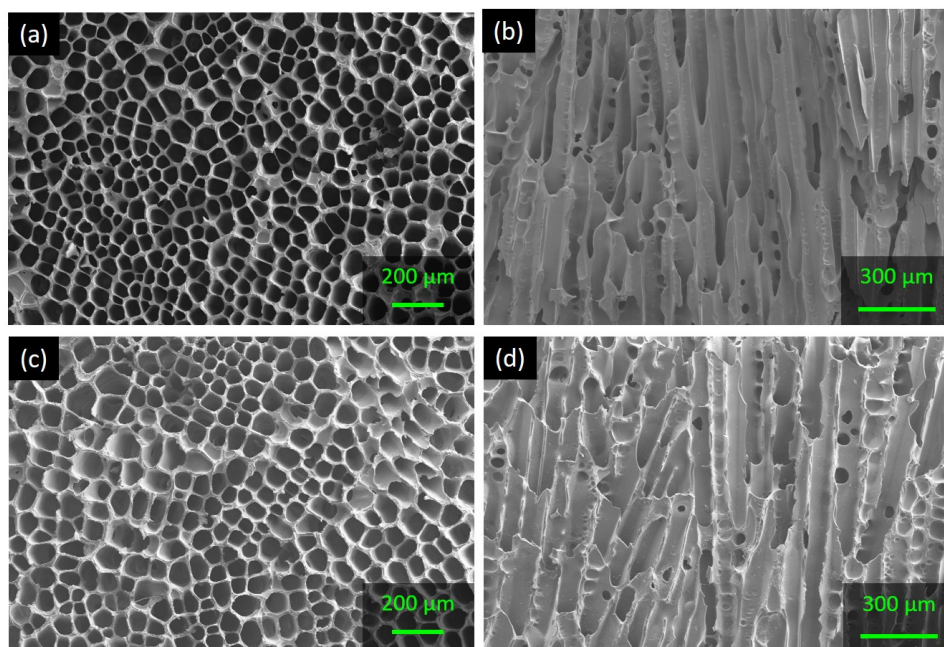


Figure 5.6: SEM images of the samples coarsened at 4  $^{\circ}\text{C}$  for three hours (a: Transverse image, b: Longitudinal image) and five hours (c: Transverse image, d: Longitudinal image).

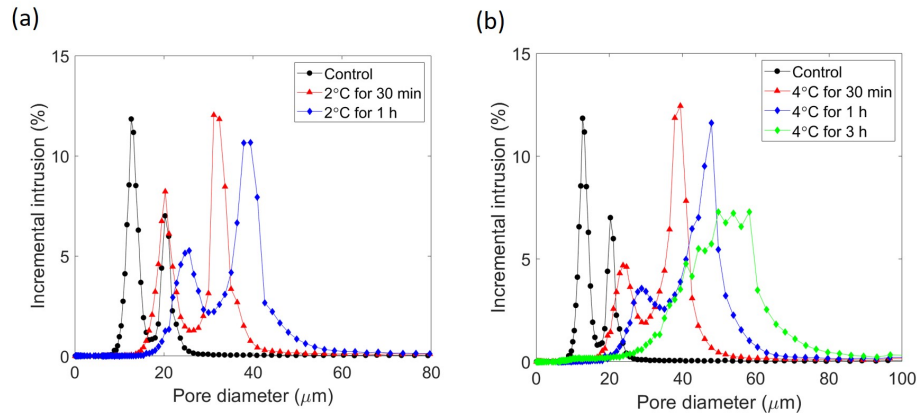


Figure 5.7: Pore size distribution data of samples coarsened for 30 minutes and one hour at (a) 2 °C and (b) 4 °C (including three hours).

#### 5.4.2 Pore size distribution

Pore size distributions, which illustrate pore diameters, obtained from MIP for each coarsening temperature are shown in Figure 5.7. Figure 5.7a shows the pore size distribution from samples coarsened at 2 °C compared to the control sample. All samples exhibit a bimodal distribution, which can be attributed to large primary pore diameters and small secondary pore diameters. As the samples are coarsened, primary pores and secondary pores become larger with the distributions shifting to the right, consistent with SEM images. Dendritic structures typically have a secondary pore volume that exceeds the primary pore volume because of the large number of secondary arms that grow from each primary dendrite [24]. In contrast, in the current coarsening studies, not only does the pore size distribution shift to larger pores, but also the primary pore volume eclipses the secondary pore volume. For coarsening at 4 °C, the same trend can be observed (Figure 5.7b). For the sample coarsened at 4 °C for one hour, the distributions for primary and secondary pores begin to overlap; this is more significant in the sample coarsened for three hours. Distinct bimodal distributions disappear in favor of a unimodal distribution. This corresponds well with Figures 5.4i and j in which the majority of secondary pores disappear, yielding the honeycomb-like structure. The primary pore volume can be established, calculated by using the software Fityk [25], and is plotted as a function of coarsening time in Figure 5.8. The primary pore fraction increased by 146% and 160% after coarsening for one hour at 2 °C and 4 °C, respectively.

To compare the coarsening behavior of freeze-cast systems with typical alloy systems (Eqn. 5.2), primary and secondary pore sizes are plotted as a function of the



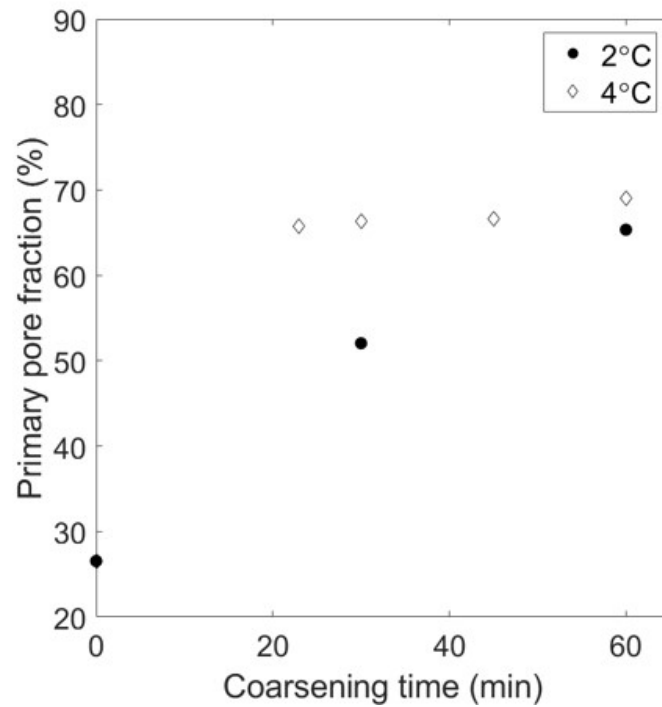


Figure 5.8: Primary pore fraction as a function of coarsening time.

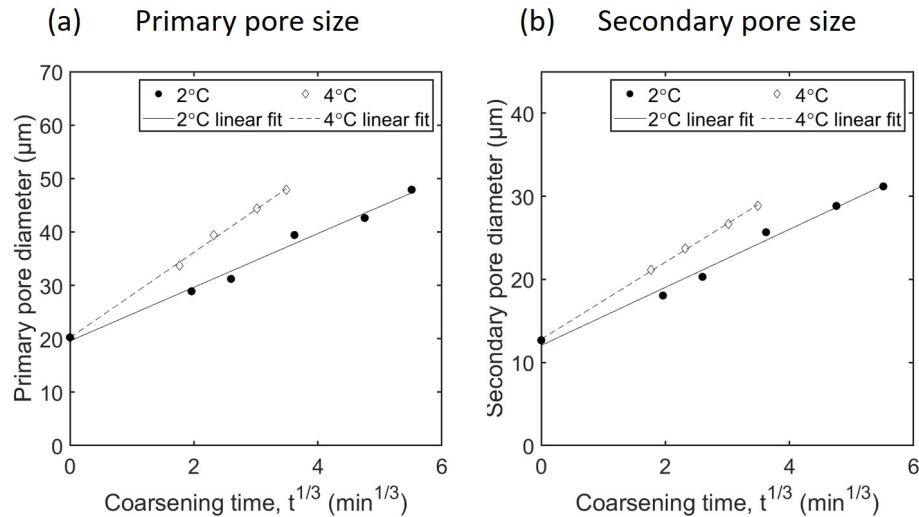


Figure 5.9: Plots of (a) Primary pore size and (b) secondary pore size as a function of the cube root of coarsening time at different coarsening temperatures.

cube root of coarsening time<sup>2</sup>,  $t^{1/3}$ , in Figures 5.9a,b. In this plot, the peak values

<sup>2</sup>Coarsening time is defined as the time interval over which the thermoelectric plates are at the prescribed coarsening temperature adjusted by the time it takes the frozen sample to reach the equilibrium coarsening temperature.

of the pore size distribution were plotted as representatives of primary pore size and secondary pore size. The  $t^{1/3}$  dependence is obeyed for both coarsening temperatures, consistent with coarsened dendrites in alloys. Typically, only the dependence of the secondary arm spacing on  $t^{1/3}$  is reported [12], but it was found in the current study that the diameters of primary dendrites have a similar dependence. The slopes of the linear fit are summarized in Table 5.1. As expected, the slopes increase as coarsening temperature increases, in agreement with the observations of Chen and Kattamis who studied Al-Cu-Mn dendrite coarsening [26]. For both coarsening temperatures, the slopes of primary dendrites are larger than those for the secondary arms of dendrites. Specifically, increasing the coarsening temperature increased the slope for primary pores by a factor of 1.6, whereas the slope increased for secondary pores by a factor of 1.3, indicating that primary dendrites coarsen at a faster rate.

We attribute this difference to active coarsening mechanisms for primary dendrites and secondary arms (Figure 5.10). As shown in Figure 5.10, the secondary arm coarsening can be explained by 4 models: radial remelting, axial remelting, arm detachment, and arm coalescence. Radial remelting could occur by radial dissolution of small arms surrounded by a larger arm and diffusion of the material to adjacent larger arms. If radial remelting is a dominant mechanism for coarsening in freeze-cast systems, the secondary pore diameter would show a decrease in size in the pore size distribution. However, in all the pore size distributions, the secondary pore diameter is larger than that of the control samples, indicating that the radial remelting is not the dominant mechanism. Another mechanism is axial remelting. Axial remelting takes place by melting at the tip of the arms and solidifying at the root of the arms. Since this would require remelting of the arms, the secondary pore size would not increase from this mechanism. Since arm detachment would yield closed pores and pores formed by this mechanism are not measurable by MIP, arm detachment is not considered here. As a result, it appears that arm coalescence could be a major mechanism to increase secondary pore diameter in a freeze-cast system. On the other hand, primary dendrite could coarsen by two mechanisms - the coalescence of primary dendrites and axial remelting. Since axial remelting takes place by solidifying the root of the arms, it will increase the primary dendrite diameter, resulting in the increase of primary pore diameter. Hence, primary dendrites coarsen by two mechanisms while secondary arms coarsen by arm coalescence, which could qualitatively explain the faster coarsening rate for primary pores.

Table 5.1: The slope of linear fit from Figure 5.9

Coarsening temperature	Primary dendrites	Secondary arm of dendrites
2 °C	5.0	3.5
4 °C	8.0	4.6




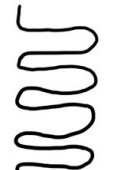







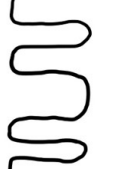
Initial				
Intermediate				
Last				
	Model 1	Model 2	Model 3	Model 4

Figure 5.10: Illustration showing four different coarsening models for secondary arm coarsening: (1) radial remelting, (2) axial remelting, (3) arm detachment, and (4) arm coalescence. Based on ref. [27].

It is worth mentioning that coarsening times in this study are much shorter than those in alloy studies. In the latter, dendrites were coarsened from a few to several days to observe the significant morphological change from dendrites to cylinders, while coarsening requires only a few hours in solution-based freeze casting. Here, the freeze-cast system is compared with Sn-rich Pb-Sn alloys studied by Kammer and Voorhees [10], where the dendrites evolve into cylinders after coarsening for two days. The model by Kirkwood [28] for secondary arm coarsening provides some insight to explain the faster morphological changes in freeze-cast system:

$$\lambda = \left( \frac{128D\sigma T_m}{LmC_L(1-k)} \right)^{1/3} t^{1/3} \quad (5.4)$$

where  $\lambda$  is secondary arm spacing,  $D$  is diffusion coefficient of solute in liquid,  $\sigma$  is solid-liquid interface tension,  $T$  is absolute melting temperature,  $L$  is volumetric heat of fusion,  $m$  is liquidus slope,  $C_L$  is mean composition in the liquid region,  $k$  is distribution coefficient, and  $t$  is coarsening time. Here the assessment of a few known variables,  $T$ ,  $L$ , and  $m$ , are possible. Even though liquidus temperature,  $T$ , of Sn-rich Pb-Sn alloy (from 456 K to 504 K) is higher than that of the freeze-cast system (278 K for 20 wt.% solution), this contribution to the coarsening rate remains small. On the other hand, there are significant differences in  $m$  and  $L$  between two systems. The absolute value of the liquidus slope,  $m$  for Sn-rich Pb-Sn alloy is  $\sim 1.4$  while that of freeze-cast system (0 wt.% - 40 wt.% preceramic polymer concentration) ranges from around 0.07 to 0.16 [29], which is an order of magnitude different. Furthermore, due to the higher density of Sn-Pb alloy, the heat of fusion,  $L$  of eutectic Pb-Sn alloy is around 300 J/cc, while pure cyclohexane's is around 25 J/cc, which is also an order of magnitude difference. Although only three variables are examined here, an order of magnitude difference in  $m$  and  $L$  is consistent with higher coarsening rate in freeze-cast system based on the Kirkwood model. Finally, although the mean composition,  $C_L$ , is not known during the coarsening process in freeze-cast systems, one can look at the homologous temperature at the coarsening temperature to provide insight into the liquid fraction. For example, in Kammer's study [10], the coarsening of Pb-80 wt.% Sn alloy, which at the coarsening temperature of 185°C (2°C above the eutectic temperature), consists of 51% Sn-rich dendrites and 49% Sn-lean liquid. The homologous temperature is 0.953 at 185°C. By contrast, in the freeze-cast system, the homologous temperatures are 0.992 and 0.999 for 2 °C and 4 °C, respectively, based on the liquidus temperature reported by Naviroj [29]. Hence, it is likely that the liquid fraction during the coarsening in the freeze-cast system is greater than the alloy system, or equivalently  $C_L$  of freeze-cast system is lower, resulting in faster morphological changes.

#### 5.4.3 Tailoring pore morphology and network by coarsening temperature

Coarsening time and coarsening temperature are two major parameters to tailor pore size and morphology. In the previous section, it was demonstrated that primary and secondary pore sizes linearly depend on the cube root of coarsening time. Here, the effects of coarsening temperature in the resulting freeze-cast structure are examined in detail.

It was demonstrated above that a higher coarsening temperature could accelerate the morphological transition from dendrites to honeycomb-like structures along with the increase of pore size. Again, this acceleration of coarsening at higher temperature can also be explained by Kirkwood's model (Eqn. 5.4). Changing the coarsening temperature can alter the diffusion coefficient. However, if the diffusion coefficient,  $D$ , follows Arrhenius behavior [30] or, for the case of long-chained polymers, a reptation model, the temperature dependence of  $D$  is sufficiently small (less than 1% increase) that it cannot account for the 70% and 40% increase in coarsening rate for primary pores and secondary pores, respectively. Instead, the enhanced coarsening rate with temperature is likely due to the increase in liquid fraction by increasing coarsening temperature, causing  $C_L$  to decrease. Furthermore, a decrease in  $C_L$  is expected to increase  $D$  [31]. Hence, it can be hypothesized that the changes in  $C_L$  and  $D$  as a result of a higher coarsening temperature give rise to acceleration of the coarsening process.

In addition to the aforementioned acceleration, different coarsening temperatures could further lead to different freeze-cast structures. In order to highlight this difference in structure as a function of coarsening time and temperature, Figure 5.11 presents pore size distributions and SEM images for samples coarsened at 2°C for three hours and 4°C for one hour. As demonstrated by MIP data, both samples have nearly identical pore size distributions, with marginally larger secondary pores present in the sample coarsened at 2°C for three hours. The pore morphologies shown in SEM images, however, reveal distinct differences. In the transverse direction, some of the primary pores in the sample coarsened at 2°C retain four-fold symmetry (Figure 5.11b), whereas primary pores in the sample coarsened at 4°C lose such symmetry and are more cellular-like in shape (Figure 5.11d). In the longitudinal direction, additional differences can be observed. First, primary pores connect to neighboring primary pores by coalescence of secondary arms at 2°C (Figure 5.11c). Second, a closer look at secondary pores shows some large elliptical-shaped pores. Since the major axis of the ellipse is along the dendrite growth direction, it is likely that these large elliptical pores are the result of coalescence of secondary pores in the dendrite growth direction, as indicated by red arrows in Figure 5.11c. These large elliptical pores likely give rise to a slight shift of the secondary pore peak in the sample coarsened at 2°C (Figure 5.11a). It is hypothesized that this morphological difference can be attributed to the difference in liquid fraction during coarsening. When samples were coarsened at 4°C, close to the melting point of the solution, a sufficient fraction of the liquid phase is present to surround the dendrites,

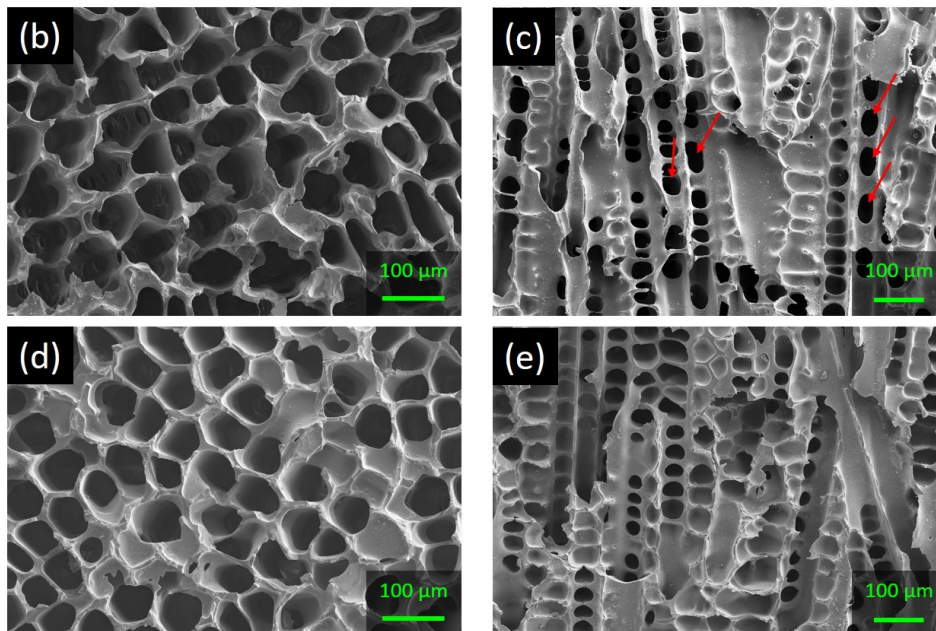
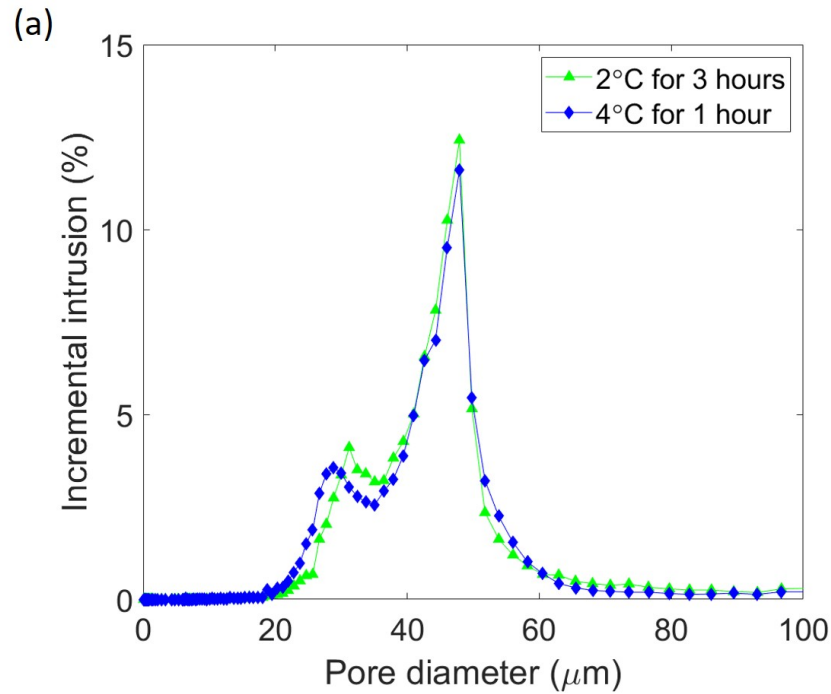


Figure 5.11: Pore size distribution from samples coarsened at 2 °C for three hours and 4 °C for one hour (a). SEM images showing a sample coarsened at (b, c) 2 °C for three hours, and (d, e) 4 °C for one hour. (Red arrows indicate some of the thin solid tubes).

providing pathways for mass diffusion. This allows the structure to coarsen all the parts of the dendrites, hence, both primary pores and secondary pores change their

morphologies. In contrast, if the coarsening temperature is lower, the liquid phase still exists, but there are regions rich in liquid phase and those poor in liquid phase. This creates a large discrepancy in coarsening rates within an individual dendrite, and results in disparate coarsening behavior. This demonstrates that the change in coarsening temperature gives one further tool in tailoring pore morphology and pore network.

#### 5.4.4 Coarsening mechanisms in solution-based freeze casting

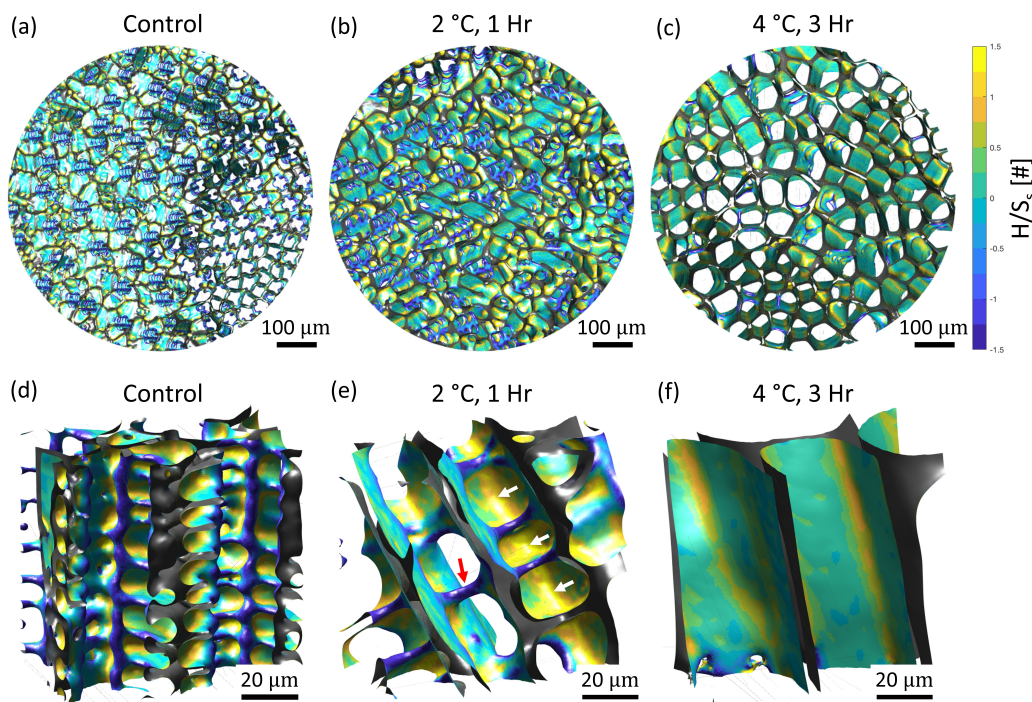


Figure 5.12: 3D XCT reconstructions and subsections for the (a, d) control sample, (b, e) the sample coarsened at 2 °C for one hour, and (c, f) sample coarsened at 4 °C for three hours. The sides of the solid-pore interfaces that face the dendritic pores are colored according to the normalized mean curvature ( $H/S_s$ ), as indicated by the color bar in (c). White arrows in (e) show secondary pores with positive curvature caps, while the red arrow indicates a ligature with negative curvature.

Since the coarsening proceeds as a result of the Gibbs-Thomson effect, the mean curvature of the dendritic pores provides insight on the coarsening mechanism. Figure 5.12 shows three-dimensional reconstructions of the control sample (Figure 5.12a), the sample coarsened at 2 °C for one hour (Figure 5.12b), and the sample coarsened at 4 °C for three hours (Figure 5.12c). The datasets are plotted such that the solidification direction is pointing out of the page. Subsections from each of the three reconstructions are shown in Figs. 7d-f. The interface sides that face the solid

SiOC are colored dark gray. The interface sides that face the dendritic pores are colored according to their normalized mean curvature  $H/S_S$ . The specific interface area ( $S_S$ ) is a characteristic microstructural length scale and is calculated as the total interface area divided by the total pore volume in the dataset. Normalizing curvatures by  $S_S$  is used to facilitate visual comparison between coarsening datasets and to check for self-similarity.

Comparing Figures 5.12a, b and c, a significant change in pore size and pore morphology is observed, consistent with earlier SEM images and pore size distributions. The control sample (Figures 5.12a and d) has patches with large positive mean curvature (yellow) mainly located at the tips and sides of the secondary pores, and patches with small and negative mean curvature (purple) primarily present at the roots of secondary pores. The interfaces with nearly zero mean curvature (light blue and light green) are at the flat sections along secondary pores. (See top and bottom faces of secondary pores in Figure 5.5a). There are two distinct domains of dendritic pores in the control sample that vary by dendritic pore spacing. While the domain with smaller spacing (bottom right) is well aligned along the temperature gradient, that with large spacing is slightly misaligned. This is consistent with the other observations [32, 33, 34], which show that dendrite spacing generally increases with misorientation.

Morphological changes in the dendritic pore network and secondary arms are evident when comparing the three XCT datasets. Most secondary pores in the control sample have capped ends such that each dendritic pore was isolated from adjacent dendritic pores, as shown in the SEM image (Figure 5.4b). In the sample coarsened at 2 °C for one hour, some of the secondary pore caps remain (white arrows in Figure 5.12e). However, some caps are lost during coarsening resulting in connections between secondary pores and formation of ceramic ligatures (red arrow in Figure 5.12e). The sample coarsened at 4 °C for three hours no longer contains secondary pores and the microstructure is instead primarily composed of larger channels with nearly-flat sides, as indicated by the green and light-blue coloring in Figure 5.12f. Areas of higher curvature (yellow stripes in Figure 5.12f) are present where the flatter sections intersect.

The color-coded 3D reconstructions can explain why dendritic morphologies evolve to honeycomb-like structures through coarsening. Large positive mean curvatures are preferentially found at the tips and sides of secondary pores. During coarsening, these regions contain high solvent content and equivalently low preceramic polymer



concentration due to the Gibbs-Thomson effect. In contrast, small and negative mean curvatures are found at the roots of the secondary pores, which are high in preceramic polymer concentration. Hence, the preceramic polymer diffuses from the roots of secondary arms to the tips and sides of secondary arms, which melts the tips and sides, but solidifies the roots. As a result, secondary arms will disappear, resulting in honeycomb-like structures.

#### 5.4.5 Quantitative microstructure analysis

It is challenging to quantitatively compare highly complex microstructures using only 2D SEM images and visualizations of the 3D XCT reconstructions. A major advantage of the XCT technique is the ability to measure volumetric and interfacial properties. Metrics from the three XCT datasets are reported in Table 5.2. The pore volumes and volume fractions are similar between the datasets, and consistent with MIP measurements. As indicated by the interface area measurements, the control sample contains  $\sim 17$  times more interface area than the 2 °C coarsened sample, and  $\sim 25$  times more interface area than the 4 °C coarsened sample. The inverse specific interface area ( $S_S^{-1}$ ) is found to be equal to roughly half of the secondary pore size. The control and 2 °C datasets have  $S_S^{-1} = 6.1$  and  $10.7 \mu\text{m}$ , and MIP-measured secondary pore sizes of  $12.7$  and  $25.7 \mu\text{m}$ , respectively. The tilt angle reported in Table 5.2 is a measurement of the angle between the average dendrite growth direction and the solidification direction (discussed in detail in Subsection 5.4.6).

Table 5.2: Metrics from the three XCT datasets.  $S_S^{-1}$  is the inverse specific interface area, calculated as the total pore volume divided by the total solid-pore interface area.

Sample	Pore volume ( $\times 10^7 \mu\text{m}^3$ )	Pore volume fraction (%)	Interface area ( $\times 10^6 \mu\text{m}^2$ )	$S_S^{-1}$ ( $\mu\text{m}$ )	Tilt angles ( $^\circ$ )
Control	4.1	72	67.0	6.1	$\sim 5, \sim 28$
2 °C, 1 hr	4.3	77	4.0	10.7	$\sim 35$
4 °C, 3 hrs	4.2	75	2.7	15.6	$\sim 15, \sim 20, \sim 30$

Interface Shape Distributions (ISDs) are also used to quantitatively compare the complex microstructures. For example, freeze-casting has been used to fabricate structures which mimic bone for medical implants, and the morphology of freeze-cast foams have been characterized by ISD to investigate the similarity with bone [3]. In this section, in addition to quantitatively defining the structures, ISDs are used to

compare to an alloy systems to investigate if the similar morphological evolution is observed.

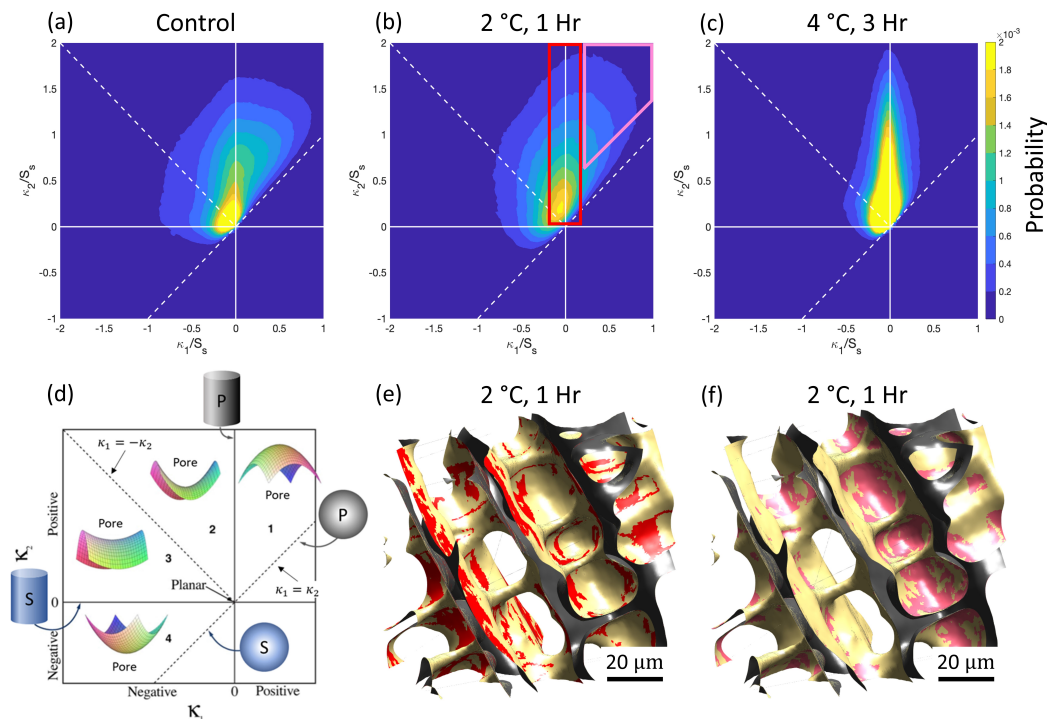


Figure 5.13: Interface Shape Distributions (ISDs) for the (a) control sample, (b) sample coarsened at 2 °C for one hour, and (c) sample coarsened at 4 °C for three hours. (d) Map of the interface shapes possible in an ISD where P is pore and S is solid. This is a modified figure from ref. [20]. Sections of the 2 °C coarsened sample cylindrical patches colored in red (e) and porous caps colored in pink (f).

Figures 5.13a-c show the interfacial shape distributions (ISDs) and Figure 5.13d shows a map of interfacial shapes of patches for the ISD, the same figure as Figure 5.3. The three ISDs span the range of interfacial shapes, although the shapes of the distributions differ, implying that all of the structures are not self-similar, despite following the  $t^{1/3}$  power law. For the control sample, since the probability distribution of the cylindrical shaped region and cap shaped region extends to large values of  $\kappa_1/S_S$  and  $\kappa_2/S_S$ , the interfacial patches are predominantly cylindrical in shape and cap-shaped (Figure 5.13a). This is expected since the sides of secondary pores are cylindrical and the tips of secondary pores are cap shaped. The probability distribution also extends to the origin, indicative of a flat interface region, consistent with SEM observations (Figure 5.5a) and the 3D reconstruction of the control sample in Figure 5.12a. This is in stark contrast with the ISD of freeze-cast lamellar structures reported by Fife et al. [3], which shows a well-defined peak near the origin,

resulting from the flat interfaces of plate-like structures. For the sample coarsened at 2 °C for one hour (Figure 5.13b), a few changes can be highlighted. First, the peak shifts away from the origin which represents the flat interface and a larger fraction of the distribution is now located in the saddle-shaped region. Second, compared to the control sample, the distribution no longer extends along  $\kappa_1/S_S = 0$ . This is consistent with the SEM images of decreased secondary pore length. For the sample coarsened at 4 °C for three hours, the probability distribution shifts to the region near  $\kappa_1/S_S = 0$ , indicating that the cylindrical patches are the dominant morphology (Figure 5.13c) consistent with the honeycomb structures viewed via SEM and 3D reconstructions.

Figures 5.13e and f show the same section of the sample coarsened at 2 °C for 1 hour as in Figure 5.12e, but the structures are colored according to interfacial shapes of interest. Patches with cylindrical shapes were isolated from the red-box region in the ISD in Figure 5.13b and displayed on the microstructure in Figure 5.13e. The majority of these cylindrical features are primarily found along the walls of primary pores, but some patches are also present along the walls of secondary pores. The porous caps in the pink region of Figure 5.13b are shown on the reconstruction in Figure 5.13f. As expected, these high-curvature features are mostly present at the tips of secondary pores.

Since the dendrites in freeze casting undergo similar morphological evolution to cylinder-like shapes as alloy system, the ISDs for control sample and the sample coarsened at 4 °C for three hours are compared to the dendrite coarsening in Pb-Sn alloys reported by Cool and Voorhees [35]. The ISD of the least-coarsened dendrites (10 min coarsening) in the Cool and Voorhees study looks similar to the ISD of the control sample. Both ISDs show significant peaks in the cylindrical shaped region and cap shaped region as both structures contain a significant number of interfacial patches from secondary arms or secondary pores. When the structures are coarsened to cylindrical shapes, the resulting ISDs for the freeze-cast system and the Pb-Sn alloy look similar, too. Hence, the general trends of ISDs, such as the shapes of the probability distributions and their changes after coarsening, are similar to those seen in dendrite coarsening in Pb-Sn alloys.

#### **5.4.6 Directionality of dendritic pores**

Directionality is of great interest because it influences the transport [36] and mechanical properties [37] of freeze-cast solids. As clearly observed in 3D reconstruction

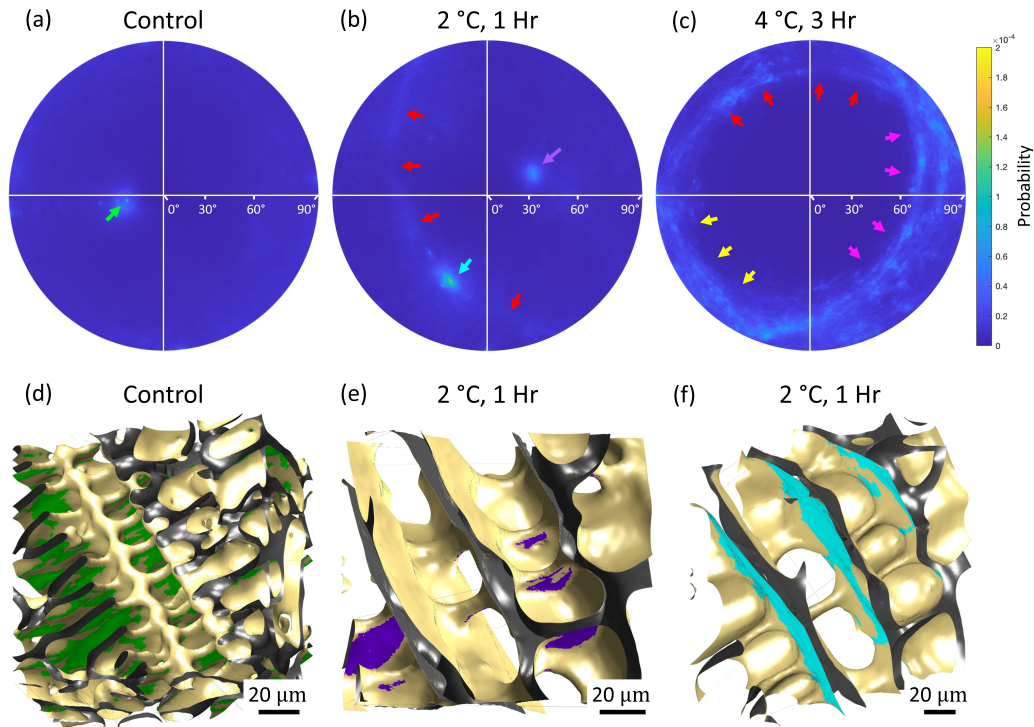


Figure 5.14: Interface Normal Distributions (INDs) for the (a) control sample, (b) sample coarsened at 2 °C for one hour, and (c) sample coarsened at 4 °C for three hours. The green arrow in (a) corresponds to the green patches in (d). The purple arrow in (b) corresponds to purple patches in (e). The blue arrow in (b) corresponds to the blue patches in (f).

of the control sample (Figure 5.12a), not all dendrites grow along a temperature gradient. Interface Normal Distributions (INDs) are used to quantitatively measure the averaged dendritic growth directions. The [001] stereographic projections are presented as INDs in Figure 5.14 for the (a) control sample, (b) sample coarsened at 2 °C for one hour, and (c) sample coarsened at 4 °C for three hours. The IND center where the white lines intersect is the [001] direction, parallel to the temperature gradient. The colormap used for all three INDs is at the right side of Figure 5.14c.

The IND for the control sample (Figure 5.14a) is uniformly blue except for one spot (green arrow) at  $\sim 28^\circ$  from the IND center (green arrow). Some of the interfacial patches which contribute to this IND spot have been highlighted on the microstructure section in Figure 5.14d. The green patches are primarily present on flat top faces of secondary pores. These interfaces have normal vectors that point in roughly the same direction, thus yielding a spot on the IND. Owing to the cubic symmetry of the system, the plate-like pores are roughly perpendicular to the

primary pore growth direction. Thus, the primary dendrites grew at  $\sim 28^\circ$  from the temperature gradient direction.

The IND of the sample coarsened at  $2^\circ\text{C}$  for one hour (Figure 5.14b) contains a spot (purple arrow) at  $\sim 35^\circ$  from the center. The microstructure section in Figure 5.14e has purple patches corresponding to the spot in the IND. As in the control sample, these interfaces are mostly present at secondary pores. The IND also has an arc-like band, marked by four red arrows and one blue arrow at the highest-intensity spot. Figure 5.14f shows a section of the microstructure where patches that contribute to the IND spot are highlighted in blue. These areas are primarily found on the flatter regions of primary pores. The primary pores in the  $2^\circ\text{C}$  coarsened sample have walls with normal vectors that point in many directions, all of them nearly perpendicular to the primary dendrite growth direction. This is manifested as an arc-band in the IND (red arrows in Figure 5.14b). The band is tilted at  $\sim 55^\circ$  away from the temperature gradient direction, and  $\sim 90^\circ$  away from the secondary arm spot (purple arrow in Figure 5.14b). Together, these observations indicate that the average dendrite growth misalignment for the  $2^\circ\text{C}$  coarsened sample is  $\sim 35^\circ$ .

The IND of the sample coarsened at  $4^\circ\text{C}$  for three hours (Figure 5.14c) contains many light-blue bands. The bands appear smeared largely because the honeycomb-like structure is composed of large channels, each with a slightly different orientation. Three main orientations are identified (red, yellow, and pink arrows), indicating misorientations of  $\sim 20^\circ$ ,  $\sim 15^\circ$ , and  $\sim 30^\circ$ , respectively. In contrast, freeze-cast lamellar pores identified from INDs by Fife et al. show two peaks located  $180^\circ$  apart due to the plate-like pores [3].

The misalignment of dendritic pores is expected since dendrites were randomly oriented at nucleation. As the dendrites grow, misoriented dendrites tend to impinge on aligned dendrites and stop growing. However, some fraction of off-axis dendrites are retained. Although the misalignment of  $\sim 35^\circ$  affects transport properties of freeze-cast solids, nucleation control by a grain selector can be used in freeze casting to align dendritic pores and has been shown to improve the Darcian permeability constant more than 6-fold [36].

## 5.5 Conclusions

This study demonstrates that coarsening processes can be applied to solution-based freeze casting to give rise to changes in both pore morphology and pore size. Coarsening temperature and coarsening time were explored. Two important findings

were reported. First, the morphological evolution from dendrites to cylindrical-like crystals was demonstrated in solution-based freeze casting, and ultimately resulted in honeycomb-like structures. Second, dendritic pore size, both primary pore size and secondary pore size, was found to scale with the cube root of coarsening time. Both findings are well-known in dendrite coarsening in metal alloy systems.

While many studies in freeze casting have focused on controlling crystal growth, to best of our knowledge, this is the first study to use X-ray tomography to quantitatively explore morphological evolution during coarsening of freeze-cast systems, specifically with interfacial shape distributions and interfacial normal distributions. In freeze casting, the characterization of pore morphologies previously has been limited to the qualitative interpretation of 2D or 3D images, which would cause the characterization of coarsened dendritic structures to be challenging. However, curvature analysis by ISDs, in this case, were used quantitatively to determine that non-coarsened and coarsened pore structures are not self-similar, the same findings as coarsened dendrites in alloys [10, 35]. INDs were used further to elucidate the preferential direction of pores, which is important for mechanical and transport properties of porous solids. Since the dendritic structures can be obtained by a variety of solvents, ISDs and INDs provide a useful platform to investigate morphological evolution of other dendritic structures. Finally, morphological evolution by coarsening in freeze casting was found to be similar to those in alloy systems. Following other freeze-casting studies to apply solidification theory, the current study validated that even post-crystal growth processes, coarsening, in alloy systems can be applied to freeze casting, offering an additional strategy to control pores in freeze casting.

## References

- [1] Gerko Oskam et al. “Coarsening of metal oxide nanoparticles”. In: *Physical Review E* 66.1 (2002), p. 011403.
- [2] S.C. Hardy and P.W. Voorhees. “Ostwald ripening in a system with a high volume fraction of coarsening phase”. In: *Metallurgical Transactions A* 19.11 (1988), pp. 2713–2721.
- [3] J.L. Fife and P.W. Voorhees. “The morphological evolution of equiaxed dendritic microstructures during coarsening”. In: *Acta Materialia* 57.8 (2009), pp. 2418–2428.

- [4] D. Kammer, R. Mendoza, and P.W. Voorhees. “Cylindrical domain formation in topologically complex structures”. In: *Scripta materialia* 55.1 (2006), pp. 17–22.
- [5] Peter W. Voorhees. “The theory of Ostwald ripening”. In: *Journal of Statistical Physics* 38.1-2 (1985), pp. 231–252.
- [6] Danan Fan et al. “Phase-field simulation of 2-D Ostwald ripening in the high volume fraction regime”. In: *Acta Materialia* 50.8 (2002), pp. 1895–1907.
- [7] L.K. Aagesen et al. “The evolution of interfacial morphology during coarsening: A comparison between 4D experiments and phase-field simulations”. In: *Scripta Materialia* 64.5 (2011), pp. 394–397.
- [8] Ashwin J. Shahani et al. “Ostwald ripening of faceted Si particles in an Al-Si-Cu melt”. In: *Materials Science and Engineering: A* 673 (2016), pp. 307–320.
- [9] Enyu Guo et al. “Dendritic evolution during coarsening of Mg-Zn alloys via 4D synchrotron tomography”. In: *Acta Materialia* 123 (2017), pp. 373–382.
- [10] D. Kammer and P.W. Voorhees. “The morphological evolution of dendritic microstructures during coarsening”. In: *Acta materialia* 54.6 (2006), pp. 1549–1558.
- [11] Emine Begum Gulsoy et al. “Four-dimensional morphological evolution of an aluminum silicon alloy using propagation-based phase contrast X-ray tomographic microscopy”. In: *Materials transactions* (2014), p. M2013225.
- [12] Terry F. Bower, H.D. Brody, and Merton C. Flemings. “Measurements of solute redistribution in dendritic solidification”. In: *Transaction of the Metallurgical Society of AIME* 236 (1966), pp. 624–633.
- [13] K.M. Pawelec et al. “Altering crystal growth and annealing in ice-templated scaffolds”. In: *Journal of materials science* 50.23 (2015), pp. 7537–7543.
- [14] Xin Liu, Mohamed N. Rahaman, and Qiang Fu. “Oriented bioactive glass (13-93) scaffolds with controllable pore size by unidirectional freezing of camphene-based suspensions: Microstructure and mechanical response”. In: *Acta biomaterialia* 7.1 (2011), pp. 406–416.
- [15] THERMOCOUPLEINFO.COM. *THERMOCOUPLE Info*. URL: <http://thermocoupleinfo.com/>.
- [16] David Paganin et al. “Simultaneous phase and amplitude extraction from a single defocused image of a homogeneous object”. In: *Journal of microscopy* 206.1 (2002), pp. 33–40.
- [17] Nobuyuki Otsu. “A threshold selection method from gray-level histograms”. In: *IEEE transactions on systems, man, and cybernetics* 9.1 (1979), pp. 62–66.

- [18] Tiberiu Stan, Zachary T. Thompson, and Peter W. Voorhees. “Building towards a universal neural network to segment large materials science imaging datasets”. In: *Developments in X-Ray Tomography XII*. Vol. 11113. International Society for Optics and Photonics. 2019, 111131G.
- [19] Tiberiu Stan, Zachary T. Thompson, and Peter W. Voorhees. “Optimizing convolutional neural networks to perform semantic segmentation on large materials imaging datasets: X-ray tomography and serial sectioning”. In: *Materials Characterization* 160 (2020), p. 110119.
- [20] J.L. Fife et al. “The dynamics of interfaces during coarsening in solid–liquid systems”. In: *Acta Materialia* 70 (2014), pp. 66–78.
- [21] Maninpat Naviroj et al. “Directionally aligned macroporous SiOC via freeze casting of preceramic polymers”. In: *Journal of the European Ceramic Society* 35.8 (2015), pp. 2225–2232.
- [22] Valentina Naglieri and Paolo Colombo. “Ceramic microspheres with controlled porosity by emulsion-ice templating”. In: *Journal of the European Ceramic Society* 37.7 (2017), pp. 2559–2568.
- [23] Y. Shao, G. Hoang, and T.W. Zerda. “Solid-solid phase transitions of cyclohexane in porous sol-gel glass”. In: *Journal of non-crystalline solids* 182.3 (1995), pp. 309–314.
- [24] Maninpat Naviroj, Peter W. Voorhees, and Katherine T. Faber. “Suspension- and solution-based freeze casting for porous ceramics”. In: *Journal of Materials Research* 32.17 (2017), pp. 3372–3382.
- [25] Marcin Wojdyr. “Fityk: a general-purpose peak fitting program”. In: *Journal of Applied Crystallography* 43.5-1 (2010), pp. 1126–1128.
- [26] M. Chen and T.Z. Kattamis. “Dendrite coarsening during directional solidification of Al–Cu–Mn alloys”. In: *Materials Science and Engineering: A* 247.1-2 (1998), pp. 239–247.
- [27] Dimitris Kammer. “Three-Dimensional Analysis and Morphological Characterization of Coarsened Dendritic Microstructures”. PhD thesis. Northwestern University, 2006.
- [28] D.H. Kirkwood. “A simple model for dendrite arm coarsening during solidification”. In: *Materials Science and Engineering* 73 (1985), pp. L1–L4.
- [29] Maninpat Naviroj. “Silicon-based porous ceramics via freeze casting of preceramic polymers”. PhD thesis. Northwestern University, 2017.
- [30] Lile Cai et al. “Dynamic Analysis Model for the Diffusion Coefficient in High-Viscosity Polymer Solution”. In: *Industrial & Engineering Chemistry Research* 57.46 (2018), pp. 15924–15934.



- [31] J.S. Vrentas and J.L. Duda. “Diffusion in polymer–solvent systems. II. A predictive theory for the dependence of diffusion coefficients on temperature, concentration, and molecular weight”. In: *Journal of Polymer Science: Polymer Physics Edition* 15.3 (1977), pp. 417–439.
- [32] Chubin Yang et al. “Dendrite morphology and evolution mechanism of nickel-based single crystal superalloys grown along the  $\langle 001 \rangle$  and  $\langle 011 \rangle$  orientations”. In: *Progress in Natural Science: Materials International* 22.5 (2012), pp. 407–413.
- [33] C.H. A. Gandin, M. Eshelman, and Rohit Trivedi. “Orientation dependence of primary dendrite spacing”. In: *Metallurgical and Materials Transactions A* 27.9 (1996), pp. 2727–2739.
- [34] R.N. Grugel and Y. Zhou. “Primary dendrite spacing and the effect of off-axis heat flow”. In: *Metallurgical Transactions A* 20.5 (1989), pp. 969–973.
- [35] T. Cool and P.W. Voorhees. “The evolution of dendrites during coarsening: Fragmentation and morphology”. In: *Acta Materialia* 127 (2017), pp. 359–367.
- [36] Maninpat Naviroj et al. “Nucleation-controlled freeze casting of preceramic polymers for uniaxial pores in Si-based ceramics”. In: *Scripta Materialia* 130 (2017), pp. 32–36.
- [37] Aaron Lichtner et al. “Effect of macropore anisotropy on the mechanical response of hierarchically porous ceramics”. In: *Journal of the American Ceramic Society* 99.3 (2016), pp. 979–987.

*Chapter 6***APPLICATION OF FREEZE-CAST STRUCTURE:  
MICROSTRUCTURAL ENGINEERING OF MATERIAL SPACE  
FOR FUNCTIONAL PROPERTIES**

This chapter is based on the work from the journal article, "Robust cellular shape-memory ceramics via gradient-controlled freeze casting" by X. M. Zeng, N. Arai, and K.T. Faber. X. Zeng and N. Arai both contributed to this work equally. This article has been published in *Advanced Engineering Materials*.

Zeng X, Arai N, Faber KT. Robust cellular shape-memory ceramics via gradient-controlled freeze casting *Advanced Engineering Materials*. 2019;21(12):1900398. <https://doi.org/10.1002/adem.201900398>

**6.1 Introduction**

Shape-memory ceramics are ceramics which undergo martensitic (diffusionless) phase transformations by the aid of heat or stress. Figure 6.1 shows two properties of shape memory ceramics: the shape-memory effect and the superelastic effect. In the former, the material is deformed upon application of stress, but recovers its original shape only when it is heated. The deformation and shape recovery are the result of a forward martensitic transformation and reverse martensitic transformation between tetragonal and monoclinic phases. For the superelastic effect, the material undergoes reverse martensitic transformation when the applied stress is removed, hence, it will deform with a large recoverable strain ( $\sim 1.9\%$  [1]). Shape-memory ceramics, however, are known to experience a volume change and shape change which leads to intergranular cracking. As a result, the shape-memory performance is historically limited to only a few cycles [1].

Recently, a new strategy to mitigate this intergranular cracking has been reported by Lai et al. It was demonstrated that the shape-memory effect in micro-/submicro-scale pillars and particles exhibited superelastic behavior with significant deformation, full recovery and over 500 load cycles [3]. Despite their promising potential in applications like actuation and energy damping [4], shape-memory properties are found to be limited to small volumes to accommodate mismatch stresses along grain boundaries [5]. Though the microscale dimensions are convenient for elucidating

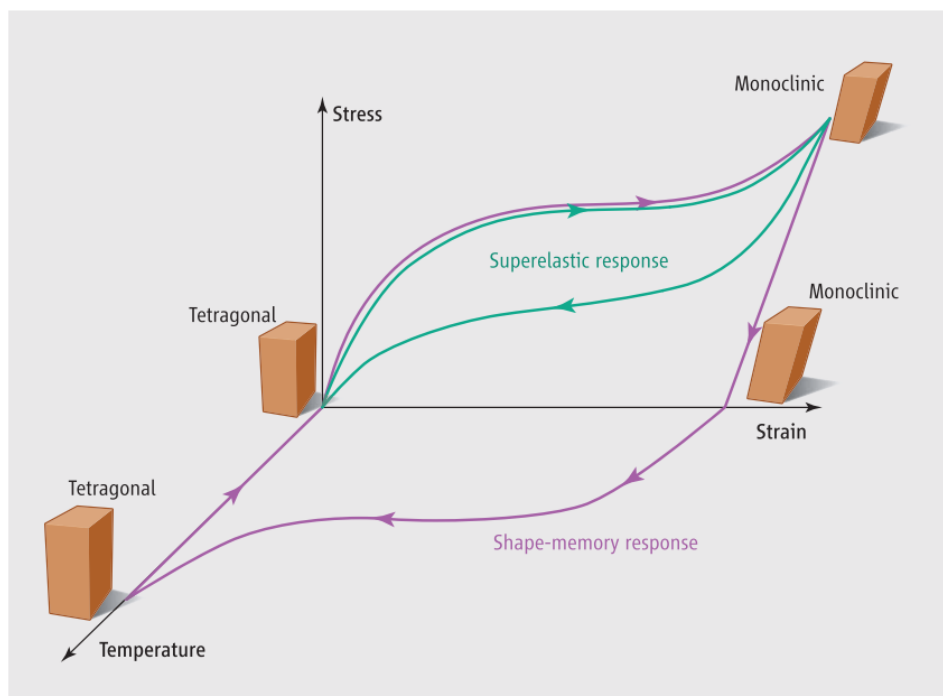


Figure 6.1: A schematic showing shape-memory effect and superelastic effect [2]. This figure is reproduced with permission.

the fundamentals of material behavior [6], the challenge remains to transfer such shape-memory properties into desirable 3D bulk forms for practical applications. Addressing this challenge, therefore, involves the design of a suitable bulk structure that locally mimics the characteristic features of oligocrystalline pillars and the development of appropriate fabrication approaches to realize such structures. One approach involving the scale-up of particles in a granular form, where each particle acts as a transformation site, has proven effective in demonstrating high-energy damping capacity at a pseudo-bulk scale [7]. Additionally, Crystal et al. reported a single crystal shape memory zirconia and demonstrated repeatable transformation without significant damages compared to polycrystals [8]. Alternatively, a one-piece porous foam with thin oligocrystalline walls has been reported, showing that a significant volume fraction of the porous material (>60%) could experience martensitic transformations under an applied stress [9]. These studies motivate the concept that a high specific surface area with oligocrystalline features accommodates stress during martensitic transformation of grains and the associated large deformation in bulk form [10]. However, the full potential in shape-memory ceramics is characterized by their unique properties of large recoverable strain at high mechanical stress, which are not present in the aforementioned investigations. We propose that

its realization relies on a desirable 3D geometry with the following properties: 1) a homogeneous feature size comparable with microscale pillars for transformation events to occur uniformly in the structure [11]; 2) a particular cellular configuration that can resolve the applied uniaxial force into uniform compressive stress to trigger the martensitic transformation without introducing tensile or bending stress [12]; and 3) sufficient strength to survive a large compressive transformation stress before reaching the fracture stress [6].

The approach in this work is to develop zirconia-based ceramics with a directionally aligned honeycomb-like cellular porous structure, afforded by the structural tunability offered by gradient-controlled freeze casting. As shown in Chapter 3, the effects of temperature gradient on pore morphologies were demonstrated in solution-based freeze casting. Here, the same method is applied to suspension-based freeze casting to achieve cellular porous structure.

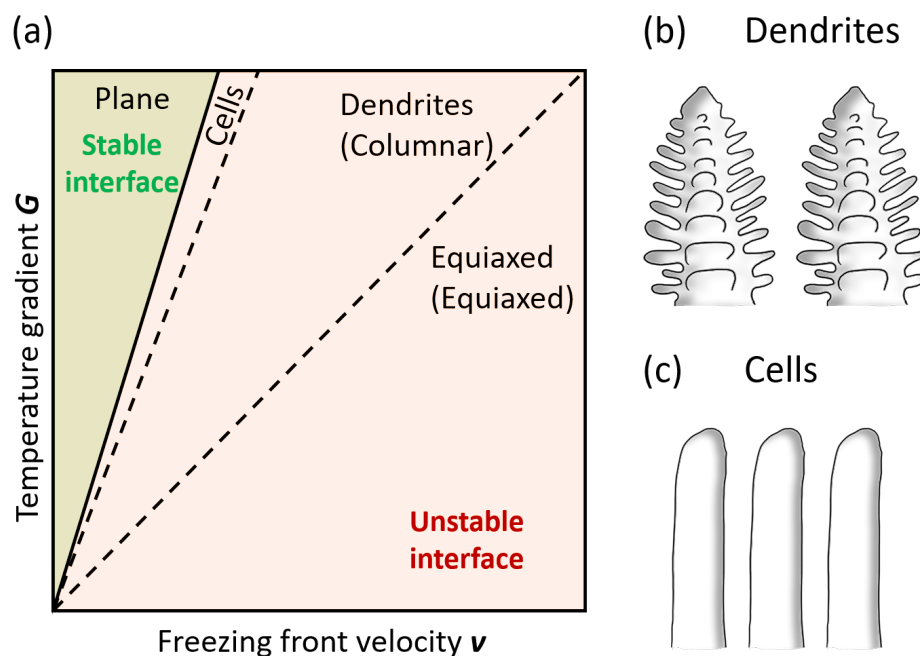


Figure 6.2: Stability-microstructure map based on constitutional supercooling of a solid–liquid interface controlled by freezing front velocity and temperature gradient (modified based on Rettenmayr and Exner [13]). Schematic illustration of b) dendrites and c) cells.

The cellular structure can be considered an intermediate structure between the stable planar front and the dendrites [14]. Thus, cellular structures span a narrow region on the stability-microstructure map, referred as stability map, (Figure 6.2a) and can

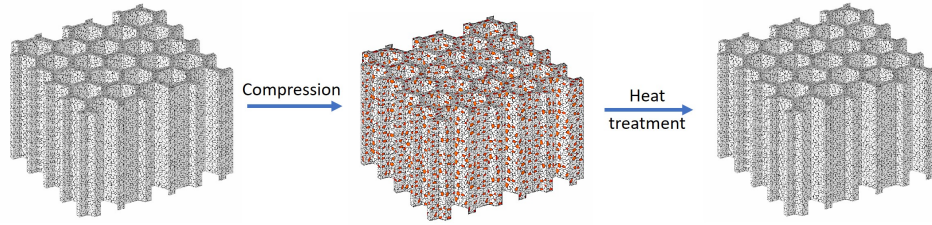


Figure 6.3: The proposed shape-memory effect in a unidirectional cellular structure during uniaxial compression and heat treatment. The red highlights represent transformed grains within the cellular walls.

only be achieved with very limited conditions of low freezing front velocity and high temperature gradient [15].

By precisely controlling freezing front velocity and temperature gradient, the resulting cellular crystals are expected to yield a homogeneous unidirectional cellular pore morphology (Figure 6.3). The unidirectional cellular structure in principle would have high strength in the out-of-plane direction [12] for the material to be mechanically deformed to reach phase transformation stress prior to fracture. The thin cellular walls would mimic the features of oligocrystalline pillars, offering a feasible approach for exhibiting the shape-memory effect in a bulk structure. During mechanical compression, grains with suitable crystal orientations can experience the martensitic transformation that leads to large deformation, whereas those nontransformed grains serve as the framework to provide sufficient mechanical strength for structural integrity. With such a design, shape recovery can be achieved through subsequent heat treatment to trigger reverse martensitic transformation to demonstrate a full cycle of shape-memory effects. In this study, in addition to the shape-memory effect, the superelastic effect was also examined.

## 6.2 Experimental methods

### 6.2.1 Suspension preparation

A ceramic powder suspension was prepared by mixing zirconia ( $ZrO_2$ ) nanopowders and ceria ( $CeO_2$ ) nanopowders (99.9%, Inframat Advanced Materials) with cyclohexane (99.5%, Sigma-Aldrich). The suspension compositions were set to a 10 vol.% solid loading for a target porosity of 70 %. A powder mixture having a composition of 12.5 mol%  $CeO_2$ –87.5 mol%  $ZrO_2$  and 14.5 mol%  $CeO_2$ –85.5 mol%  $ZrO_2$  was chosen so that the ceria-doped zirconia exhibits the shape-memory effect and the superelastic effect, respectively. For shape memory, the composition

was deliberately selected to control the characteristic transformation temperature, at which the thermally induced tetragonal/monoclinic phase transformation occurs, to be in the vicinity of room temperature. For superelasticity, the composition was selected to make the austenite finishing temperature to be below the room temperature. In the bulk,  $\sim 13$  mol.% is a superelastic composition [16] while  $\sim 15$  mol.% is a superelastic composition for granular particles [7] due to the less constraint from the matrix [17]. Hence, 14.5 mol.% was chosen for porous form as superelastic composition. Among various suspension media used in freeze casting [18], cyclohexane was chosen in this study to produce dendritic/cellular pore structures. A dispersant of Hypermer KD-4 (Croda Inc.) was added at a concentration of 7 wt.% of solid powders. The mixture was ball milled for 48 h with zirconia milling balls to achieve a homogenous suspension.

### 6.2.2 Gradient-controlled freeze casting

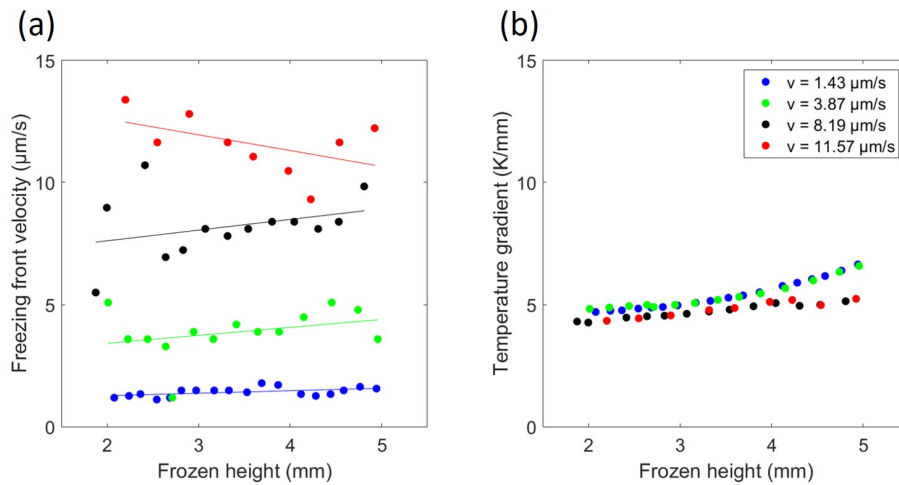


Figure 6.4: Plots showing (a) freezing front velocity and (b) temperature gradient as a function of frozen height.

The suspension was freeze-cast in a glass mold with an inner diameter of 24 mm and a height of 12.5 mm. The freezing front velocity of pure cyclohexane solvent and dispersant with no ceramic powders (Figure 6.4a) was measured. The method to measure freezing front velocity and temperature gradient can be found in Chapter 3. The temperature at the freezing front was assumed to be  $6^\circ\text{C}$ , the melting point of cyclohexane. The melting point depression effect from the dispersant is not taken into account when temperature gradient is calculated. Four different freezing front velocity conditions at the constant temperature gradient were studied in this work

(Figure 6.4b). The frozen samples were placed in a freeze dryer (VirTis AdVantage 2.0; SP Scientific, Warminster, PA, USA) to fully sublimate cyclohexane. Finally, the samples were sintered in air at 1500°C for 3 h at a ramping rate of 2°C/min, after holding at 550°C for 2 h to burn out any residual organic compounds.

### 6.2.3 Characterization

The microstructures were observed using a scanning electron microscope (SEM; Zeiss 1550VP, Carl Zeiss AG, Oberkochen, Germany). The pore size distribution was characterized using mercury intrusion porosimetry (MIP; Auto Pore IV, Micromeritics, Norcross, GA, USA). The samples were uniaxially compressed along the longitudinal direction (parallel to the freezing direction) with a universal testing machine (Instron 5982, Norwood, MA, USA), with a displacement rate of 0.06 mm/min. An X-ray diffractometer (PANalytical X'Pert Pro, Cu K $\alpha$ , I= 40 mA, V=45 kV) was used to analyze the phase content before and after compression tests, with  $2\theta$  ranges between 25–35° and a scan rate of 1°/min.

## 6.3 Results and discussion

### 6.3.1 Morphological control

As can be seen in Figure 6.5, the chosen conditions allow one to horizontally shift the locus on the stability map between dendritic and cellular regions, as evidenced by the obtained microstructure corresponding to each condition. The secondary arms of the dendrites (at  $v$  of 11.57 and 8.19  $\mu\text{m s}^{-1}$ ) become shorter at a lower  $v$  of 3.87  $\mu\text{m s}^{-1}$  to form a transitional structure with wavy surface cellular walls. At a low  $v$  of 1.43  $\mu\text{m s}^{-1}$ , a cellular structure with well-aligned straight walls and no secondary arms is developed. As ceramics are much stronger under compression than under tension or bending [4], the cellular structure is considered critical to effectively constrain the resolved applied force to be mainly compressive on the walls, instead of the complex stress field expected in a dendritic structure which can easily lead to local fracture. Even though similar freezing front velocities and temperature gradients were used to freeze-cast the preceramic polymer solution in Chapter 3, the pore structure was still dendritic. Three possible reasons can explain this difference. First, this could be due to the dissolved preceramic polymer at higher concentrations, which would cause a large degree of constitutional supercooling [18]. Although, in the suspension, the interfacial undercooling is caused by the particulate constitutional supercooling and solute constitutional supercooling, You et al. showed that interfacial undercooling mainly comes from solute constitutional supercooling caused by solutes in the

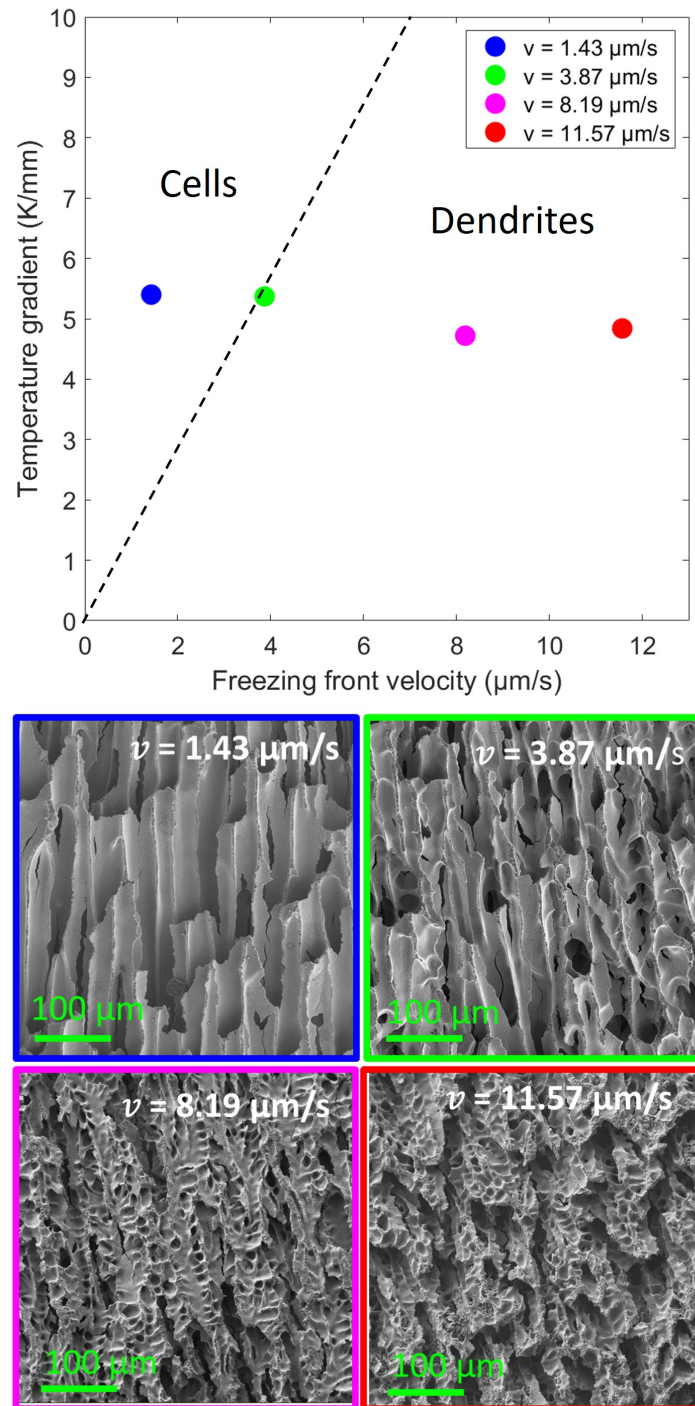


Figure 6.5: Stability-microstructure map based on measured freezing front velocity and temperature gradient of cyclohexane, with the corresponding longitudinal microstructures of freeze-cast zirconia-based ceramics.



solvent and particulate constitutional supercooling is minor based on quantitative measurements [19]. In suspension, the dispersant can be considered as the solute dissolved in small concentration, which makes it easier to achieve cells with the conditions examined in this study. Second, the diffusivity of the solute also affects the degree of constitutional supercooling. The preceramic polymer has a high molecular weight to avoid volatilization during the pyrolysis, and low diffusivity of preceramic polymer results in a larger degree of constitutional supercooling. Third, it has been observed by Sekhar and Trivedi that the presence of particles changes morphologies from dendritic to cellular due to solute accumulation between the particle and the freezing front. This results in a smaller concentration gradient in front of the interface, hence it leads to a small degree of constitutional supercooling [20].

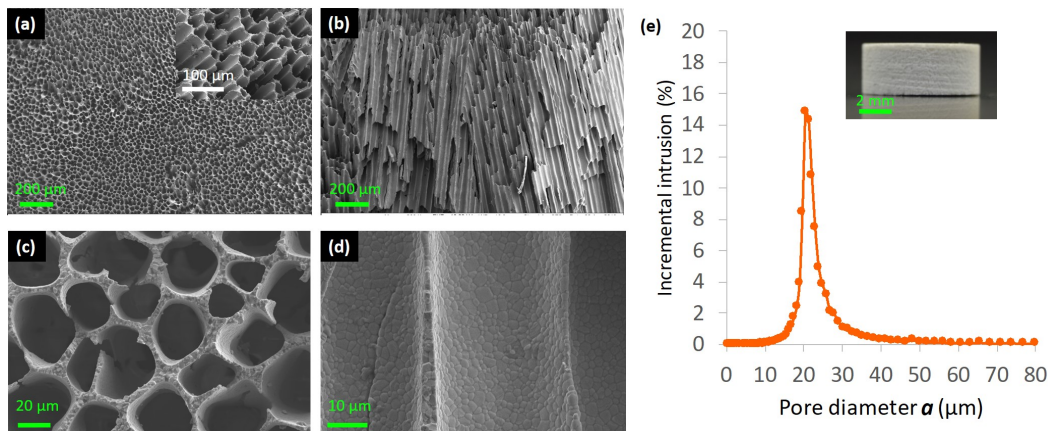


Figure 6.6: Microstructure of freeze-cast cellular zirconia-based ceramics viewed from (a) the transverse (the inset image shows an off-axis view of pores) and (b) the longitudinal directions. Oligocrystalline cellular walls from (c) the transverse and (d) longitudinal directions. (e) Pore size distribution within the measurement range of 100 nm–80  $\mu\text{m}$  from mercury intrusion porosimetry, with inserted sample image after machining.

The cellular structure obtained with the lowest freezing front velocity is homogeneous throughout the sample with a height of 3 mm and porosity of 70% (Figure 6.6a,b). The structure is honeycomb-like with an array of pores formed between thin vertical walls that align along the freezing direction. The average grain size is 2  $\mu\text{m}$ , whereas the wall thickness is 2–4  $\mu\text{m}$ , indicating that the walls are largely oligocrystalline with only one or two grains in the thickness direction (Figure 6.6c, d), thereby successfully mimicking the oligocrystalline pillar structures. The pore size measured with mercury intrusion porosimetry shows a narrow unimodal distribution

around 20.3  $\mu\text{m}$  (Figure 6.6e).

### 6.3.2 Compressive response of shape-memory system

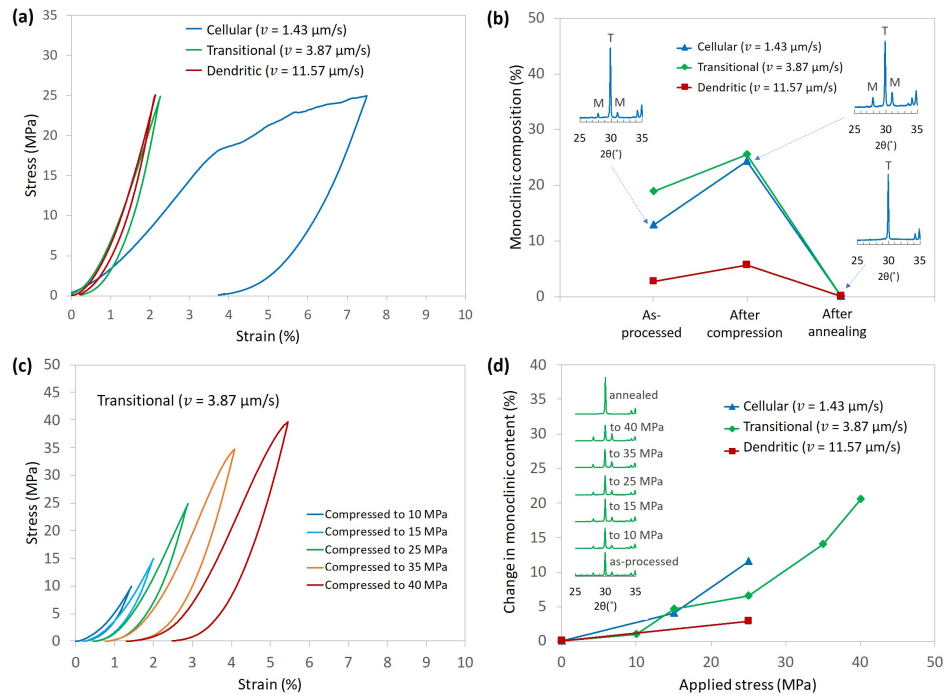


Figure 6.7: Stress–strain behavior of the cellular structure ( $v = 1.43 \mu\text{m s}^{-1}$ ), transitional structure ( $v = 3.87 \mu\text{m s}^{-1}$ ), and dendritic structure ( $v = 11.57 \mu\text{m s}^{-1}$ ) under a compressive stress of 25 MPa (a). (b) The evolution of phase content on compression and after heat treatment, with inserted XRD patterns of cellular structure corresponding to each condition. (c) Stress–strain curves of the transitional structure tested consecutively at stresses from 10 to 40 MPa. (d) The change in the monoclinic content of all samples after compression as a function of applied stress, with inserted XRD patterns of the transitional structure in between each compression test.

The mechanical response of porous ceramics with various microstructures was studied by applying a uniaxial compressive force along the longitudinal direction; a second set of mechanical tests was accompanied by a phase content study with X-ray diffraction (XRD) between stress increments. Under monotonic loading to 25 MPa (Figure 6.7a), linear elastic behavior was observed for all samples up to 20 MPa. The major difference lies in their behavior above 20 MPa, where cellular structures experience a marked decrease in slope, reaching a maximum strain of 7.5% at 25 MPa. Upon unloading, a residual strain of 3.9% persists, a magnitude comparable with shape-memory pillars [5, 6]. The dendritic and transitional structures both exhibit much smaller deformations with residual strains of less than 0.4%. The significant

variation of stress–strain behavior in cellular, transitional, and dendritic structures supports the hypothesis that only with a precisely designed 3D cellular structure can the shape-memory effect be observed in bulk form. The phase composition was calculated based on the intensity ratio of XRD peaks:  $(11\bar{1})_m$ ,  $(111)_t$  and  $(111)_m$  between  $27$  to  $32^\circ 2\theta$ . All samples were composed of  $2.7\sim 18.9\%$  monoclinic phase before compression (Figure 6.7b).

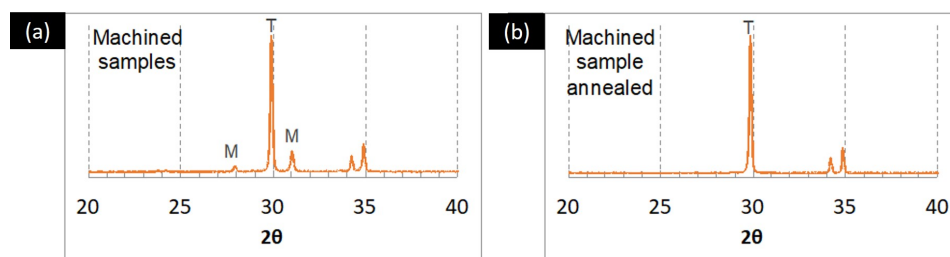


Figure 6.8: XRD spectrum of a sample (a) after machining, and (b) after annealing without experiencing mechanical compression.

The monoclinic phase in the as-processed samples was introduced during the machining process to obtain a disk-like shape for compression tests (Figure 6.8). An annealed sample after machining was determined by XRD to have no monoclinic phase content. Cellular structures experienced a significant tetragonal  $\rightarrow$  monoclinic phase change of  $11.5\%$  during compression, whereas the transitional and dendritic structures experienced only  $6.6\%$  and  $3.0\%$  transformation, respectively. All samples remained intact after compressive tests without any noticeable macroscale cracks. The typical abrupt stress drop in a brittle honeycomb structure that signifies the beginning of the brittle fracture of cell walls [14] was not observed in any cellular structures. No further mechanical tests were conducted on cellular structures since the as-compressed samples were composed of a  $24.3\%$  monoclinic phase, which we consider to be significant enough for shape deformation, whereas  $75\%$  of the parent tetragonal phase would provide sufficient mechanical support to preclude fracture. All compressed samples were annealed at  $700^\circ\text{C}$  for 2 h, after which only the tetragonal phase was observed, suggesting a complete reverse phase transformation during heat treatment. To confirm the thermal-induced shape recovery in the cellular structure, the dimensions of a second identically processed sample were recorded before compression, after compression to a maximum strain of  $6.4\%$ , and after heat treatment. The compression test was halted as soon a drop in load was detected, which suggested the onset of structural failure (Figure 6.9). Hence, we expected only partial strain recovery from heat treatment, measured here to be

43–48% (Table 6.1).

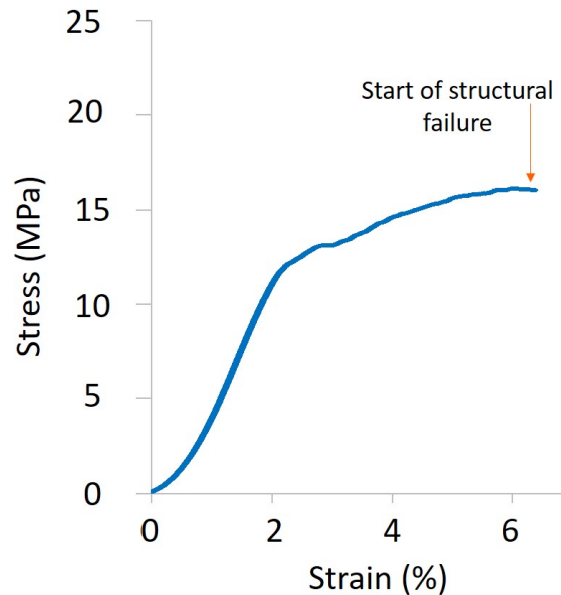


Figure 6.9: The stress-strain curve of the sample used for the shape recovery measurement.

The large residual strain on loading above 20 MPa, the XRD evidence of the stress-induced phase transformation, and the fully reversible phase transformation on heating indicate that the cellular structures exhibited the shape-memory effect. The critical stress of martensitic transformation of grains is highly orientation dependent, varying between 100 MPa and 2 GPa [11]. Therefore, the random distribution of grain orientations in these cellular structures leads to a continual tetragonal  $\rightarrow$  monoclinic transformation at different stress levels and a marked decrease in slope, instead of a single flat plateau in the strain, as observed in single-crystal pillars [6] or a step-wise plateau, as in oligocrystalline pillars [21]. According to Gibson and Ashby [12], for perfect cellular structures, walls are effectively compressed when a compressive stress is applied, whereas more poorly aligned structures like foams experience a complex stress field under compression. For the dendritic structure, a complex stress field involving compression, tension, and bending is expected and therefore limits the material fraction that participates in phase transformation through compressive deformation. In the transitional structure, the walls are well aligned but with high surface waviness, leading to an inhomogeneous compressive stress distribution across the walls. Consequently, a smaller fraction of grains is

Table 6.1: Sample height and diameter before compression, after compression, and after heat treatment; associated residual and recovered displacements used to establish recovered strain.

Height (mm)	Before compression	After compression	After heat treatment	Residual displacement	Displacement recovery	Recovered strain
Measurement	2.43	2.33	2.39	0.10	0.06	
	2.44	2.33	2.36	0.11	0.03	
	2.43	2.35	2.38	0.08	0.03	
	2.43	2.33	2.38	0.10	0.03	
	2.44	2.32	2.37	0.12	0.05	
Average	2.43	2.33	2.38	0.10	0.04	43%
Diameter (mm)	Before compression	After compression	After heat treatment	Residual displacement	Displacement recovery	Recovered strain
Measurement	9.77	9.80	9.80	0.03	0.00	
	9.77	9.87	9.83	0.10	0.04	
	9.78	9.85	9.81	0.07	0.04	
	9.79	9.85	9.82	0.06	0.03	
	9.76	9.83	9.78	0.07	0.05	
Average	9.77	9.84	9.81	0.07	0.03	48%

able to reach the critical transformation stress, resulting in a negligible change in slope (Figure 6.7a and  $v = 3.87 \mu\text{m s}^{-1}$ ). This limited nonlinearity is reminiscent of the stress–strain behavior of granular shape-memory powders [7], where transformation is limited by nonuniform stress distribution. The extent of this effect is further evaluated by applying ascending stresses from 10–40 MPa to the transitional structure (Figure 6.7c). The transitional structure survived a maximum stress of 40 MPa without any macroscale fracture, providing latitude for a significant volume of the ceramics to experience transformation prior to fracture. The stress–strain curves are plotted with the residual strain of each test accounted for; the total residual strain of 2.5% lies between that of cellular and dendritic structures. The change in monoclinic content in between each compression test is shown in Figure 6.7d, together with those of cellular and dendritic structures. The slope of the change

in monoclinic content against applied stress, an indication of the effectiveness in triggering the transformation through compression, increases from dendritic to transitional to cellular structures. The general trend of the increasing slope with applied stress is due to a nonlinear distribution of transformation stress over random crystal orientations [6]. The high correlation between the change in monoclinic content and residual strain further supports the idea that a homogeneous compressive stress in the walls is most desirable for inducing shape-memory effect in ceramics. The difference in the monoclinic phase introduced during the machining process in the as-processed samples also qualitatively suggests the variation in difficulty in triggering the deformation through shear cutting.

### 6.3.3 Cyclic experiments

Up to this section, only one cycle of forward and reverse martensitic phase transformation was demonstrated. Here, multiple cycles are demonstrated for both the shape-memory effect and superelasticity. The materials were subjected to multiple cycles of forward and reverse martensitic phase transformations to see if honeycomb-like structures are robust. Microcrack formation of the materials were also investigated by analyzing the slope of the stress-strain curve.

All the cyclic experiments were performed on the samples frozen at velocities of  $3.87 \mu\text{ms}^{-1}$  (transitional structure) since these can sustain higher stresses, and therefore, yield higher monoclinic contents, as can be seen in Figure 6.7(d). For the samples with shape-memory composition, the samples were annealed after machining to start with a fully tetragonal phase.

#### Shape-memory effect

When the sample was compressed at 35 MPa once, it was found that the monoclinic phase after compression reaches only 3-4%, compared to the sample experiencing a 14% tetragonal phase transforming into a monoclinic phase at 35 MPa compression (Figure 6.7c). Hence, having a residual monoclinic phase in the starting material helps the nucleation and growth processed of the monoclinic phase. In order to induce further phase transformation, the samples were compressed to 35 MPa five consecutive times (Figure 6.10a). Specifically, the samples were tested by five loading-unloading cycles, annealing at 700°C for 2 hours followed by XRD, and the next set of five loading-unloading cycles resumed.

The first loading-unloading cycle has a larger hysteresis compared to other loading-

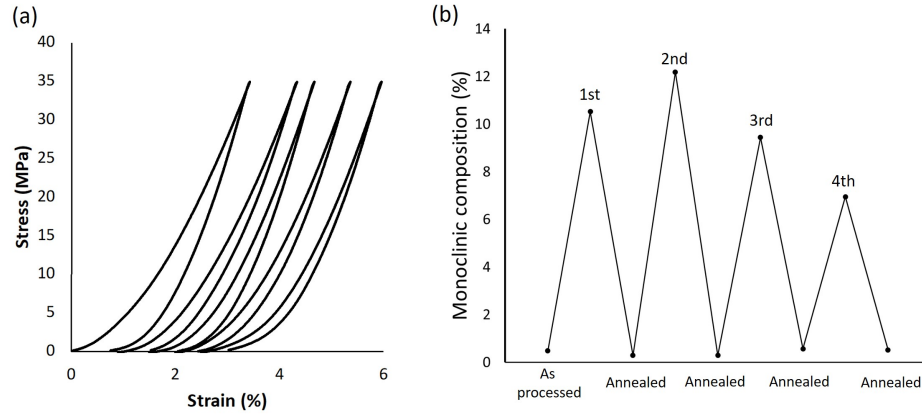


Figure 6.10: Stress-strain curves showing (a) five loading-unloading cycles. (b) Monoclinic composition after each five cycles and after each anneal.

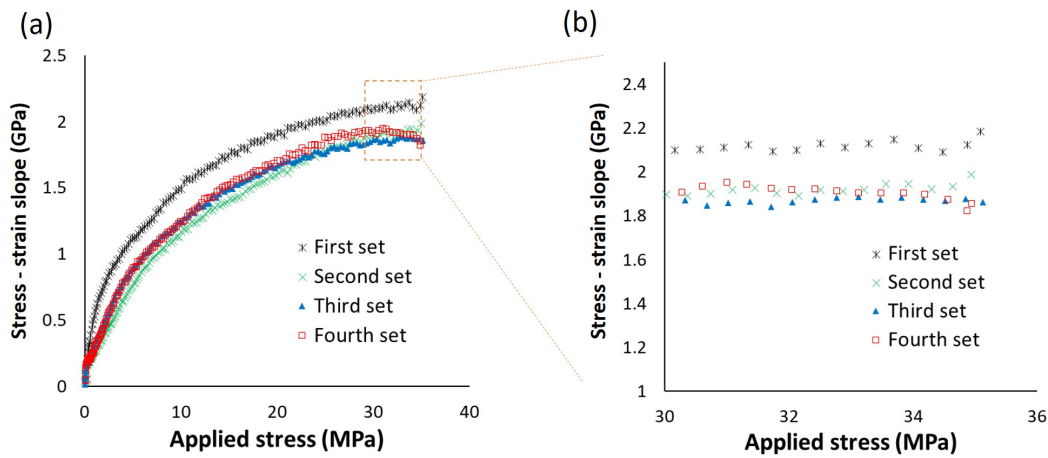


Figure 6.11: Slope of stress-strain curves as a function of applied stress (a). Each data represents the slope of the 5th loading cycles from each set of five loading-unloading cycles. (b) Magnified plateau region.

unloading cycles (Figure 6.10a), which is due to the alignment of the sample. After the first loading-unloading cycle, however, the other curves are consistent and reproducible. After five loading-unloading cycles, the monoclinic phase increased to a maximum of 12% (2nd set of in Figure 6.10b). This is similar to the monoclinic fraction of shape-memory nanofiber yarns after bending five times [22]. As Figure 6.10b shows, the monoclinic composition gradually decreased after the second set of five loading-unloading cycles. One possible explanation is due to the so-called training effect, which is observed in both shape-memory ceramics [8] and shape-memory alloys [23]. During the training effect, the material tries to find a favored kinematic transformation pathway, and it takes some cycles for the material to

exhibit a consistent response [3, 8]. As a result, due to this effect, the transformed monoclinic fraction might not be the same even if the same stress is applied.

In order to investigate microcrack formation during the test, the slope of the stress-strain curve during loading was plotted as a function of applied stress (Figure 6.11a). This is similar to the study of Gu and Faber to investigate stress-induced microcracking [24]; they observed an elastic modulus decrease after a multiple loading-unloading cycle of the specimen. The stress-strain curves from the 5th cycle of each set of loading-unloading cycles were chosen as representative. As the stress is applied, the slope continues to increase, and this is due to the non-linearity caused by the realignment of the sample. At approximately 30 MPa, the slope reaches a plateau; Figure 6.11b shows a magnified version of this region. The first set has the highest slope, but the slope remains within similar values at subsequent loadings. In addition to the possible microcrack formation at the first set, the fourth set also has gradual change in the slope, indicating the microcrack formation.

### **Superelastic effect**

Superelasticity was also demonstrated with compositions of 14.5 mol% CeO<sub>2</sub>-85.5 mol% ZrO<sub>2</sub>. Figure 6.12 shows five loading-unloading cycles at increasing compressive stress levels (10 MPa, 20 MPa and 24 MPa). Hence, except for the first loading-unloading cycle at 10 MPa, which shows a large hysteresis due to the realignment of the sample, the loading-unloading cycles are consistent at all the stress levels. With increasing stress, the size of the hysteresis increases, consistent with a superelastic transformation. However, this is insufficient to determine if the material underwent martensitic transformation. To provide further evidence of the transformation, the slope change in the loading curve was investigated. Shape-memory ceramics exhibit slope changes in stress strain curves [1] due to the shape deformation resulting from the formation of detwinned martensite (monoclinic phase in this study) [25] [26]. Hence, if a slope decrease is observed, it suggests that the martensitic phase transformation takes place, although careful analysis is needed to distinguish the transformation from microcrack formation and will be discussed in the next paragraph. Figure 6.13 shows the slope of selected loading curves as a function of applied stress. The slope shows a continuous increase when the sample was compressed to 10 MPa. When the material was compressed to 20 MPa, the slope reached the maximum values of ~ 2.9 GPa at the stress of ~ 18 MPa and does not increase further. When the applied stress is increased to 24 MPa, the slope



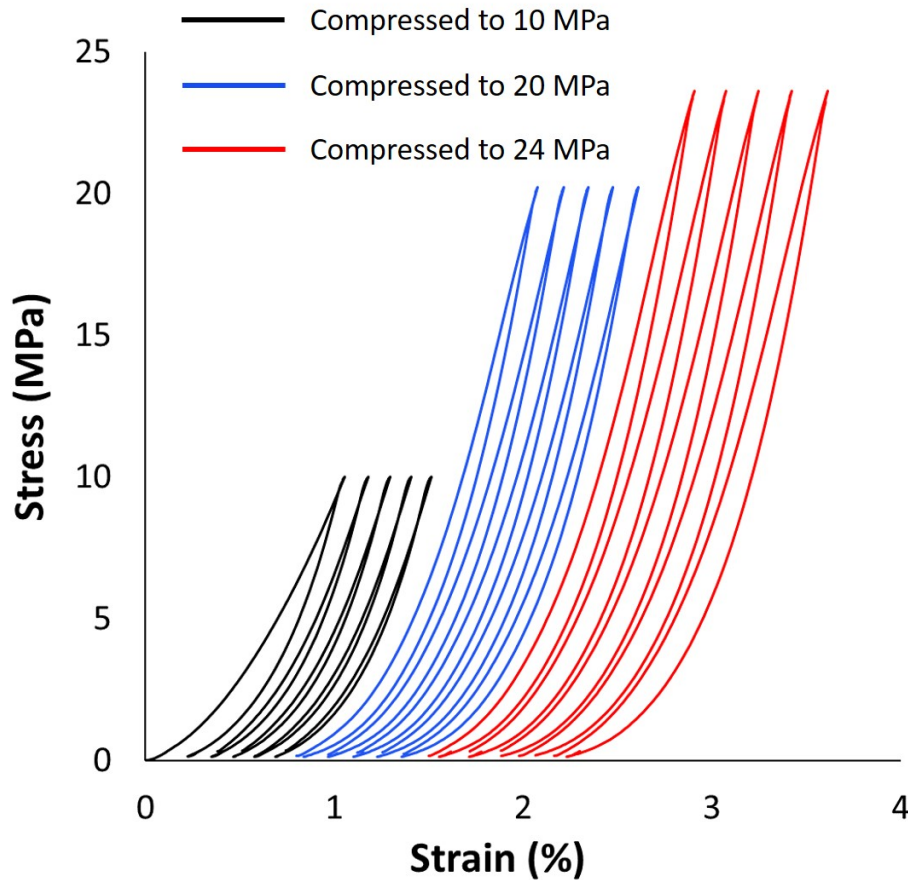


Figure 6.12: Stress-strain curves showing five loading-unloading steps at 10 MPa, 20 MPa, and 24 MPa.

started to decrease, which can be indicative of the martensitic phase transformation. The sample was further compressed to higher stress, but the sample failed. After the compression test, the phase composition was analyzed by XRD, and confirmed that the sample remained a tetragonal phase before and after the compression test.

To assess if the observed slope change is a consequence of the phase transformation or from microcrack formation, Figure 6.14 shows the change in slope of five loading curves when the material was compressed to 24 MPa and above (denoted as “Higher loading”). The slopes of the first four loading curves show consistent and repeatable cycles although the slope is lower than others on the 5th loading, indicating microcrack formation. At “Higher loading”, the slope is significantly lower than others, indicating further microcrack formation and possibly material failure. Hence, it is possible that the material experienced the superelastic effect accompanied by microcrack formation and failure after the 4th loading-unloading

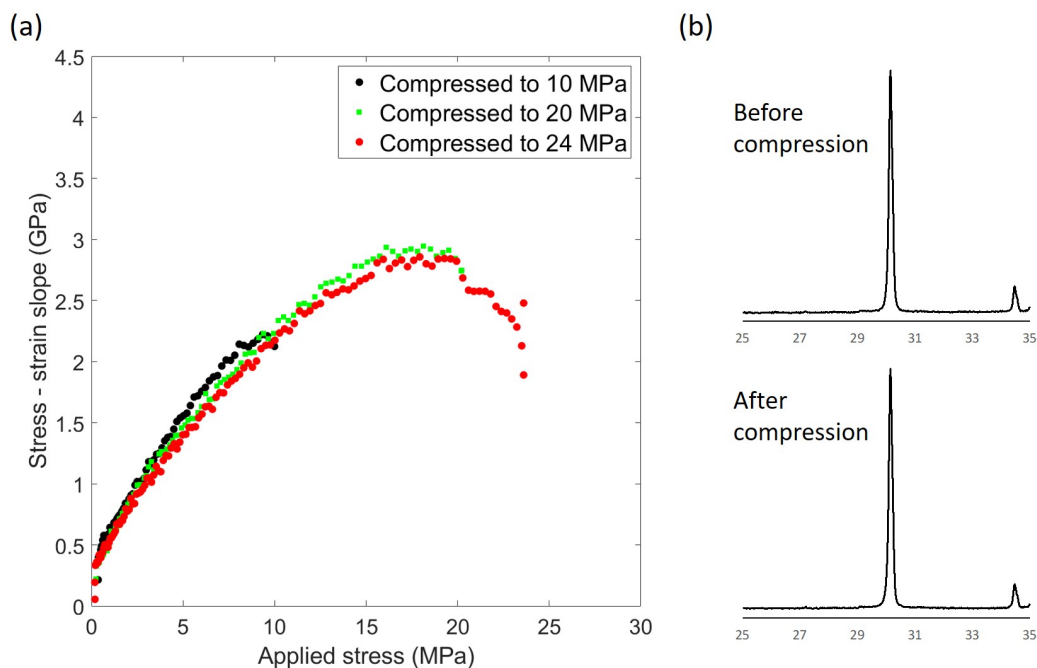


Figure 6.13: Slopes of stress-strain curves as a function of applied stress(a). XRD peak before and after compression (b).

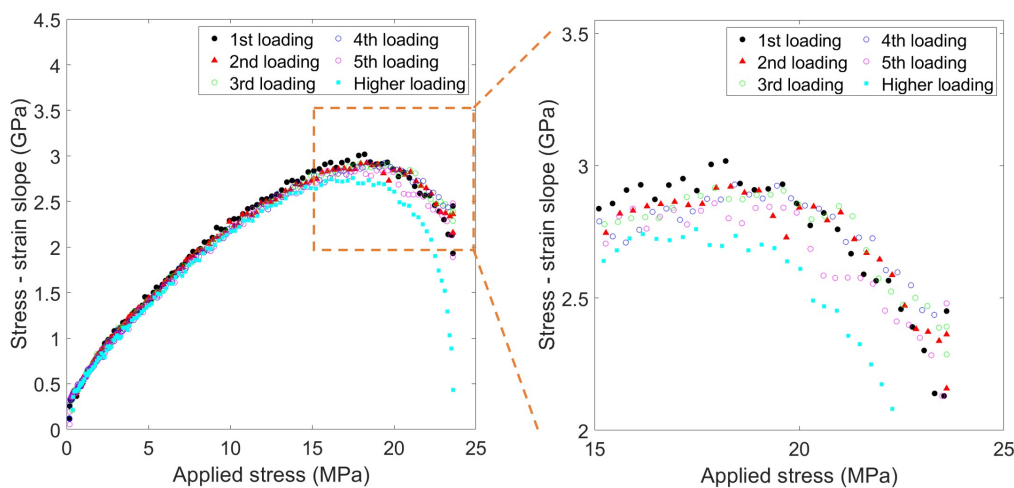


Figure 6.14: Slope of stress-strain curves as a function of the applied stress. The material was compressed to 24 MPa for 5 times, and above.

cycle. As a future direction, in-situ investigation of monoclinic phase evolution, for example by neutron diffraction [27], during compression testing might be useful to confirm the superelastic effect.

## 6.4 Conclusions

In summary, with a precisely designed honeycomb-like cellular structure, the single- and oligocrystalline martensitic transformations have been successfully extended to bulk-scale deformation to achieve the shape-memory effect in a 3D geometry. With independent control of freezing front velocity and temperature gradient through gradient-controlled freeze casting, the freeze-cast microstructures can be fine-tuned into the desired cellular structure with feature sizes similar to those of shape-memory ceramic micropillars. The resultant cellular structure can experience a significant recoverable deformation of up to 7.5% under compression at a stress of 25 MPa. The cyclic experiments were performed to assess shape-memory and superelastic effects. The shape memory material had initially 100 % tetragonal phase and resulted in a 7–12 % tetragonal phase upon compressing to 35 MP. Cellular shape-memory zirconia demonstrated four cycles of the shape-memory effect. The superelastic effect was also studied by looking at the hysteresis and slope changes of stress-strain curves. Both were consistent with the superelastic effect. After multiple loading steps, however, a decrease in the stress-strain slope suggested that microcracks started to form and ultimately led to the material failure.

## References

- [1] Patricio E. Reyds-Morel, Jyh-Shiarn Cherng, and I-Wei Chen. “Transformation plasticity of CeO<sub>2</sub>-stabilized tetragonal zirconia polycrystals: II, pseudoelasticity and shape memory effect”. In: *Journal of the American Ceramic Society* 71.8 (1988), pp. 648–657.
- [2] Katherine T. Faber. “Small Volumes Create Super (elastic) Effects”. In: *Science* 341.6153 (2013), pp. 1464–1465.
- [3] Zehui Du et al. “Synthesis of monodisperse CeO<sub>2</sub>–ZrO<sub>2</sub> particles exhibiting cyclic superelasticity over hundreds of cycles”. In: *Journal of the American Ceramic Society* 100.9 (2017), pp. 4199–4208.
- [4] Xiaomei Zeng et al. “Enhanced shape memory and superelasticity in small-volume ceramics: a perspective on the controlling factors”. In: *MRS Communications* 7.4 (2017), pp. 747–754.
- [5] Zehui Du et al. “Size effects and shape memory properties in ZrO<sub>2</sub> ceramic micro- and nano-pillars”. In: *Scripta Materialia* 101 (2015), pp. 40–43.
- [6] Xiao Mei Zeng et al. “Crystal orientation dependence of the stress-induced martensitic transformation in zirconia-based shape memory ceramics”. In: *Acta Materialia* 116 (2016), pp. 124–135.

- [7] Z. Yu Hang et al. “Granular shape memory ceramic packings”. In: *Acta Materialia* 132 (2017), pp. 455–466.
- [8] Isabel R. Crystal, Alan Lai, and Christopher A. Schuh. “Cyclic martensitic transformations and damage evolution in shape memory zirconia: Single crystals vs polycrystals”. In: *Journal of the American Ceramic Society* (2020).
- [9] Xueying Zhao, Alan Lai, and Christopher A. Schuh. “Shape memory zirconia foams through ice templating”. In: *Scripta Materialia* 135 (2017), pp. 50–53.
- [10] Xiao Mei Zeng et al. “In-situ studies on martensitic transformation and high-temperature shape memory in small volume zirconia”. In: *Acta Materialia* 134 (2017), pp. 257–266.
- [11] Zehui Du et al. “Superelasticity in micro-scale shape memory ceramic particles”. In: *Acta Materialia* 123 (2017), pp. 255–263.
- [12] Lorna J. Gibson and Michael F. Ashby. *Cellular solids: structure and properties*. Cambridge university press, 1999.
- [13] M. Rettenmayr and H.E. Exner. “Directional Solidification”. In: (2001).
- [14] W. Kurtz and D.J. Fisher. *Fundamentals of solidification, Trans Tech*. 1998.
- [15] Martin Eden Glicksman. *Principles of solidification: an introduction to modern casting and crystal growth concepts*. Springer Science & Business Media, 2010.
- [16] Edward L. Pang, Caitlin A. McCandler, and Christopher A. Schuh. “Reduced cracking in polycrystalline ZrO<sub>2</sub>-CeO<sub>2</sub> shape-memory ceramics by meeting the cofactor conditions”. In: *Acta Materialia* 177 (2019), pp. 230–239.
- [17] Paul F. Becher and Michael V. Swain. “Grain-size-dependent transformation behavior in polycrystalline tetragonal zirconia”. In: *Journal of the American ceramic society* 75.3 (1992), pp. 493–502.
- [18] Maninpat Naviroj, Peter W. Voorhees, and Katherine T. Faber. “Suspension- and solution-based freeze casting for porous ceramics”. In: *Journal of Materials Research* 32.17 (2017), pp. 3372–3382.
- [19] Jiaxue You et al. “Interfacial undercooling in solidification of colloidal suspensions: analyses with quantitative measurements”. In: *Scientific reports* 6.1 (2016), pp. 1–7.
- [20] J.A. Sekhar and R. Trivedi. “Solidification microstructure evolution in the presence of inert particles”. In: *Materials Science and Engineering: A* 147.1 (1991), pp. 9–21.
- [21] Alan Lai et al. “Shape memory and superelastic ceramics at small scales”. In: *Science* 341.6153 (2013), pp. 1505–1508.
- [22] Zehui Du et al. “Shape-Memory Actuation in Aligned Zirconia Nanofibers for Artificial Muscle Applications at Elevated Temperatures”. In: *ACS Applied Nano Materials* 3.3 (2020), pp. 2156–2166.

- [23] Carmine Maletta et al. “Fatigue properties of a pseudoelastic NiTi alloy: Strain ratcheting and hysteresis under cyclic tensile loading”. In: *International Journal of Fatigue* 66 (2014), pp. 78–85.
- [24] Wei-Hwa Gu and Katherine T. Faber. “Tensile Behavior of Microcracking SiC-TiB<sub>2</sub> Composites”. In: *Journal of the American Ceramic Society* 78.6 (1995), pp. 1507–1512.
- [25] J. Wang and Huseyin Sehitoglu. “Twinning stress in shape memory alloys: theory and experiments”. In: *Acta materialia* 61.18 (2013), pp. 6790–6801.
- [26] Yong Liu and Zeliang Xie. “Detwinning in shape memory alloy”. In: *Progress in smart materials and structures* 3 (2007), p. 29.
- [27] Hunter A. Rauch et al. “In situ investigation of stress-induced martensitic transformation in granular shape memory ceramic packings”. In: *Acta Materialia* 168 (2019), pp. 362–375.

*Chapter 7***APPLICATIONS OF FREEZE-CAST CERAMICS: PORE SPACE DESIGN FOR FILTRATION**

The work in Section 7.1 was done in collaboration with Orland Bateman. N. Arai fabricated and analyzed freeze-cast ceramics. O. Bateman performed flow-through experiments and analyzed the data. N. Arai performed SEM imaging on the membranes after flow-through experiments. N. Arai and O. Bateman performed *in-situ* observation of particle flows by laser scanning confocal microscope.

The work in Section 7.2 was done in collaboration with Orland Bateman. N. Arai fabricated and analyzed freeze-cast ceramics. O. Bateman performed *in-situ* polymerization with phase separation micromolding. N. Arai performed SEM imaging and water flux measurement.

Up to this Chapter, it was demonstrated that from a single solvent (cyclohexane), not only can pore size be controlled through solidification parameters, but also pore morphology can be tailored from dendritic pores to cellular pores. In this chapter, the unique pore space provided by dendrites and cylinder-like crystals are utilized for filtration applications.

**7.1 Size-based filtration by dendritic pores****7.1.1 Introduction**

Sepsis is a life-threatening condition caused by the body's response to an infection. Each year, at least 1.7 million adults in USA have sepsis, and nearly 270,000 die from sepsis according to the Centers for Disease Control and Prevention (CDC). It is a medical emergency which requires a timely diagnosis and antibiotic therapies since the patient survival rate drops significantly after 36 hours [1] (Figure 7.1). Antibiotic therapies start with broad-spectrum antibiotics until the pathogens are identified by methods such as blood cultures [2] for effective treatment. Although blood cultures are considered to be the gold standard to determine pathogens in bloodstream and can be detected as low as 1 colony-forming unit (CFU) of bacteria in 10 ml blood, cultures can take up to 96 hours [3]. As a result, the fraction of patients treated with the most effective treatment remains low at a point when the survival rate is high.

### Sepsis is a medical emergency <sup>8</sup>

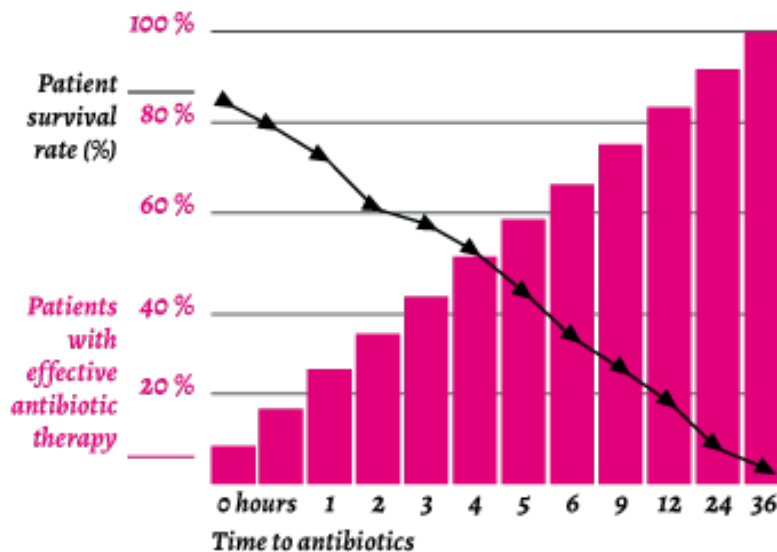


Figure 7.1: A graph showing patient survival rate and patients with effective antibiotic therapy [1].

However, these challenges are currently being addressed by the recent development of digital quantitative detection. Schlappi et al. developed a method to capture and detect nucleic acid at zeptomolar concentration from MES (2-(N-morpholino)ethanesulfonic acid) buffer with *in-situ* amplification in a short period of time [4]. In addition, it was demonstrated that the digital detection can be applied to antimicrobial susceptibility testing, reducing the time of the test to within 30 minutes [5]. Furthermore, a study by Rolando et al. demonstrated a phenotypic antibiotic susceptibility test on urine samples from patients who were diagnosed with urinary tract infections. Because this assay can be performed by using commercially available microfluidic chips and reagents and open-source components, the advance is significant [6]. Although studies mentioned above are critical for fast diagnosis for sepsis, the remaining challenge is the development of membranes which can rapidly capture and concentrate pathogens from the bloodstream into a small volume so that digital detection can be applied to complete the workflow to diagnose and treat sepsis. Hence, the goal of this study is to develop a membrane which captures pathogens in a sample of blood with a high capture efficiency and concentrates them into a small volume in 30 minutes.

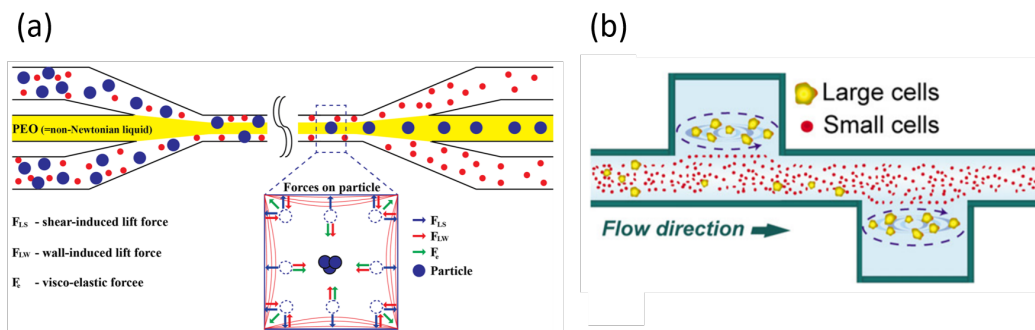


Figure 7.2: Illustration of (a) elasto-inertial based particle focusing and separation [7] (Reproduced under Creative Commons) and (b) larger cells enter into vortices due to the larger net-force acting on larger cells [8] (Reproduced with permission.)

Faridi et al. demonstrated the removal of red blood cells from blood to isolate bacteria using elasto-inertial-based particle focusing and separation [7] (Figure 7.2a). Although the bacteria were captured with an efficiency of 76 % from blood, the method was limited due to a slow flow rate ( $\sim 60 \mu\text{L/h}$ ) and faced challenges with scalability. Work by Hur et al. demonstrated that laminar vortices inside a cavity can selectively isolate large cancer cells [8] (Figure 7.2b). This separation is based on the net-force acting on the particles, which pushes the larger particles toward the vortex centers in the cavity and traps them while small particles flow through the channel. Although this method achieves high throughput with a processing rate of ml/min scale, this method is particularly useful to selectively isolate larger cells or particles. Hence, there is a need to develop membranes which can isolate and concentrate small pathogens from the bloodstream with high throughput.

To achieve high throughput and isolate pathogens from the complex fluids, freeze-cast dendritic pores were examined in this work. Figure 7.3 shows an illustration of how blood containing small pathogens flow in the dendritic pores. When fluid flows through primary pores, secondary pores will exhibit recirculating flow which is much slower than the flow in the primary pores. This phenomenon, sometimes called "flow over cavities," has been investigated in a number of studies [9, 10]. Since primary and secondary pore sizes can be controlled through solidification parameters during freeze casting, dendritic pores can be designed and fabricated such that larger blood cells flow through primary pores while pathogens and platelets are small enough to diffuse into recirculating flows in secondary pores. In this section, this mechanism is referred to as hydrodynamic trapping. Capturing small pathogens relies on diffusion, hence, slower flow velocity is essential to ensure sufficient time



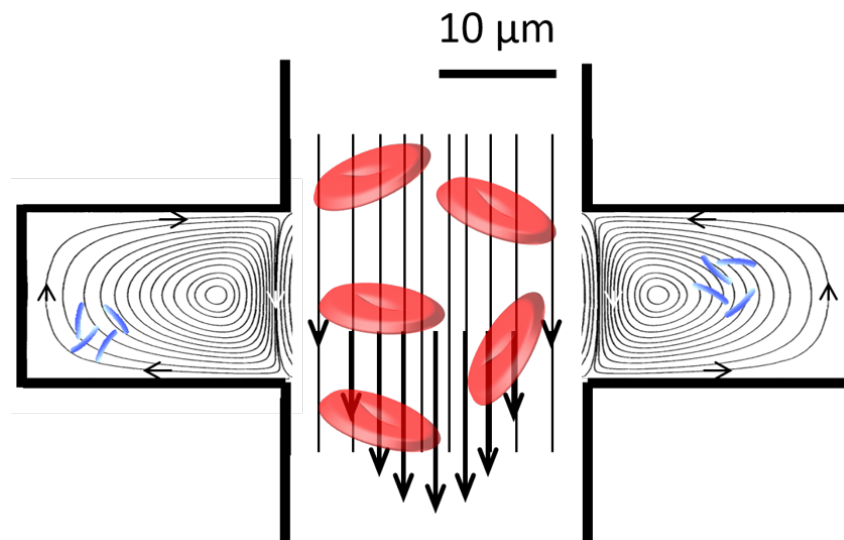


Figure 7.3: An illustration showing fluid flow in the dendritic pores. Large blood cells flow through the primary pores while small pathogens enter a recirculating flow in secondary pores.

for diffusion of pathogens. While this concept might contradict the necessity of high-throughput, high primary pore density (more than thousands of primary pores per square centimeter) tunable by gradient-controlled freeze-casting would enable high-throughput processing. For example, by increasing the primary pore density, the throughput can be set to constant while the fluid flow velocity in each primary pore can be decreased. In this chapter, the following results are reported:

- Preferential capture of small particles with dendritic pores
- In-situ observation of a particle captured by a secondary pore using confocal microscopy
- Design of a dual structure to mitigate surface accumulation of particles.

### 7.1.2 Experimental methods

#### Fabrication characterization of freeze-cast membranes

The preceramic polymer (Silres®MK Powder) was dissolved in cyclohexane at a concentration of 20 wt.%. A cross-linking agent (Geniosil GF 91) was added at a concentration of 1 wt.% with respect to the solution and stirred for 5 min. Four different freeze-cast structures were fabricated in this study. The first structure was freeze-cast using a conventional freeze-casting setup, in which temperature is

controlled on only one side (bottom side) of the mold. The solutions were frozen at a freezing front velocity of  $15 \mu\text{m/s}$ . The second sample type was freeze-cast with the coarsening process described in Chapter 5. The freezing front velocity and temperature gradient were  $15 \mu\text{m/s}$  and  $2.6 \text{ K/mm}$ , respectively, and the sample was coarsened at  $4 \text{ }^\circ\text{C}$  for three hours. This resulted in a honeycomb-like structure. These freeze-cast structures were used for flow-through experiments. The third freeze-cast structure was fabricated for confocal microscope observation using the gradient-controlled freeze-casting setup discussed in Chapter 3. The membrane was freeze-cast with a freezing front velocity of  $15 \mu\text{m/s}$  and a temperature gradient of  $2.6 \text{ K/mm}$ . As a fourth freeze-cast structure, a dual structure was fabricated with the cooling profiles shown in Figure 7.4. This structure contains dendritic pores and cellular pores, and will be described in detail later. Top and bottom temperatures refer to the temperature of the top and bottom thermoelectrics, respectively.

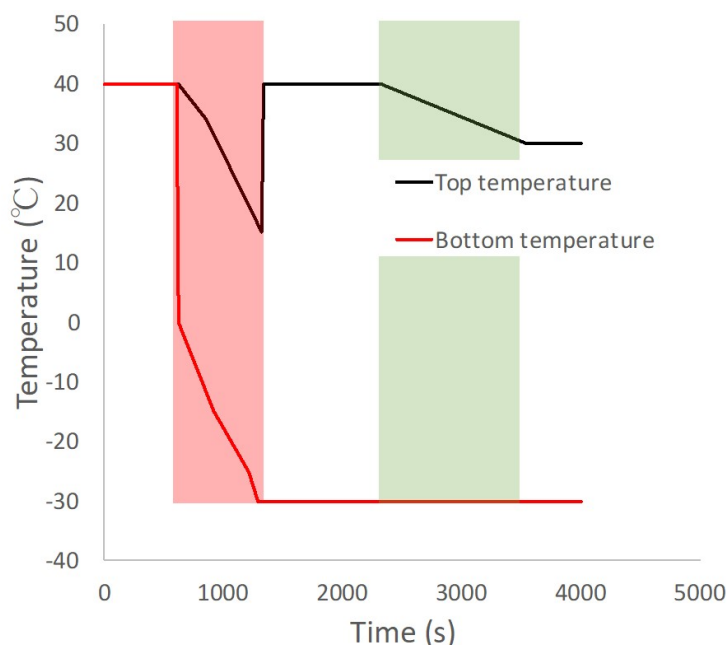


Figure 7.4: Cooling profiles for top and bottom thermoelectric plates to create a dual structure. The red-shaded region creates dendritic pores and the green-shaded region creates cellular pores.

For a flow-through experiment, the samples were pyrolyzed under argon. For the samples prepared for confocal microscopy and the dual structure, pyrolysis was done in the presence of water vapor in addition to argon to remove free carbon in the SiOC. A beaker containing water kept at  $90 \text{ }^\circ\text{C}$  provided the source for water vapor. This was feed into the argon line flowing into the tube furnace. Argon gas flow rate

was kept at 1.5 standard cubic feet per hour (SCFH). Freeze-cast membranes of 3.2 mm thickness were sectioned using a diamond saw. After flow-through experiments, membranes were imaged by a SEM (ZEISS 1550VP, Carl Zeiss AG, Oberkochen, Germany). Pore size of the dual structure was characterized by mercury intrusion porosimetry (Auto Pore IV, Micromeritics, Norcross, GA, USA).

### **Flow-through experiments**

In preparation of flow-through experiments, a glycerol solution was prepared by dissolving glycerol in water at a concentration of 30 vol.%. This solution was prepared to eliminate density mismatch between particles and the suspending medium. The ceramic membrane was immersed into the glycerol solution and left under in-house vacuum (25 mmHg) overnight to fully infiltrate the solution in dendritic pores. The particle suspension was prepared with 300  $\mu\text{L}$  of glycerol solution and 20  $\mu\text{L}$  of poly(diallyldimethylammonium chloride) solution (Sigma-Aldrich, St. Louis, MO, USA) added to 1,660  $\mu\text{L}$  of water. Subsequently, 20  $\mu\text{L}$  of 2  $\mu\text{m}$  fluorescent particle suspensions (Spherotech, Inc, Lake Forest, IL, USA) were added. After mixing, 20  $\mu\text{L}$  of the 0.3  $\mu\text{m}$  fluorescent particle suspensions (Spherotech, Inc, Lake Forest, IL, USA) were further added and mixed thoroughly.

The flow-through experimental setup is shown in Figure 7.5. A syringe was filled with 30 vol.% glycerol solution, which served as the working fluid. A microfluidic device holding a membrane was connected to the syringe. A syringe pump was used to drive flow of the working fluid at rates of 10  $\mu\text{L}/\text{min}$  and 40  $\mu\text{L}/\text{min}$ . After a steady stream of droplets were obtained at the outlet tube, the flow rate was set to 10  $\mu\text{L}/\text{min}$ , and 300  $\mu\text{L}$  of the particle suspension was added from the in-line injection connector. Twenty-four aliquots, each with a volume of 200  $\mu\text{L}$  were collected in a 96-well plate. Then, the membrane was washed with several milliliters of working fluid using the same setup<sup>1</sup>. Subsequently, the same flow-through experiment was performed on the same membrane but with a flow rate of 40  $\mu\text{L}/\text{min}$ . Three membranes were tested using this procedure.

A plate reader (FlexStation®3 Microplate Reader, Molecular Devices, LLC, San Jose, CA, USA) was used to measure the fluorescence signal from two particle populations. To determine the background signal from the working fluid, the flu-

---

<sup>1</sup>Several aliquots were collected and analyzed by the plate reader to see if the aliquots contained any particles. It was confirmed that the fluorescent signal was within the error of the background reading of the working fluid. Hence, it was assumed that the particles in the membrane were irreversibly captured.

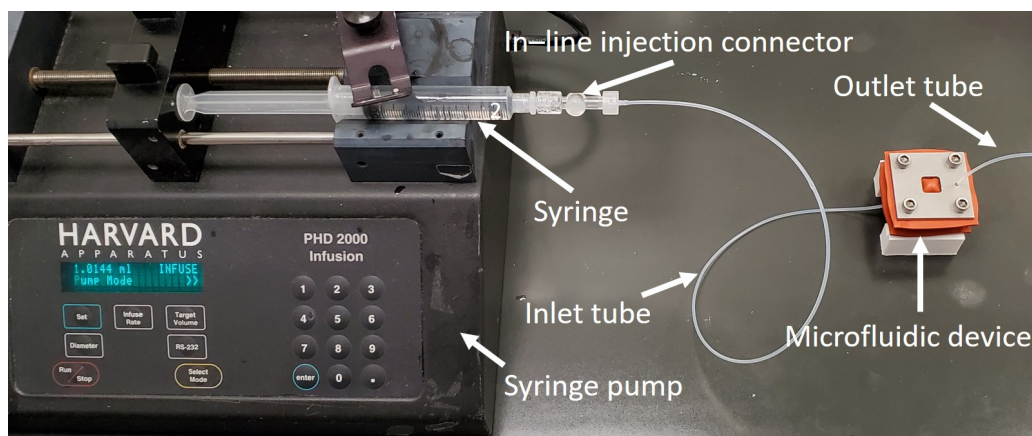


Figure 7.5: A picture of the flow-through experimental setup.

orescent signal from glycerol solution was measured and subtracted. The total particles retained in membranes after flow-through experiments were reported.

### Confocal microscopy

A stock suspension (30  $\mu\text{L}$ ) of 2  $\mu\text{m}$  polystyrene particles (Spherotech, Inc, Lake Forest, IL, USA) was dried to remove the suspending medium. After being completely dried, particles were suspended in 20 mL of canola oil by sonication. Canola oil was chosen as a suspending medium since the refractive index of white SiOC and canola oil are similar so that the *in-situ* observation of particle flow in pores is possible. The ceramic membrane was sliced into a 500  $\mu\text{m}$  thick parallelepiped and assembled into a device as shown in Figure 7.6. The sample was sandwiched between a microscope slide and acrylic plates with Teflon tape to seal. Confocal microscopy images were taken with a Zeiss LSM 710 (Carl Zeiss AG, Germany). The setup for *in-situ* observation is shown in Figure 7.6. During the experiment, the syringe pump was set to a flow rate of 10  $\mu\text{L}/\text{min}$ .

## 7.1.3 Results and discussion

### Flow through experiments

Figure 7.7 shows an SEM image of a dendritic structure in the transverse direction and the corresponding pore size distribution. This membrane was chosen for flow-through experiments since both primary ( $\sim 20 \mu\text{m}$ ) and secondary pore sizes ( $\sim 14 \mu\text{m}$ ) are larger than the particles used in this study. Hence, the capture of particles due to clogging of pores is unlikely. Additionally, the secondary pore volume fraction is sufficiently large so there is ample space for particles to be captured.

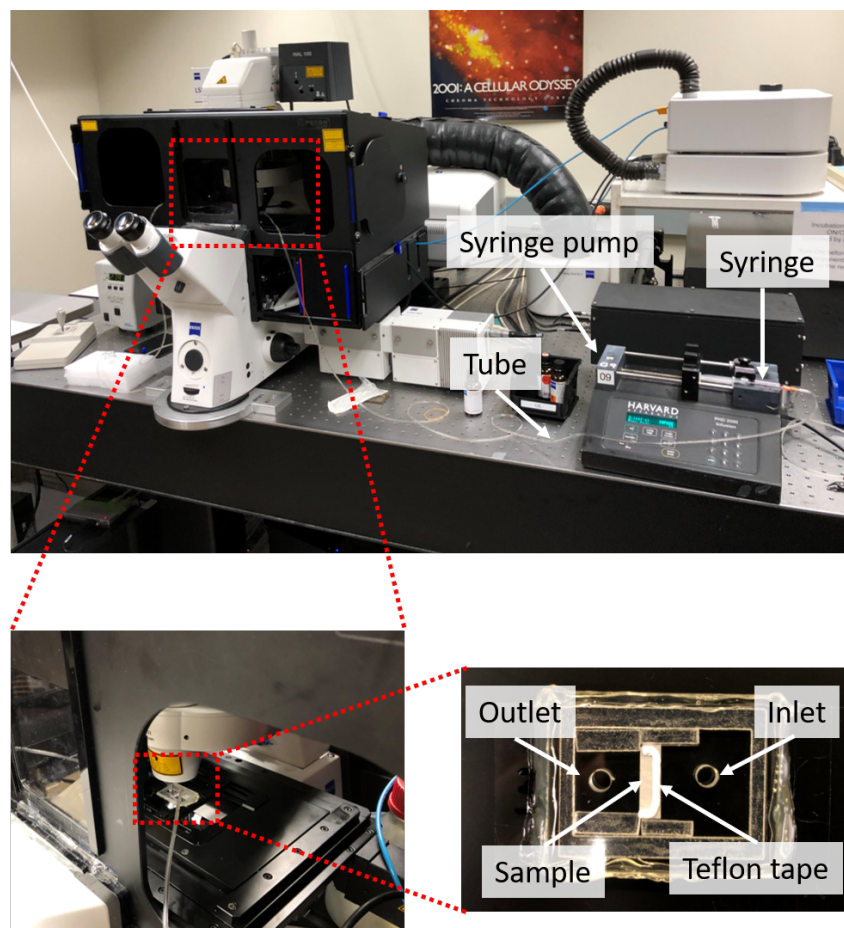


Figure 7.6: A picture of the confocal microscope setup.

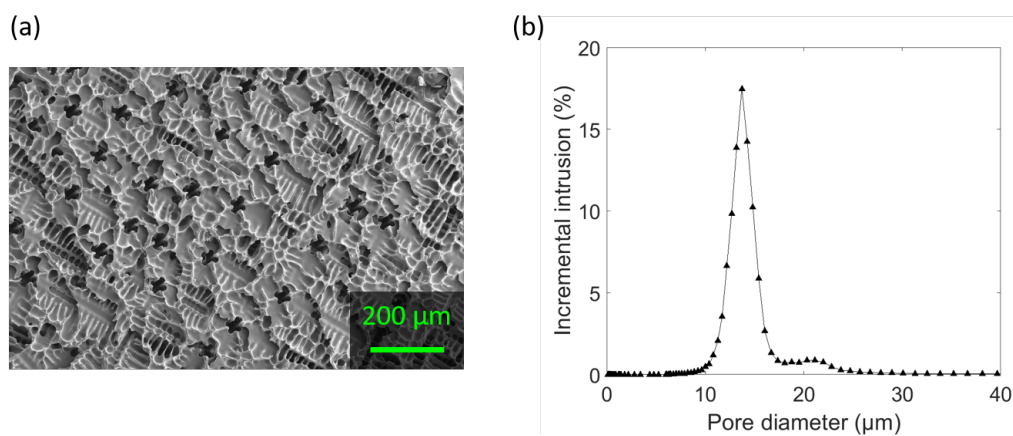


Figure 7.7: An SEM image and pore size distribution of a membrane used in the flow-through study.

The flow-through experiments were conducted by flowing two different size particles ( $0.3 \mu\text{m}$  and  $2 \mu\text{m}$ ) at two different flow rates,  $10 \mu\text{L}/\text{min}$  and  $40 \mu\text{L}/\text{min}$ , and the

Table 7.1: Particles captured in the flow-through experiments.

	10 $\mu\text{L}/\text{min}$		40 $\mu\text{L}/\text{min}$	
	0.3 $\mu\text{m}$	2 $\mu\text{m}$	0.3 $\mu\text{m}$	2 $\mu\text{m}$
Membrane 1	74.7%	57.1%	59.3%	40.7%
Membrane 2	74.7%	81.3%	55.8%	43.9%
Membrane 3	79.4%	72.4%	60.8%	42.6%

results are summarized in Table 7.1. Two important trends can be observed. First, comparing the two different flow rates, a larger number of particles are captured with a slower flow rate (10  $\mu\text{L}/\text{min}$ ). This is not surprising; particles have longer residence time inside membranes, which allows diffusion into the secondary pores. Second, membranes tend to preferentially capture 0.3  $\mu\text{m}$  particles. Although membrane 2 captures more 2  $\mu\text{m}$  than 0.3  $\mu\text{m}$  at 10  $\mu\text{L}/\text{min}$ , all other samples and flow rate show that smaller 0.3  $\mu\text{m}$  particles were captured preferentially. This is consistent with Stokes-Einstein equation:

$$D = \frac{k_B T}{6\pi\eta r}$$

where  $D$  is the diffusion coefficient of spherical particle,  $k_B$  is Boltzmann's constant,  $T$  is the absolute temperature,  $\eta$  is the dynamic viscosity, and  $r$  is the radius of spherical particles. Smaller particles have a higher diffusion coefficient, hence, they are captured by membranes with higher probability.

Although further investigations are necessary to understand discrepancies in capture efficiency, one possible reason is air bubbles in the microfluidic device. Although great care was taken to avoid air bubbles when the membrane was assembled in the microfluidic device, sometimes air bubbles can be trapped in the device. Since the fluorescent particles are hydrophobic and suspended with a surfactant, they could remain at bubble/water interface. In such a case, the capture efficiency would be overestimated.

### Observation of particle flow inside the dendritic pores

In order to confirm if particles are captured by secondary pores, *in-situ* observation of particle flow in dendritic pores was conducted. Although SiOC is black in color

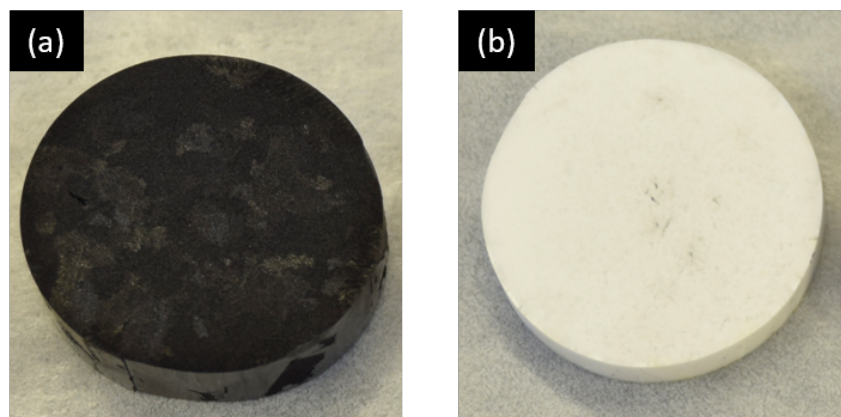


Figure 7.8: Pictures of freeze-cast SiOC pyrolyzed under (a) Ar and (b) Ar with water vapor.

due to the presence of  $sp^2$  carbon, this carbon can be removed by introducing water vapor during the pyrolysis, making the SiOC white in color [11]. Figures 7.8a and b show pictures of freeze-cast SiOC pyrolyzed under argon and argon with water vapor, respectively. As shown, when the preceramic polymer is pyrolyzed in the presence of water vapor, SiOC turned white. This is necessary to observe particle flow inside dendritic pores using the confocal microscope since white SiOC does not absorb light. Thus, by refractive index matching, white SiOC can be transparent as demonstrated in Figure 7.9. It was found that canola oil is a promising working fluid to use in this experiment.

A series of confocal microscope images (left column: overlaid bright field and fluorescent images, right column: fluorescent images) were shown in Figure 7.10. The fluid flow direction is from right to left in the images. This image focuses on the movement of one of the particles, which is indicated by a red arrow in each image. From  $t = 0$  s to  $t = 45$  s, the particle travels along a primary pore. After  $t = 45$ s, the particle was captured by a secondary pore, demonstrating that secondary pores are essential for capturing particles.

### Dual structure

One of the challenges which must be overcome is particle accumulation on the surface of the membrane. The idea of hydrodynamic trapping is to capture small particles (pathogens and platelets) by secondary pores while the large particles (white blood cells and red blood cells) flow through primary pores. Hence, the design of a membrane which allows the majority of particles to enter primary pores is essential

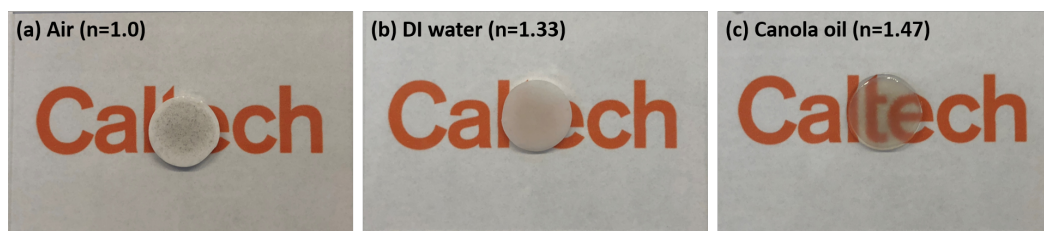


Figure 7.9: Pictures showing SiOC pyrolyzed under Ar and H<sub>2</sub>O atmosphere with pores filled with (a) air, (b) DI water, and (c) canola oil (n: refractive index).

for this concept. Figure 7.11a shows the inlet surface of the dendritic structures after flow-through experiments, and the majority of the surface consists of SiOC walls. This leads to the accumulation of particles on the surface of the membrane as shown in the magnified image (Figure 7.11b). On the other hand, Figure 7.11c shows honeycomb-like structures with smaller areas of SiOC walls. As shown in a magnified image in Figure 7.11d, the amount of particles accumulated on the surface was significantly reduced. This motivated the design of a dual structure, which contains both cellular pores and dendritic pores. This dual structure is possible by controlling the freezing front velocity and temperature gradient afforded by gradient-controlled freeze casting developed in Chapter 3. Figure 7.12a shows a longitudinal image of dual structure revealing ~400  $\mu\text{m}$  of cellular pore region and a large portion of dendritic pores. Figures 7.12b and c show transverse images of the cellular pore region and dendritic pore region, respectively. This structure might be an ideal structure to capture particles of interest by secondary pores. Cellular pores act as funnels so that the majority of particles enter into primary pores. As particles travel along the cellular pore region, they enter into the dendritic pore region where particles are captured by secondary pores. Pore size distribution further confirmed the presence of cellular pores in addition to dendritic pores (Figure 7.12d).

#### 7.1.4 Summary

Dendritic pores were investigated to see if they could be used for size-based filtration. Flow-through experiments demonstrate higher capture efficiency when the fluid flow rate is decreased. Moreover, smaller particles are preferentially captured by dendritic pores. Both results indicate that diffusion is an important mechanism in capturing particles. A slower flow rate provides longer residence time in the membranes to provide sufficient time for particle diffusion into secondary pores. Smaller particles have higher diffusion coefficients so smaller particles diffuse faster to secondary pores. Furthermore, capture of a 2  $\mu\text{m}$  particle by secondary pores is confirmed by



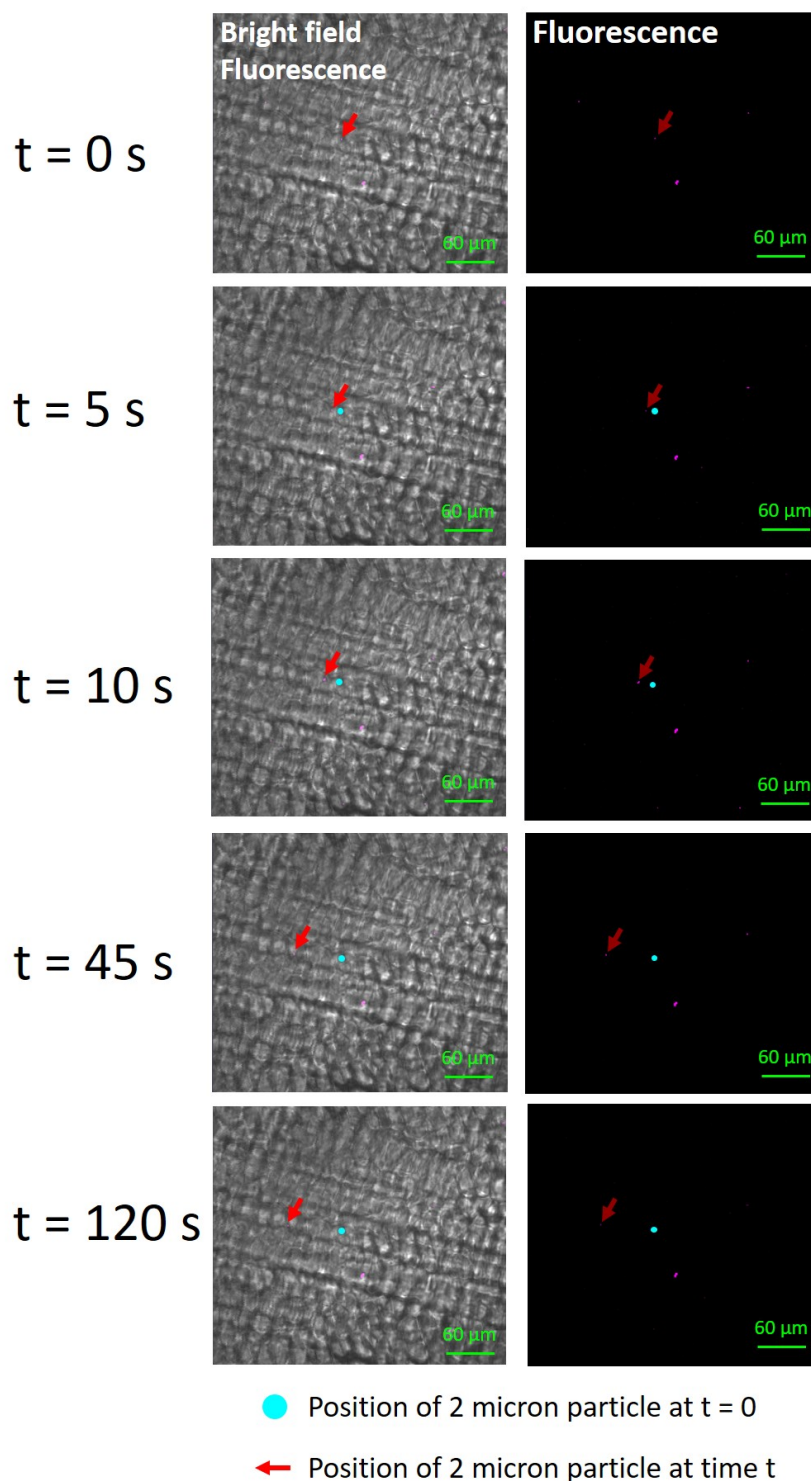


Figure 7.10: Overlay of bright field and fluorescence micrographs from laser scanning confocal microscope. The series of micrographs shows a 2  $\mu$ m particle (indicated by the red arrow) flowing along the main channel and being captured at the side cavity after 45 seconds.

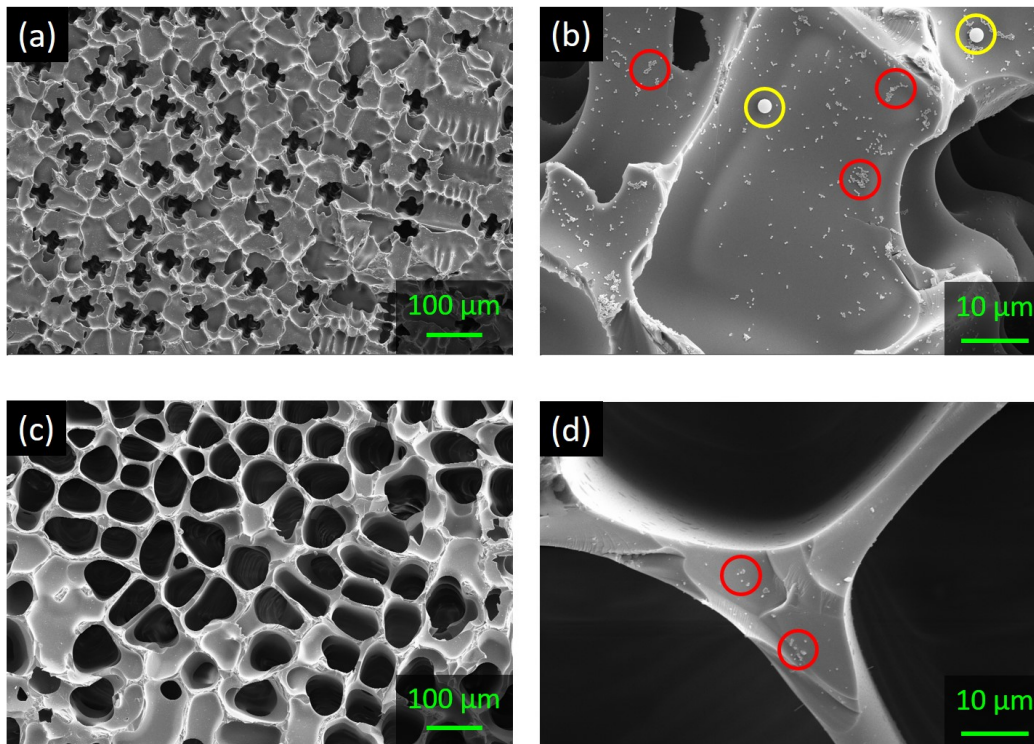


Figure 7.11: SEM images showing transverse direction of dendritic structure after flow-through experiment at (a) low magnification and (b) high magnification. SEM images showing transverse direction of honeycomb-like structure after flow-through experiment at (c) low magnification and (d) high magnification. Some of the 2  $\mu\text{m}$  and a group of the 0.3  $\mu\text{m}$  particles are indicated by yellow and red circles, respectively.

*in-situ* particle flow observation by confocal microscopy. Finally, a dual structure was fabricated to facilitate particle capture in secondary pores by mitigating surface capture.

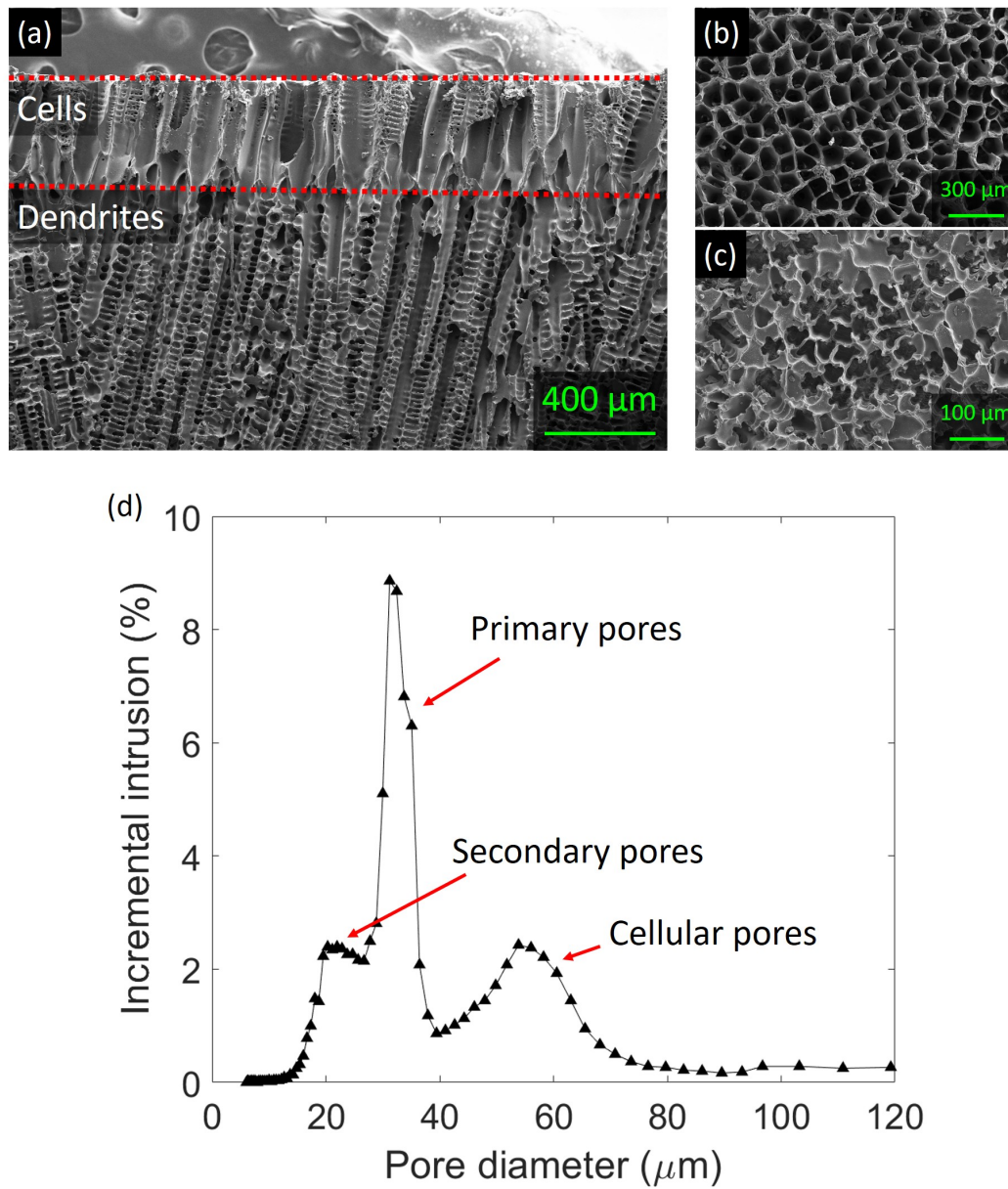


Figure 7.12: SEM images showing (a) longitudinal direction and transverse direction of (b) cellular pore region, and (c) dendritic pore region. (d) Pore size distribution of a dual structure.

## 7.2 Ceramic/polymer composites for membrane chromatography

In the next example, honeycomb-like structures as developed by coarsening described in Chapter 5 will be applied to create ceramic/polymer composites for membrane chromatography.

### 7.2.1 Introduction

The monoclonal antibody (mAb) therapeutic market is fast-growing and is expected to generate revenue of \$300 billion by 2025 [12]. However, the downstream processing such as mAb capture and impurity removal, also known as product polishing, comprised 80% of the manufacturing cost. Membrane chromatography has been receiving attention to replace conventional resin-based column chromatography to reduce the cost, increase throughput, and reduce operating pressure. However, the challenges which current membrane chromatography is facing are: (1) low protein binding capacity and (2) costly pleating steps. Recently, Kotte et al. demonstrated fabrication of mixed matrix polyvinylidene fluoride (PVDF) membranes with embedded polyethylenimine (PEI) particles by in-situ polymerization with phase inversion casting [13]. The significance of this work is that it demonstrates a high binding capacity and selectivity for proteins. The work in this section is built upon this development of PVDF membranes to overcome the challenges of the current commercial membrane chromatography.

In this section, a ceramic/polymer composite is explored to demonstrate the following advantages of the composites. First, by combining phase separation micromolding [14] and *in-situ* polymerization [13], functional polymer microgels can fill the honeycomb-like structures of ceramics, which would allow thicker membranes with uniform thickness. Typically, membrane thickness is limited to several hundred micrometers. As a result, the membrane requires a pleating process to maximize the filtration area within a small volume, and this pleating process needs to be carefully designed to produce optimal filtration performance [15]. However, if a composite can be fabricated with thicker dimensions, it would provide the ability to configure the composite into scalable modules without the pleating process. Additionally, creating polymer membranes with uniform thickness has been a challenge and a focus of research since membrane thickness variations were known to significantly broaden the breakthrough curve (lower binding capacity) [16]. Hence, creating thicker membrane with uniform thickness by phase separation micromolding would be beneficial for improving binding capacity and module configuration. Second, ce-

ramic stiffness will add mechanical integrity to the membranes. This is particularly important since cross-linking density and the type of cross-linker affect mechanical properties of polymeric membranes [17] as well as other functional properties such as adsorption [18]. Hence, if superior mechanical properties of composites are demonstrated, one can then explore and optimize polymer composition for functional properties such as binding capacity while mechanical properties are ensured by the ceramic scaffold.

This section reports two results: (1) successful demonstration of in-situ polymerization with phase separation micromolding in freeze-cast ceramics to create thick membranes and (2) superior mechanical stability of the ceramic/polymer composite during fluid flow.

## **7.2.2 Experimental methods**

### **Fabrication of freeze-cast ceramics**

Freeze-cast ceramics were fabricated using the coarsening process, the details of which can be found in Experimental Methods (Subsection 5.2.1) of Chapter 5. The freeze-cast solution was prepared by dissolving a polysiloxane (Silres® MK Powder) preceramic polymer in cyclohexane with a concentration of 15 or 20 wt.%. A cross-linking agent (Geniosil® GF 91) was added in concentrations of 1 wt.% and stirred for an additional 5 minutes. Subsequently, the polymer solution was degassed for 10 minutes. Next, the solution was quenched to -30°C and coarsened at 4 °C for 1 hour. After sublimation, the freeze-cast preceramic polymer was pyrolyzed at 1100 °C for 4 hours under argon and water vapor unless otherwise mentioned. Water vapor was introduced in the same way as described in Subsection 7.1.2. SiOC has a silanol group [19] and water vapor was introduced to remove carbon and expose more silanol groups on the surface for functionalization of the SiOC. The freeze-cast ceramics were core-drilled into ~13 mm diameter cylinders. A disc with a thickness of 1.5~1.6 mm was sectioned from the midsection by a diamond saw prior to the functionalization with polymers.

### **Functionalization with polymers**

Polyvinylidene fluoride (PVDF; Kynar, Arkema, Inc., Colombes, France) was dissolved in triethyl phosphate (TEP; Sigma Aldrich) at 80 °C. Under nitrogen, polyethylenimine (PEI; Polysciences, Inc., Warrington, PA) dissolved in TEP was added to the PVDF solution. After producing a homogeneous solution, ~500 µL of

concentrated hydrochloric acid (HCl; EMD millipore, Burlington, MA) was added to the solution. After mixing for 15 minutes, a crosslinker, epichlorohydrin (ECH; Sigma Aldrich), was added to the solution. After 4 hours of the cross-linking reaction, 10 mL of TEP was added and the resulting solution was mixed for 30 minutes. This solution is called a dope solution, and its composition is 12.42 wt.% PVDF, 5.39 wt.% PEI, 3.55 wt.% ECH, and 78.64 wt.% TEP. The dope solution was then put under vacuum for 10 minutes in preparation for infiltration into the pores of the functionalized ceramic membranes.

Next, the surfaces of the freeze-cast ceramics were functionalized with amine groups by the following procedures. Freeze-cast ceramics were immersed in concentrated sodium hydroxide (NaOH; Avantor, Radnor, PA) for 90 minutes. After washing freeze-cast ceramics with water, they were incubated in a 0.1 M HCl solution for 30 minutes. The freeze-cast ceramics were washed with water again and dried at 110 °C for 1 hour. Then, they were immersed in a 2 vol.% solution of (3-Aminopropyl)trimethoxysilane (ATMS; Sigma-Aldrich, St. Louis, MO, USA) in isopropanol. After being incubated for 3 hours at 60 °C, the samples were washed with water, and then isopropanol. After washing, they were cured at 110 °C for 30 minutes.

Next, the freeze-cast ceramics were coated with a PEI gel layer using the following procedure. A solution for a gel layer was prepared by mixing 0.78g of PEI and 1.68mL of ECH in 3mL of IPA. The freeze-cast ceramics were immersed in the solution and left in the solution overnight at room temperature to form a PEI gel layer. Finally, dimethyl sulfoxide (DMSO; Sigma Aldrich) was added and heated to 80 °C for 1 hour to remove excess PEI. The sample was then washed with isopropanol and dried at room temperature. One sample was fabricated without a PEI gel layer to show its effect on bonding between the ceramic and the PVDF membrane.

The dried ceramics were placed inside an infiltration device and infiltrated with the dope solution using a syringe pump. During the infiltration, the flow rate of the dope solution was maintained at 100  $\mu$ L/min. To promote cross-linking between the ceramic gel layer and amine groups in the dope solution, the infiltrated samples were heated to 80 °C for 1 hour. Following the incubation, the samples were removed and placed in isopropanol for overnight incubation. The samples were immersed in water to remove trace solvents before characterization and testing.

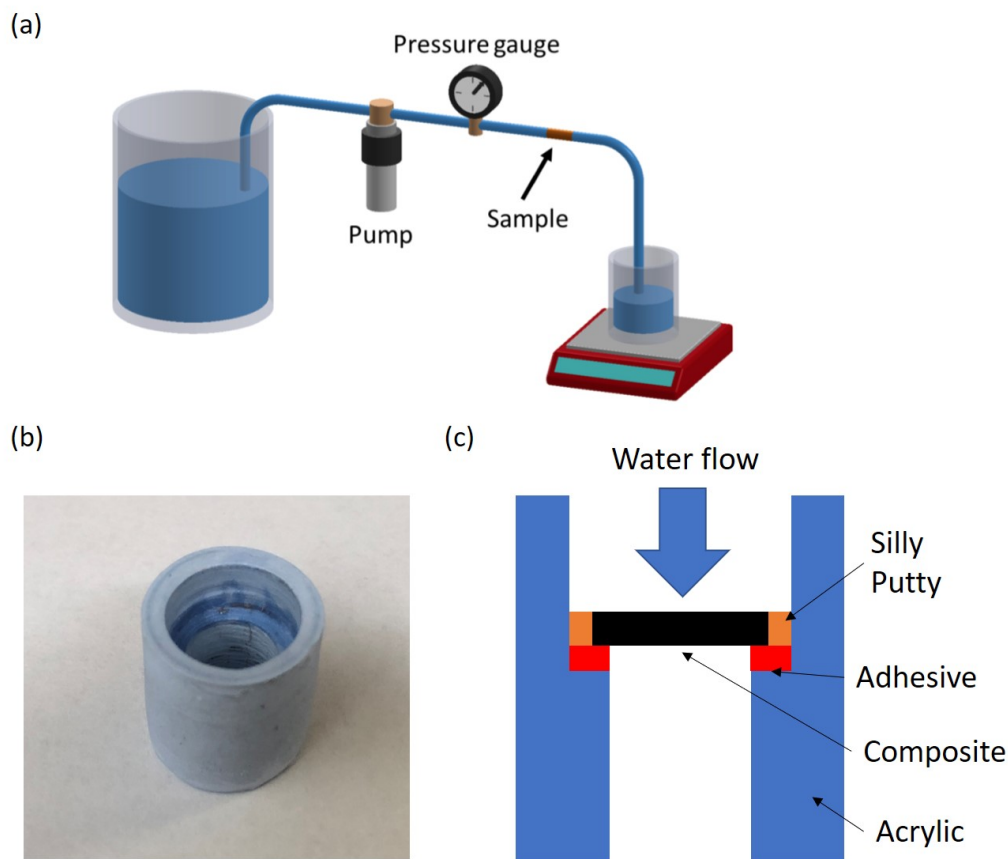


Figure 7.13: A schematic of (a) permeability setup. A figure taken from [20]. (b) A picture of an acrylic fixture. (c) An illustration of side view of the acrylic fixture holding a composite.

### Characterization

The mechanical stability of the composites was characterized by flowing deionized water for 95 minutes using a voltage-controlled pump using the setup shown in Figure 7.13a [20]. Both the pressure drop and water flow rate were measured simultaneously using a pressure transducer and an electronic scale, respectively. Samples were held by acrylic fixture shown in Figure 7.13b. This fixture has an outer diameter of 19mm and inner diameters of 13.8 mm and 10 mm due to the internal step. A schematic illustration of the side view of the acrylic fixture holding the composite is shown in Figure 7.13c. The composite was stuck to the acrylic fixture by adhesives and Silly Putty was filled in the spaces between the composite and acrylic fixture to avoid water leaks. This fixture holding the composite was placed and clamped in the setup.

SEM images of composites were taken in both transverse and longitudinal directions. To image the longitudinal direction, the composites were simply snapped in half and imaged.

### 7.2.3 Results and discussion

#### Ceramic/polymer composites

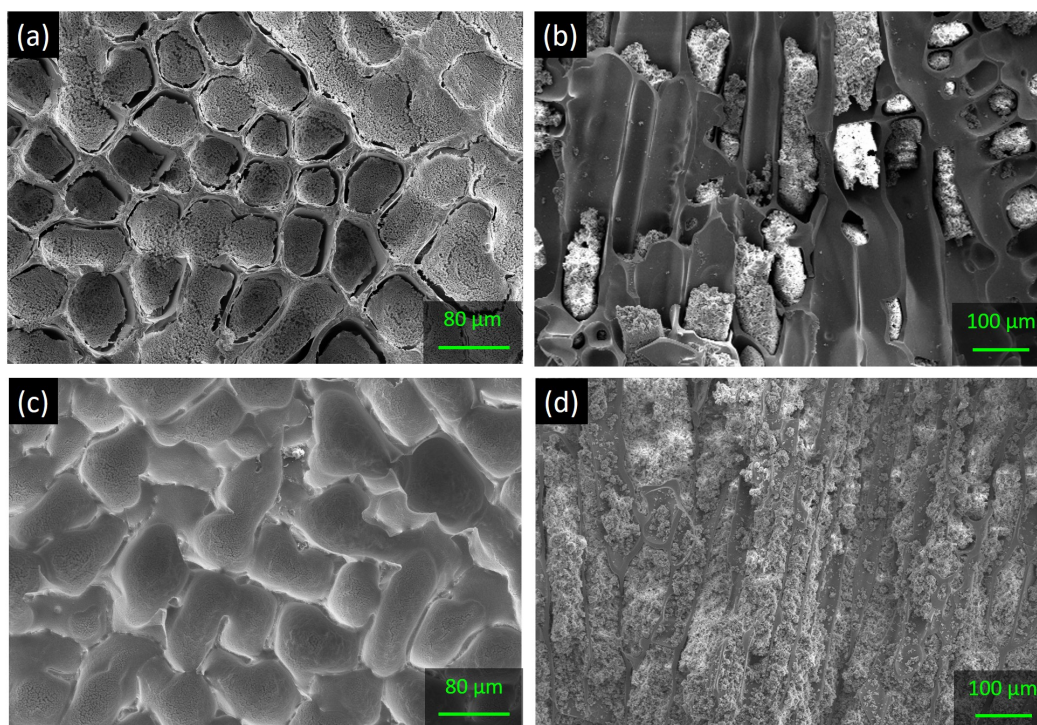


Figure 7.14: SEM images showing a composite without gel layer ((a) transverse and (b) longitudinal direction) and a composite with gel layer ((c) transverse and (d) longitudinal direction)

Figure 7.14 shows SEM images of ceramic/polymer composites and compares the effect of the PEI gel layer on bonding between the ceramic and the mixed matrix PVDF membrane, referred to here as a microgel. Figures 7.14a and b show a composite fabricated without PEI gel layer between ceramics and the microgel in transverse and longitudinal directions. The bonding between the ceramics and the microgel is poor and transverse image show debonded regions. This debonding is likely due to the shrinkage of the microgel during the drying process prior to SEM imaging. The resulting stress by the shrinkage caused the microgel to peel off from the ceramic. The longitudinal image also shows evidence of poor bonding. The microgel had peeled off from the ceramic walls, probably caused by the fracture of a



composite for imaging purposes. In contrast, Figure 7.14c and d show a composite with PEI gel layer between the ceramics along with the microgel, and demonstrate enhanced bonding in both transverse and longitudinal directions. A significant difference can be seen in the longitudinal direction. When the PEI gel layer is present, the microgel is torn rather than peeled from the ceramic walls as shown in Figure 7.14d. Hence, the PEI gel layer helps to hold the microgel and the ceramic together and prevents the microgel from peeling off.

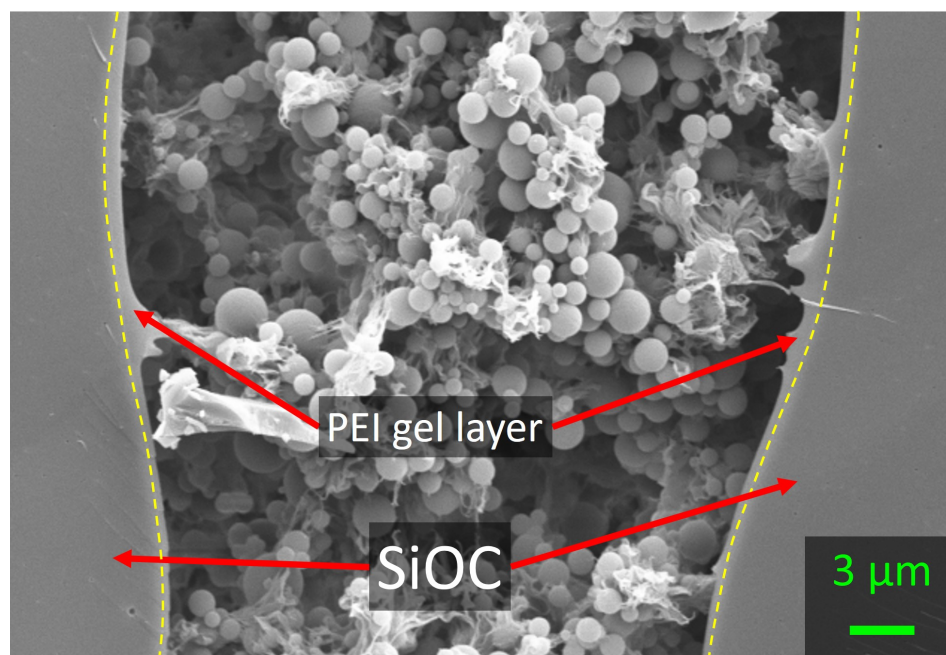


Figure 7.15: An SEM image showing a PVDF membrane, PEI gel layer, and SiOC wall. Yellow dashed lines indicate boundaries between a gel layer and SiOC wall.

Figure 7.15 shows a magnified image of one of the fabricated composites, which demonstrates characteristic features of the PVDF membrane with embedded PEI particles, consistent with those reported by Kotte et al. on the same composition [13]. The structure contains a matrix of PVDF spherulites with a fibrous texture. This image proves that in-situ polymerization and phase separation micromolding inside the honeycomb-like structure of ceramics was successful. The microgel is bonded to a thin layer of PEI gel, which adheres to the SiOC wall. The yellow dashed lines in the figure indicate the boundary between the PEI gel layer and ceramic walls. The PEI gel layer is effective at holding the ceramic and the microgel together due to a sufficient amount of amine groups to bond functionalized amine-terminated ceramics and PEI particles of PVDF membrane through the cross-linker, ECH.

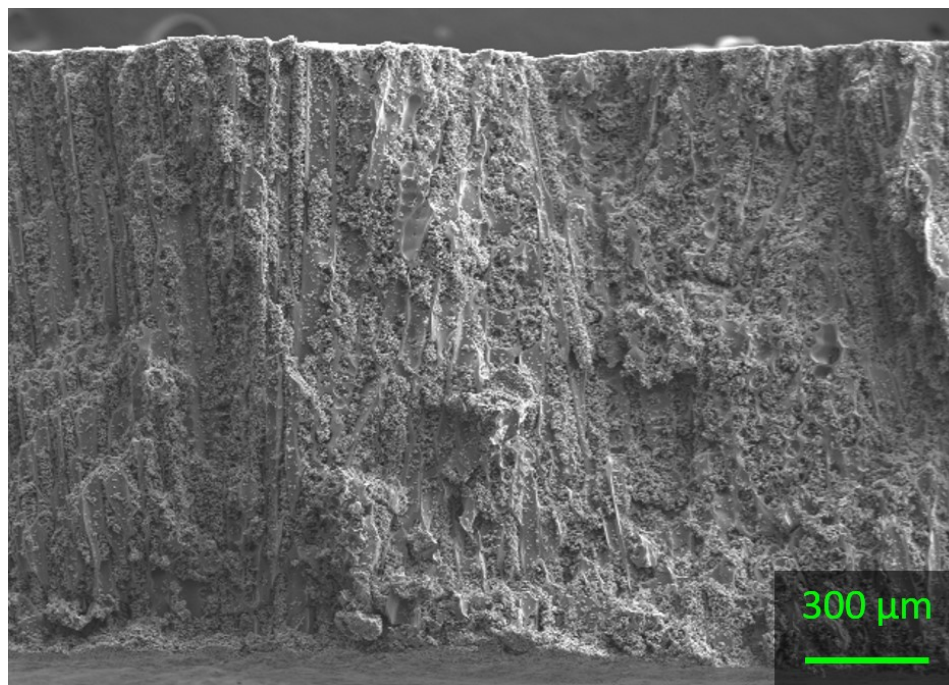


Figure 7.16: An SEM image showing a thickness of around 1.5 mm composite.

Figure 7.16 shows a composite with a thickness of  $\sim 1.5$  mm. (This ceramic scaffold was pyrolyzed without the presence of water vapor.) As demonstrated, *in-situ* polymerization with phase separation micromolding was successfully used to create a ceramic/polymer composite thicker than conventional polymeric membrane with uniform thickness.

### **Mechanical stability during fluid flow**

The mechanical stability of the composite was characterized by flowing water for 95 minutes through the composite membrane. Figure 7.17a shows water flux and pressure drop as a function of time. During the experiment, the pressure drop remained between 1 and 1.2 bar and measured water flux is around  $2200 \text{ Lh}^{-1} \text{ m}^{-2}$ . In contrast, Figure 7.17b shows the water flux measurement of the PVDF membrane at a different pressure by Kotte et al. [13]. Although the porous structure by Kotte et al. and resulting transport properties are different from the ones of the current study, the microgels in both studies were made with the same materials and composition. Hence, these data can be used to compare mechanical stability (Figure 7.17a). The composite in this study is shown to have superior mechanical stability to the PVDF membrane by Kotte et al. For the PVDF membrane, after 45 minutes of flowing water at 1 bar, the water flux decreased by roughly 21% due to the compaction of

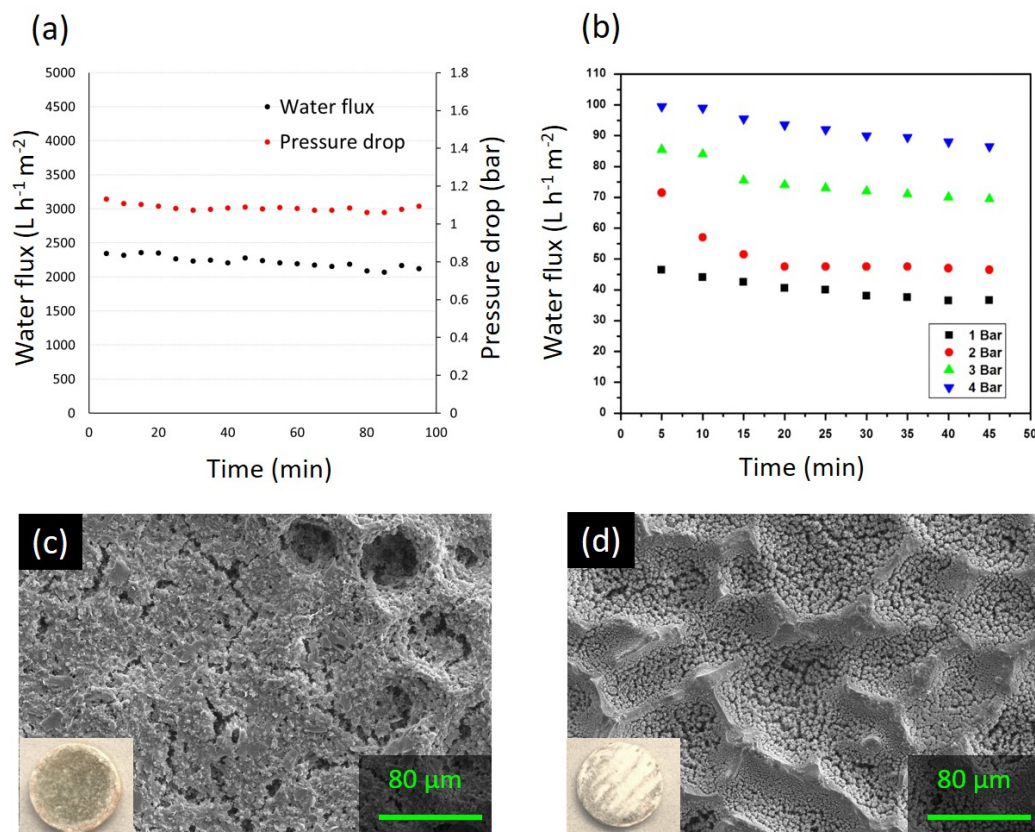


Figure 7.17: A plot of (a) water flux and pressure drop as a function of time. (b) Water flux at different pressure drops as a function of time (from the study by Kotte et al. [13]). This figure is reproduced with permission. SEM images of (c) inlet and (d) outlet side after permeability measurement with sample pictures as insets.

PVDF membrane. In contrast, there is only a 5% drop of water flux in 45 minutes for the composite. The experiment was maintained for more than 90 minutes and the total water flux drop reached only 10%. This demonstrates that the ceramic scaffold prevented compaction, which resulted in more stable water flux. After the water flux measurement, the inlet and outlet sides of a composite were imaged by SEM (Figures 7.17c and d) to check if the microgels were still held by the ceramics. For both sides, the microgel still remained within the ceramics scaffold, indicative of robust bonding between ceramics and the microgels. The picture of the inlet side shows a gray color possibly due to contaminants from the permeability setup (inset image of Figure 7.17c), as confirmed by the SEM image. Although it is still possible that compaction of microgels might take place in the composite, it is likely that the water flux drop in the composite is due to clogging of pores by these contaminants. Hence, the ceramic scaffold provides mechanical stability during fluid flow, and this

superior mechanical property would allow this composite to be used in conditions where other polymeric membranes might collapse or fail.

#### 7.2.4 Summary

Ceramic/polymer composites were successfully created by in-situ polymerization with phase separation micromolding in freeze-cast pore structures. Composite membranes, 1.5 to 1.6 mm thick, were produced with characteristic features of PVDF membranes reported by Kotte et al. [13]. The PEI gel layer between the microgel and ceramic walls were necessary to ensure the robust bonding between the ceramics and the microgel. The mechanical stability of composites was demonstrated by flowing water for 95 minutes. The water flux drop of the composite remained lower than the polymer-only membrane, which implies that the composite can be used in conditions where the polymer-only membrane will collapse or fail.

#### References

- [1] Niranjana Kissoon. *Sepsis*. URL: <http://www.wfpiccs.org/projects/sepsis-initiative/>.
- [2] Nils G. Morgenthaler and Markus Kostrzewa. "Rapid identification of pathogens in positive blood culture of patients with sepsis: review and meta-analysis of the performance of the sepsityper kit". In: *International journal of microbiology* 2015 (2015).
- [3] Arash Afshari et al. "Bench-to-bedside review: Rapid molecular diagnostics for bloodstream infection—a new frontier?" In: *Critical care* 16.3 (2012), p. 222.
- [4] Travis S. Schlappi et al. "Flow-through capture and in situ amplification can enable rapid detection of a few single molecules of nucleic acids from several milliliters of solution". In: *Analytical chemistry* 88.15 (2016), pp. 7647–7653.
- [5] Nathan G. Schoepp et al. "Rapid pathogen-specific phenotypic antibiotic susceptibility testing using digital LAMP quantification in clinical samples". In: *Science Translational Medicine* 9.410 (2017), eaal3693.
- [6] Justin C. Rolando et al. "Real-time, digital lamp with commercial microfluidic chips reveals the interplay of efficiency, speed, and background amplification as a function of reaction temperature and time". In: *Analytical chemistry* 91.1 (2018), pp. 1034–1042.
- [7] Muhammad Asim Faridi et al. "Elasto-inertial microfluidics for bacteria separation from whole blood for sepsis diagnostics". In: *Journal of nanobiotechnology* 15.1 (2017), p. 3.

- [8] Soojung Claire Hur, Albert J. Mach, and Dino Di Carlo. “High-throughput size-based rare cell enrichment using microscale vortices”. In: *Biomicrofluidics* 5.2 (2011), p. 022206.
- [9] Vivian O’Brien. “Closed streamlines associated with channel flow over a cavity”. In: *The Physics of Fluids* 15.12 (1972), pp. 2089–2097.
- [10] C Shen and JM Floryan. “Low Reynolds number flow over cavities”. In: *The Physics of fluids* 28.11 (1985), pp. 3191–3202.
- [11] Tian Liang et al. “Silicon oxycarbide ceramics with reduced carbon by pyrolysis of polysiloxanes in water vapor”. In: *Journal of the European Ceramic Society* 30.12 (2010), pp. 2677–2682.
- [12] Ruei-Min Lu et al. “Development of therapeutic antibodies for the treatment of diseases”. In: *Journal of biomedical science* 27.1 (2020), pp. 1–30.
- [13] Madhusudhana Rao Kotte, Manki Cho, and Mamadou S. Diallo. “A facile route to the preparation of mixed matrix polyvinylidene fluoride membranes with in-situ generated polyethyleneimine particles”. In: *Journal of membrane science* 450 (2014), pp. 93–102.
- [14] Laura Vogelaar et al. “Phase separation micromolding: a new generic approach for microstructuring various materials”. In: *Small* 1.6 (2005), pp. 645–655.
- [15] A.I. Brown et al. “Membrane pleating effects in 0.2  $\mu\text{m}$  rated microfiltration cartridges”. In: *Journal of Membrane Science* 341.1-2 (2009), pp. 76–83.
- [16] Raja Ghosh. “Protein separation using membrane chromatography: opportunities and challenges”. In: *Journal of Chromatography A* 952.1-2 (2002), pp. 13–27.
- [17] Kuen Yong Lee et al. “Controlling mechanical and swelling properties of alginate hydrogels independently by cross-linker type and cross-linking density”. In: *Macromolecules* 33.11 (2000), pp. 4291–4294.
- [18] Maria P. Tsyurupa et al. “Physicochemical and adsorption properties of hypercross-linked polystyrene with ultimate cross-linking density”. In: *Journal of separation science* 37.7 (2014), pp. 803–810.
- [19] Aitana Tamayo et al. “Mesoporous silicon oxycarbide materials for controlled drug delivery systems”. In: *Chemical Engineering Journal* 280 (2015), pp. 165–174.
- [20] Maninpat Naviroj. “Silicon-based porous ceramics via freeze casting of pre-ceramic polymers”. PhD thesis. Northwestern University, 2017.

## SUMMARY AND FUTURE WORK

### **8.1 Summary and conclusions**

Directional freeze casting was investigated from the standpoint of alloy solidification principles. The growth and time evolution of dendrites were studied to control pore morphology and size. Pore controls through established solidification parameters led to pore structure designs for applications such as robust shape-memory ceramics and pharmaceutical filtration.

Although freezing front velocity had been a major solidification parameter to control pores in freeze casting, temperature gradient had often been neglected. Through gradient-controlled freeze casting, both temperature gradient and freezing front velocity were controlled independently and the resultant dendritic pore structures were investigated. While freezing front velocity changed primary pore size, temperature gradient did not significantly change primary pore size, but rather, primary pore spacing. In contrast, secondary pore sizes were found to depend on cooling rate, the product of freezing front velocity and temperature gradient. As the freezing front velocity was decreased at a constant temperature gradient, secondary pores began to disappear and the freeze-cast microstructure evolved to a honeycomb-like structure, indicating the transition from dendrites to cells. As demonstrated by the stability criterion for planar solidification front, the transition to cellular crystals were not only determined by solidification parameters but also by other variables such as the concentration of the preceramic polymer. It was shown that dendritic pores further turned into honeycomb-like structures by reducing the concentration of preceramic polymer. These observations were consistent with the solidification principles of alloys. In addition to controllable solidification parameters, effects of a ubiquitous external force, gravity, was investigated. It was found that gravity-induced convection reduced the degree of constitutional supercooling in the liquid phase and yielded long-range cellular pores ( $\sim 2$  mm of cellular pores).

Although dendrite size and morphology were manipulated by dendrite growth conditions, post-crystal growth processing also significantly were found to impact the dendritic structures. Thus, coarsening of dendrites and resulting pore structure were investigated. Two important results were reported. First, primary pore size and

secondary pore size were found to depend on the cube root of coarsening time. Second, when the dendrites were coarsened at the temperature close to the liquidus temperature of the solution, the pore structure evolved to honeycomb-like structures. Both findings agreed well with the observation in alloy systems. Tomography-based analysis on curvature of dendritic pores aided the understanding of the coarsening mechanisms. Interfacial shape distributions (ISDs) and interfacial normal distributions (INDs) were used to quantitatively define the shape and directionality of dendritic pores, respectively, and confirmed similar coarsening behavior as alloy systems.

The above studies provided foundations for pore designs to create freeze-cast ceramics for specific applications. The first example was porous shape memory ceramic. The pore structures were designed and fabricated such that the structure was a mechanically robust honeycomb structure and, most importantly, the wall thickness was comparable to grain size to mitigate intergranular cracking during the martensitic phase transformation. The structure was sustained through the martensitic phase transformation as well as the accompanying deformation. While this was an example of improving functional properties by microstructural engineering of material spaces, other explored applications focused on unique pore space. A dendritic structure with tailorable primary and secondary pore sizes was examined for filtration of pathogens in the bloodstream. Particle capture by secondary pores were demonstrated. Flow-through experiments showed that particle capture efficiency improves with decreasing the flow rate due to the longer residence time for diffusing into secondary pores. In addition, smaller particles diffused faster to secondary pores, and hence, were captured with higher probability. In-situ observation by confocal microscopy confirmed particle capture by secondary pores. These results demonstrated a potential application of dendritic pores as size-based filtration. Finally, honeycomb-like structures were filled with functional microgels for membrane chromatography. Ceramic scaffolds for infiltration provided a template for thicker membranes with uniform thickness, which had been a challenge in conventional polymeric membrane fabrication. This design would potentially eliminate a costly pleating step for polymer-only membranes and offer an opportunity to readily configure scalable membrane modules. Additionally, ceramics added mechanical stability during the fluid flow, which might broaden operating conditions where polymeric membranes might collapse or fail.

## 8.2 Suggestions for Future work

### 8.2.1 Different solvent systems

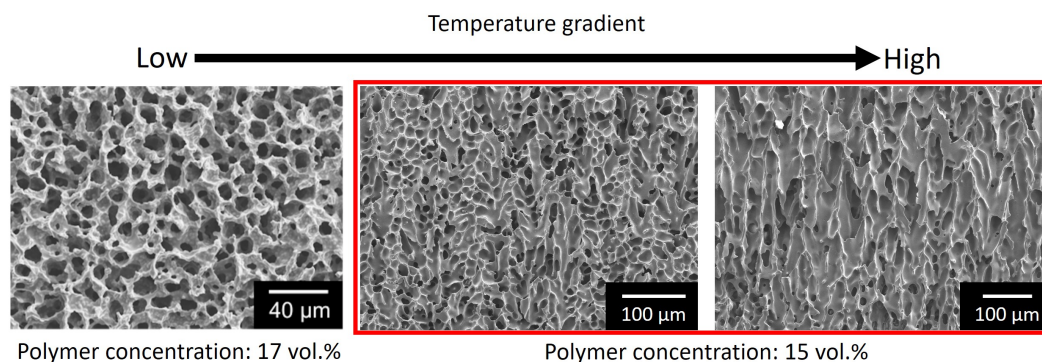


Figure 8.1: SEM images of freeze-cast structures using cyclooctane as a solvent in longitudinal direction. As the higher temperature gradient is applied, the directionality of pores improved. Left image is taken from a study by Naviroj et al. [1]

In this work, effects of temperature gradient and coarsening process in solution-based freeze casting were studied in detail. However, only cyclohexane was studied as a solvent, and there are other solvents which produce seaweed structures, lamellar structures, and highly anisotropic, two-dimensional dendritic structures [1] which deserve attention. Figure 8.1 shows freeze-cast structures templated by cyclooctane crystals. Cyclooctane-based microstructure is seaweed-like [2] and the resulting ceramic microstructure is isotropic and non-directional, as shown in the left image. However, as the higher temperature gradient is applied, pore directionality is improved (the middle and right images were freeze-cast with a slightly lower preceramic polymer concentration than the one from the left image).

### 8.2.2 Rheology

Rheology is another important parameter in solution-based freeze casting. In suspension-based freeze casting, changing viscosity requires additives or higher solid loading. However, in solution-based freeze casting, rheology can be controlled by changing the molecular weight of preceramic polymers through chemical cross-linking or thermal cross-linking. This gives further control in pore structure and material property, and should be studied further.



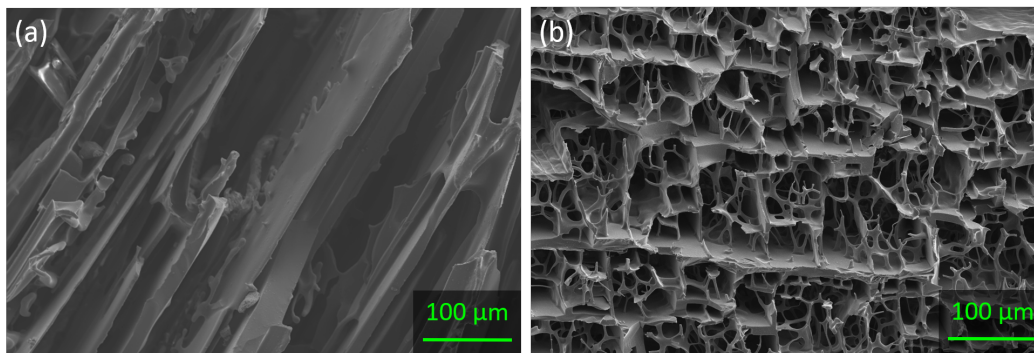


Figure 8.2: SEM images showing freeze-cast lamellar structures with (a) 5 minutes and (b) 6 hours of stirring after adding the cross-linking agent.

### Enhanced mechanical properties

In most freeze-casting studies, the preceramic polymer solution is directionally frozen right after a cross-linking agent is added. Figure 8.2 shows SEM images of freeze-cast lamellar structures from dimethyl carbonate. Although they are freeze-cast from the same solvent and preceramic polymer, they exhibit significantly different morphologies due to the different cross-linking time, the time the solution had been stirring after addition of the cross-linking agent. Figure 8.2a shows a typical lamellar structure which was fabricated after five minutes of cross-linking time. In contrast, Figure 8.2b shows a porous structure after six hours of cross-linking time. This porous structure has bridges between lamellar walls. Although bridges are effective at enhancing the mechanical properties of lamellar structures, the mechanism by which bridge formation occurs is unknown. Further investigations are required to elucidate this morphology change. In addition, it would be interesting to explore how viscosity affects different porous structures, such as dendritic and isotropic-like structures, and the resultant mechanical and transport properties.

### Precise control of pore structure

As shown in Chapter 3, the stability criterion for stable planar front can be expressed as follows:

$$\frac{G}{v} = \frac{m}{D} \frac{k_0 - 1}{k_0} C_0 .$$

In most examples of freeze-casting of preceramic polymers, a cross-linking agent is added prior to solidification. Once the cross-linking agent is added, the cross-linking

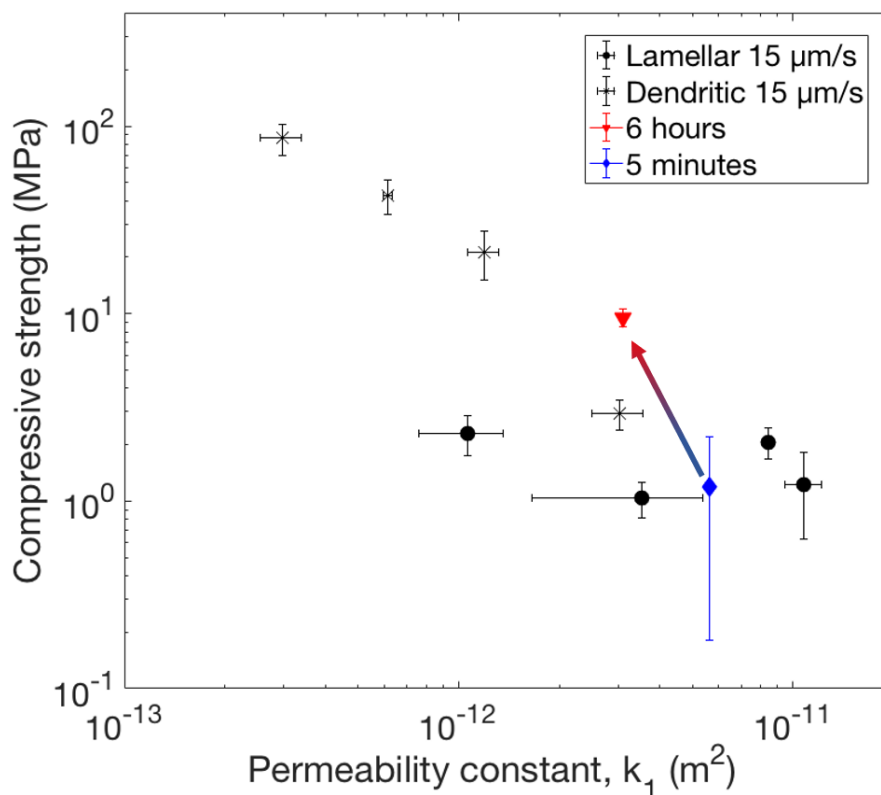


Figure 8.3: Compressive strength and permeability constants of different structures. Data for "Lamellar 15  $\mu m/s$ " and "Dendritic 15  $\mu m/s$ " are taken from the work by Naviroj [2].

process starts and increases the molecular weight of preceramic polymer, resulting in a change in the diffusion coefficient,  $D$ , as a function of time. This is one of the reasons why it is challenging to achieve cellular pores in solution-based freeze casting because the stability criterion becomes more stringent as the time proceeds (Figure 8.4).

However, recent developments of photopolymerization-assisted freeze casting [3] enables the precise control of the diffusion coefficient. With this photopolymerization route, one can start with desired molecular weight of the polymer or viscosity of solution, freeze-cast the solution with fixed rheological properties of the solution, and then cross-link after solidification to ensure the integrity of the sample for pyrolysis. With photopolymerization and gradient-controlled freeze casting, freezing front velocity, temperature gradient and diffusion coefficient can be independently controlled, which allows to fine-tuning of the porous structure. Hence, it would be interesting to investigate how primary pore spacing, primary pore size and

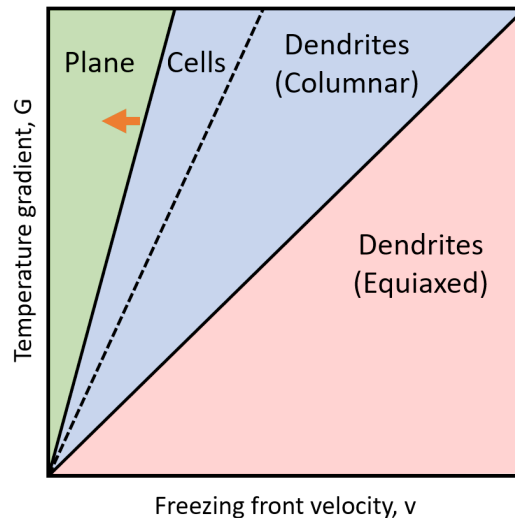


Figure 8.4: A stability-microstructure map with an arrow indicating an increase of diffusion coefficient results in change in stability criterion.

secondary pore size change with the diffusion coefficient of preceramic polymers. Additionally, one can explore how conditions for cellular growth can be altered with a change of diffusion coefficient.

### 8.2.3 Porous shape-memory zirconia with precise dopant control

In Chapter 6, it was demonstrated that improved shape-memory properties were possible by making honeycomb structures. However, the suspension contains both zirconium oxide (zirconia) and cerium oxide (ceria) were mixed by ball-milling. Because there are two different materials in suspension, one of them might sediment faster during the directional solidification, leading to a variation in composition. As demonstrated by Pang et al., the transformation-induced cracking can be mitigated by tuning the composition of  $ZrO_2$ - $CeO_2$  by manipulating the crystallographic phase compatibility [4]. In their study, it was shown that a variation in composition as small as 0.5 mol.% could have significant impact on crack-resistance properties. Hence, preparing pre-doped powders [5] and freeze-casting them would be ideal to avoid composition variation within samples, and warrants exploration.

### References

- [1] Maninpat Naviroj, Peter W. Voorhees, and Katherine T. Faber. "Suspension- and solution-based freeze casting for porous ceramics". In: *Journal of Materials Research* 32.17 (2017), pp. 3372–3382.

- [2] Maninpat Naviroj. “Silicon-based porous ceramics via freeze casting of pre-ceramic polymers”. PhD thesis. Northwestern University, 2017.
- [3] Richard Obmann et al. “Porous polysilazane-derived ceramic structures generated through photopolymerization-assisted solidification templating”. In: *Journal of the European Ceramic Society* 39.4 (2019), pp. 838–845.
- [4] Edward L. Pang, Caitlin A. McCandler, and Christopher A. Schuh. “Reduced cracking in polycrystalline ZrO<sub>2</sub>-CeO<sub>2</sub> shape-memory ceramics by meeting the cofactor conditions”. In: *Acta Materialia* 177 (2019), pp. 230–239.
- [5] A.L. Quinelato et al. “Synthesis and sintering of ZrO<sub>2</sub>-CeO<sub>2</sub> powder by use of polymeric precursor based on Pechini process”. In: *Journal of Materials Science* 36.15 (2001), pp. 3825–3830.

## HIERARCHICAL PORE STRUCTURE

This chapter is based on the work from the journal article, "Hierarchical porous ceramics via two-stage freeze casting of preceramic polymers," by N. Arai, and K.T. Faber. This article has been published in *Scripta Materialia*.

Arai N., and Faber K. T. Hierarchical porous ceramics via two-stage freeze casting of preceramic polymers. *Scripta Materialia*. 2019;162:72–76. <https://doi.org/10.1016/j.scriptamat.2018.10.037>

### **A.1 Introduction**

Recently, solution-based freeze casting of preceramic polymers have demonstrated advantages over suspension-based freeze casting with more precise control over the freezing process due to the homogeneity and transparency of solutions [1, 2, 3]. During freezing, phase separation between the solvent and preceramic polymer occurs, analogous to suspension-based freeze casting, followed by sublimation of the solvent, and pyrolysis of the preceramic polymer for conversion to the ceramics. Zhang et al. demonstrated that freeze-cast silicon oxycarbide (SiOC) has suitable anisotropic thermal properties for cryogenic wicking for space applications [4]. While both suspension- and solution-based freeze-cast solids have desirable porous microstructures, enhancing the mechanical properties is also of great importance.

Various studies have reported improved strength of freeze-cast ceramics by reducing pore size [5] and tuning the sintering temperature [6]. Another approach is to create ceramic bridges between lamellae [7, 8, 9], which enhance the compressive strength by limiting Euler buckling and crack propagation parallel to lamellae. Porter et al. found changes in viscosity or pH influence the number of bridges and improve compressive strength [8]. Work by Munch et al. demonstrated that additives such as trehalose and sucrose changed interfacial tension and interparticle forces, creating bridges [7]. Another method by Ghosh et al. mixed large anisotropic ceramic platelets with small isotropic ceramic particles, and engulfed ceramic platelets resulted in interlamellar bridges that improved compressive strength and stiffness [9]. It is important to note that all the bridge formation methods mentioned here were developed for suspension-based freeze casting and, to the best of our knowledge,

comparable methods for solution-based freeze casting have not been explored. In addition, among various pore morphologies, lamellar pores are of greatest interest since they inherently possess high permeability and their highly anisotropic pore structure results in anisotropic thermal properties which are useful in applications such as insulation or cryogenic wicking [2,8][10, 4]. A recent study in solution-based freeze casting by Naviroj showed that lamellar pore structures possess high permeability, but low compressive strength ranging from around 0.5 MPa to 3 MPa [11], motivating this study to improve strength while maintaining high permeability by solution-based freeze casting.

In this chapter, two-stage freeze casting is explored to create a second set of lamellae bridges between (and perpendicular to) lamellae in a hierarchical fashion by solution-based freeze casting. In two-stage freeze casting, after freezing the solution and freeze drying, a porous polymer green body is infiltrated with a second polymer solution and frozen along the same direction with the aims to create a lamellar pore structure in the first step and to form bridges between lamellar walls in the second. Bridge formation is investigated by scanning electron microscopy (SEM) and image analysis, and its effect on compressive strength and permeability is also studied.

## A.2 Experimental methods

### A.2.1 Two-stage freeze casting

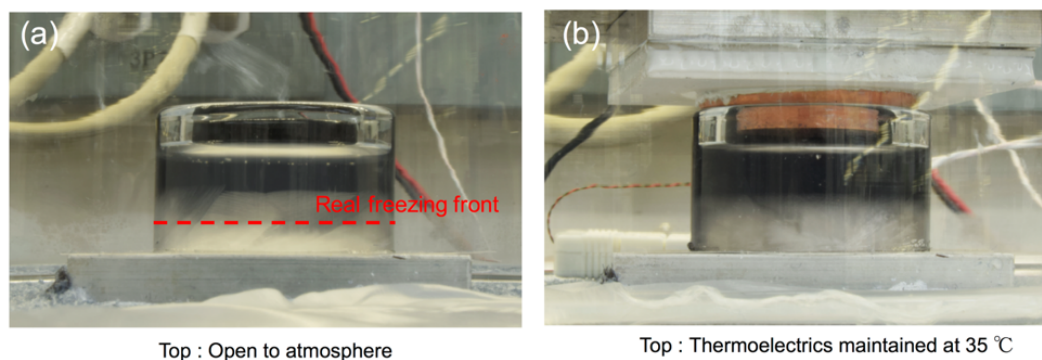


Figure A.1: Freezing solution by (a) conventional unidirectional freezing and (b) conventional conditions coupled with mold heating.

A polymer solution is prepared by dissolving preceramic polymer, polymethylsiloxane (Silres®MK Powder, Wacker Chemie, CH<sub>3</sub>-SiO<sub>1.5</sub>, Munich, Germany), in dimethyl carbonate (DMC) (Sigma-Aldrich, St. Louis, MO, USA), followed by the addition of 1 wt.% of a cross-linking agent (Geniosil®GF 91, Wacker Chemie, Munich, Germany). The polymer solution was degassed at ~30 kPa for 5 minutes

to avoid air bubbles during freezing. In the first stage of two-stage freeze casting, a solution with 20 vol.% polymethylsiloxane was poured into a cylindrical glass mold ( $h = 20$  mm;  $\phi = 25$  mm) placed on a PID-controlled thermoelectric plate which was continuously cooled by silicone oil recirculated in a heat sink. In addition, another thermoelectric plate was placed on top of the glass mold and maintained at  $35$  °C to avoid crystal growth along the mold and achieve unidirectional solidification (designated as mold heating, Figure A.1). Freezing front velocity was adjusted to be in the range of 12-14  $\mu\text{m/s}$  to keep pore sizes homogeneous within the samples [12]. Once frozen, the samples were moved to a freeze drier (VirTis AdVantage 2.0, SP Scientific, Warminster, PA, USA) where the solvents were completely sublimated at  $\sim 25$  Pa. Subsequently, the samples were cured at  $200$  °C in air. In the second stage, the cured green body was infiltrated with another solution with 5 vol.%, 7.5 vol.% or 10 vol.% of polymethylsiloxane by using vacuum. Samples were frozen in the same direction as in the first stage, and the same cooling profiles (12-14  $\mu\text{m/s}$ ) were maintained. After sublimation, the green body was pyrolyzed at  $1100$  °C in Argon for 4 hours with a ramp rate of  $2$  °C/min to convert polymethylsiloxane into SiOC. Control samples were also prepared by the same first-stage process as above, but pyrolysis followed instead of curing; this process is referred to as single-stage freeze casting in this paper. Polymer concentrations with 20 vol.%, 25 vol.%, and 30 vol.% for single-stage freeze casting were selected. Porosity of the samples was determined using the Archimedes method. The average porosity of all samples are summarized in Table A.1.

Table A.1: Average porosity of single-stage freeze-cast samples and two-stage freeze-cast samples.

	Polymer concentration	Average porosity (%)
Single-stage freeze casting	20 vol.%	75
	25 vol.%	69
	30 vol.%	63
	Second stage polymer concentration	Average porosity (%)
Two-stage freeze casting	5 vol.%	70
	7.5 vol.%	67
	10 vol.%	65

### A.3 Results and discussion

#### A.3.1 Two-stage freeze casting

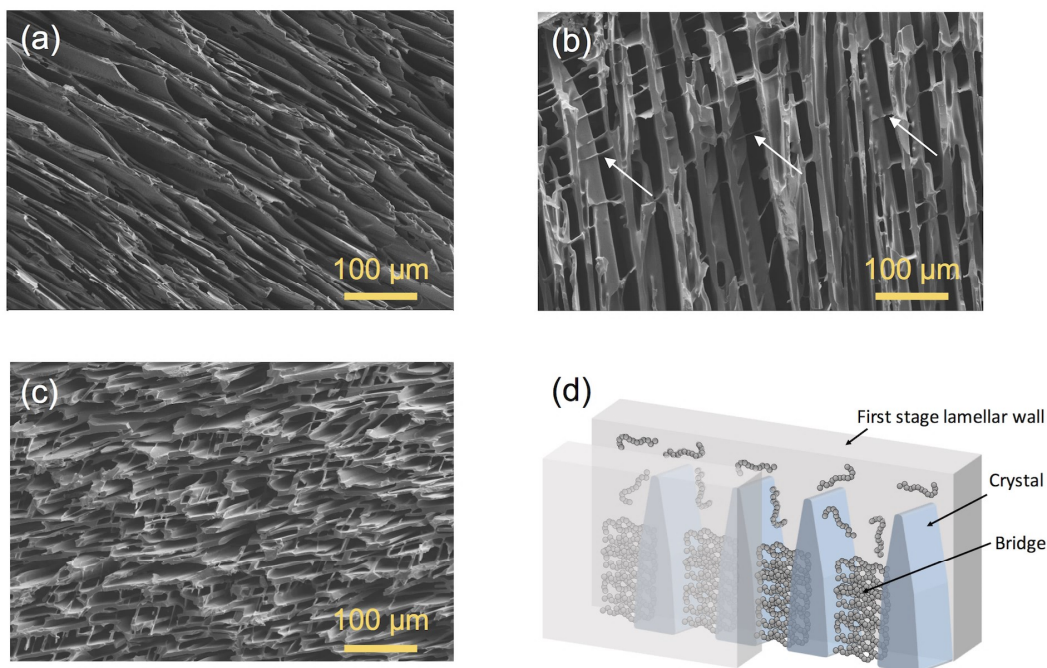


Figure A.2: SEM images of a plane perpendicular to the freezing direction from (a) single-stage freeze casting with 20 vol% polymer concentration, (b) two-stage freeze casting with 5 vol% polymer concentration at the second stage, (c) two-stage freeze casting with 10 vol% polymer concentration at the second stage. (d) Schematic illustration showing bridge formation during the second stage.

Figure A.2 shows SEM images of a plane perpendicular to the freezing direction. Figure A.2a shows an SEM image of SiOC prepared with single-stage freeze casting. The lamellar structure characteristic of DMC solidification is clearly visible [3]. In contrast, Figure A.2b and A.2c show SEM images of two-stage freeze-cast SiOC produced with 5 vol.% and 10 vol.% polymer concentration at the second stage, respectively. Some of the bridges, produced during the second stage, are indicated by arrows in Figure A.2b. These bridges were created by crystals of infiltrated polymer solution which nucleated and grew inside the pore generated during the first stage. When more than two crystals grow inside a single pore, the polymethylsiloxane is segregated between crystals which results in bridges (Figure A.2d). The inter-bridge spacing ranges from approximately 20  $\mu\text{m}$  to 100  $\mu\text{m}$ , consistent with the pore size distribution achieved in single-stage freeze casting DMC; prior pore size measurements by mercury intrusion porosimetry range from 10  $\mu\text{m}$  to 90  $\mu\text{m}$  for a sample produced with a 15  $\mu\text{m/s}$  freezing front velocity [3]. Another consideration



is the high anisotropy of DMC crystals. Similar to ice which produces lamellar structures [13], DMC exhibits preferred growth directions. If a preferred growth plane of the DMC during the second stage is perpendicular to the preferred growth plane of DMC of the first stage, i.e., what produced the lamellar walls, one would expect high bridge densities with small spacings. Alternatively, when a preferred growth plane is parallel to the preferred growth plane existed during the first stage, the bridge spacing tends to be larger. In order to measure the bridge density, two-stage freeze-cast samples were infiltrated with low viscosity, low shrinkage epoxy resin (EpoThin 2, Buehler, Lake Bluff, Illinois, USA), polished and imaged. The number of bridges was evaluated over areas of at least  $2 \text{ mm}^2$ . The results show that bridge density increased as polymer concentration at the second stage increased in agreement with observations in Figs. 1b and 1c (Table A.2). Based on the result, bridge density increased almost linearly with polymer concentration, implying that the thickness of bridges did not significantly change. This further implies that increasing polymer concentration created smaller crystals during freezing, which is similar to observations of Kurtz et al. who found that dendrite tip radius decreases with increasing solute concentration [14].

Table A.2: Bridge density of two-stage freeze-cast samples.

Second stage polymer concentration	5 vol.%	7.5 vol.%	10 vol.%
Average bridge density ( $\text{mm}^{-2}$ )	38	57	82

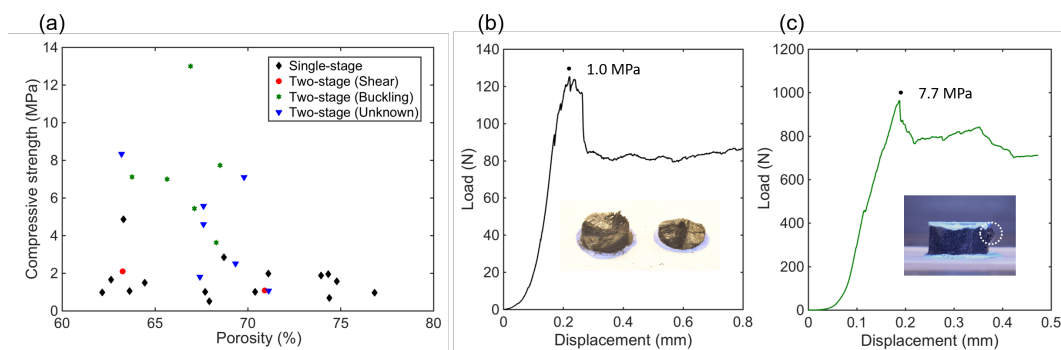


Figure A.3: Compressive strength by single-stage freeze casting and two-stage freeze casting (a). (b) Load displacement curve of single-stage freeze-cast sample. (c) Load displacement curve of two-stage freeze-cast sample. The insets show samples after compression. Note the difference in y-axis scales in (b) and (c).

Compression tests were performed using an Instron 5982 universal testing machine (Instron, Norwood, MA, USA). Cylindrical samples (approximately 7 mm height and 13 mm diameter) were uniaxially compressed parallel to the freezing direction with displacement rate of 0.05 mm/min. A low-shrinkage and high-hardness acrylic system (VariDur 3003, Buehler, Lake Bluff, Illinois, USA) was applied to the top and bottom surfaces of the sample to avoid contact fracture at the sample ends [15]. The compressive strength was calculated based on the peak load in the elastic region. Figure A.3a shows compressive strength as a function of porosity of single-stage and two-stage freeze-cast samples, along with representative load-displacement curves for single-stage (Figure A.3b) and two-stage (Figure A.3c) freeze-cast samples typical of the compressive failure of porous brittle materials with a characteristic linear elastic region followed by a sudden load drop corresponding to initiation of material failure, and a plateau region representing progressive failure [16]. A clear trend is observed that the majority of two-stage freeze-cast samples demonstrate higher compressive strengths than single-stage freeze-cast samples. The compressive strength of single-stage freeze-cast samples shows little dependence on porosity over the range of porosities studied, contrary to other studies of water-based suspension freeze-cast yttria-stabilized zirconia and lanthanum strontium manganite [17]. The inset picture in Figure A.3b shows evidence of shear failure, indicating fracture of struts connecting lamellar walls [11]. This is in contrast to failure behavior in another study on compressive strength of suspension-based freeze-cast ceramics with lamellar pores which showed buckling fracture or wall splitting [5, 17]. There are two possible reasons. First, in suspension-based freeze casting, the bridges are said to be formed by tip splitting and subsequent healing of the crystals [18], whereas polymer chains tend to be expelled from solvent crystals so bridges are rarely formed. These bridges prevent shear failure and samples fail by buckling instead. Second, observations in this study are more similar to a study by Lichtner et al., who observed ceramic sliding along broken walls when samples with poorly oriented pores and walls are loaded [17]. Hence, the freeze-cast SiOC in this study likely has relatively misaligned pores with respect to the freezing and loading axis. On the other hand, the compressive strength for two-stage freeze-cast samples increases as bridge density increases (and porosity decreases). Bridges between lamellar walls enhance compressive strength; an example of one which failed by buckling is shown in the inset image in Figure A.3c. In addition to bridges between lamellar walls, bridges were also observed in domain boundaries in two-stage freeze-cast samples (Figure A.4). These observations imply that any

defects such as cracks or domain boundaries generated during the first stage will be mitigated or eliminated at the second stage. However, two samples demonstrated shear failure (noted by red circles in Figure A.3a). Their compressive strength falls squarely among single-stage freeze-cast samples, where shear failure is likely due to the significant misaligned pores. (Figure A.5)

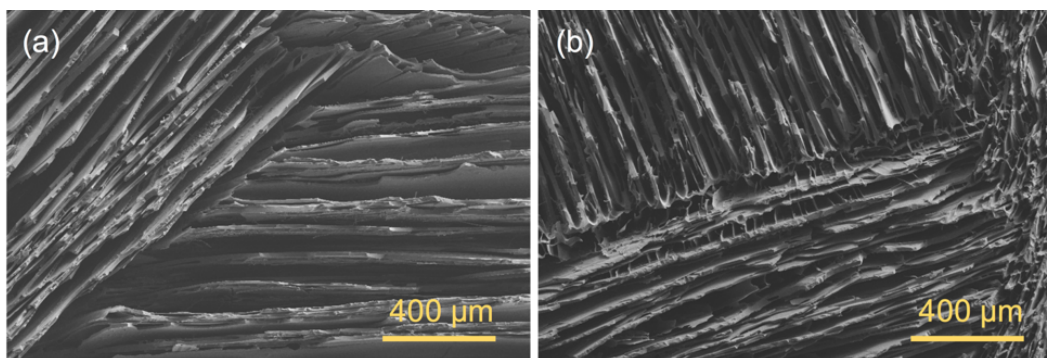


Figure A.4: Example of a domain boundary in (a) single-stage freeze-cast sample (20 vol.%), and (b) two-stage freeze-cast sample (5 vol.% at the second stage).

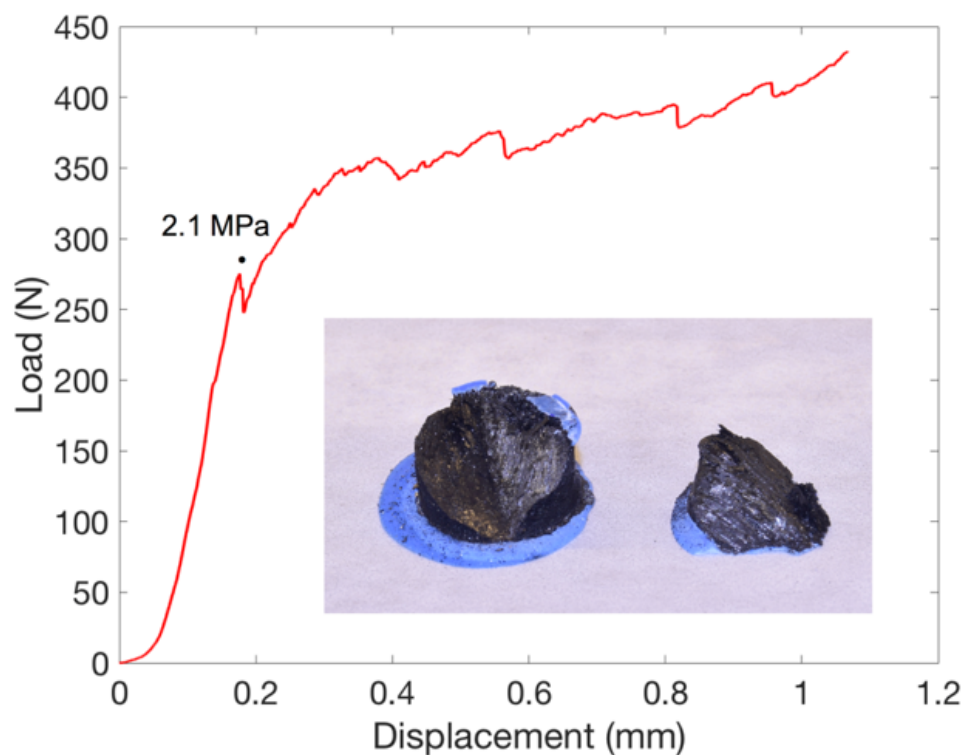


Figure A.5: Load-displacement curve of the two-stage freeze-cast sample which exhibited noticeable low strength. The inset shows sample after compression.

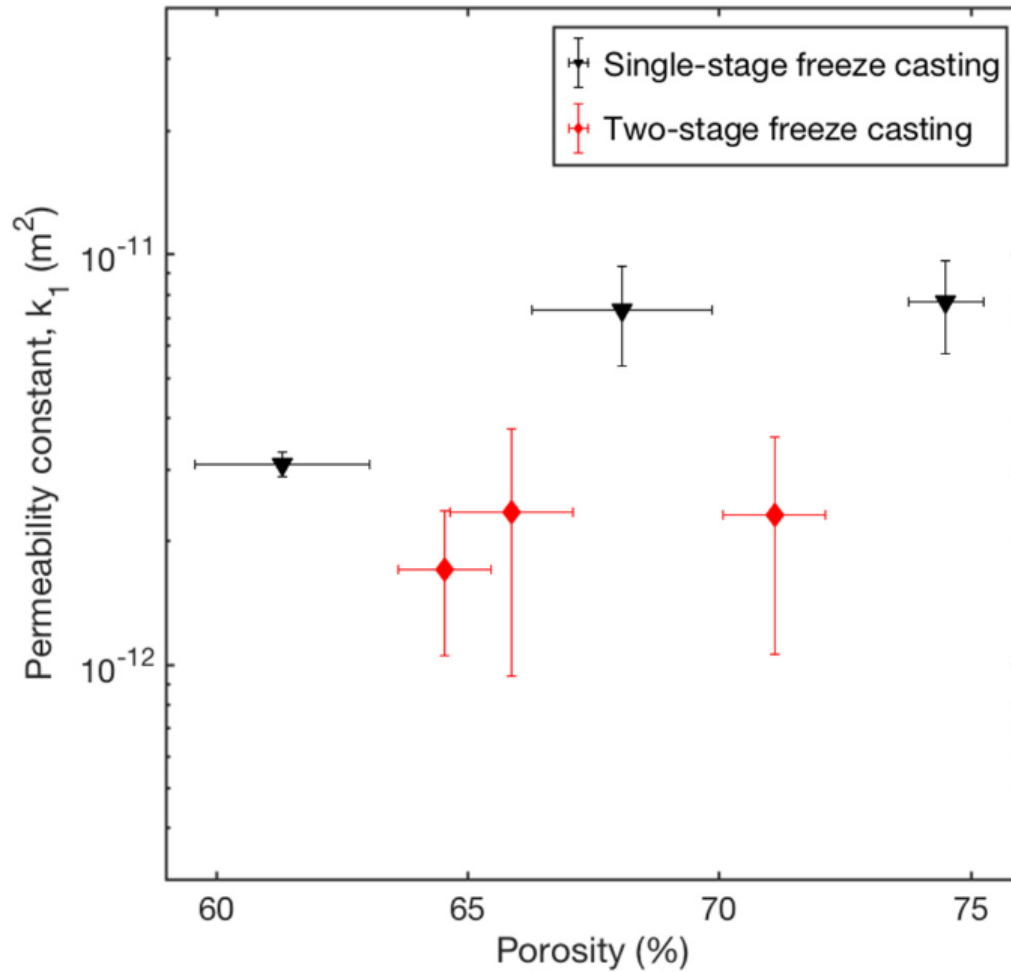


Figure A.6: Permeability constants of samples by single-stage freeze casting and two-stage freeze casting.

The permeability of single-stage freeze-cast and two-stage freeze-cast samples were compared. During permeability measurements, deionized water was pumped through the sample at pressures ranging from 6 kPa to 145 kPa by a voltage-controlled pump; pressure and water mass flow were measured simultaneously using a pressure transducer and an electronic scale, respectively. The permeability of porous media can be determined from the Forchheimer equation [21–23][19, 20, 21],

$$\frac{\Delta P}{L} = \frac{\mu}{k_1} v + \frac{\rho}{k_2} v^2$$

where  $\Delta P$  is the pressure drop across the samples,  $L$  is sample thickness along flow direction,  $v$  is flow velocity,  $\mu$  is viscosity of liquid,  $\rho$  is density of liquid, and  $k_1$  and

$k_2$  are Darcian and non-Darcian permeability constants. The second term on the right hand side represents non-linearity in the pressure drop and flow velocity, which corresponds to a high Reynolds number where the inertial force is non-negligible as with gas flow [20]. In this experiment, since the pressure drop was linear with flow velocity, the second term was ignored and only Darcian constants are reported. Figure A.6 shows permeability constants of single-stage freeze casting and two-stage freeze casting. As expected, permeability constants decrease as porosity decreases. Similarly to compression testing results, the variation in permeability constant for a given condition is likely due to variation in pore alignment. Additionally, it is notable that two-stage freeze cast samples always have lower permeability than single-stage freeze-cast samples. The reduction in permeability in two-stage freeze-cast samples is likely due to higher pressure drop resulting from the additional surface area of the bridges.

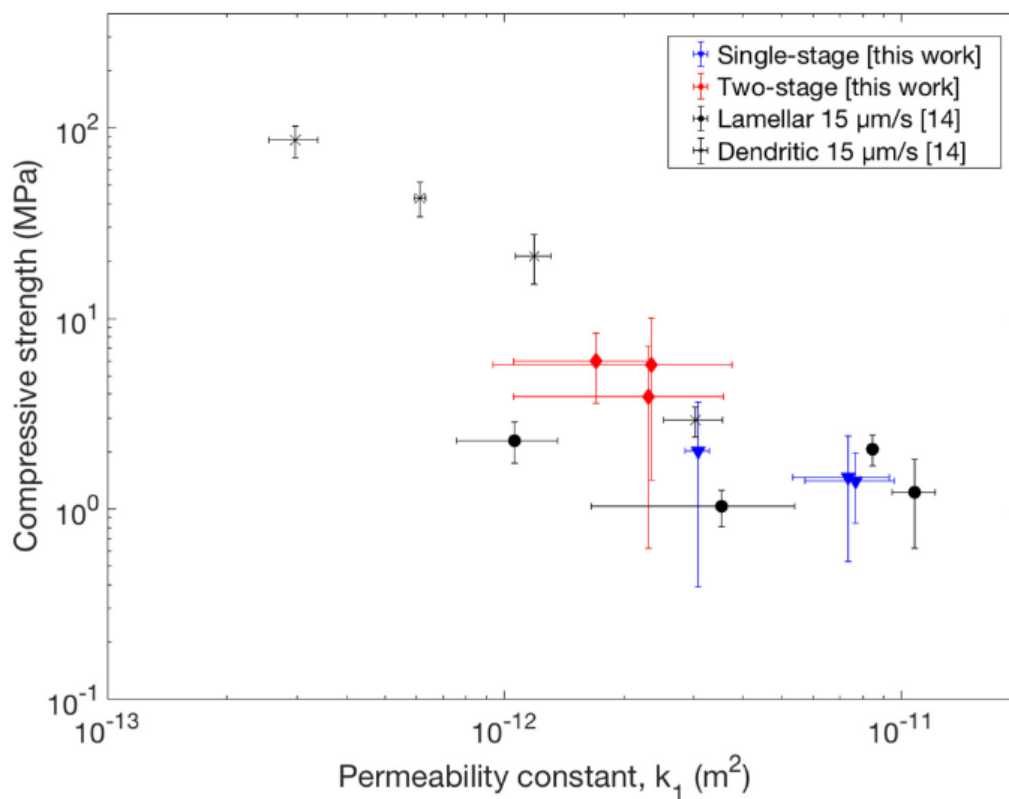


Figure A.7: Compressive strength and permeability constants compared to the Naviroj study on lamellar and dendritic pore structures [11].

Figure A.7 shows compressive strength and permeability constants for single-stage freeze-cast samples and two-stage freeze-cast samples along with reported val-

ues by Naviroj [11]. Two-stage freeze-cast samples have comparable compressive strength to dendritic pore structures with similar permeability constants. The samples produced via two-stage freeze casting show a greater range of permeability and compressive strength than freeze-cast SiOC reported by Naviroj [11]. This likely can be attributed to mold heating employed in this study, which prevents nucleation and growth from the mold, leading to fewer domains of different pore alignment; compressive strength and permeability are very sensitive to a pore orientation. From the result of compression and permeability measurements, control of pore alignment is crucial to take further advantage of two-stage freeze casting. It has been shown that significant misalignment of pore channels with respect to freezing direction resulted in shear failure and low compressive strength despite the presence of bridges, and also low permeability. However, large-scale pore alignment is possible by introducing a wedge between the cold plate and the solution to control nucleation and growth with a dual temperature gradient [22] or placing a grain selection template to align pores by reducing off-axis crystals [23]. Two-stage freeze casting combined with these large-scale pore alignment methods is expected to produce porous ceramics with high strength, high permeability, as well as highly anisotropic thermal properties which will be useful in earlier mentioned applications.

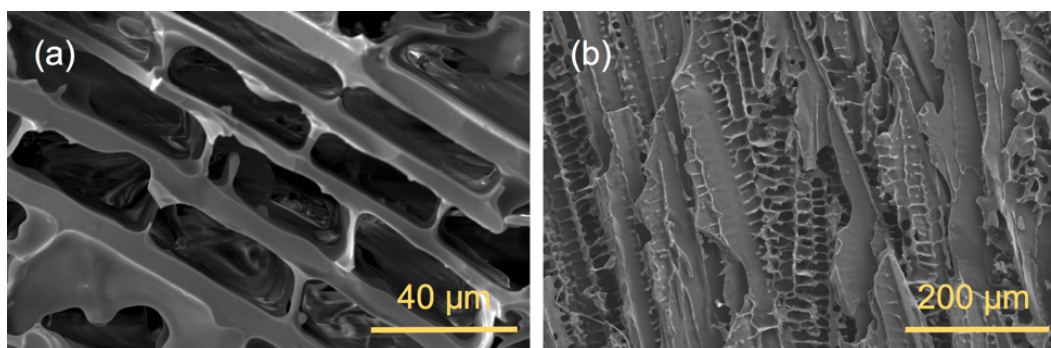


Figure A.8: SEM images of two-stage freeze-cast SiOC using DMC as the solvent in the first stage and cyclohexane at the second stage. (a) Transverse image (a plane perpendicular to freezing direction) and (b) longitudinal image (a plane parallel to freezing direction).

It should be noted that any appropriate solvent for preceramic polymers can be used to tailor the pore network using two-stage freeze casting. For example, cyclohexane, which forms dendrites, has been used as a second stage solvent to create bridges. (Figure A.8). In addition, two-stage freeze casting enables hierarchical pore networks (Figure A.9). Cyclohexane as a first stage solvent creates dendritic pores, while cyclooctane forms isotropic pores [3] during the second stage.

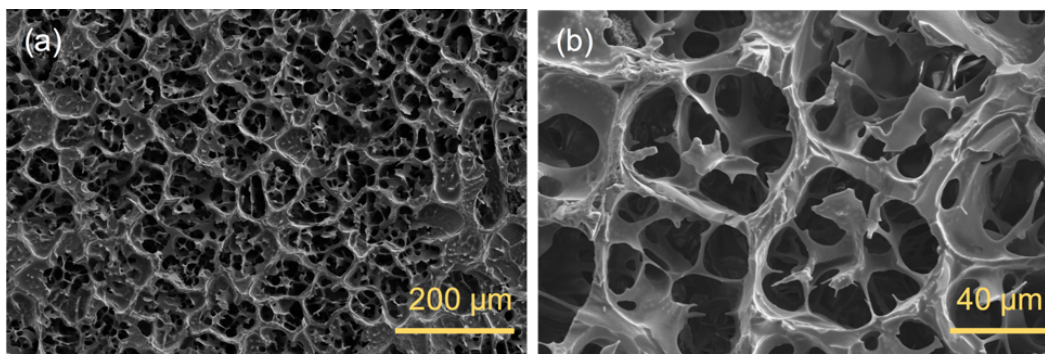


Figure A.9: SEM images of the hierarchical pore structure in two-stage freeze-cast SiOC using cyclohexane as the solvent in the first stage and cyclooctane at the second stage at (a) low magnification and (b) high magnification. A grain-selection template [25] was used at the first stage.

In summary, hierarchical lamellar microstructures with interlamellar bridges were created by two-stage freeze casting of a preceramic polymer. Unlike other bridge formation methods developed in suspension-based freeze casting, bridge density can be controlled simply by changing polymer concentration during the second stage. As the bridge density increased, the compressive strength increased by nearly threefold over those produced by single-stage freeze casting. It was shown that two-stage freeze-cast samples tend to exhibit dendritic-like properties which show a stronger correlation between compressive strength and permeability. Compressive strength and permeability measurements show that misalignment of pores is not favorable for either property, however, two-stage freeze casting coupled with pore alignment methods [22, 23] would enable to tune compressive strength and permeability for desired applications. Finally, the two-stage freeze casting method is potentially applicable to suspension-based freeze casting as long as the green body at the first stage can sustain infiltration of the suspension during the second stage, which is possible by choosing a suitable binder.

## References

- [1] Byung-Ho Yoon et al. “Highly aligned porous silicon carbide ceramics by freezing polycarbosilane/camphene solution”. In: *Journal of the American Ceramic Society* 90.6 (2007), pp. 1753–1759.
- [2] Maninpat Naviroj et al. “Directionally aligned macroporous SiOC via freeze casting of preceramic polymers”. In: *Journal of the European Ceramic Society* 35.8 (2015), pp. 2225–2232.

- [3] Maninpat Naviroj, Peter W. Voorhees, and Katherine T. Faber. “Suspension- and solution-based freeze casting for porous ceramics”. In: *Journal of Materials Research* 32.17 (2017), pp. 3372–3382.
- [4] Huixing Zhang et al. “Macro/mesoporous SiOC ceramics of anisotropic structure for cryogenic engineering”. In: *Materials & Design* 134 (2017), pp. 207–217.
- [5] Jordi Seuba et al. “Mechanical properties and failure behavior of unidirectional porous ceramics”. In: *Scientific reports* 6 (2016), p. 24326.
- [6] Qiang Fu et al. “Freeze casting of porous hydroxyapatite scaffolds. II. Sintering, microstructure, and mechanical behavior”. In: *Journal of Biomedical Materials Research Part B: Applied Biomaterials: An Official Journal of The Society for Biomaterials, The Japanese Society for Biomaterials, and The Australian Society for Biomaterials and the Korean Society for Biomaterials* 86.2 (2008), pp. 514–522.
- [7] Etienne Munch et al. “Architectural control of freeze-cast ceramics through additives and templating”. In: *Journal of the American Ceramic Society* 92.7 (2009), pp. 1534–1539.
- [8] Michael M. Porter et al. “Bioinspired scaffolds with varying pore architectures and mechanical properties”. In: *Advanced Functional Materials* 24.14 (2014), pp. 1978–1987.
- [9] Dipankar Ghosh et al. “Platelets-induced stiffening and strengthening of ice-templated highly porous alumina scaffolds”. In: *Scripta Materialia* 125 (2016), pp. 29–33.
- [10] Emily Catherine Hammel, O.L.-R. Ighodaro, and O.I. Okoli. “Processing and properties of advanced porous ceramics: An application based review”. In: *Ceramics International* 40.10 (2014), pp. 15351–15370.
- [11] Maninpat Naviroj. “Silicon-based porous ceramics via freeze casting of pre-ceramic polymers”. PhD thesis. Northwestern University, 2017.
- [12] Sarah M Miller, Xianghui Xiao, and Katherine T. Faber. “Freeze-cast alumina pore networks: Effects of freezing conditions and dispersion medium”. In: *Journal of the European Ceramic Society* 35.13 (2015), pp. 3595–3605.
- [13] Sylvain Deville. “Freeze-casting of porous ceramics: a review of current achievements and issues”. In: *Advanced Engineering Materials* 10.3 (2008), pp. 155–169.
- [14] W. Kurz, B. Giovanola, and R. Trivedi. “Theory of microstructural development during rapid solidification”. In: *Acta metallurgica* 34.5 (1986), pp. 823–830.
- [15] Mehrad Mehr et al. “Epoxy interface method enables enhanced compressive testing of highly porous and brittle materials”. In: *Ceramics International* 42.1 (2016), pp. 1150–1159.



- [16] Lorna J. Gibson and Michael F. Ashby. *Cellular solids: structure and properties*. Cambridge university press, 1999.
- [17] Aaron Lichtner et al. “Effect of macropore anisotropy on the mechanical response of hierarchically porous ceramics”. In: *Journal of the American Ceramic Society* 99.3 (2016), pp. 979–987.
- [18] Sylvain Deville et al. “Freezing as a path to build complex composites”. In: *Science* 311.5760 (2006), pp. 515–518.
- [19] E.A. Moreira, M.D.M. Innocentini, and J.R. Coury. “Permeability of ceramic foams to compressible and incompressible flow”. In: *Journal of the European Ceramic Society* 24.10-11 (2004), pp. 3209–3218.
- [20] Jean-François Despois and Andreas Mortensen. “Permeability of open-pore microcellular materials”. In: *Acta materialia* 53.5 (2005), pp. 1381–1388.
- [21] M.D.M. Innocentini et al. “Permeability of porous gelcast scaffolds for bone tissue engineering”. In: *Journal of Porous Materials* 17.5 (2010), pp. 615–627.
- [22] Hao Bai et al. “Bioinspired large-scale aligned porous materials assembled with dual temperature gradients”. In: *Science advances* 1.11 (2015), e1500849.
- [23] Maninpat Naviroj et al. “Nucleation-controlled freeze casting of preceramic polymers for uniaxial pores in Si-based ceramics”. In: *Scripta Materialia* 130 (2017), pp. 32–36.

*Appendix B*

## FREEZING CONDITIONS

Table B.1: List of freezing front velocities and temperature gradients used in Chapter 3 for 20 wt.% polymer-cyclohexane solution.

	Freezing front velocity	Temperature gradient
1	$1.1 \pm 0.3 \mu\text{m/s}$	$2.3 \pm 0.0 \text{ K/mm}$
2	$1.8 \pm 0.5 \mu\text{m/s}$	$2.4 \pm 0.1 \text{ K/mm}$
3	$5.7 \pm 0.8 \mu\text{m/s}$	$2.4 \pm 0.0 \text{ K/mm}$
4	$8.4 \pm 0.7 \mu\text{m/s}$	$2.7 \pm 0.0 \text{ K/mm}$
5	$15.5 \pm 1.6 \mu\text{m/s}$	$2.6 \pm 0.1 \text{ K/mm}$
6	$17.2 \pm 1.8 \mu\text{m/s}$	$2.2 \pm 0.1 \text{ K/mm}$
7	$0.6 \pm 0.2 \mu\text{m/s}$	$5.2 \pm 0.4 \text{ K/mm}$
8	$0.7 \pm 0.2 \mu\text{m/s}$	$4.9 \pm 0.2 \text{ K/mm}$
9	$1.5 \pm 0.4 \mu\text{m/s}$	$5.0 \pm 0.3 \text{ K/mm}$
10	$2.9 \pm 0.8 \mu\text{m/s}$	$4.6 \pm 0.2 \text{ K/mm}$
11	$8.4 \pm 1.2 \mu\text{m/s}$	$5.3 \pm 0.3 \text{ K/mm}$
12	$10.3 \pm 1.2 \mu\text{m/s}$	$5.1 \pm 0.3 \text{ K/mm}$

### Appendix C

## COMPARISON OF THE CONVENTIONAL FREEZING AND THE GRADIENT CONTROLLED FREEZING

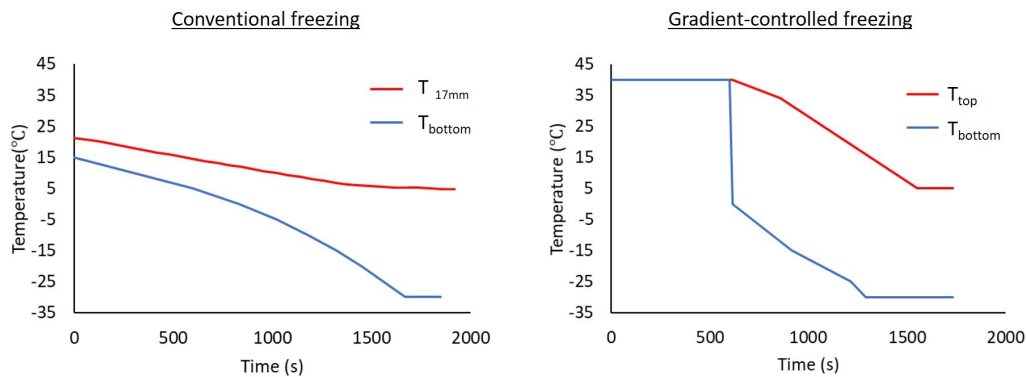


Figure C.1: Freezing profile of Conventional freezing ( $V = 15 \mu\text{m/s}$ ) and gradient-controlled freezing ( $V = 15 \mu\text{m/s}$ ,  $G = 2.6 \text{ K/mm}$ )

Figure C.1 shows freezing profiles for a conventional freezing and a gradient-controlled freezing. Since the temperature at the top side is not controlled in the conventional freezing, a thermocouple was inserted in the solution to measure the temperature during the freezing. The thermocouple measured a temperature at  $\sim 17$  mm from the bottom and the temperature is plotted as  $T_{17\text{mm}}$  in Figure C.1. As shown, the temperature difference between two points gets larger as time proceeds. In this conventional freezing, the temperature gradient cannot be controlled. In contrast, the temperature difference between top and bottom sides are similar during the gradient-controlled freezing. With the temperature control from both sides, temperature gradient can be maintained at  $2.6 \pm 0.1 \text{ K/mm}$ . Another advantage of the gradient-controlled freeze casting is that one can change or control temperature gradient by two ways. First, one can simply change the mold height, which was demonstrated in Chapter 3. Another way is to change the temperature difference between top and bottom sides. This demonstrates the advantages of controlling freezing front velocity and temperature gradient by the gradient controlled freeze-casting setup.

The homogeneity of the freeze-cast structure was investigated. A sample was freeze-cast under freezing front velocity of  $15 \mu\text{m/s}$  and temperature gradient of  $2.6$

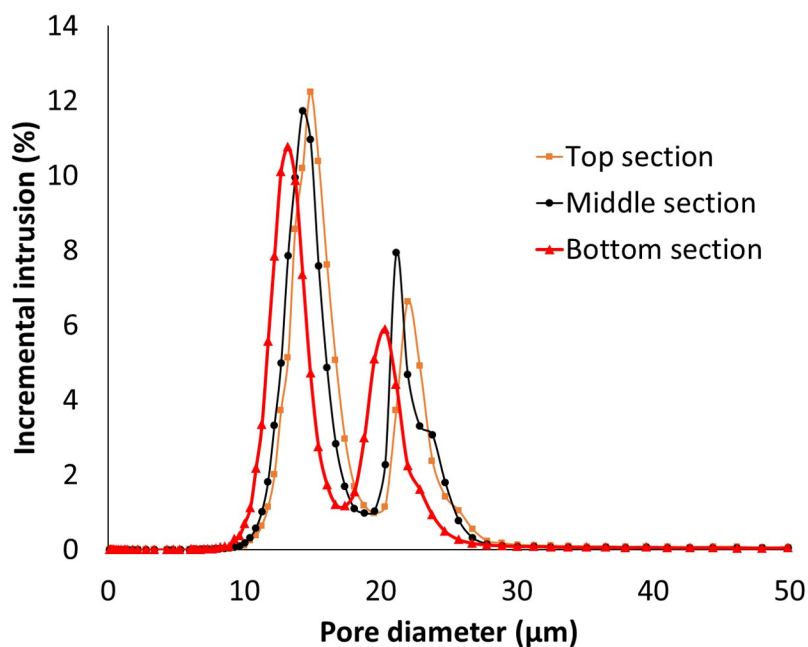


Figure C.2: Pore size distribution from three different sections.

Table C.1: List of the peak pore diameters for primary and secondary pores from Figure C.2

	Primary pore diameter	Secondary pore diameter
Top section	22.0 $\mu\text{m}$	14.8 $\mu\text{m}$
Middle section	21.1 $\mu\text{m}$	14.3 $\mu\text{m}$
Bottom section	20.3 $\mu\text{m}$	13.7 $\mu\text{m}$

K/mm. The sample was pyrolyzed under the presence of water vapor in addition to argon as described in subsection 7.1.2 (pyrolysis at 1100 °C under a mixed argon/water atmosphere created by flowing argon over a beaker of water at 85 °C before entering the furnace). The three specimens (top, middle, bottom section) were sectioned from a sample and characterized by mercury intrusion porosimetry. A pore size distribution and peak pore diameters are shown in Figure C.2 and Table C.1, respectively. As shown, the peak primary and secondary pore sizes are similar in the three sections, and the differences were found to be around 8% or smaller.

## Appendix D

## INFLUENCE OF PRECERAMIC POLYMER CONCENTRATION

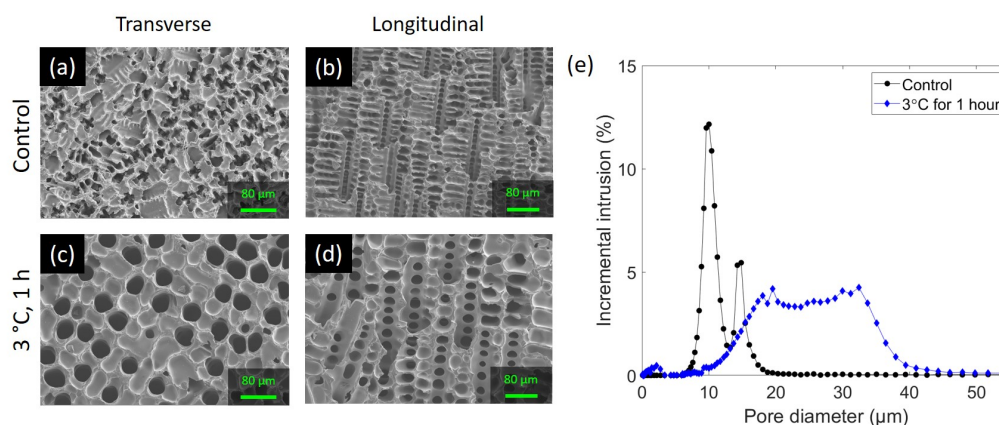


Figure D.1: SEM images showing (a, b) a control sample, and (c,d) a sample coarsened at 3 °C for 1 hour. (e) Pore size distribution from 30 wt.% preceramic polymer solution.

Figure D.1 displays SEM images and the pore size distribution of the control sample and the sample coarsened at 3 °C for 1 hour created from the 30 wt.% solution. The morphologies of primary pores and secondary pores change similarly to the 20 wt.% solution (Figures D.1 a-d). In 20 wt.% solution, the volume fraction of secondary pores decreased by coarsening (Figure 5.8), making the primary pores dominant pores as shown by pore size distribution (Figure 5.7). SEM images also demonstrated that the sample coarsened at 4 °C for 1 hour exhibited honeycomb-like structure (Figure 5.4g). This is, however, not the case in the 30 wt.% solution as shown in the SEM image (Figure D.1c). In the 30 wt.% solution, although the secondary pore size increases, the structure still remains dendritic, leaving a large volume of secondary pores even after 1 hour coarsening (Figure D.1e). We hypothesize that the presence of long secondary pores after coarsening can be attributed to the low diffusion coefficient of polymer in the solution. With higher polymer concentrations, the solution has higher viscosity and shorter gelling time, which both contribute to the reduction of diffusion coefficient in the solution. This could slow the shortening of secondary arms.

Chen and Kattamis proposed a model to describe the increase in secondary arm spacing and decrease of secondary arm length [1], in which the secondary arm

spacings increase by mass diffusion from small secondary arms to large adjacent secondary arms. Alternatively, a decrease in secondary arm length can occur by the mass diffusion between the tip of the secondary arms and the root of the secondary arms. This latter case requires a longer diffusion distance. Because of low diffusivity in the 30 wt.% solution, the latter process was slowed down, maintaining long secondary pores. As a result, a large volume of secondary pores are still present in pore size distributions of materials with higher solute content.

### References

- [1] M. Chen and T.Z. Kattamis. "Dendrite coarsening during directional solidification of Al-Cu-Mn alloys". In: *Materials Science and Engineering: A* 247.1-2 (1998), pp. 239–247.